Synthesis and Characterization of Functional Thin Ultra-Low Density Coatings Inside Hollow Spheres

DISSERTATION

Doctoral thesis approved for the fulfillment of the requirements for the degree of Dr. rer. nat.
at the
Department of Materials Science,
Technische Universität Darmstadt

TECHNISCHE UNIVERSITÄT DARMSTADT

Submitted by

Dipl. Phys. Tom Braun

Date of thesis submission: January 15th, 2018
Date of examination: July 13th, 2018

Thesis approved by

Supervisor Prof. Dr. Horst Hahn
Co-supervisor Prof. Dr. Wolfgang Donner

Darmstadt, 2018

Verfasser: Braun, Tom
Titel: Synthesis and Characterization of Functional Thin Ultra-Low Density Coatings Inside Hollow Spheres

Dissertationsort: Darmstadt, Technische Universität Darmstadt

Jahr der Veröffentlichung der Dissertation auf TUprints: 2018

Tag der mündlichen Prüfung: 13. Juli 2018

Board of examiners

Head:	Prof. Dr. Wolfram Jaegermann
Supervisor:	Prof. Dr.-Ing. Horst Hahn
Co-supervisor:	Prof. Dr. Wolfgang Donner
Examiner:	Prof. Dr. Wolfgang Ensinger
Examiner:	Prof. Dr. Steffen Hardt

Declaration

I hereby declare that the presented dissertation is based on original research and is the result of my own work. I certify that this dissertation contains no material which has been accepted for the award of any other degree in my name, in any university or other tertiary institution and, to the best of my knowledge and belief, contains no material previously published or written by another person, except where due reference has been made in the text.

Darmstadt, December 12th, 2017

Abstract

Uniform coatings on the inner surface of hollow spheres have applications in optical devices, time- or site-controlled drug release, and heat storage devices. Spherical shells that contain a thin layer of ultra-low density polymer foam have also attracted attention in the inertial confinement fusion community where they can be used to bring dopants for diagnostics and nuclear physics experiments in direct contact with the deuterium-tritium (DT) fuel or to study new ignition regimes by enabling the formation of uniform liquid DT fuel layers. The uniformity of these coatings is often critical for the application performance and, therefore, requires precise understanding and control over the coating process and its parameters.

Rather than trying to fabricate free-standing foam shells, as it was reproducibly done in the fusion community, a new approach can be explored: using prefabricated hollow spherical shells as molds to cast concentric, thin-walled, low-density foam layers using sol-gel chemistry. For this purpose, a molecular precursor solution is inserted into the shell through a tiny hole using a pressure gradient filling process, where it transforms into a high-viscosity polymer fluid and ultimately gels during rotation, creating a uniform gel layer. The remaining solvent is then removed from the shell via supercritical drying, leaving a uniform, ultra-low density aerogel layer in the sphere.

This thesis presents a detailed step by step study on the synthesis and characterization of functional, ultra-low density coatings inside hollow spheres using this novel approach. It will describe how polymer-based sol–gel chemistry can be utilized to achieve ultra-low density coatings and report on in situ real-time radiography experiments that provide critical spatiotemporal information about the distribution of fluids inside hollow spheres during uniaxial rotation. An approach to remove the solvent from the gel in the shell without damaging the coated layer is presented and lastly a methodology on casting doped polymer films on the inside of spherical capsules is developed.

Kurzfassung

Gleichmäßige Beschichtungen auf der Innenseite von Hohlkugeln haben vielseitige Anwendungen, unter anderem in Instrumenten der Optik, in der orts- oder zeitspezifischen Freisetzung von Medikamenten und in der Wärmespeicherung. Kugelförmige Kapseln, deren Innenseite mit einer dünnen Schicht eines Polymerschaums mit extrem geringer Dichte beschichtet sind, sind ebenfalls von großem Interesse für Trägheitsfusionsexperimente. Hier wird die Beschichtung dazu benutzt, Fremdatome in direkten Kontakt mit dem Fusionsbrennstoff zu bringen, welches zur Diagnose und für Kernphysikexperimente genutzt wird. Die gleichmäßige Beschichtung der kugelförmigen Kapsel mit einem Polymerschaum erlaubt es ebenfalls, verschiedene Kompressionsbedingungen des zu zündenden Brennstoffs zu studieren, indem sie Experimente mit flüssigen Fusionsbrennstoffen in Hohlkugeln ermöglicht. Die Gleichmäßigkeit der Beschichtungen ist hierbei kritisch für die erfolgreiche Ausführung der oben genannten Anwendungen und benötigt daher ein präzises Verständnis und genaue Kontrolle des Beschichtungsprozesses und der jeweiligen Parameter.

Anstatt zuerst eine frei stehende Polymerschaumschale zu produzieren, auf die später eine nicht poröse Schicht aufgetragen wird, wird in dieser Arbeit ein neuer Ansatz verfolgt: eine vorgefertigte, formgebende Hohlkugel wird benutzt, um auf deren Innenseite mithilfe eines Sol-Gel-Prozesses eine konzentrische, dünne Polymerschaumschicht mit geringer Dichte aufzutragen. Die dazu benötigte flüssige Reaktionsmischung wird mithilfe eines Vakuumsprozesses durch ein 30 bis 50 Mikrometer großes Loch in die Hohlkugel gebracht, wo diese unter Rotation in einen viskoelastischen Festkörper übergeht. Dies erzeugt einen Gelfilm auf der Innenseite der Hohlkugel, welcher aus einem Gelgerüst und dem von ihm eingeschlossenen Lösungsmittel besteht. Der so erzeugte Gelfilm wird durch überkritisches Trocknen in einen Polymerschaumfilm überführt.

In dieser Dissertation wird der detaillierte Synthese- und Charakterisierungsprozess dieses neuen Ansatzes vorgestellt, der für die Beschichtung von Hohlkugeln mit funktionalen Polymerfilmen geringer Dichte geeignet ist. Zuerst wird beschrieben, wie mithilfe eines Sol-Gel-Prozesses gleichmäßige Beschichtungen mit geringer Dichte

erreicht werden. Weiter wird ein eigenständig entwickeltes Experiment erläutert, welches es mit Hilfe von Röntgenaufnahmen ermöglicht, die Verteilung von Flüssigkeiten in Hohlkugeln in-situ und in Echtzeit unter Rotation zu untersuchen. Weiterhin wird ein Ansatz zur zerstörungsfreien Entfernung von Lösungsmitteln aus Gelfilmen in Hohlkugeln präsentiert und zuletzt eine Methode aufgezeigt, die es erlaubt, dotierte Polymerfilme auf die Innenseite einer Hohlkugel aufzutragen.

Acknowledgements

It is my great pleasure to thank the many persons who have made my graduate studies a unique and fulfilling experience.

First and foremost, I would like to express my sincere gratitude to Jürgen Biener without whom this thesis would not exist. Over the last couple of years his guidance, patience, and continuous support helped me tremendously on my scientific and personal path.

I would like to thank my advisor Prof. Horst Hahn for his helpful discussions and suggestions; also, in particular, for his support of this external dissertation and for bearing the administrative burden connected with that.

I would like to thank Alex Hamza for hosting me at Lawrence Livermore National Laboratory (LLNL) and the very friendly and motivating atmosphere he created in the Nanoscale Synthesis and Characterization Laboratory. Within the laboratory, I would like to thank the many people who contributed to this thesis, specifically Sung Ho Kim, Christopher Walton, Marcus Worsley, Monika Biener, Kuang Jen Wu, Christoph Dawedeit, Trevor Willey, Anthony van Buuren, Bernie Kozioziemski, Jim Sater, John Sain, and Joe Satcher.

My gratitude goes out to Michael Stadermann and Abbas Nikroo, for believing in me and allowing me the opportunity to advance this project to today's level.

I also would like to thank my friends, in particular, Kari and Chris Hammond, Marco Mehl, Vanessa Nowak, Liesa Zackor, Josefine Messing, Vicky Anspach, Amy Hale, Judith Pierce, and Bernhard Haux, who kept things in perspective during my studies no matter what continent they were on.

Most importantly, I would like to thank my parents, Kerstin and Udo, my sister Sabine, and my beloved girlfriend Brianna for their unconditional love and support. Words alone cannot express my feelings for how much I owe them.

Table of Contents

Chapter 1: Introduction

Functional, uniform thin film coatings on spherical surfaces are increasingly being applied by the scientific community and industry. Examples include, but are not limited to, spherical reflectors[1], integrating spheres[2-3], site[4-5] or time specific[6] drug delivery, and high-power latent heat storage devices or floating heat capacities.[7] Foam lined hollow spheres are also of interest to the inertial confinement fusion community[8-12], where the porous coating on the inside of the spherical target can be used as surrogate for the cryogenic deuterium-tritium (DT) fuel ice layer[8, 12-13] or to bring dopants for diagnostics and nuclear physics experiments in direct contact with the DT fuel.[14-15] More importantly, the foam-lined ICF targets can also be used to study new ignition regimes by enabling the formation of uniform liquid DT fuel layers.[13]

The shell diameter for all applications mentioned above is usually 0.5-2 mm[7, 16-17] with the exception of integrating spheres, where the sphere diameter can be as large as 3 m. In all cases, the coating uniformity is crucial for the application performance and thus requires deterministic control of the coating process.[3, 18-21] In reality, however, most spherical coatings are not ideal, leading to potential error[18] and performance deterioration[9, 21-22].

This thesis will describe the synthesis and characterization of functional, ultra-low density coatings inside hollow spheres that meet the requirements for coating uniformity and mechanical stability for the use in inertial confinement fusion experiments. Specifically, it will address how 1) polymer-based sol–gel chemistry was utilized to achieve ultra-low density coatings, 2) how prefabricated ablator shells can be used as molds to cast thin-walled foam shells, 3) how the viscosity of the sol-gel and the coating parameters need to be tuned to produce highly uniform films in hollow spheres, 4) how to remove the solvent from the gel without damaging the coated layer, and 5) how to cast doped polymer films on the inside of spherical capsules. The successful development of this wetted foam target design, as described in this thesis, enables a new experimental platform that was recently used to study new ignition regimes with the first ever liquid deuterium-tritium (DT) fuel layer implosion at the National Ignition Facility, Lawrence Livermore National Laboratory.

1.1. NIF

The National Ignition Facility (NIF) at Lawrence Livermore National Laboratory in California is the largest and most energetic laser facility in operation to date. It comprises of a precision laser system that is capable of delivering 1.8 MJ at 500 TW of 350 nm light to a target[23] and has been operational since 2009. The NIF laser consists of 192 beams and can be focused onto a variety of targets that allow scientist to create extreme states of matter, such as temperatures exceeding 10^8 K, pressures in the TPa regime, and densities that are similar to those in the cores of planets and stars.[24] It has, for example, successfully been used to replicate the properties of materials deep within the core of Jupiter by compressing diamond, one of the least compressible materials, to 5 TPa.[25] NIF is also extensively used to study controlled nuclear fusion reactions by compressing and heating a solid or liquid deuterium-tritium mixture until the product of temperature and density is high enough, that a nuclear fusion reaction is initiated. However, Lawson stated that to achieve controlled nuclear fusion reactions "not only must the temperature be sufficiently high, but also the reaction must be sustained long enough for a definite fraction of the fuel to be burnt."[26-27] Therefore, the plasma that is created in the reaction needs to be confined so that the product of temperature and pressure necessary for the fusion reaction reaches the required threshold. Three approaches to confine the plasma are currently being explored in the scientific community: Magnetic Confinement, Z-Pinch, and Inertial Confinement.

In *Magnetic Confinement Fusion* experiments magnetic fields are used to confine the plasma as the charged particles within the plasma can only move freely along the magnetic field lines. Two of the most advanced geometrical designs in Magnetic Confinement Fusion are the Tokamak[28] and Stellarator[29] design. Tokamaks currently in operation are JET in Culham, United Kingdom and ASDEX Upgrade in Garching, Germany. ITER, an experimental tokamak reactor, in Caderache, France is in the process of construction. Wendelstein 7-X in Greifswald, Germany, is an experimental stellarator that theoretically allows continuous operation and prevents potential instabilities caused by the plasma current. It produced the first hydrogen plasma in February 2016.

The *Z-Pinch*[30-31] could be classified as an Inertial Confinement Fusion approach; however, since it uses an electrical current in the plasma to generate a magnetic field that compresses it, it is listed as a separate confinement approach here. The current into the plasma is provided by releasing the charge of large capacitors, which creates a large magnetic field that causes the plasma to be pinched into a smaller cylinder to reach fusion conditions. Some Z-Pinch facilities currently in operation are the Nevada Terawatt Facility, Reno, USA, the MAGPIE facility in London, United Kingdom, or the Z Pulsed Power Facility at Sandia National Laboratory in Albuquerque, USA.

The National Ignition Facility uses an *Inertial Confinement Fusion* approach to compress and heat a solid or liquid deuterium-tritium mixture until the product of temperature and density is high enough, that the reaction reaches the Lawson criterion. Nuckolls et al. published an approach to reach the high densities that are required that suggested a spherical implosion of a microsphere filled with the deuterium-tritium-mixture, or *fuel*.[32-33] This microsphere, which in this thesis is often referred to as a *target*, can be compressed by high-powered laser or ion beams that hit the spherical target symmetrically from all sides. “This causes the ablator, the outer layer of the target, to vaporize in an outward direction, creating a reaction force, which accelerates the residue of the target in the opposite inward direction. The compressed deuterium-tritium mixture is extremely densified and heated up, causing the atoms to fuse. The confinement time is short enough that the inertia of the plasma itself is enough to confine it, leading to the name Inertial Confinement Fusion.”[34] At the NIF, a laser is used to compress the target, however, the laser is not shot directly onto the target, but into a hohlraum surrounding the target, which is why the approach is often referred to as *indirect drive*. The cylindrical hohlraum is usually about 1 cm long by 6 mm diameter, and made of a high atomic number Z element such as Au.[35] However, different hohlraum designs have been proposed and are under investigation.[36-38] In the indirect drive approach currently used at the NIF, the laser light is converted into X-rays that are absorbed by the target, which cause a more symmetric implosion of the target. (Figure 1-1 a)

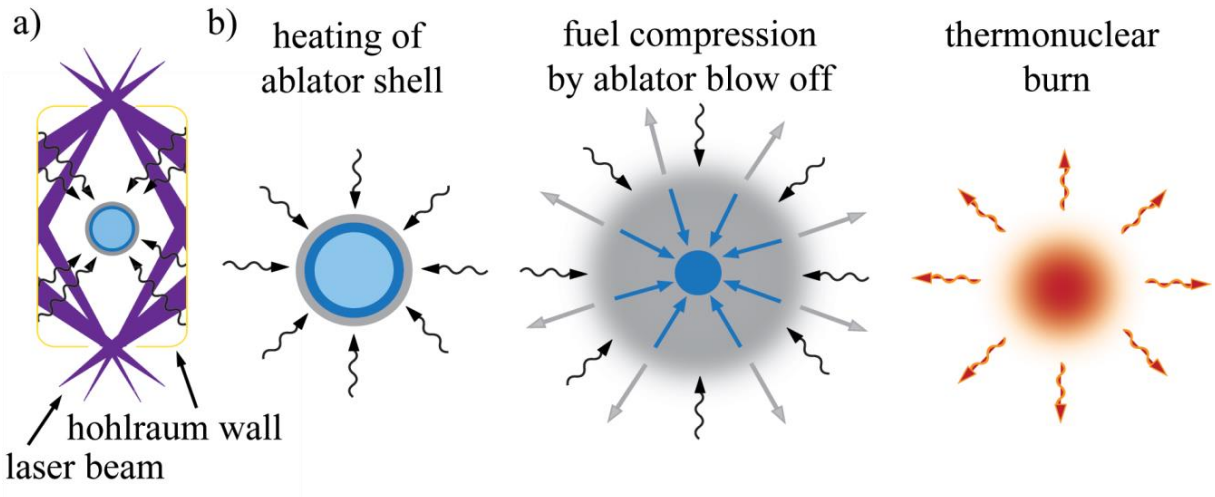

Figure 1-1: Indirect drive approach to inertial confinement fusion. a) The energy of the laser is directed into a hohlraum, converting the light into X-rays. b) The X-rays rapidly heat the outer layer of the target, the ablator (gray). As the ablator blows off rapidly, the fuel (blue) is compressed as the remaining part of the shell implodes. This causes the target to be heated to more than 10^6 K and densified to roughly 1000 g/cm^3 creating energies on the order of 10 to 35 MJ.

The X-rays inside of the hohlraum rapidly heat the outer layer of the target and as this ablator blows off, the DT fuel inside of the shell is compressed to densities of the order 10^3 times of solid hydrogen. The compression of the target is done within a few nanoseconds, creating the required energy and density to fulfill the Lawson criterion and reach conditions for fusion reactions.

1.2. Targets for laser driven ICF experiments

The majority of the concepts developed for laser driven inertial confinement fusion experiments propose hollow spheres as a target with a cryogenic DT fuel layer on the inside.[39-41] The hollow ablator shell used at NIF requires a 60-75 µm thick deuterium-tritium layer inside of a ~2 mm (ID) spherical ablator,[35, 42] which is illustrated schematically in Figure 1-2.

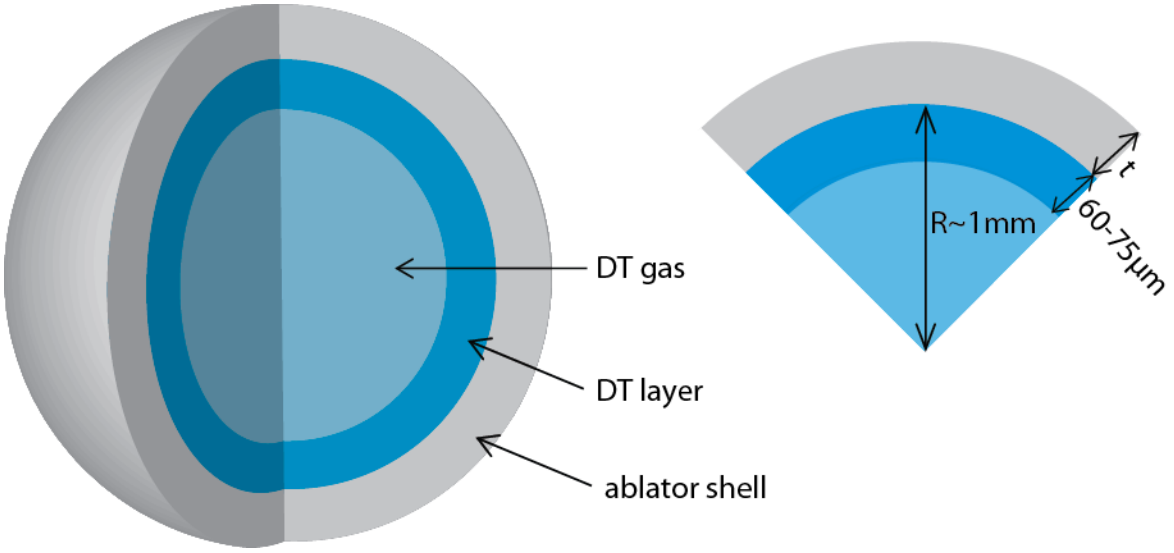

Figure 1-2: Simplified schematic of a target developed for laser driven inertial confinement fusion experiments. The hollow ablator shell contains a 60-75 µm thick layer of deuterium-tritium (DT). The radius of the ablator shell is usually on the order of 1 mm, while its thickness t depends on the material used and the experiment.

The ablator's thickness depends on the material used and the experiment, which was summarized well by Haan: "If the ablator is too thin, it burns through and the target fails to ignite. When the shells are too thick, the velocity is inadequate and again the target fails. In between is the operating space."[43] The wall thickness can range from 40 to 165 µm[42] depending on the experiment. Ablator materials include plastic,[43-44] beryllium,[43, 45-46] and high density carbon.[17, 47-49] Each ablator material has different properties and requires different capsule dimensions and X-ray drive profiles. The choice of ablator material additionally includes "fabrication and material characteristics, such as attainable surface finishes, permeability, strength, transparency to radio frequency and infrared radiation, thermal conductivity, and material homogeneity."[50] Many different target designs for inertial confinement fusion experiments have been proposed and developed over time. The details of any particular target design depend on the specific ICF experiment, the ignition type (such as hot spot ignition or fast ignition) and the driver type (such as direct or indirect drive). The discussion of the advantages and disadvantages of each target design is beyond the scope of this thesis, however, Hahn's,[35, 51-52] Dittrich's,[50] and Lindl's[53-54] publications and the references within give a good overview.

As described above, for most of their ICF experiments the NIF uses an indirect drive approach with a spherical hot spot ignition target. The formation of the 60-75 µm

thick deuterium-tritium layer inside these spherical targets is a grand technical and scientific challenge. The common approach of the deuterium-tritium fuel layer formation for experiments at the National Ignition Facility consists of several steps:

1. Filling the hollow capsule with deuterium-tritium fuel through a small fill hole via a fill tube
2. Condensing the fuel in the shell and then solidifying the DT
3. Re-melting the solid DT in the shell until only a single seed crystal remains as DT layers with the fewest defects were found to be single crystalline[55-56]
4. Re-cooling the shell and slowly forming a DT ice layer in the shell with a process called beta-layering, which is a consequence of the self-heating of DT from the radioactive decay that causes the inner ice surface to slowly conform to the local temperature isotherms.[57]

A very good overview of the deuterium-tritium fuel layer formation for the National Ignition Facility is given by Kozioziemski.[42] Growing acceptable DT ice layers however can be difficult and time-consuming. To complement the existing target production it was, therefore, decided to explore a different approach to build an inertial confinement fusion target – a foam lined indirect drive ICF target.

1.3. Development of foam lined ignition targets: The *Chemistry-in-a-Capsule* approach

The approach that was explored was first proposed by R.A. Sacks and D.H. Darling for direct drive fusion targets, which recommended "the use of a small pore size, open cell, rigid foam structure as a sponge to precisely define the [fuel] layer contours."[8] Instead of growing an ice layer inside the shell, the deuterium and tritium fuel would be sustained by a foam matrix made of low density, which has several advantages that complement the existing layering approach. For example, most of the required precision manufacturing and characterization can be done at room temperatures instead of cryogenic temperatures, the laser-coupling efficiency might be increased compared to pure DT fuel,[58] and the foam layer provides the opportunity to bring dopants in contact with the DT fuel, which may be useful in providing spectroscopic diagnostics of the implosion.[59] Additionally, the foam can be used as a surrogate to simulate a cryogenic fuel layer. This requires the foam to have a density similar to the

deuterium-tritium at 14K (roughly 250 mg/cm^3) and a thickness comparable to the DT ice layer (roughly 60-75 µm), which may simulate the mass effect of deuterium-tritium ice to measure the implosion velocity. This wetted foam target design would, however, raise the ignition temperature compared to a pure DT fuel layer in the same shell as the foam material mixes with the fuel. To minimize this effect, it is therefore necessary to use ultra-low density (≤50 mg/cm^3), low-Z materials for the foam.

Due to their many potential advantages, various foam lined inertial confinement fusion targets have been developed for direct drive[10, 59-64] and fast ignition[65-66] experiments. The majority of these approaches use a dual-nozzle-in-orifice droplet generator, triple-orifice droplet generator, or T-microchannel droplet generator to integrate hydrocarbon foams into an inertial confinement fusion target.[10-11, 65, 67-75] In these methods, usually, an unsupported foam shell is fabricated using a droplet generator followed by coating the dried foam shell with a full density permeation barrier that needs to be deposited for holding the fill gas at room temperature and the ice at cryogenic temperatures.[10] For most current applications, however, these foams have too high densities, too large pores, do not meet uniformity specifications, or shrink too much during supercritical drying. In addition, thick uniform ablator layers are difficult to grow on these foam shells and the ablator foam interface tends to be rough.

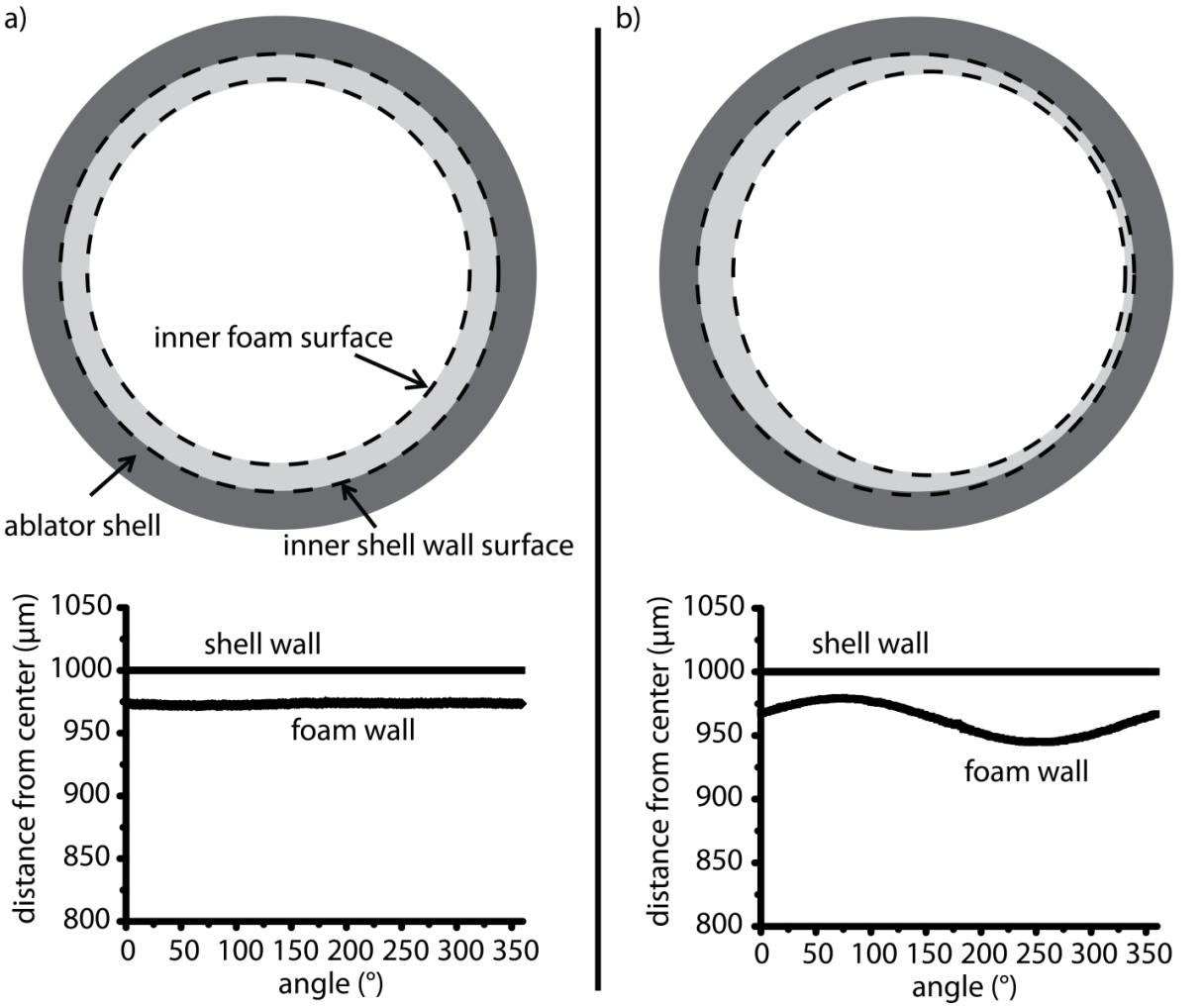

Figure 1-3: Definition of non-concentricity (mode 1 or thickness non-uniformity) of the inner and outer foam layer surfaces: a) in the cross-sectional view the inner and outer foam layer surfaces are concentric and the layer has the same thickness around the full circle of 360°. b) The two wall layer surfaces are not concentric, which leads to a mode 1 or thickness non-uniformity.

The uniformity specifications are especially critical for the fabrication of ICF targets as non-uniformities in the target can lead to Rayleigh-Taylor instabilities and non-symmetric implosions.[21, 76-79] The thickness uniformity of a foam layer in an spherical ignition target is necessary for a successful implosion and efficient burn rate in the ICF experiments[8, 62] and can be measured by analyzing the concentricity and sphericity of the inner and outer wet gel layers surfaces in a series of cross-sectional images as illustrated in Figure 1-3. This method has been used extensively for this thesis. Shape and roughness of the foam layer are analyzed using power spectral density plots obtained from a Fourier analysis of the inner foam surface radius as a function of the angular position.[80-81]

Due to the constrains mentioned above and to avoid the challenges that arise from handling freestanding foam shells, our strategy to fabricate foam layered targets that meet the required specifications for ICF targets consists of a different method: filling a prefabricated hollow sphere with the required amount of a liquid foam precursor followed by the continuous rotation of the sphere to form a smooth uniform layer and subsequent drying. This method is illustrated in Figure 1-4.

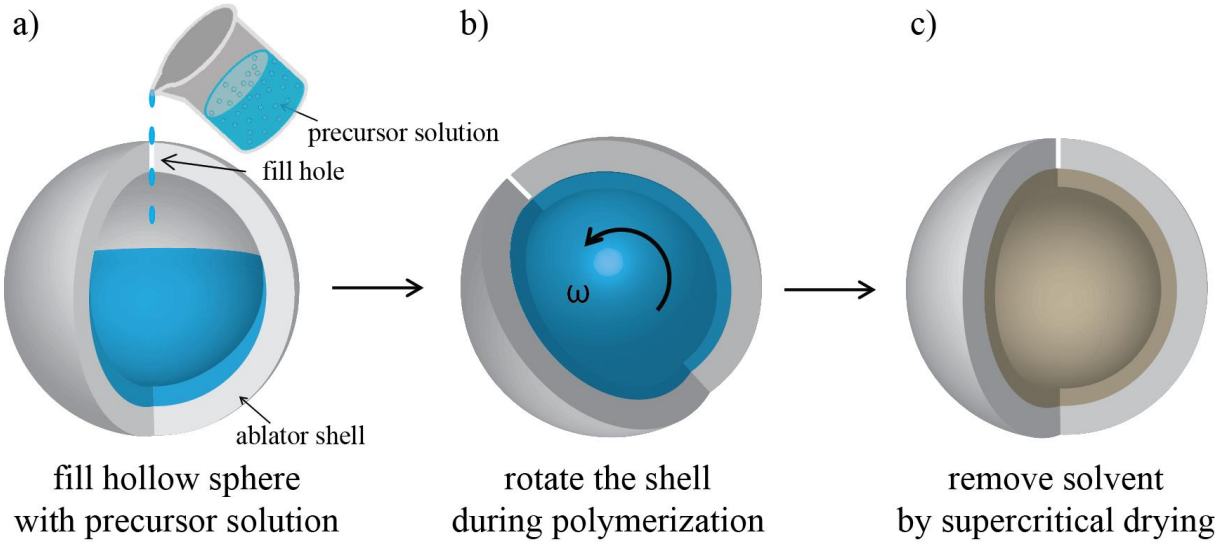

Figure 1-4: Schematic fabrication process of foam-lined ICF targets: a) filling a prefabricated hollow ablator shell with the desired amount of an aerogel precursor solution; b) formation of a smooth and uniform gel layer by deterministic rotation of the capsule during polymerization; c) removing the solvent by supercritical drying.

During the course of this thesis each step of this approach will be explained in detail: Chapter 2 covers the synthesis of the polymer foam and the fundamental chemical *sol-gel* process behind it. The rheological properties during polymerization are characterized and a copolymerization approach developed by Kim[82] and Dawedeit[15] is described and adapted to coat hollow spheres with uniform films. Additionally, to better implement the developed materials into functional devices the mechanical properties of the polymer foam are analyzed. Chapter 3 describes the filling of the shell and how *in situ* real-time radiography can be used to monitor the distribution of liquids in rotating hollow spherical shells. The experiments confirm a surprising prediction made by computational fluid dynamics simulations, namely, that uniaxial rotation can result in the formation of extremely uniform thin film layers in hollow spherical shells if the right combination of the precursor's viscosity and rotational velocity is used. Chapter 4 gives a short overview of how the shells can be completely filled with foam, which enables additional experimental platforms. Proof of principle

experiments are performed and the resulting shells are characterized. Chapter 5 covers the removal of the solvent from the pores of the polymer, which is a key requirement for ultra-low density coatings in hollow spheres. A solvent exchange method is developed and a drying method using supercritical carbon dioxide is implemented and optimized to produce foam-lined ICF targets. In the last chapter of this thesis the introduction of dopants into the low-density polymer films is extensively discussed. A doping method developed by Kim[14] is described and adapted to successfully dope low-density polymer films in hollow spheres.

The *Chemistry-in-a-capsule* approach described in this thesis can be used to fabricate foam-lined indirect-drive ignition targets based on spin-coating the inside of prefabricated ablator with a polymer precursor solution and subsequent removal of the solvent. It demonstrates a credible pathway to a reliable, consistent, and economical target supply for indirect drive laser ICF experiments by changing the target production process “from one-of-a-kind to 500,000 high quality ignition targets per day”[83] and has the potential to provide “a cost-effective target supply for inertial fusion”[84] experiments.

Chapter 2: Aerogels for ultra-low density coating applications

Of all solid materials, aerogels are quite unique as they combine large intrinsic surface area, ultra-low density, and continuous open pores. They have received substantial attention due to their prospective wide range of applications in supercapacitors and energy storage,[85-92] batteries,[90, 93-95] thermal and electrical insulators,[96-101] catalysis,[90-91, 102-106] cosmic dust collection,[107-109] and life sciences.[110-114] Amongst many others, Hrubesh,[115] Pierre,[116] and Hüsing[117] each give an overview of the wide variety of properties that aerogel materials posses and outline the vast number of applications that have been developed for them.

Hüsing and Schubert describe the appearance of aerogels to be closest to "whipped egg whites or solid bubble bath" as "the main component of this material is air which is surrounded by a very filigrane, solid network."[117] They define an aerogel to be a material in which a *wet gel's* (see below) "typical structure of the pores and the network is largely maintained […] while the pore liquid of the gel is replaced by air" – a definition this thesis will adopt. The formation of the porous, three-dimensional network is a key step in the synthesis of aerogels and requires understanding of the fundamental chemical *sol-gel* process.

This sol-gel process can be described as the method of transforming a colloidal suspension of solid particles in a liquid (*sol*) into a continuous three-dimensional network extending throughout the liquid (*gel* or *wet gel*). Brinker and Scherer define a *colloid* as "a suspension in which the dispersed phase is so small that gravitational forces are negligible and interactions are dominated by short-range forces, such as van der Waals attraction and surface charges."[118] The sol-gel process is schematically illustrated in Figure 2-1.

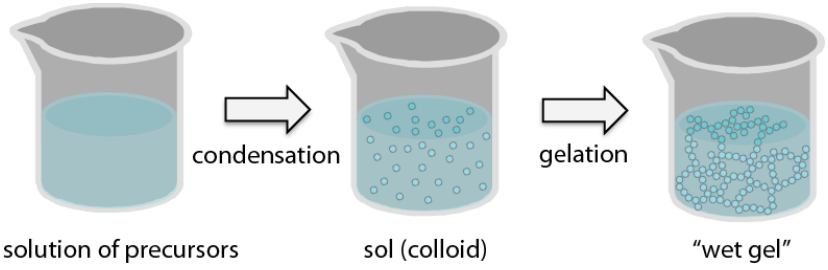

Figure 2-1: Schematic of the sol-gel process: Solid nanoparticles are dispersed in a liquid and join together to form a continuous three-dimensional network extending throughout the liquid.

The transition from sol to gel occurs when the solid particles in the liquid join together to form a gel-like material that contains both a liquid and a continuous solid phase. This transition is called *gelation*, while the time required to form the gel from the precursor solution is called *gel-time*.

The extraction of the liquid from the gel to form a solid (*drying*) usually requires special drying techniques, such as freeze drying or supercritical drying, which can lead to different materials, including, but not limited to xerogels, cryogels, and aerogels. The removal of the solvent from wet gels for thin ultra-low density coatings inside hollow spheres is a challenging task and described in great detail in chapter 5.

Most of the applications for aerogel materials mentioned above focus on the use of bulk aerogels, however, various applications of aerogel and porous polymer coatings have been reported in the literature.[119-122] As mentioned above, the goal of this thesis is to generate uniform, ultra-low density aerogel coatings on the inside of hollow spheres, which can be used to fabricate targets for inertial confinement fusion experiments. The sol–gel chemistry for these particular aerogels should be purely hydrocarbon based and yield monolithic, low-shrinkage, and mechanically robust aerogels with ultra-low densities (<35 mg/cm^3) that are able to survive wetting with liquid hydrogen.[12] Due to these constrains, our strategy to fabricate foam layered targets that meet the required specifications is the *Chemistry-in-a-capsule* approach that requires the continuous rotation of a precursor filled sphere to form a smooth uniform layer. Coating a rotating object with a uniform gel layer, however, requires a sol–gel chemistry that can tolerate a certain amount of shear during gelation. Therefore, a dicyclopentadiene(DCPD)- based aerogel chemistry[101] was further developed that is based on polymerization of DCPD monomers using a ring opening metathesis polymerization (ROMP) reaction (Figure 2-2) as described in detail in this chapter.

2.1. Experimental techniques

Porous polymer coatings were prepared from dicyclopentadiene (DCPD, $C_{10}H_{12}$, Aldrich) / norbornene (NB, C_7H_{10}, 99%, Aldrich) mixtures using a Grubbs' 1st generation catalyst, bis(tricyclohexylphosphine)benzylidene ruthenium(IV) dichloride

(+97%, Aldrich). All chemicals were used as received without further purification. As supplied, the DCPD monomer is predominantly *endo* isomer and contains butylated hydroxytoluene as a stabilizer. Toluene (anhydrous, 99.8%, Aldrich) was purged with nitrogen gas prior to use. Poly(dicyclopentadiene-random-norbornene) p(DCPD-r-NB) gels were prepared by ring opening metathesis polymerization (ROMP) with Grubbs' 1st generation catalyst.[82, 101, 123-124]

Density of the p(DCPD-r-NB) aerogels (25–100 mg/cm^3) and gelation time were adjusted by the DCPD/NB-to-toluene and the DCPD/NB-to-catalyst ratio, respectively. For example, 50 mg/cm^3 p(DCPD-r-NB) aerogels with 10 wt. % NB (relative to pDCPD) were prepared by mixing 10 ml of a 50 mg/cm^3 DCPD/toluene solution with 1 ml of a 50 mg/cm^3 NB/toluene solution and adding 0.5 ml of a 2 mg/cm^3 catalyst solution (0.2 wt. % catalyst).

Viscosity changes during gelation at room temperature were measured with a Rheometrics Fluids Spectrometer (RFS 8400) using the dynamic-time-sweep mode with a couette geometry (17 mm radius cup and 16 mm radius bob). This geometry has the advantage of a large contact area that improves the instrumental resolution. To minimize solvent evaporation, the cup was covered with a custom-built lid. Strain amplitude (5% of the 1 mm gap between cup and bob, 50 mm) and frequency (1 radian per second) were adjusted to minimize shear force while still providing high sensitivity (>1mPa·s).

High-density carbon (HDC) shells (2 mm ID)[17, 47] with 30 to 50 µm diameter fill holes (Diamond Materials GmbH, Germany) were used to study the coating behavior of various foam compositions and densities in hollow spheres. To facilitate characterization, relatively thin-walled (20–30 µm) and transparent micro-crystalline HDC shells were used. Coating experiments were either performed in a custom-made positioning machine[125] with a frame that is made of titanium and allows for rotation up to 20 rpm around two independently driven axes or were performed in a custom-built uniaxial coating setup consisting of a steel frame in the shape of a triangular prism, with two rolls on top, on which the capsule holder was placed. The coating setup is described in chapter 3, specifically in Figure 3-3. The rolls are driven by a

brushless 120 Watt EC-max motor with hall sensors (maxon motor, Switzerland) through a transfer belt, which allowed adjusting the rotation speeds.

The polymer gels were supercritically dried in a critical point dryer (E3100, Electron Microscopy Sciences) with liquid CO_2 after first exchanging toluene with acetone using an agitated acetone bath for three days (2-step solvent exchange drying process). In some experiments, an additional solvent exchange step replacing toluene against hexane was performed to avoid sample shrinkage during the final CO_2 drying (3-step solvent exchange drying process). The supercritical drying process is described in detail in chapter 5. The morphologies of the dried aerogels were investigated with a Jeol JSM-7401F scanning electron microscope at a low acceleration voltage of 2–3 kV in a lower secondary electron image (LEI) mode.

Radiographic images of foam-coated shells were taken with an Xradia MicroXCT imaging system using an X-ray source with a tungsten anode that was operated at a peak voltage of 50 kV and a current of 200 µA. The focal spot size is 7 µm for these operating conditions. The imaging optics magnification is 10x with an effective detector pixel width of 1.35 µm and an effective pixel width at the object center of 1.15 µm. Digital radiography data shown in this chapter were collected by John Sain, LLNL.

Tomography data were acquired at beamline 8.3.2 at the Advanced Light Source, Lawrence Berkeley National Laboratory,[126] using a photon energy of 34 keV. Every 20 views, bright field images were acquired to normalize incident X-ray flux and changes in the delivered synchrotron X-ray flux at the detector; dark field images were also acquired. The transmitted X-rays impinge upon a $CdWO_4$ single crystal scintillator and were recorded by a Cooke PCO 4000 CCD camera. In order to minimize phase effects, the camera and scintillator box were moved as close as possible to the specimen, resulting in a distance of about 7 cm between sample and scintillator. Tomographic slices were reconstructed via filtered back projection using the LLNL-developed ImageRec code as well as the commercially available Octopus package (Ghent University, Belgium).

2.2. Synthesis of ultra-low density pDCPD aerogels

To synthesize pDCPD wet gels, DCPD monomers were crosslinked via ring opening metathesis polymerization with Grubbs' 1st generation catalyst[82, 101, 123-124] at room temperature and atmospheric pressure to form the three-dimensional network using toluene as the solvent. Figure 2-2 shows the scheme of the reaction to form p(DCPD-r-NB) copolymer gels from the ROMP reaction of a mixture of DCPD and NB in toluene.

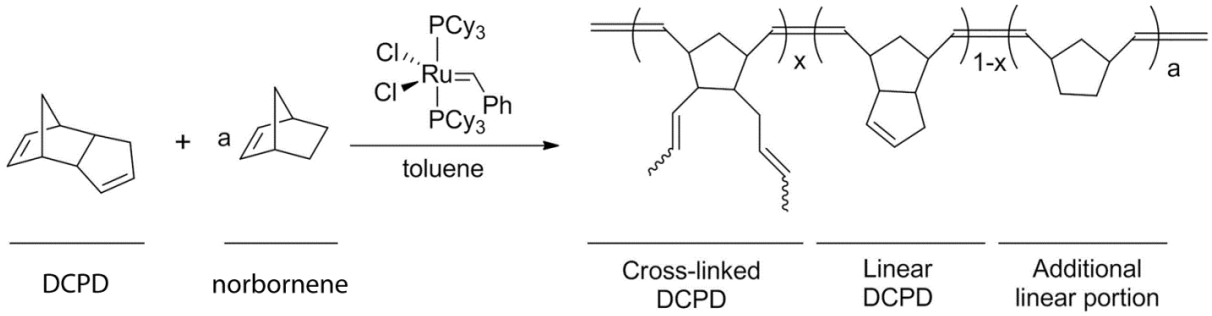

Figure 2-2: Ring opening metathesis polymerization (ROMP) of dicyclopentadiene (DCPD) and norbornene (NB) in toluene using Grubbs 1st generation catalyst.

The dicyclopentadiene molecule contains two carbon-carbon double bonds that can both undergo metathesis. Davidson and Wagner report that polymerization of the strained norbornene ring in the DCPD monomer occurs first and is then followed by the metathesis of the cyclopentene unit[127] to form a crosslinked pDCPD polymer. When using a Grubbs catalyst, linear and crosslinked DCPD polymers may coexist.[101] The exact curing kinetics of ring opening metathesis polymerization of dicyclopentadiene have been studied extensively[128-133] and a good overview about olefin-metathesis catalysts for the preparation of molecules and materials can be found in Grubbs' Nobel Lecture from 2005.[134]

During the polymerization of dicyclopentadiene the precursor solution goes from a transparent solution to an opaque gel. The opaqueness is a first indicator that the feature size of the wet gel is larger than the wavelength of visible light.

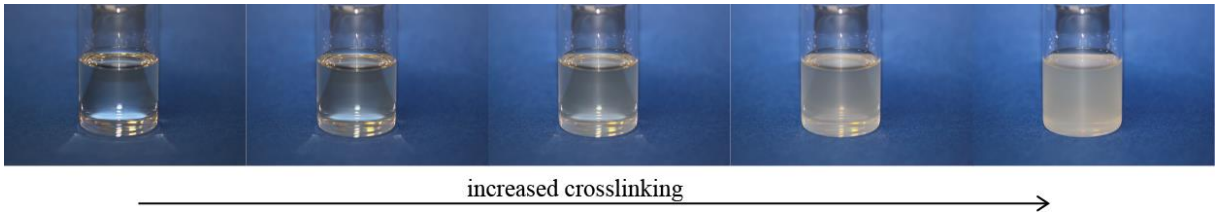

Figure 2-3: Phase transition of a p(DCPD) aerogel (50 mg/cm³, 10% NB, 0.2 wt.% catalyst) from a transparent solution to an opaque gel as crosslinking of the polymer increases.

The evolution of the storage shear modulus G' and loss shear modulus G" during polymerization of a 50 mg/cm^3 p(DCPD) in toluene using 0.2 wt.% Grubbs 1st generation catalyst at room temperature is illustrated in Figure 2-4a). The *gel point*, or the initial formation of an infinite continuous three-dimensional network extending throughout the liquid, is defined (in this thesis) as the crossover of the storage shear modulus G' and loss shear modulus G"[135]. However, it should be noted that several different methods to determine the gel point have been reported in the literature.[136-137] During the first 400 s the viscosity of the precursor solution is determined by the viscosity of toluene (575.3 µPa·s),[138] but increases rapidly by several orders of magnitude in the vicinity of the sol-gel transition. (Figure 2-4b)

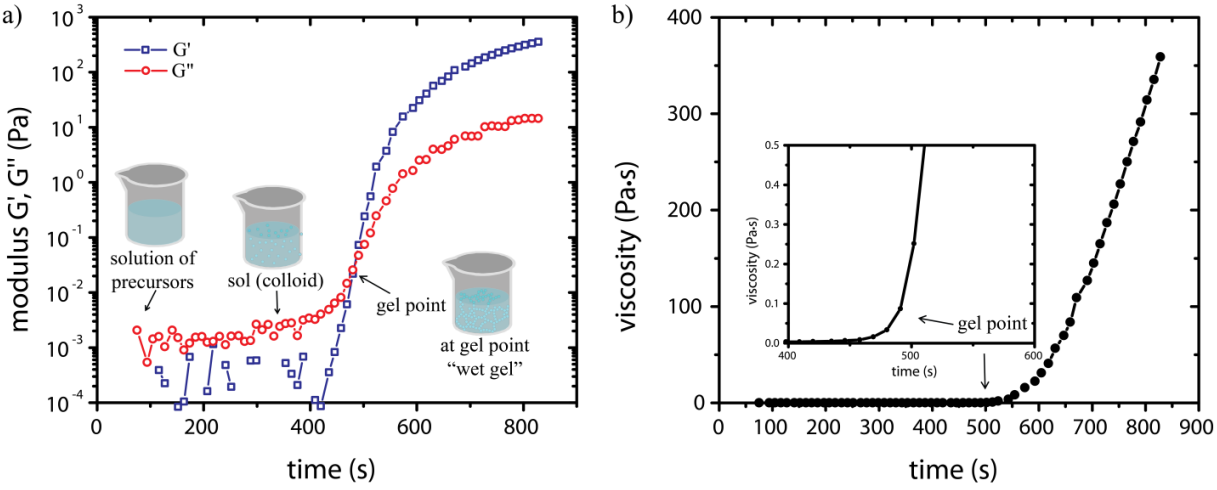

Figure 2-4: Polymerization of a 50 mg/cm^3 dicyclopentadiene gel in toluene using 0.2 wt.% Grubbs 1st generation catalyst. a) Evolution of the storage shear modulus G' and loss shear modulus G" during polymerization of p(DCPD) at room temperature. The gel point of the system was determined from the crossover of G' and G". b) Viscosity of the reaction as a function of reaction time. Once the gel point is reached the viscosity increases very rapidly by several orders of magnitude. The inlet shows the viscosity as a function of reaction of reaction time around the gel point.

Comparing the viscosity of the material during the reaction as a function of reaction time for p(DCPD) gels in toluene using 0.2 wt.% Grubbs 1st generation catalyst at room temperature and at different densities illustrates how the time to reach the gel point is dependent on the density of the aerogel. (Figure 2-5)

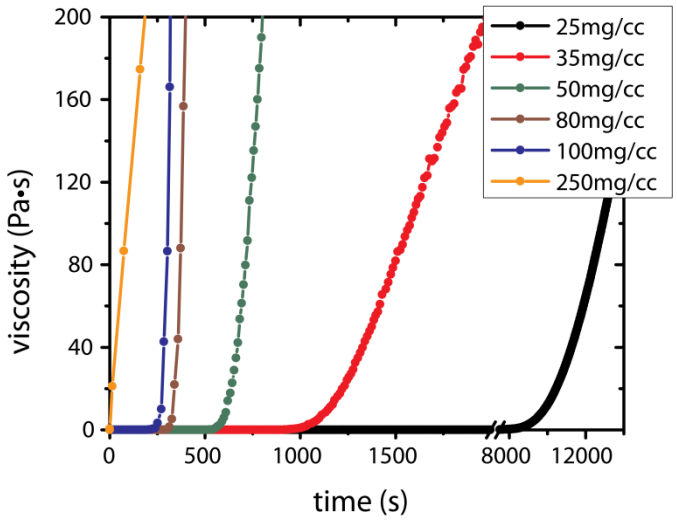

Figure 2-5: Polymerization of dicyclopentadiene gels in toluene using 0.2 wt.% Grubbs 1st generation catalyst at different densities. The viscosity of the reaction as a function of reaction time shows that the time to reach the gel point is dependent on the density of the aerogel. Once the gel point is reached the viscosity increases very rapidly by several orders of magnitude.

Since the sol-gel chemistry changes depending on the properties of the precursor solution, the rheological properties have to be tuned depending on the experiment. These modifications will be discussed in the next chapter.

The solvent (toluene in our case) can be removed from the pDCPD gels via supercritical drying, which is described in great detail in chapter 5. The morphology of a 30 mg/cm^3 pDCPD dried aerogel is fibrous and web-like as illustrated in Figure 2-6.

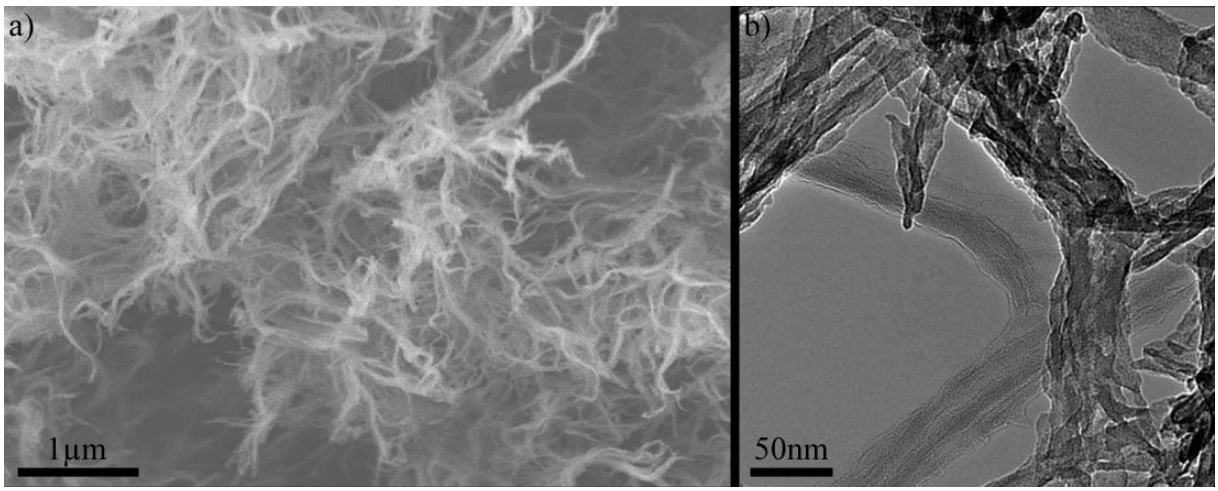

Figure 2-6: a) Scanning electron microscopy image of a p(DCPD) aerogel (30 mg/cm^3, 0.1 wt.% catalyst) illustrating the web-like morphology of the ultra-low density material. (image credit: Sung Ho Kim, LLNL) b) Transmission electron microscopy image of a p(DCPD) aerogel (30 mg/cm^3, 0.1 wt.% catalyst) showing the fibers and pores of the material. The majority of space within the aerogel is occupied by air. (image credit: Y. Morris Wang, LLNL)

The three-dimensional porous network of the aerogel consists of randomly oriented fibers with an irregular pore structure. Transmission electron microscopy images of the same p(DCPD) aerogel (30 mg/cm^3, 0.1 wt.% catalyst) show the fibers and pores of the ultra-low density material in great detail. (Figure 2-6) As implied by the name, the majority of space within the aerogel is occupied by air.

2.3. **Tuning rheological properties of aerogels**

Coating a rotating object with a uniform layer of a liquid precursor solution results in shear forces due to the velocity gradient within the liquid that is caused by friction and gravity. This velocity gradient within a liquid inside a uniaxially rotating hollow sphere is illustrated schematically in Figure 2-7. The velocity of the liquid tangential to the wall $u(\mathrm{x}, h(\theta,t))$ in the cross section perpendicular to the rotational axis depends on the distance to the sphere's inner wall x, the angle θ and the time t.

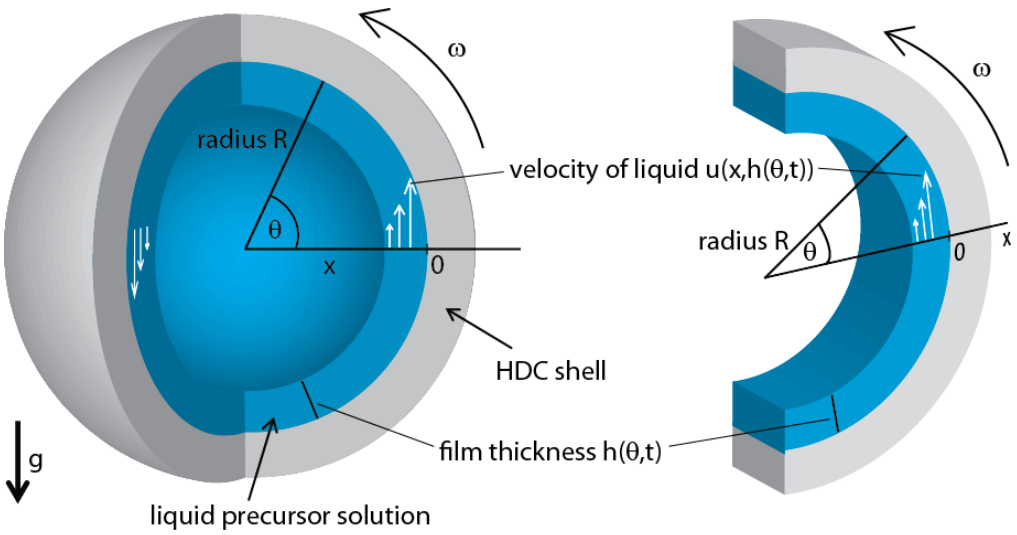

Figure 2-7: Schematic representation of the shear flow due to the velocity gradient $u(\mathrm{x}, h(\theta,t))$ within the liquid that is caused by friction and gravity.

If we assume that the liquid film thickness, h, is small compared to the hollow sphere's radius, R, the steady state thin layer (lubrication) approximation of the Navier-Stokes equation can be written as

$$\mu \frac{\partial^2 u(x,\theta)}{\partial x^2} = g\cos\theta,$$

where μ is the liquid's viscosity and $g\cos\theta$ is the tangential component of gravitational acceleration.[139-140] At the free liquid boundary $x = h$ the boundary

condition is $\frac{\partial u}{\partial x} = 0$ and at the capsule wall $x = 0$ the liquid's velocity is $u\big(0, h(\theta, t)\big) = \omega R$. Using these boundary conditions, the equation of motion for the circumferential component of velocity can be solved for thin films on the surface of rotating cylinders. Moffat[139] obtained for the flux $Q(\theta, t) = \int_0^h u\mathrm{d}x$ at the angle θ with a local film thickness h

$$Q(\theta, t) = h(\theta, t)R\omega - \frac{g\cos\theta\,[h(\theta, t)]^3}{3\mu}.$$

Melo used this work when studying the profiles and dynamics of disturbances of a fluid in a partially filled cylinder that rotates horizontally.[140] He found that the shear rate, which is proportional to the angular velocity ω, experienced by the liquid in a rotating cylinder is inversely "proportional to the dynamic viscosity of the liquid μ

$$\omega > \frac{2.14 g\rho h^2}{R\mu},$$

where g is the acceleration of gravity, ρ the fluid density, R the cylinder radius, and h the layer thickness."[15]

This knowledge can partly be transferred to polymer coatings in hollow spheres. While the flow of liquids on the outside of spherical surfaces has been studied extensively[139, 141-145], few publications addressed thin films flowing on the inner surface of a rotating sphere[146-152] with most of them focusing on granular mixtures in spherical tumblers.

Initial experiments with pure pDCPD coatings in 2 mm inner diameter rotating hollow spheres (25 mg/cm^3 DCPD, 0.2 wt.% catalyst, filled with a pressure differential Δp = 83.5 Torr (see chapter 3), and rotated for ~16 h on the positioning machine with one axis rotation set to 10 rpm and the other to 14.142 rpm) revealed that the above mentioned shear forces on the polymer during the gelation cause the inner surface of the hollow sphere to be covered with irregular foam fragments. (Figure 2-8) The initially weak gel network is irreversibly broken up by the shear forces during rotation, leaving an inhomogeneous coating.

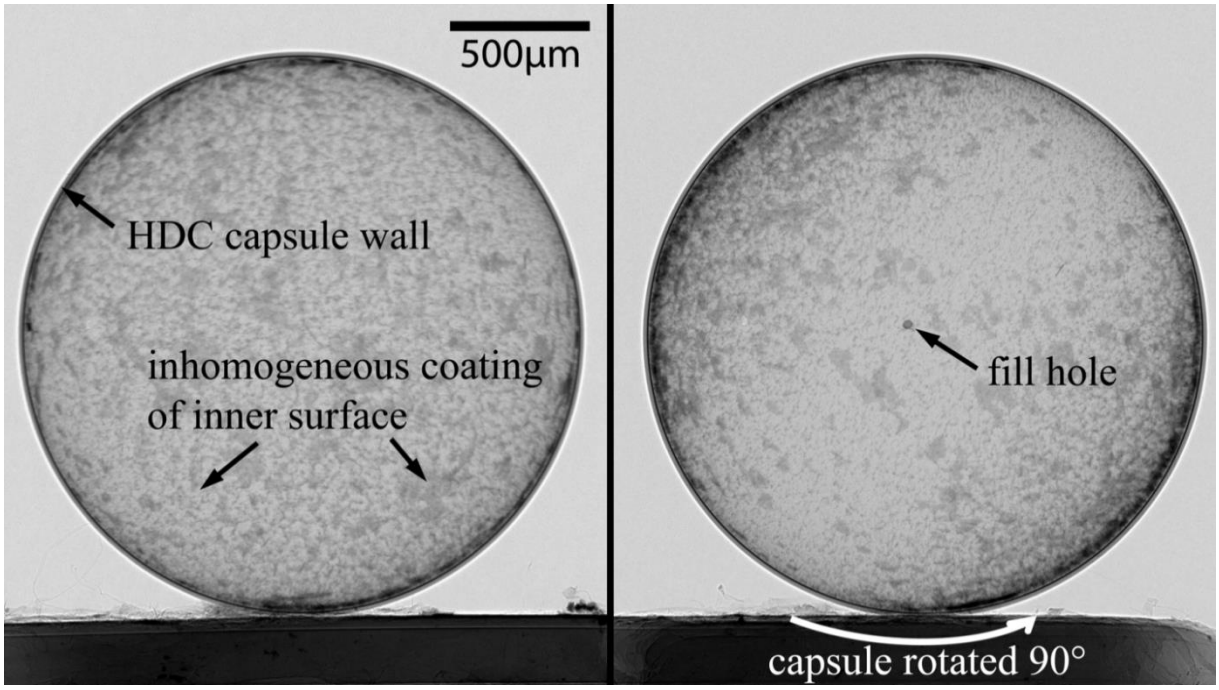

Figure 2-8: Cross-sectional radiographic image of a 2 mm diamond sphere coated with a p(DCPD) foam layer (25 mg/cm³ DCPD, 0.2 wt.% catalyst, filled with Δp = 83.5 Torr, and coated on the positioning machine with the axis rotation set to 10 rpm and 14.142 rpm, respectively, for 16h). The coating is clearly inhomogeneous due to the shear forces exerted onto the polymer during rotation. (radiographs taken by John Sain, LLNL)

Although the irregular foam fragments are distributed on the entire inner surface of the hollow sphere, the heterogeneity of the foam layer is evident. To further illustrate the distribution of the inner surface coating the hollow sphere was rotated by 90° and an additional cross-sectional radiographic image was taken. (Figure 2-8, image on the right) It seems that, on top of the irregular foam fragments in the shell, the foam layer is thicker on two poles and thinner or even absent around the equator. This thickness non-uniformity is a result of the rotational parameters which are addressed in detail in chapter 3 of this thesis. This chapter focuses on the foam fragments caused by shear forces during rotation and on how to avoid them. Since the comprehensive three dimensional foam structure is not known from the two radiographs alone a computerized tomography (CT) scan and additional 3D rendering of the foam only was done at beamline 8.3.2 at the Advanced Light Source, Lawrence Berkeley National Laboratory[126] by Trevor Willey and Tony van Buuren, LLNL. (Figure 2-9)

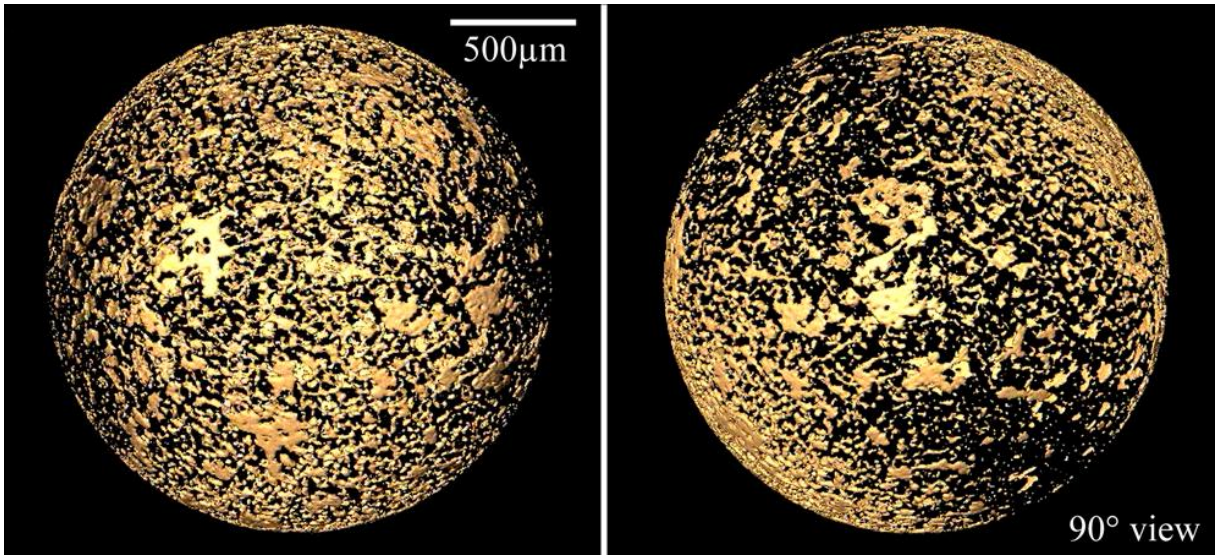

Figure 2-9: Three dimensional rendering of only the p(DCPD) foam coating inside a 2 mm diamond sphere (25 mg/cm^3 DCPD, 0.2 wt.% catalyst, filled with Δp = 83.5 Torr, and coated at 10/14.142 rpm for 16 hours). The heterogeneity of the foam layer is even more evident than in Figure 2-8. (image credit: Trevor Willey and Tony van Buuren)

The irregular foam fragments are clearly visible and are an indicator that pure pDCPD gels do not form uniform thin films under rotation in hollow spheres. Instead, the inner surface is covered with irregularly shaped lumps of foam, which is consistent with the observations of pure pDCPD coatings in cylinders.[15, 34, 82] The effect was reproducible for different densities and layer thicknesses as illustrated in Figure 2-10.

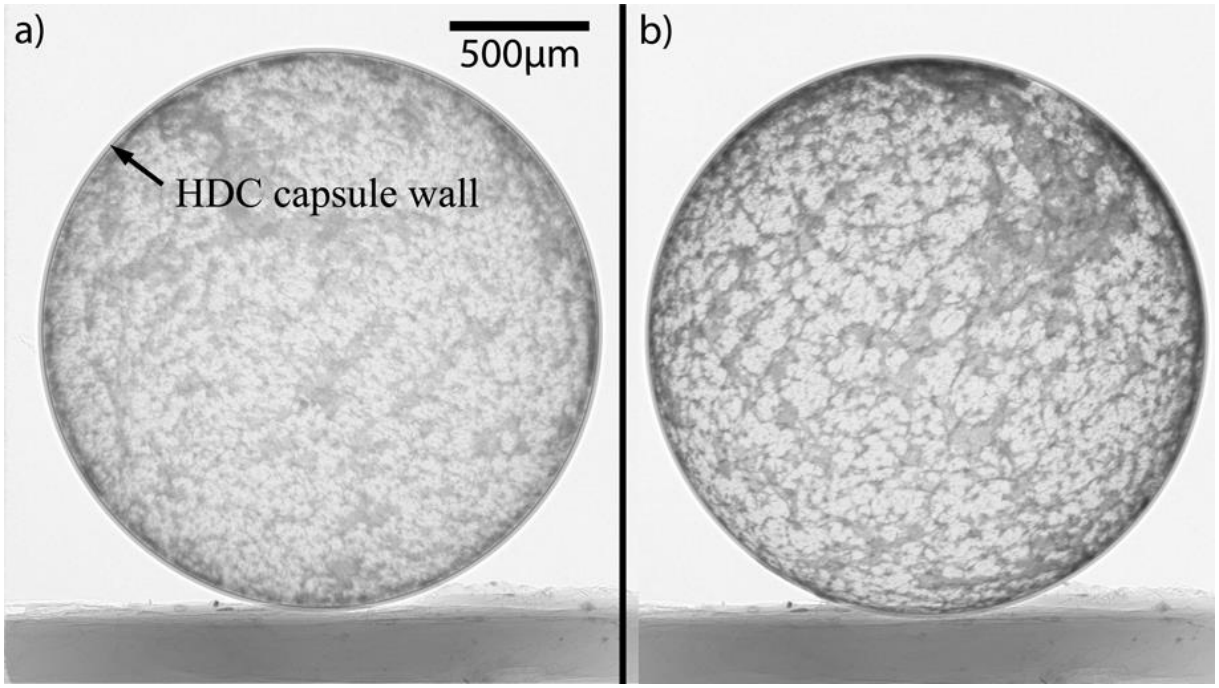

Figure 2-10: Cross-sectional radiographic image of two different 2 mm diamond spheres coated with p(DCPD) foam layers. a) 50 mg/cm³ DCPD, 0.1 wt.% catalyst, filled with Δp = 95 Torr, and coated at 10/14.142 rpm for 16h. b) 50 mg/cm³ DCPD, 0.1 wt.% catalyst, filled with Δp = 100 Torr, and coated at 10/14.142 rpm for 1h. The coatings in both cases are clearly inhomogeneous due to the shear forces exerted onto the polymer during rotation. (radiographs taken by John Sain, LLNL)

These experiments clearly show that in order to achieve uniform coatings of spheres, the aerogel must be able to withstand shear forces during polymerization under rotation. As we learned above from Melo's and Moffat's calculations, an elevated viscosity at the gel point can reduce the shear that the pDCPD gel experiences during polymerization. One approach to control the gel point viscosity is to copolymerize the DCPD-based polymer aerogels with norbornene – a monomer that can only form linear chains in the network. This copolymerization, in theory, influences the rheological properties of the gel by increasing the gel time and viscosity at the gel point, which would reduce the amount of shear-induced damage in the forming polymer network. The increase in gel time and viscosity can be explained with the classical theory of gelation[118, 153] that states that for a polymer with a functionality z the critical condition for gel formation is that the fraction of all bonds p_c that could be formed in the polymer network is[118]:

$$p_c = \frac{1}{z-1}$$

Adding norbornene with its single double bond (z=2) to the precursor solution decreases the average functionality of the system compared to pure p(DCPD) with its two double bonds and a functionality of z=4. Since the average functionality of the system is decreased, the fraction of all bonds required for gelation increases, which then increases the gel time and viscosity at the gel point.[15] Dawedeit[15], Kim[82], and Braun[34] used this copolymerization approach to achieve uniform coatings in cylinders, which can be transferred to polymer coatings in hollow spheres.

Comparing the viscosities of 35 mg/cm³ p(DCPD-r-NB) aerogels with increasing norbornene concentrations as a function of reaction time shows how copolymerization with norbornene delays the gelation. (Figure 2-11) Adding 2.5% NB delays the gelation time by 170 s, which increases the viscosity at the gel point from $\eta^{35\ \mathrm{mg/cm3}}_{\mathrm{pure\_DCPD}} = 0.013\ \mathrm{Pa \cdot s}$ for pure pDCPD to $\eta^{35\ \mathrm{mg/cm3}}_{2.5\%\ \mathrm{NB}} = 0.046\ \mathrm{Pa \cdot s}$ for a ratio of DCPD to NB = (100:2.5). The same trend can be observed for higher norbornene concentrations as the gel time and the viscosity at the gel point increases with increased ratio of norbornene with its single double bond (z=2).

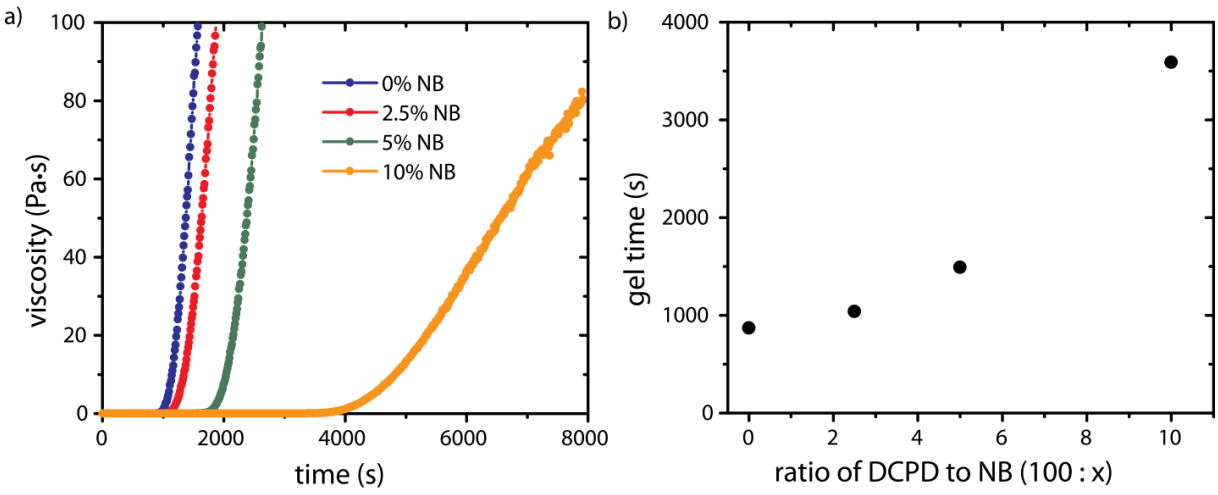

Figure 2-11: Polymerization of 35 mg/cm³ p(DCPD-r-NB) wet gels in toluene using 0.2 wt.% Grubbs 1st generation catalyst. a) Viscosity of the polymerization reaction of p(DCPD-r-NB) wet gels at room temperature reaction as a function of reaction time for different norbornene concentrations. Once the gel point is reached the viscosity increases very rapidly by several orders of magnitude. b) Gelation time as function of norbornene concentration. As predicted, increasing the norbornene concentration in the precursor solution delays the gels time.

For a ratio of DCPD to NB = (100:10) the gelation time increases to $t_{\mathrm{gel}} = 3500\ \mathrm{s}$ with a gel point viscosity of $\eta^{35\ \mathrm{mg/cm3}}_{10\%\ \mathrm{NB}} = 0.065\ \mathrm{Pa \cdot s}$. This is an increase by a factor of 5 for the viscosity at the gel point.

The same effect can be observed for p(DCPD-r-NB) aerogels at different densities as illustrated in Figure 2-12 (80 mg/cm^3) and Figure 2-13 (100 mg/cm^3). For an 80 mg/cm^3 p(DCPD-r-NB) wet gel in toluene, the gel time increases almost linearly with the norbornene concentration, while for the 100 mg/cm^3 wet gel, the effect of norbornene addition on the gel time becomes weaker for higher norbornene concentrations.

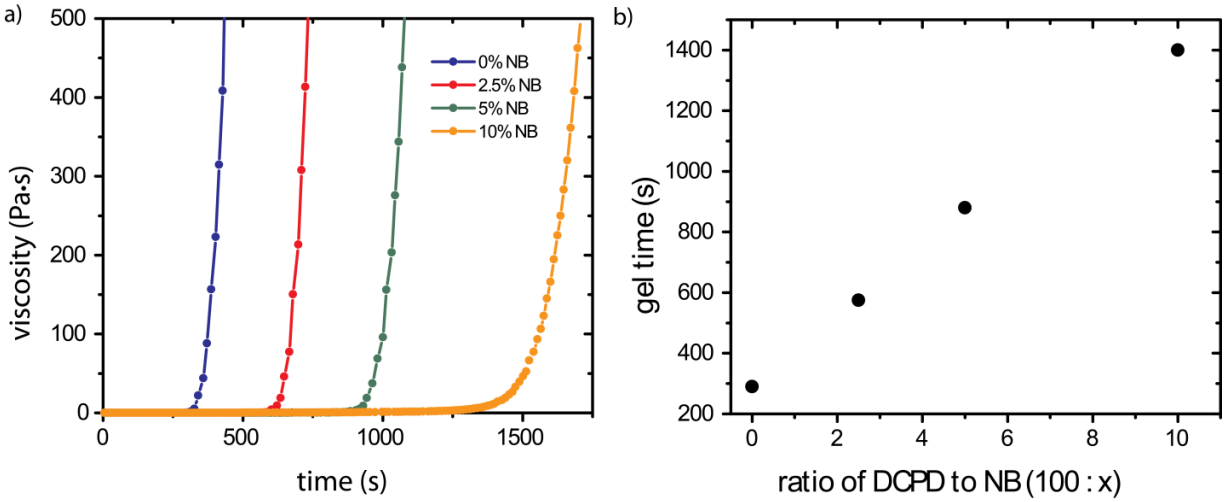

Figure 2-12: Polymerization of 80 mg/cm^3 p(DCPD-r-NB) wet gels in toluene using 0.2 wt.% Grubbs 1st generation catalyst. a) Viscosity of the polymerization reaction of p(DCPD-r-NB) wet gels at room temperature reaction as a function of reaction time for different norbornene concentrations. Once the gel point is reached the viscosity increases very rapidly by several orders of magnitude. b) Gelation time as function of norbornene concentration seems to indicate a linear behavior for 80 mg/cm^3 wet gels.

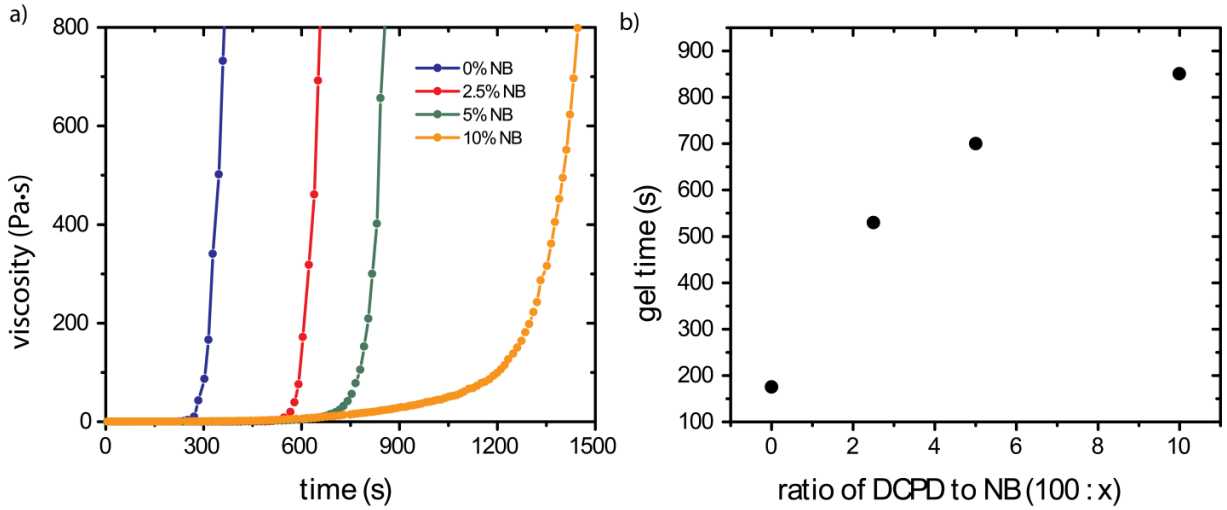

Figure 2-13: Polymerization of 100 mg/cm^3 p(DCPD-r-NB) wet gels in toluene using 0.2 wt.% Grubbs 1st generation catalyst. a) Viscosity of the polymerization reaction of p(DCPD-r-NB) wet gels at room temperature reaction as a function of reaction time for different norbornene concentrations. Once the gel point is reached the viscosity increases very rapidly by several orders of magnitude. b) Gelation time as function of norbornene concentration. The function shows a different behavior than for 35 mg/cm^3 and 80 mg/cm^3.

As expected, the overall gel time decreases with higher densities. It can also be observed that the effect of norbornene addition on the viscosity at the gel point becomes more pronounced at higher densities. Figure 2-14 illustrates how adding norbornene to the precursor solution increases the gel point viscosity by several orders of magnitude.

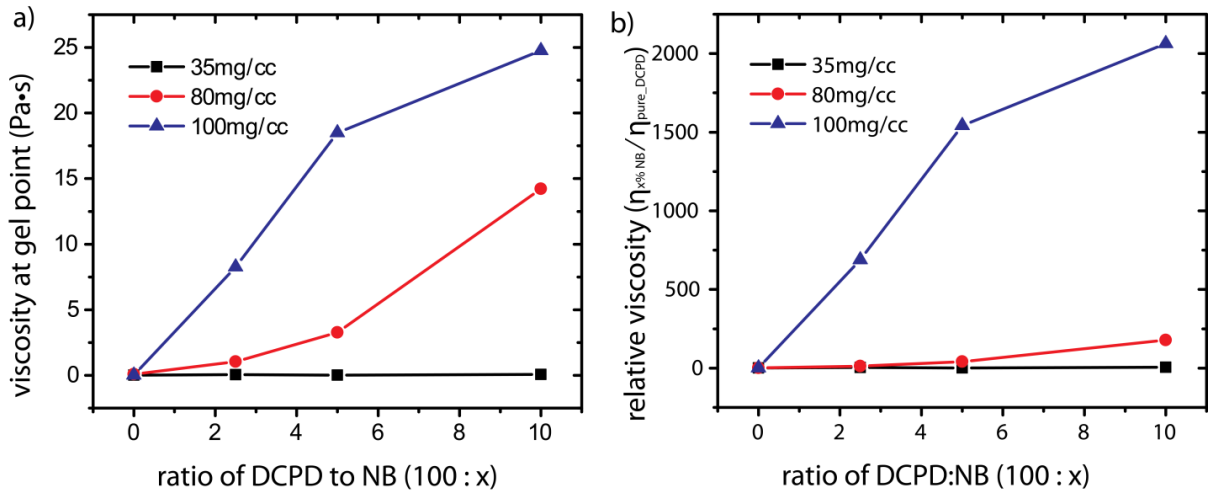

Figure 2-14: a) Gel point viscosity for p(DCPD-r-NB) wet gels in toluene at different densities using 0.2 wt.% Grubbs 1st generation catalyst as a function of norbornene concentration. Adding norbornene increases the gel point viscosity by several orders of magnitude. b) The normalized relative viscosity for the aerogels shows that the effect becomes more pronounced at higher densities.

For example, for an 80 mg/cm^3 p(DCPD-r-NB) wet gel in toluene, the gel point viscosity increases from $\eta_{\text{pure\_DCPD}}^{80\ \text{mg/cm3}} = 0.08\text{Pa}\cdot\text{s}$ for pure pDCPD to $\eta_{2.5\%\ \text{NB}}^{80\ \text{mg/cm3}} = 1.05\text{Pa}\cdot\text{s}$ for a ratio of DCPD to NB = (100:2.5) and to $\eta_{10\%\ \text{NB}}^{80\ \text{mg/cm3}} = 14.22\text{Pa}\cdot\text{s}$ for a ratio of DCPD to NB = (100:10).

As outlined above, a higher gel point viscosity has the potential to reduce the amount of shear experienced by the developing polymer network and thus reduce the shear-induced damage in the wet gel. Coating 2 mm inner diameter rotating hollow spheres with wet gels containing 10% norbornene (35 mg/cm^3 DCPD, 10% NB, 0.2 wt.% catalyst, filled with Δp = 102.6 Torr, and rotated at 10/14.142 rpm for ~17h) revealed that the initially weak gel network is considerably stronger, as the coating uniformity of the inner surface of the hollow sphere significantly improves. (Figure 2-15)

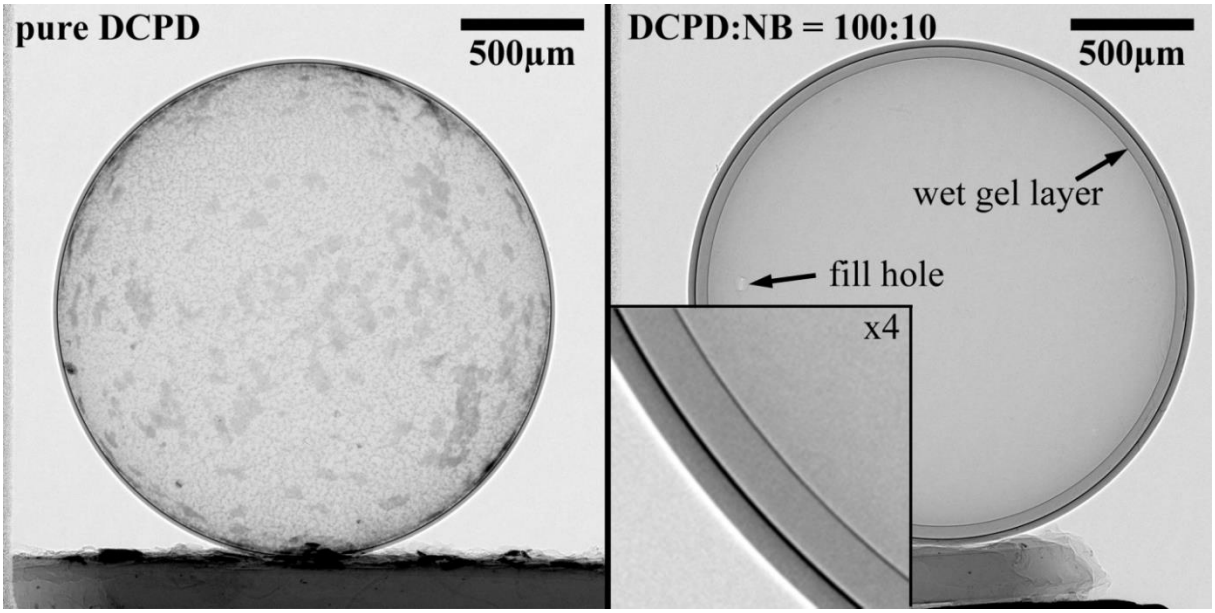

Figure 2-15: Cross-sectional radiographic image of 2 mm diamond spheres coated with a p(DCPD) and a p(DCPD-r-NB) wet gel layer: a) 30 mg/cm^3 DCPD, 0.2 wt.% catalyst, filled with Δp = 81 Torr, and rotated at 10/14.142 rpm for ~2.5h. b) 35 mg/cm^3 DCPD, 10%NB, 0.2 wt.% catalyst, filled with Δp = 102.6 Torr, and rotated at 10/14.142 rpm for ~17h). The coating of the inner surface of the hollow sphere becomes very homogeneous and smooth, rendering the addition of norbornene a success. (radiographs taken by John Sain, LLNL)

Comparing to the pure pDCPD wet gel layer in a hollow sphere to the p(DCPD-r-NB) wet gel layer illustrates the vital effect of norbornene addition to the precursor solution.

Additionally to the effect of changing the rheological properties of the wet gel during gelation, norbornene addition changes the morphology and densities (see chapter 5.2.1) of the resulting aerogels formed by supercritical drying. p(DCPD-r-NB) aerogels that were copolymerized with norbornene show the same structure of randomly oriented fibers as the pure pDCPD aerogels (compare to Figure 2-6), but, with an increasing norbornene concentration, the length of the individual fibers decreases. (Figure 2-16)

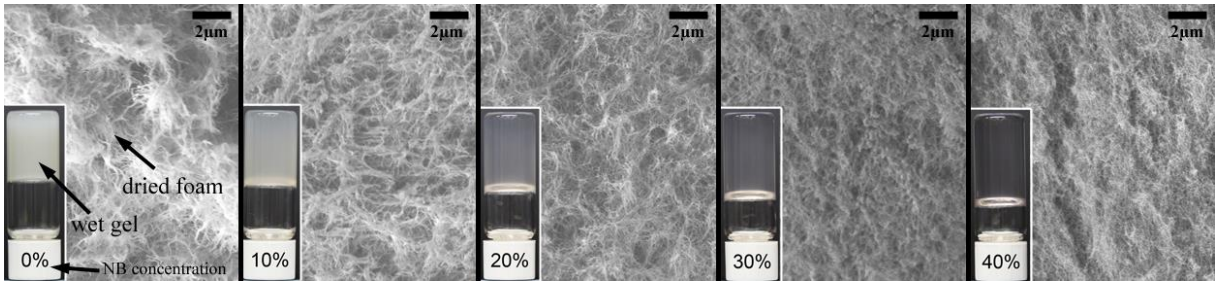

Figure 2-16: Scanning electron microscopy image of p(DCPD-r-NB) aerogels (50 mg/cm^3, 0.1 wt.% catalyst) with increasing norbornene concentration. p(DCPD-r-NB) aerogels copolymerized with NB have the same web-like morphology as pDCPD aerogels, but the length of the individual fibers decreases with higher norbornene concentration. The inlet in the picture for each norbornene concentration shows a photograph of the respective p(DCPD-r-NB) wet gel in a 2 ml vial. (image credit: Sung Ho Kim and Christoph Dawedeit, LLNL)

The length of the individual fibers decreases from a few micrometers in pure pDCPD aerogels to hundreds of nanometers with higher norbornene concentrations in the p(DCPD-r-NB) aerogels. The same effect can be observed in pDCPD aerogels with different densities as illustrated in Figure 2-17.

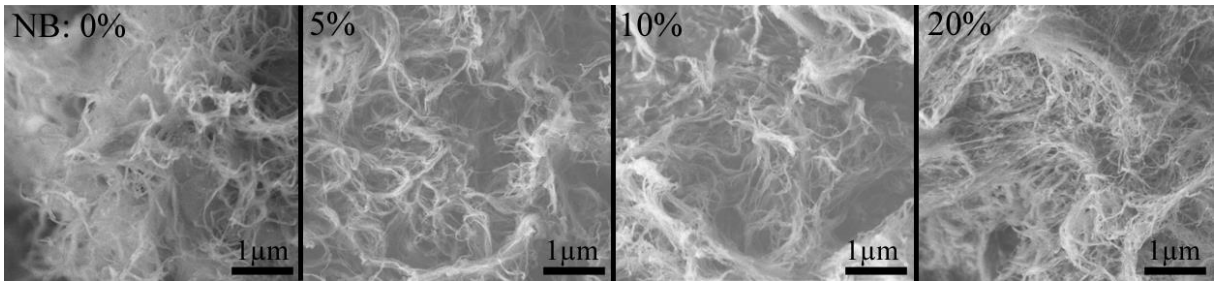

Figure 2-17: Scanning electron microscopy image of p(DCPD-r-NB) aerogels (25 mg/cm^3, 0.2t.% catalyst) with increasing norbornene concentration. As with the 50 mg/cm^3 pDCPD aerogels the 25 mg/cm^3 aerogels copolymerized with NB have a web-like morphology, with a decreasing length of the individual fibers for higher norbornene concentrations. (image credit: Sung Ho Kim, LLNL)

The 25 mg/cm^3 p(DCPD-r-NB) aerogels have a very similar morphology, which also depends on the concentration of the added norbornene copolymer.

A systematic study in a cylindrical geometry revealed that the ideal ratio of DCPD to norbornene depends on different factors, such as desired density of the coating, catalyst concentration[34], and thickness. For 25 mg/cm^3 p(DCPD-r-NB) aerogel coatings, a combination of 15% norbornene and 0.2 wt.% catalyst was found ideal to produce uniform coatings in hollow spheres. Figure 2-18 shows two representative radiographs of wet gel coatings in hollow 2 mm inner diameter diamond spheres.

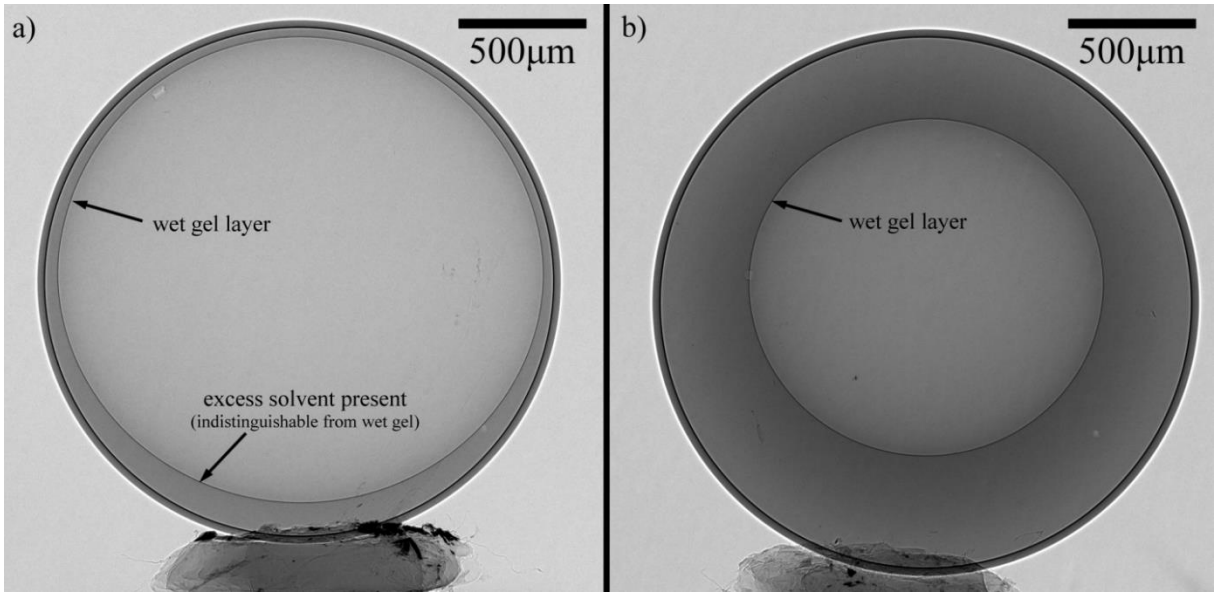

Figure 2-18: Cross-sectional radiographic image of 2 mm diamond spheres coated with p(DCPD-r-NB) wet gel layers: a) 25 mg/cm^3 p(DCPD-r-NB), 15%NB, 0.2 wt.% catalyst, filled with Δp = 104.5 Torr, and rotated at 10/14.142 rpm for ~17 h. The coating appears to be homogeneous and smooth, albeit some excess solvent present at the bottom of the shell. b) 25 mg/cm^3 p(DCPD-r-NB), 15%NB, 0.2 wt.% catalyst, filled with Δp = 422 Torr, and rotated at 10/14.142 rpm for ~16 h). The coating of the inner surface of the hollow sphere appears to be homogeneous for thicker wet gel layers as well. (radiographs taken by John Sain, LLNL)

For a 50 µm thick 25 mg/cm^3 p(DCPD-r-NB) wet gel layer (Figure 2-18a) the coating appears to be homogenous and free of irregular foam fragments. Increasing the thickness of the 25 mg/cm^3 p(DCPD-r-NB) wet gel layer to 350 µm (Figure 2-18b) and keeping the norbornene concentration in the precursor solution constant also results in a smooth gel layer. However, increasing the density of the wet gel requires adjusting the ratio of DCPD to norbornene in the precursor to achieve optimal conditions for coatings free of irregular gel fragments. For example, for 50 mg/cm^3 p(DCPD-r-NB) aerogels, a combination of 10% norbornene and 0.1 wt.% catalyst was found ideal to achieve uniform layers.[34] The combination of added norbornene, catalyst concentration, and rotational parameters needs to be adjusted specifically for the different desired properties (thickness, density, dopants, etc.) of the resulting foam layer.

It should be noted that a detailed analysis of the wet gel layers rotated under two-axis rotation as shown in Figure 2-18 in concentricity, sphericity, and roughness revealed non-uniformities mostly dominated by the non-concentricity (mode 1 thickness non-uniformity) of the inner and outer wet gel layers surface. This issue and its solution are particularly addressed in chapter 3.

The morphology of p(DCPD-r-NB) aerogels formed *under rotation* was assessed by cracking open a 2 mm HDC capsule (ID) that was coated with a p(DCPD-r-NB) aerogel (50 mg/cm^3 DCPD, 10 wt.% NB, 0.1 wt.% catalyst, filled at $\Delta p = 102.1$ Torr, rotated at 10/14.142 rpm for ~2.5 hours), doped with liquid phase iodine, and then supercritically dried. It is identical to the non-rotated aerogels and shows the same web-like morphology and pore distribution. (Figure 2-19)

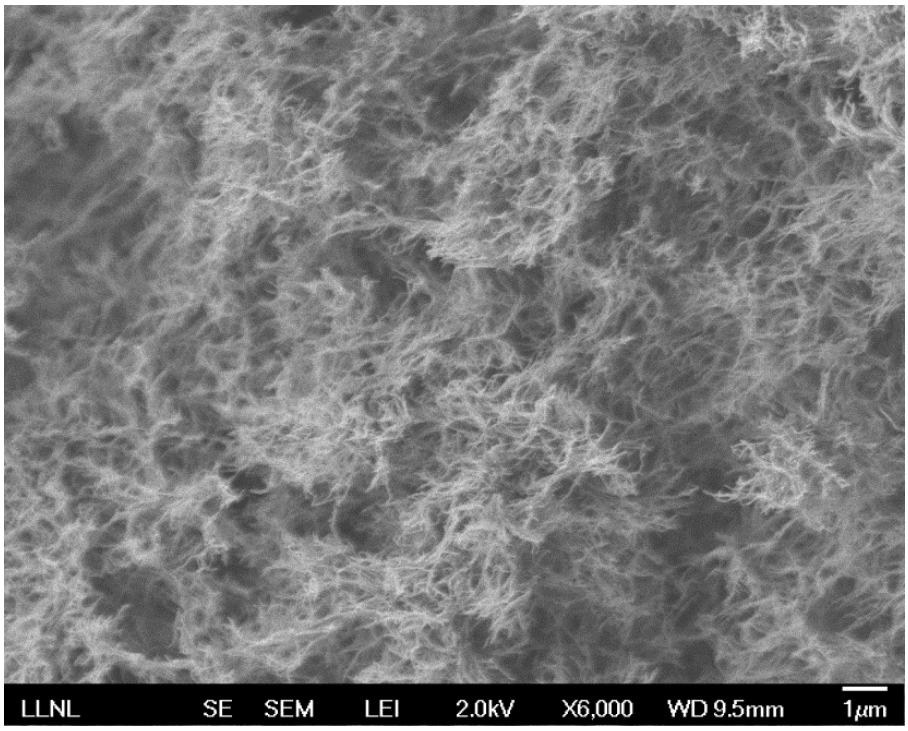

Figure 2-19: Scanning electron microscopy image of a p(DCPD-r-NB) aerogel (50 mg/cm^3 DCPD, 10 wt.% NB, 0.1 wt.% catalyst) that was coated into a 2 mm HDC capsule (ID) (filled at $\Delta p = 102.1$ Torr, rotated at 10/14.142 rpm for ~2.5 hours, doped with liquid phase iodine) and then supercritically dried. The ultra-low density foam still has the same web-like morphology as the non-rotated foams do. (SEM taken by Monika Biener, LLNL)

2.4. **Mechanical properties of p(DCPD-r-NB) aerogels**

As noted in the introduction of this thesis, low density porous materials have a wide range of applications. Polymer foams are of particular interest due to their interconnected pore structure, ultralow densities, and their importance in fabrication of various materials.[97, 117, 154-155] Incorporating these materials into functional devices, however, requires detailed understanding of their mechanical properties as some applications are limited by the above mentioned properties.[156-157] Several reports that

investigate the mechanical properties of low density porous materials can be found in the literature.[97, 117, 124, 156-161]

Spherical nanoindentation tests, or "depth-sensing indentation testing,"[162] allow the characterization of elastic and inelastic behavior of materials by using the measured depth of penetration of the indenter and its known geometry. For this purpose, a spherical indentation probe with radius R is brought into contact with the sample and whilst being indented into it, the load-displacement data are recorded. Figure 2-20 shows the schematic cross section of an indentation test and the respective schematic load as a function indenter displacement. It illustrates the necessary parameters used in this chapter.

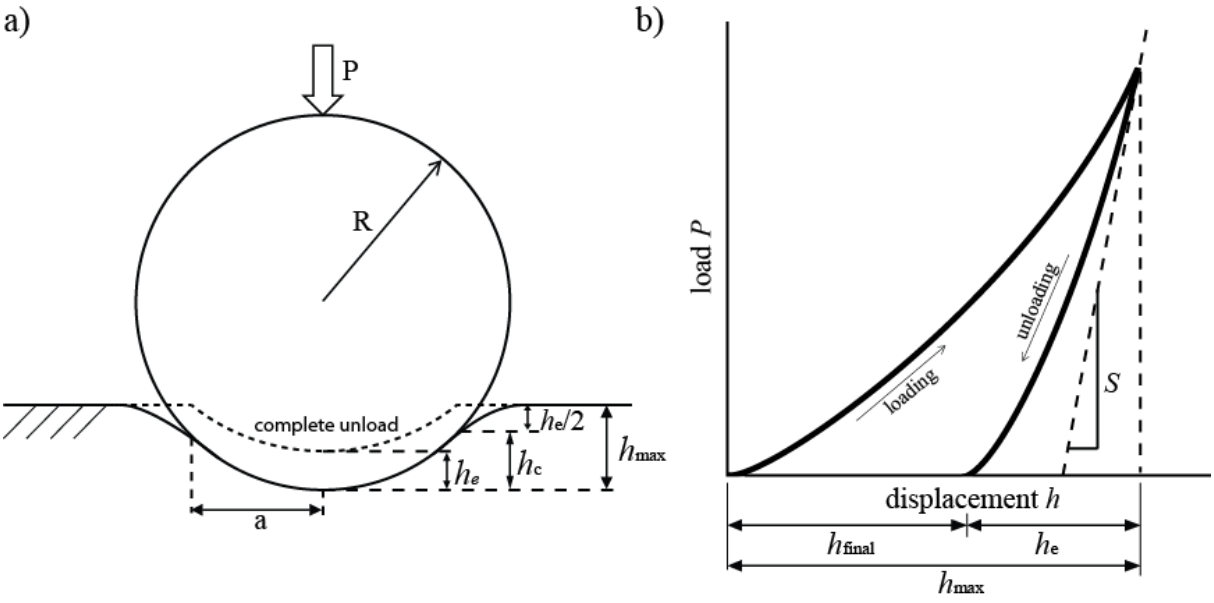

Figure 2-20: Schematic representation of spherical indentation: a) Geometry of elastic/plastic indentation, where P is the indentation load, R the radius of the spherical indenter, a the radius of the contact boundary, h_{max} the total displacement into the sample's surface, h_e the elastic depth of penetration, and h_c is the vertical distance along which contact is made; b) Schematic representation of the load P as a function of indenter displacement h, adapted from Oliver, Pharr (1992), where h_{max} is the indenter displacement at peak load, h_{final} the final depth of contact impression after unloading, and S the initial unloading stiffness.

The displacement at peak load h_{max} can be written as

$$h_{max} = h_e + h_{final}$$

where h_e is the elastic depth of penetration and h_{final} is the final depth of contact impression after unloading. Figure 2-20 a) shows that the displacement at peak load h_{max} can also be written as

$$h_{\max} = h_c + \frac{h_e}{2},$$

where h_c is the vertical distance along which contact is made, or "contact depth."[163]

Field and Swain[164] used Sneddon's work[165] to show that the "elastic displacements of a plane surface above and below the circle of contact" (see Figure 2-20 a) are equal for elastic loadings. Therefore, if the penetration depth is small compared to the radius of the indenter, the depth of penetration h_e can be written as

$$h_e = \frac{a^2}{R},$$

where a is the radius of the circle of contact. The elastic modulus or Young's modulus of the sample E_{sample} can then be derived from the elastic part of the load displacement curve using Hertz's well documented theories[165-167] with the indentation load P for a sphere with radius R

$$P = \frac{4}{3} E_{effective} \sqrt{R} h_e^{3/2}$$

and

$$\frac{1}{E_{effective}} = \frac{1 - \nu_{sample}^2}{E_{sample}} + \frac{1 - \nu_{indenter}^2}{E_{indenter}},$$

where $E_{indenter}$ and $\nu_{indenter}$ are the elastic modulus and the Poisson's ratio of the indenter. Combining these equations yields

$$\begin{aligned} P &= \frac{4}{3} E_{effective} \sqrt{R} \left(\frac{a^2}{R}\right)^{3/2} \\ &= \frac{4\pi}{3\pi} E_{effective} \sqrt{R} \left(\frac{a a^2}{\sqrt{R} R}\right) \\ &= \frac{4\pi}{3\pi} E_{effective} \left(\frac{a a^2}{R}\right). \end{aligned}$$

This equation can be rewritten to

$$\frac{P}{\pi a^2} = \frac{4}{3\pi} E_{effective} \left(\frac{a}{R}\right).$$

The term $P/\pi a^2$ is usually referred to as the Meyer hardness[163], mean contact pressure[164], or indentation stress.[168-169] The term a/R on the right side of the equation is commonly referred to as the indentation strain.[164 168, 170-171] It should be noted that different definitions for the indentation strain have been adopted in the literature,[169, 172] however, in this thesis the most widely adopted one is used.

Using the Oliver-Pharr method[163], the elastic modulus of the sample $E_{\text{effective}}$ can then be derived from the unloading stiffness $S = \left(\frac{dP}{dh}\right)$ by linear fitting the initial part of the unloading curve, (see Figure 2-20 b) which yields

$$\begin{aligned} S &= \left(\frac{dP}{dh}\right) \\ &= \frac{d}{dh}\left(\frac{4}{3}E_{\text{effective}}\sqrt{R}h_{\text{e}}^{3/2}\right) \\ &= 2E_{\text{effective}}\sqrt{R}h_{\text{e}}^{1/2} \\ &= 2E_{\text{effective}}\sqrt{Rh_{\text{e}}} \\ &= 2E_{\text{effective}}\sqrt{R\frac{a^2}{R}\frac{\pi}{\pi}} \\ &= 2E_{\text{effective}}\sqrt{\frac{A}{\pi}}. \end{aligned}$$

Consequently, the depth of penetration h_{e} can be rewritten as $h_{\text{e}} = \frac{3}{2}\frac{P}{S}$. Field and Swain showed[164] that the contact depth below the circle of contact h_{c} (Figure 2-20 a) must be rewritten when it includes a plastic component. It then is calculated by $h_{\text{c}} = R - \sqrt{R^2 - a^2}$, which yields $a = \sqrt{2Rh_{\text{c}} - {h_{\text{c}}}^2}$ with $h_{\text{c}} = h_{\max} - \frac{1}{2}h_{\text{e}}$. (Figure 2-20)

It should be noted that this derivation is motivated by the spherical geometry of the indenter and needs modifications for different indenter shapes.[163]

For the depth sensing indentation experiments of p(DCPD-r-NB) aerogels, 1 ml of p(DCPD-r-NB) wet gels at different densities (20, 30, 40, and 50 mg/cm^3) with 5 wt.% NB (relative to pDCPD) were synthesized in a 1 cm^3 glass cube with open ends on two parallel sides using 0.2 wt.% Grubbs' 1st generation catalyst[101]. Both open ends of the cube were capped with a glass microscope slide before gelation to ensure

the exposed surface is perfectly flat. After gel formation was complete, the microscope slides were removed and the wet gels in the open ends cube were dried supercritically with carbon dioxide (see chapter 5) to convert them into aerogels. One open surface of the aerogel in each cube was then tested at room temperature with an MTS XP Nanoindenter using a spherical sapphire indenter tip with a radius of R=986 µm. The Poisson's ratio of the sapphire is assumed to be 0.234 and its elastic modulus to be 441 GPa.[163] For each sample a series of partial indents with multiple load and unload cycles was performed, each with an unloading percentage of 100%. The elastic modulus and indentation stress are calculated according to the Oliver-Pharr method[163] based on the slope of the linear fit at the initial part of the unloading curve as described above. The indentation stress and strain curves are derived with the methods described above.

Figure 2-21 a) shows the load-displacement curves for different series of partial indents with multiple load and unload cycles for the p(DCPD-r-NB) aerogel with a density of 40 mg/cm^3. The load-displacement results are reproducible, which is a good indicator that the aerogel's mechanical properties are uniform on a large length scale as each indentation test series was done at least 2 mm apart from the previous test. The elastic modulus, obtained from the analysis of partial load- and unload data as described above, appears to be independent from the indenter penetration depth *h* as illustrated in Figure 2-21 b).

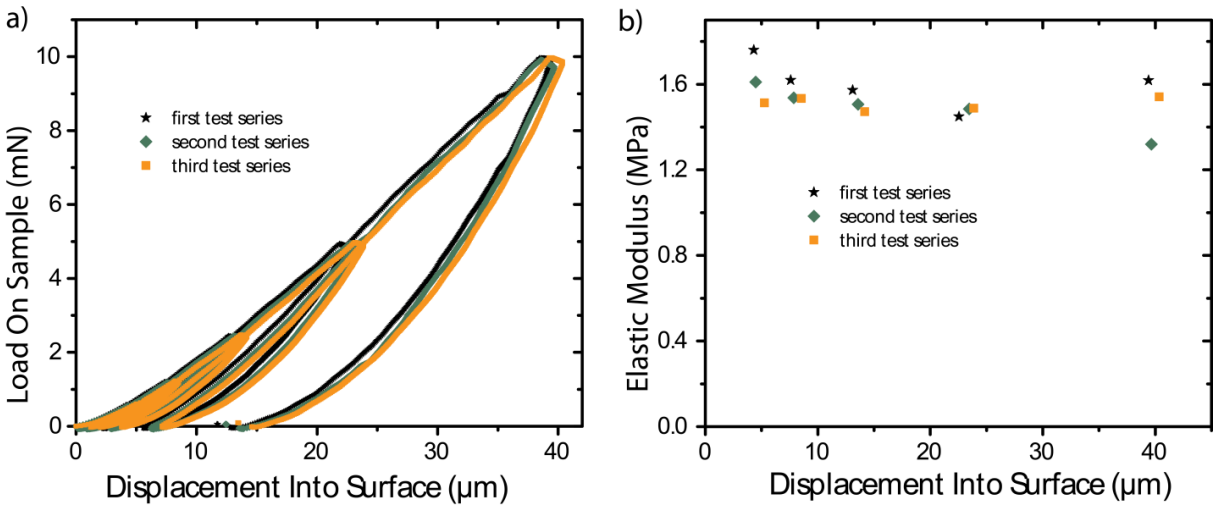

Figure 2-21: a) Load-displacement curves for a 40 mg/cm³ p(DCPD-r-NB) aerogel (5%NB, 0.2 wt.% Grubbs' 1st generation catalyst) indented with a spherical sapphire tip with a radius of 986 µm. The curves for different test series lay essentially on top of each other, showing that the material's mechanical properties are uniform throughout the sample; b) Elastic modulus as a function of displacement. The unloading elastic modulus is independent from indenter penetration depth *h*.

The 40 mg/cm³ p(DCPD-r-NB) aerogels with 5 wt.% NB measured here have an elastic modulus or Young's modulus of (1.49±0.08) MPa, which is comparable to other ultra-low density foams such as boron nitride foams,[159] carbon nanotube foams,[173] silica aerogels,[174] or even pDCPD aerogels[175]. The indentation data can now be converted to representative stress-strain curves for the material as illustrated in Figure 2-22. It shows the indentation stress-strain values for the p(DCPD-r-NB) aerogel with a density of 40 mg/cm³.

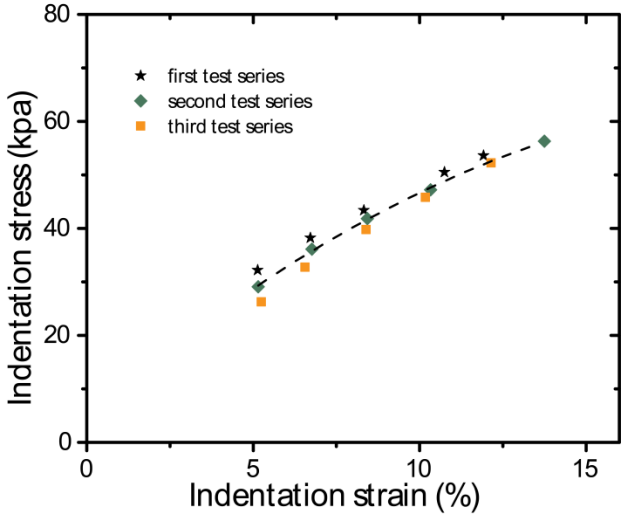

Figure 2-22: Indentation stress-strain curves for a 40 mg/cm³ p(DCPD-r-NB) aerogel (5% NB, 0.2 wt.% Grubbs' 1st generation catalyst) indented with a spherical sapphire tip with a radius of 986 µm. The dashed line is to guide the eyes.

The indentation stress, or Meyer hardness, of the aerogel increases with increasing indentation strain, which suggests that the Mayer hardness is a function of the indentation depth. This is in accordance with indentation measurements on different low-density, nanoporous materials.[156] The mechanisms of deformation in the p(DCPD-r-NB) aerogels are most likely defined by elastic bending, fracturing of the ligaments, densification, and collapse of pores. Therefore, the hardness of the material depends on the strength of the individual ligaments and the porosity of the material.

Comparing the load-displacement curves for p(DCPD-r-NB) aerogels with different densities shows a density dependence for the elastic modulus as illustrated in Figure 2-23.

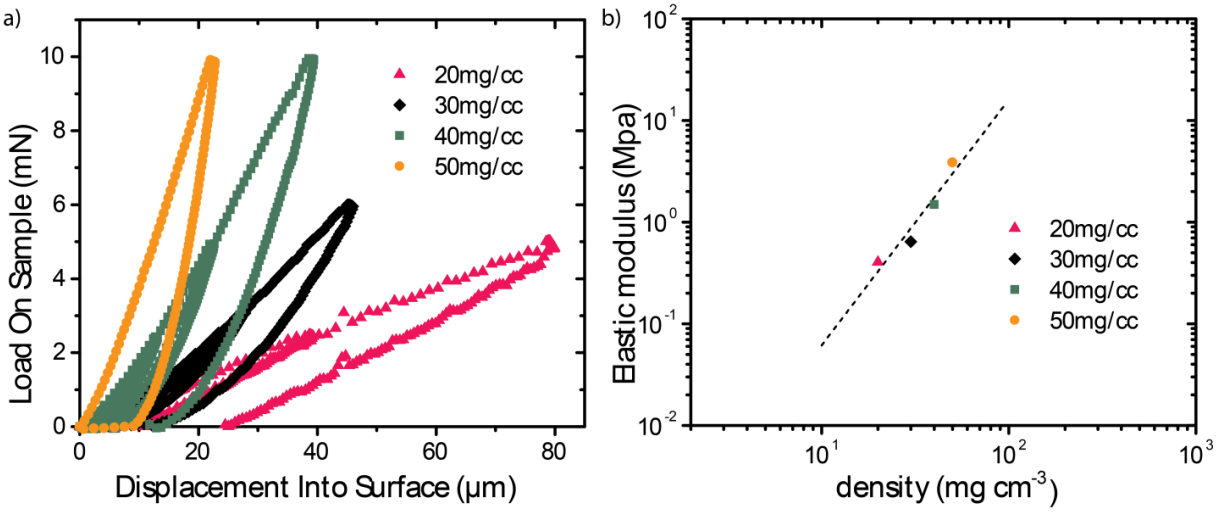

Figure 2-23: a) Comparison of load-displacement curves for p(DCPD-r-NB) aerogels (different densities, 5% NB, 0.2 wt.% Grubbs' 1st generation catalyst) indented with a spherical sapphire tip with a radius of 986 µm. b) Log-log-plot of the elastic modulus as a function of density. The dashed line is to guide the eyes.

As expected, the elastic modulus increases as function of the aerogel density ρ; in fact, the elastic modulus E appears to have a power law dependency over the range of the observed densities as illustrated in the log-log-plot in Figure 2-23. This power-law density dependency can be expressed as $E \sim \rho^n$ with $n \approx 2.41$. The same power law density has been observed in many other man-made low-density materials, such as different carbon aerogels,[158] 3D graphene-derived carbons,[160] or silica aerogels.[176-177] In comparison, in naturally occurring porous materials such as wood or bone the modulus scales roughly quadratically with the relative density,[178] however, at higher bone densities, the exponent can increase to $n = 3$.[179] At low densities the bone structure can be imagined as rods forming an open cell network, while at higher

densities the cell walls fill in to form plates and the structure becomes a closed cell network.[179] Gibson and Ashby[178] propose a model in which the exponent *n* can then be "attributed to the bending moment of the struts comprising the cell walls"[180] and that, therefore, the Young's modulus varies differently for open and closed cell structures. However, these scaling laws "assume some degree of uniformity in the distribution of mass between the interconnecting lattice 'beams' and the nodes that define their intersections"[181] and many aerogel samples with ultra-low densities (aerogel density less than 1% of its constituent density) show higher scaling exponents.[158] One explanation proposed in the literature is the presence of mass in the material that is disconnected from the load-bearing structure, which adds mass, but does not carry or transfer loads.[181] A different model to interpret the power law exponent is the aggregation of fractal clusters that are connected via thin struts,[182] which are affected in all mechanical transformations and, therefore, change the exponent.[183] Finite-element modeling and X-ray diffraction imaging experiments of ceramic nanofoams revealed structures consisting of clusters that are connected by thin beams,[181] which could explain the higher scaling exponents.

Chapter 3: Coating the inner surface of hollow spheres

The majority of this chapter was published[184] and is reprinted (adapted for this thesis) here with permission from Braun, T.; Walton, C. C.; Dawedeit, C.; Biener, M. M.; Kim, S. H.; Willey, T. M.; Xiao, X.; van Buuren, A.; Hamza, A. V.; Biener, J., In Situ Real-Time Radiographic Study of Thin Film Formation Inside Rotating Hollow Spheres. ACS Applied Materials & Interfaces 2016, 8 (4), 2600-2606. Copyright (2016) American Chemical Society.

As mentioned in the introduction, the uniformity of coatings inside hollow spheres is crucial for the performance of each respective application and requires deterministic control of the coating process.[3, 18-21] Most spherical coatings, however, are not ideal, which can lead to potential error[18] and performance deterioration.[9, 21-22] Imperfections in the foam or ice layer of a target used for inertial confinement fusion experiments could seed Rayleigh-Taylor instabilities leading to a non-symmetric implosion.[57, 76-79, 185-186] The Rayleigh-Taylor instability growth on low-density foam targets has been extensively studied,[21, 66] showing how the uniformity of the polymer foam is essential for successful inertial confinement fusion experiments.

In this chapter, the fabrication of uniform thin films on the inside of hollow spheres by using a uniaxial rotation process is described. The decision to explore a uniaxial rotation coating approach was motivated by the results of computational fluid dynamics (CFD) simulations that suggested the formation of more uniform films than those fabricated by the previously reported two-axis rotation approach.[12] In-situ real-time radiography and spatio-temporal image analysis provided critical data on the effect of liquid viscosity and rotational velocity on the resulting coating uniformity. Finally, the new uniaxial coating approach on sol-gel chemistry derived porous polymer coatings on the inside of 2 mm diameter spherical shells was tested. The results demonstrate that the uniaxial coating approach can produce highly uniform porous polymer film coatings with deterministic thickness control.

3.1. Experimental techniques

3.1.1. Computer Fluid Dynamics Simulations

Computational fluid dynamics (CFD) simulations were performed by C.C Walton, LLNL, using the commercial software package (Star-CCM+ by CD-Adapco, Melville, NY, USA) based on the Navier–Stokes equations. In short, the volume-of-fluid (VOF) method was used to track the air/liquid interface. The center region (containing air only) was meshed with coarse polyhedral elements and a stack of 60 thin prism layers (each 2.5 μm thick) was used for the liquid region near the shell wall. The prism layer thickness was a compromise between resolving the thin liquid layers while keeping a reasonable computation time (about 150 hours on 16 processors for 360 s of simulated time). The liquid was initialized as a uniform coating and allowed to settle 2 minutes, then rotation was started, with $\omega(t)$ following a sigmoid function to provide a gentle start. The liquid was modeled as having a surface tension of 0.02 N/m and a contact angle of 0°, based on manufacturer's properties of the oil (surface tension taken from a similar viscosity-standard oil). The computations were 3D at the actual physical scale and no parameters were adjusted to improve agreement with the experiment. The simulation was sensitive to accumulating numerical residuals and had to be checked carefully for conserving the total fluid volume, which was kept within about ±5%.

3.1.2. Filling setup

Various methods have been developed and tested in order to fill the capsules. Wittstock and Worsley developed a direct filling method for capsules with fill holes well above 50 μm using a commercial syringe pump (Harvard Scientific). In order to accomplish this, a micro syringe (Hamilton) is filled with the precursor solution and attached to a micro pipette via PTFE tubing. The micropipette's position in three dimensional space can be controlled with a micro manipulation stage, which is needed to accurately insert the pipette into the capsule's fill hole. The syringe is then placed onto the syringe pump and the micropipette is carefully introduced into the capsule's fill hole using the manipulation stage. The syringe pump allows for the adjustment of the plunger's position, enabling a flow of precursor solution into the capsule. The entire setup is illustrated in Figure 3-1.

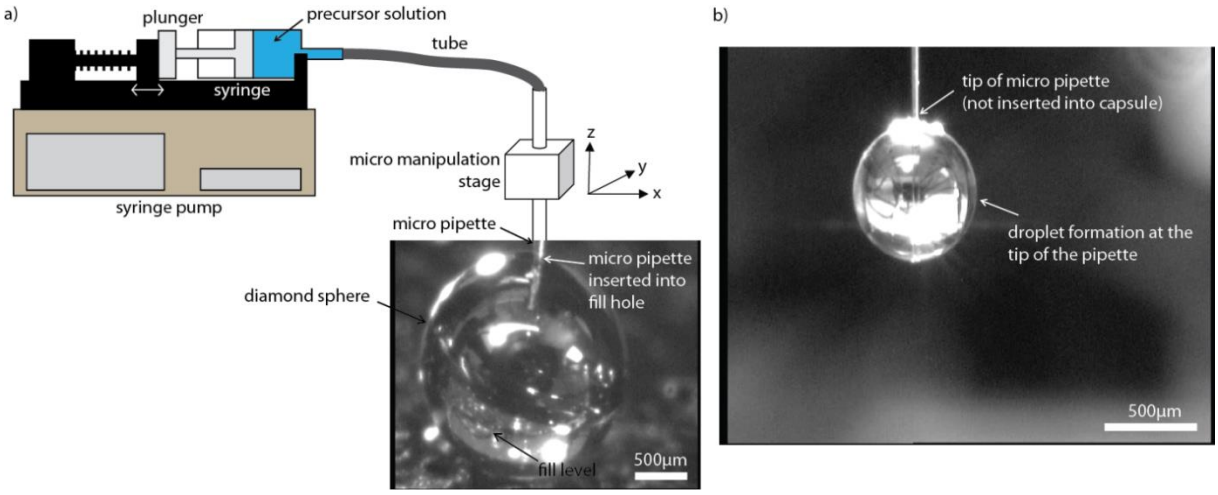

Figure 3-1: Syringe filling setup developed by Wittstock and Worsley: a) The syringe filled with the precursor solution is attached to a micro pipette via PTFE tubing. The micropipette's position can be controlled by a micro manipulation stage, allowing a precise insertion of the pipette into the capsule's fill hole. The syringe is then placed onto a syringe pump, which can adjust the plunger's position and, therefore, control the flow of precursor solution into the capsule. b) Once the precursor solution flows, a droplet forms at the tip of the micropipette. This prevents an accurate control of the liquid level in the capsule as the size of the droplet is very difficult to control.

However, due to the high pressure needed to get the liquid through the thin tip of the pipette, it is very difficult to precisely control the flow of precursor solution. Additionally, Wittstock and Worsley observed the formation of a droplet at the tip of the micropipette before the liquid drops into the capsule. The droplet has a volume of roughly 1 µl before it detaches itself from the micropipette, but its size is not always reproducible, which prevents an accurate control of the liquid fill level inside of the sphere. Since the diameter of the shells used for indirect drive laser fusion experiments is around 2 mm and consequently its volume is

$$V = \frac{4}{3}\pi(1\ \text{mm})^3 = 4.2\ \text{mm}^3 = 4.2\ \mu\text{l},$$

the size of the droplet equates to almost one fourth of the size of the sphere and, therefore the direct filling method using a syringe was not suitable for the required precision. Dawedeit, also mentioning this method, reports that the "liquid immediately plugged the gap between the fill hole and the glass-capillary" and that, consequently, "accurate control of the fill volume was not achieved".[187]

The film layer thickness inside of the spherical shell needs to be controlled reproducibly on a µm-scale. Therefore, a different filling method was developed using

a pressure gradient that allowed reproducibly injecting precursor solution into the capsule with 0.01 µl precision. The injected volume of precursor solution ΔV would, for a constant shell volume, solely depend on an applied pressure differential Δp, which can easily be derived from the ideal gas law

$$\Delta V = (V_s/p_0)\,\Delta p,$$

where ΔV is the injected volume, Δp is the applied pressure differential, and V_s and p_0 are the shell volume (4.2 µl) and standard pressure (760 Torr), respectively.

The setup is described in detail by Braun[34], Biener[12], and Dawedeit[187]: a vial containing the precursor solution and a linear feedthrough to which the ablator shell is attached are placed in a small vacuum chamber (Figure 3-2 a). The chamber is then under-pressurized (the pressure differential depends on the desired foam layer thickness) while the capsule is not in contact with the precursor solution. This prevents the formation of air-bubbles attached to the fill hole, which is critical for achieving the required reproducibility. The under-pressurized capsule is then submerged in the precursor solution and filled by re-pressurizing the chamber to atmospheric pressure.

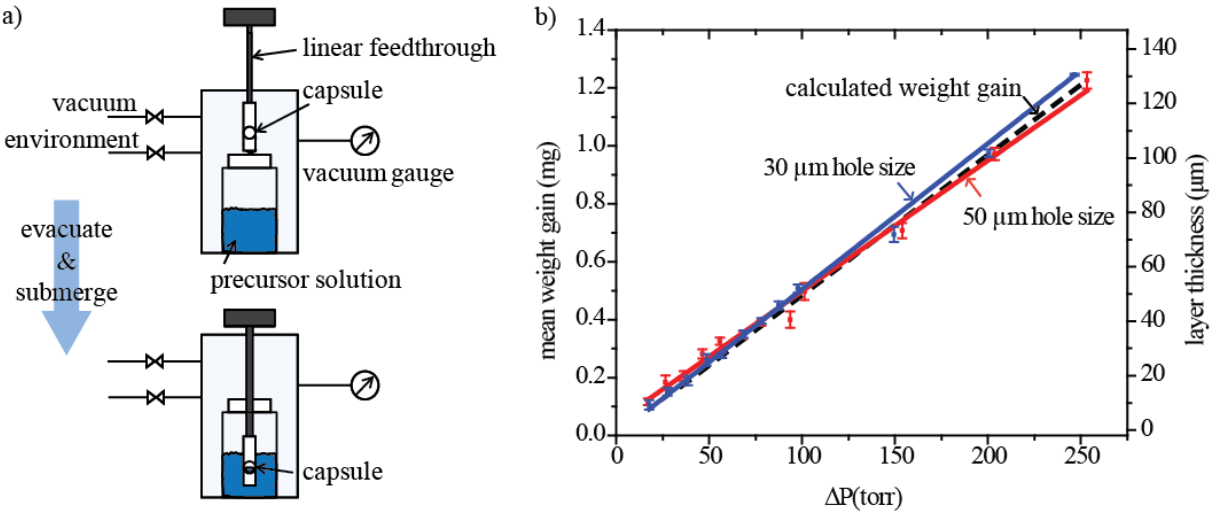

Figure 3-2: Pressure filling setup: (a) the filling setup consists of a small vacuum chamber that contains a vial with the aerogel precursor solution and a linear feedthrough to which the ablator shell is attached. To achieve high reproducibility with high accuracy, it is crucial to underpressurize the capsule before submerging it into the precursor solution. b) injected liquid and corresponding layer thickness versus applied pressure differential. The injected volume, as derived from weight gain measurements, follows the linear behavior (dashed line) expected from the ideal gas law and is almost independent of the hole diameter.[12, 34]

The injected volume in dependence of the pressure differential Δp (Figure 3-2 b) was determined by weight gain measurements using the density of toluene under ambient conditions (0.867g/cm^3). It increases linearly with the applied pressure differential and is also almost independent of the fill hole diameter.

The pressure differential filling setup has the required accuracy to precisely control the layer thickness in a spherical shell and has the advantage that is can easily be modified for different shell sizes and volumes. This self-developed method provides a novel tool to accurately fill hollow shells with nanoliter precision. The setup was further modified to completely fill a hollow sphere as described in chapter 4.

3.1.3. Coating Setup

All coating experiments were performed in a custom-built uniaxial coating setup consisting of a steel frame in the shape of a triangular prism, with two rolls on top, on which the capsule holder was placed (Figure 3-3). The rolls were driven by a brushless 120 Watt EC-max motor with hall sensors (maxon motor, Switzerland) through a transfer belt, which allowed adjusting the rotation speeds. For *in-situ* real-time radiography experiments the entire setup was placed on a high-precision translation sample stage that allowed precise alignment of the shell with the X-ray beam. To generate cross-sectional radiographs covering the full solid angle of 4π inside of the shell, most experiments were performed in two configurations with the rotational axis either coinciding (imaging axis $\parallel \vec{\omega}$) or perpendicular (imaging axis $\perp \vec{\omega}$) to the X-ray beam (Figure 3-3a). For the imaging axis $\perp \vec{\omega}$ configuration, the capsule holder blocked the X-ray beam twice every revolution, but the spatio-temporal film distribution is still clearly observable. Between each experiment enough time was allowed for the liquid to completely settle at the bottom of the shell to guarantee identical starting conditions.

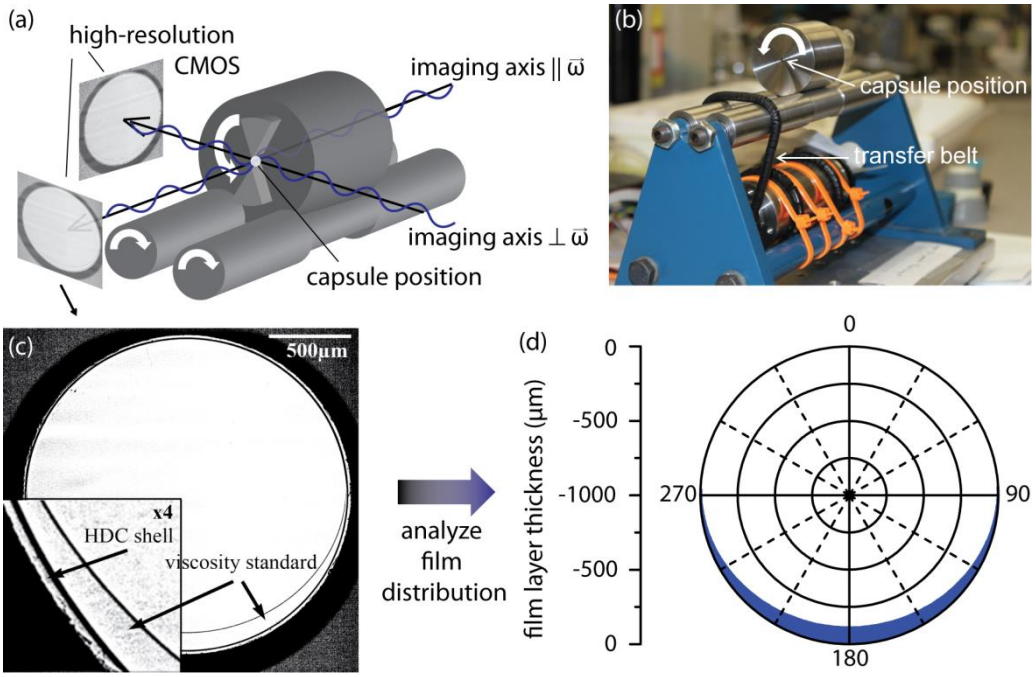

Figure 3-3: Experimental uniaxial coating setup used to analyze film formation in rotating spherical shells. Schematic (a) and photograph (b) of the uniaxial coater. The capsule, filled with enough liquid to allow formation a uniform film of the desired thickness, is placed on center axis of a small cylinder. Rotational axis and X-ray beam were adjusted to be either parallel or perpendicular to each other. (c) The cross-sectional radiographic image of the shell reveals how the liquid is distributed in the shell at a particular time. (d) These cross-sectional radiographs are subsequently analyzed with the measured data shown in solid blue. Analysis of the series of images taken during the experiment enables the reconstruction of the liquid's spatio-temporal distribution.

3.1.4. **Imaging of the shells**

The *in-situ* real-time radiography experiments, described in chapter 3.3, were performed at beamline 2BM-B at the Advanced Photon Source (APS), Argonne National Laboratory using a monochromatic beam with an energy of 24.3 keV. A 100 µm thick LuAG:Ce scintillator was used and the resulting image was projected through a 10x lens onto a *PCO.Dimax* detector with a frame size of 2016x2016. With the camera's pixel size of 11x11 μm^2 the effective pixel size for this experiment was 1.1x1.1 μm^2. The high X-ray flux and temporal resolution of beamline 2BM-B enabled *in-situ* observation of the distribution of the liquid in the rotating shell with a frame rate of 10 Hz which afforded a direct view on the influence of rotation speed and viscosity on concentricity, sphericity, and roughness of the resulting film layer. The spatio-temporal distribution of the liquid layers formed inside the shells was analyzed using self-written software.

Radiographs of foam coated shells were taken with the same X-ray setup described in chapter 2.1.

3.1.5. Coatings and Shells

Liquid coatings were prepared from General Purpose Viscosity Standards N4, N7.5, N14, N26, and N44 (Cannon Instruments). Viscosity Standards, based on the National Institute of Standards and Technology (NIST) value of 1.0016 mPa s (centipoise) for water at 20°C (68°F), were used as received. The dependence of the liquid's viscosity on temperature was taken into account by measuring the temperature under which experiments were performed (23.3°C) and calculating the viscosity for that respective temperature.

Porous polymer coatings were prepared from dicyclopentadiene with the same chemicals, compositions, method, and setup that are described in chapter 2.1.

For shells, 2 mm diameter high-density carbon (HDC, diamond) shells[17, 47] (Diamond Materials, Germany) were used because of their excellent mechanical properties and sphericity. To facilitate characterization, relatively thin-walled (20–30 μm) and transparent micro-crystalline HDC shells were used. Using a 30–50 μm diameter hole in the shell wall, the viscosity standards, toluene, or the polymer precursor solution were filled into the shells using the pressure-differential filling method as described in detail in chapter 3.1.2. The shells were then placed in the custom-built holder shown in Figure 3-3, which was sealed with polyimide film to prevent evaporation of the viscosity standards and precursor solution during rotation.

3.2. Fluid dynamics simulation experiments

Three-dimensional (3D) Computational Fluid Dynamics simulations performed by C. C. Walton, LLNL, for two different liquids under uniaxial rotation are shown in Figure 3-4. The steady state distribution of a liquid with a viscosity of 20 cP in a 2 mm sphere rotating at 20 rpm (liquid fill level equal to 50 μm uniform coating) is shown in Figure 3-4 a,b. The shell rotation pulls the liquid puddle up on the ascending side of the sphere where it stays, as the rotational velocity is not high enough to overcome the gravitational pull, resulting in a non-uniform coating. Slicing through the center plane of the sphere (Figure 3-4 a) shows that the thickest part of the liquid is at -50°

in latitude. The complete 4π picture of the liquid's distribution inside the hollow sphere (Figure 3-4 b), obtained by unwrapping the three-dimensional thickness distribution onto a longitude and latitude map, reveals that the thickest part of the liquid stays in the ascending hemisphere. If, however, the viscosity of the liquid and the rotational velocity are increased to 40 cP and 40 rpm (average coating thickness stays the same), a uniform steady state (Figure 3-4 c,d) is reached. The liquid is not only uniformly distributed along the center plane of the sphere (Figure 3-4 c), but over the full solid angle of 4π inside of the shell thus suggesting that uniform spherical coatings can be obtained by uniaxial rotation. The simulations also demonstrate the importance of choosing the correct parameter space of film thickness (fill volume), viscosity, and rotational velocity, similar to the well-documented pattern formation in rotating *cylinders*[139-141, 152, 188-191]. Moffat and Melo used the lubrication approximation (thin film layers and negligible inertial effects) of the Navier-Stokes equation and found that critical rotational velocities in an otherwise constant parameter space can describe the transitions between different steady states in cylindrical coatings.[139-140, 188] A similar approach was taken by analyzing the effects of the liquid's viscosity and the rotational velocity on coating uniformity since radius and film thickness (determines the volume of liquid) are usually predetermined by the desired application.

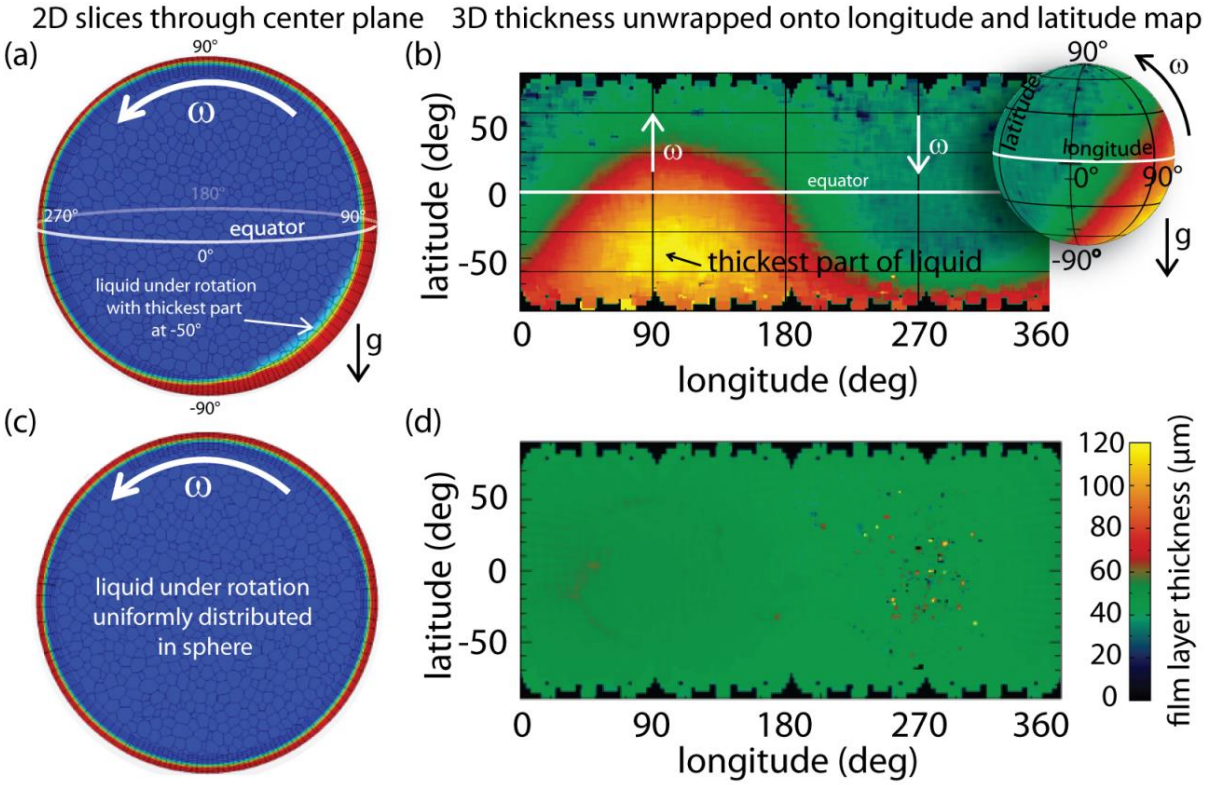

Figure 3-4: Three-dimensional (3D) Computational Fluid Dynamics (CFD) simulation of liquids in a 2 mm hollow spherical shell under uniaxial rotation. The liquid fill level is equal to a 50 μm uniform layer. (a) Snapshot of the steady state reached of a 20 cP liquid rotated with constant 20 rpm by slicing through the center plane of the sphere along 90° to 270° (longitude). The liquid is getting dragged up, but cannot overcome the gravitational pull and, therefore, the thickest part of the liquid stays at -50° (latitude). (b) Unwrapping the three-dimensional thickness distribution onto a longitude and latitude map gives a complete 4π picture of the liquid's distribution inside the hollow sphere during rotation. (c) and (d) The slice and the 3D thickness distribution of a 40 cP liquid rotated with 40 rpm show that uniaxial rotation can lead to uniform spherical coatings. The dots in the 3D thickness distribution are artifacts. (CFD simulations performed by C.C. Walton, LLNL)

3.3. **In situ synchrotron experiments**

Guided by these simulations, extensive in-situ real-time radiographic studies of the thin film formation in spherical shells were performed to explore the effect of liquid viscosity and rotational velocity of the spherical shell on the uniformity of the coating. A typical snapshot from an *in-situ* real-time radiography experiment in the imaging axis $\|\vec{\omega}$ configuration and its image analysis is shown in Figure 3.3 c,d. A complete spatio-temporal image analysis for a 10 cP viscosity standard rotating at 9.8 rotations per minute is shown in Figure 3-5. Without rotation, the measured liquid distribution (shown in solid blue) is solely determined by its wetting angle. All viscosity standards used in this study have a low contact angle thus allowing for good wetting. Without rotation (Figure 3-5a), the liquid is distributed between 87° and 272°, with the

thickest part of the liquid layer (115 µm) at the bottom of the shell (180°). Once the shell starts rotating, the liquid becomes more evenly distributed (Figure 3-5 d) and forms a continuous, but not yet uniform, film after ~ 7 rotations (66 s). After ~22 rotations (216 s), the film layer thickness equilibrates to 28(±3) µm.

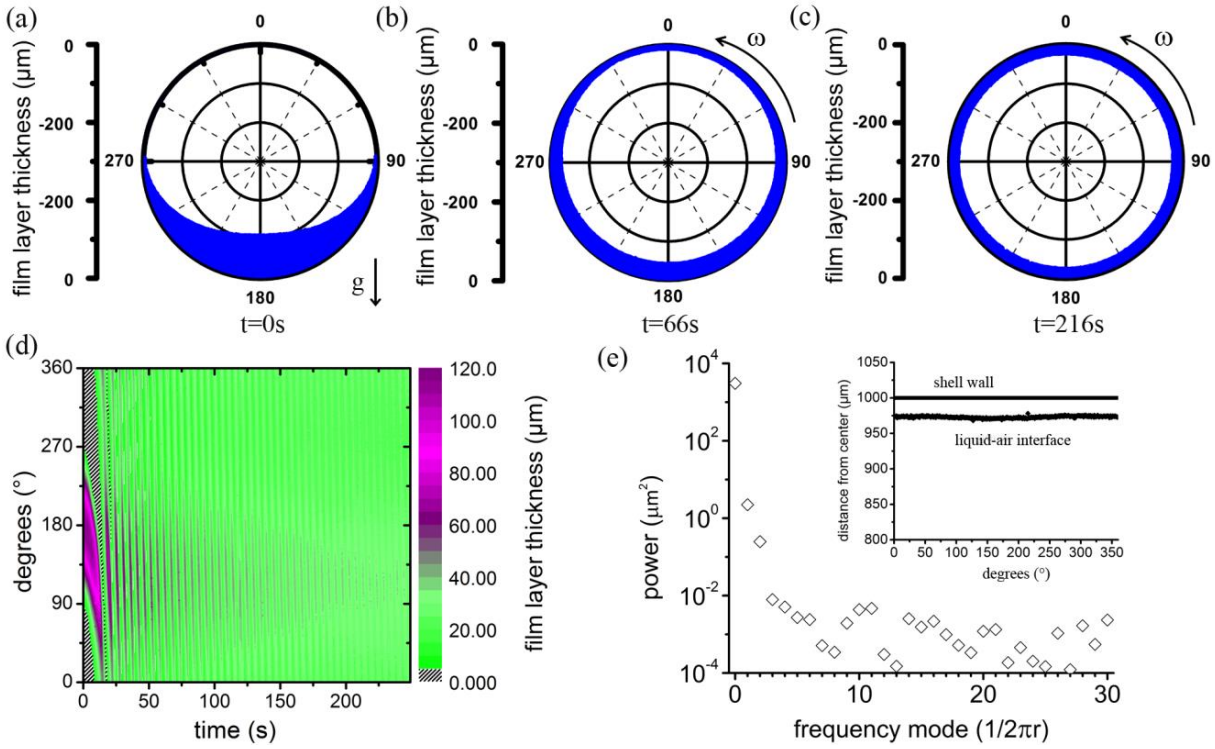

Figure 3-5: Spatio-temporal analysis of the uniform distribution of a 10 cP viscosity standard inside a hollow high density carbon sphere (2 mm ID) during uniaxial rotation with ω=9.8 rpm. (a) At initial conditions (t=0 s) all the liquid is distributed at the bottom of the sphere due to gravity. b) After t=66 s of rotation with ω=9.8 rpm, the viscosity standard is distributed completely around the shell, but hasn't reached steady state. (c) A uniform steady state is reached after t=216 s due to the right combination of rotational velocity and viscosity. (d) Complete spatio-temporal distribution of the rotation shows how the liquid is distributed in the capsule and forms a uniform film over time. (e) Power-mode spectrum of the liquid's inner surface after 216 s. The inlet is the thickness measurement at that time measured from the capsule middle point to the liquid-air interface and shell wall over the full 360°.

To further analyze the concentricity of the liquid film formed by uniaxial rotation, the power-mode spectrum of the liquid's inner surface after 216 s was computed (Figure 3-5e). It reveals a 2.2 µm^2 power in mode 1 (concentricity between capsule inner wall and liquid-air interface) and an out of roundness of the liquid's inner surface very well below 1 µm^2. This thickness variation is within the experimental error given the effective pixel size of 1.1x1.1 µm^2 during data collection and assuming an error of 2 pixels per axis per image with a frame size of 2016x2016 pixels for the image analysis.

Experiments performed in the complementary imaging axis $\perp\vec{\omega}$ configuration reveal very similar results thus demonstrating the formation of a film with uniform thickness over the full solid angle of 4π inside the shell.

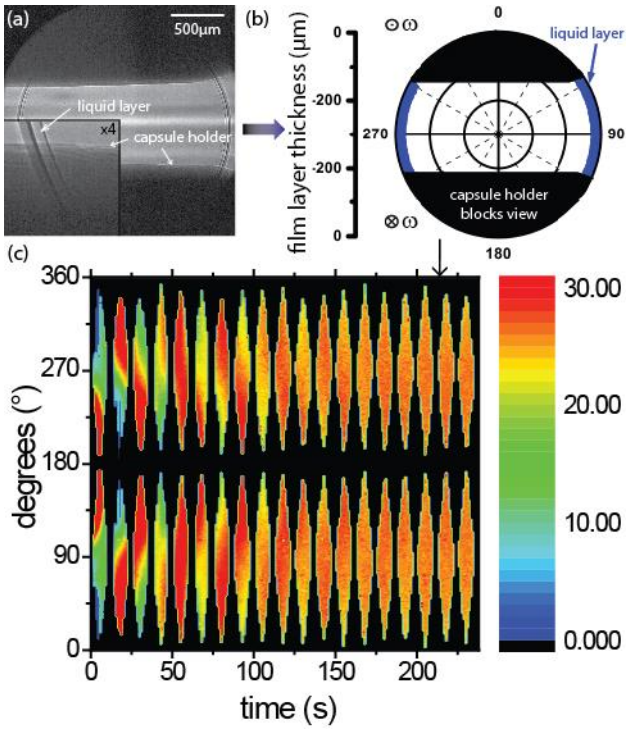

Figure 3-6: Spatio-temporal analysis of the uniform distribution of a 20.88 cP viscosity standard inside a hollow high density carbon sphere (2 mm ID) during uniaxial rotation with ω=1.95 rpm in the imaging axis $\perp\vec{\omega}$ configuration. (a) The cross-sectional radiographic image of the shell taken at 216 s reveals the steady state reached. Although the capsule holder blocks the view partially, it is evident that the liquid is distributed uniformly in the sphere. (b) These cross- sectional radiographs are subsequently analyzed with the measured data shown in solid blue. (c) The series of all images taken during the experiment allows a precise analysis of the liquid's spatio-temporal distribution. At initial conditions (t=0 s) all the liquid is distributed at the bottom of the sphere due to gravity. Once rotation is started the viscosity standard is distributed completely around the shell reaching a uniform steady state due to the right combination of rotational velocity and viscosity.

Here, the viscosity standard's initial distribution in the shell before rotation is, as expected, identical to that observed in the imaging axis $\|\vec{\omega}$ configuration, with a liquid puddle between 87° and 272°. As rotation begins, the liquid begins to distribute and starts to form a continuous film around the capsule. The film thickness in the left and right hemispheres (0° to 180° and 180° to 360°) stays symmetrical during the entire time of rotation, which can be attributed to the fact that the rotation axis is perpendicular to the gravity vector, allowing even distribution of the liquid over both sides. Experiments done under the same conditions, but with a purposely tilted axis,

indeed yield non-uniform films regarding concentricity between the capsule's inner wall and the liquid's inner surface. With a well aligned rotational axis, however, the film layer thickness reaches a uniform steady state of 27(±3) µm after 206 s.

By systematically changing the viscosity of the liquid and the rotational velocity of the capsule, three different characteristic steady state film configurations were identified. If the rotational velocity is too low for a given viscosity, the liquid cannot completely overcome the gravitational pull and therefore stays near the bottom of the shell. This is illustrated in Figure 3-7a, which shows the film thickness development for three rotations of a 10 cP viscosity standard, which was uniaxially rotated at 1.3 rpm. The liquid layer is thicker on the ascending side of the sphere (around 150°) and thinner on the descending side, reaching a steady state as the rotational velocity is not high enough to overcome the gravitational pull.

If, on the other hand, the rotational velocity is too fast or the liquid too viscous, the initially present liquid puddle is pulled over top point of the sphere and dragged around with the same rotational velocity as the capsule (Figure 3-7c). For a viscosity of 10 cP, this condition is reached at 65 rpm. However, the combination of viscosity and rotational velocity can be adjusted in such a way that, over time, the liquid becomes uniformly distributed inside of the sphere, reaching a uniform steady state (Figure 3-7b). Similar steady states have been observed in rotating cylinders.[140, 192-193]

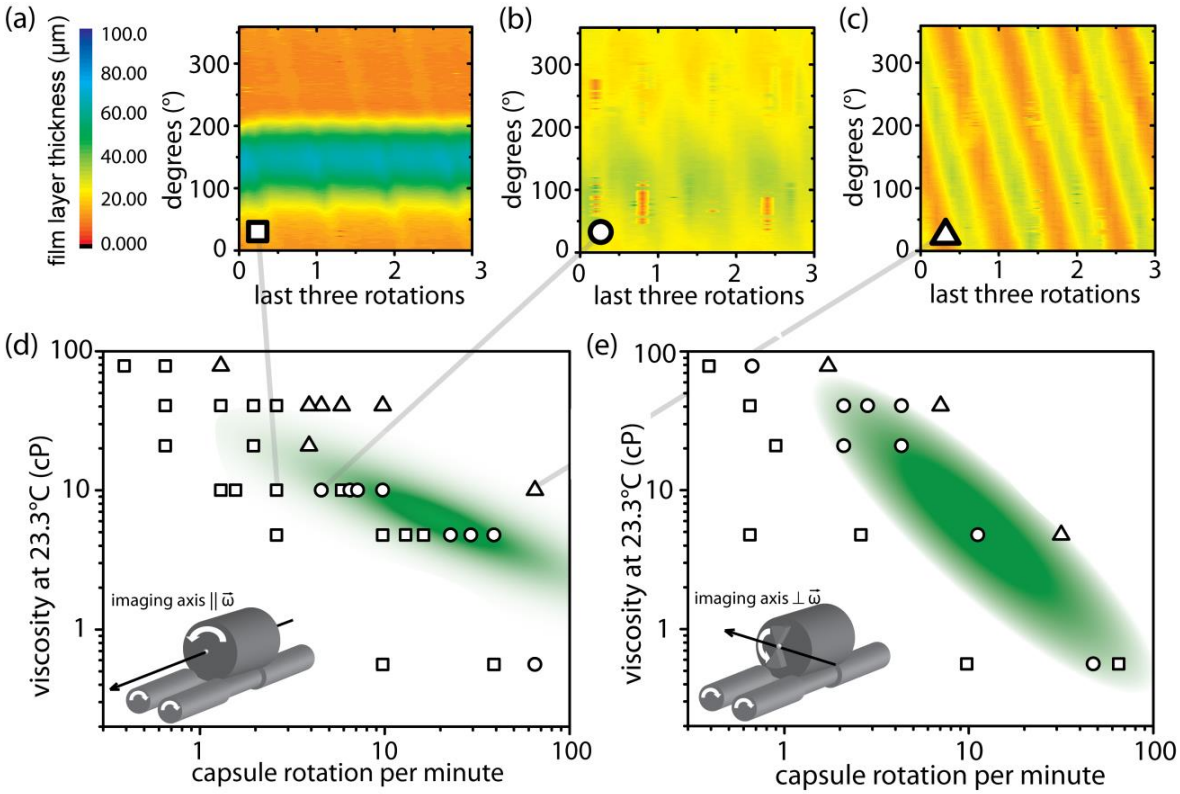

Figure 3-7: Summary of the results from different viscosity / rotational velocity combinations and the resulting steady states. (a) If the rotational velocity for a given viscosity is too slow, the liquid cannot overcome the gravitational pull and remains in same position during rotation. (b) If the combination of rotational velocity and viscosity is right, the liquid reaches a steady state forming a uniform film layer. (c) Combinations of high rotational velocities and high viscosity cause the liquid pool to be carried up and over the top before being completely distributed in the shell. (d,e) Stability regions of the steady states (a-c) in the viscosity / rotational velocity phase space for the imaging axis $\parallel \vec{\omega}$ (d) and imaging axis $\perp \vec{\omega}$ configuration (e).

Over 30 different combinations of viscosity and rotational velocity were tested and the results for both configurations are summarized in Figure 3-7d (imaging axis $\parallel \omega$) and Figure 3-7e (imaging axis $\perp \omega$). For each tested viscosity, the rotational velocity was adjusted multiple times to identify the liquid's different steady states and their transition points. For toluene (0.56 cP[194]), a rotational velocity of 65 rpm is needed to form a uniform continuous film. Lower velocities lead to non-uniform films with the thicker part of the liquid on the ascending side of the sphere (around 150° for 10 rpm and 90° for 39 rpm). Higher rotational velocities were not tested due to safety concerns as the capsule holder was not secured to the roller. These results were confirmed when repeating the experiment with the X-ray beam perpendicular to the rotational axis. At 10 rpm some of the liquid moves out of the observable plane, but the majority remains at the bottom of the shell. The same effect can be observed when

increasing the rotational velocity to 39 rpm with the exception that the liquid is moved out of the observable plane in a way that the resulting layer appears thinner, but uniform. This is why more films in the perpendicular view appear uniform, but when combining the parallel and perpendicular view of the experiments, we learn that the resulting overall 4π-film thickness is not uniform, but rather non-concentric. This can be illustrated when, for example, comparing the parallel and perpendicular view of the 0.56 cP liquid rotated at 39 rpm. The film appears to be uniform when looking from the 90°-view, but is actually non-concentric. The only experiment in the imaging axis $\perp \vec{\omega}$ configuration that is not symmetrical when comparing the left and right hemisphere is the 0.56 cP liquid rotated with 65 rpm (Figure 3-7d), which can be attributed to the capsule holder being slightly tilted.

The green regions in Figure 3-7d,e indicate the parameter space that results in the formation of uniform films. For example, for a liquid with a viscosity of 10 cP and a targeted film layer thickness of 28 µm, a uniaxial rotation with a velocity of 9.8 rpm results in the formation of a spherical uniform coating with 2 μm^2 out-of-roundness (mode 1) deviation, although maintaining a spherical concentricity of better than 4 µm was considered uniform. For liquids with viscosities of 20.88 cP and above, the window of rotational velocities that yield uniform coatings seems very narrow. For example, increasing the rotational velocity of the sphere from 2.6 rpm to 3.9 rpm for the 40.54 cP viscosity standard results in two distinctly different steady states. At 2.6 rpm the liquid cannot overcome the gravitational pull and at 3.9 rpm the liquid is already being dragged around the capsule, even though the uniformity of the film layer thickness in this case improves with time suggesting that eventually a uniform film may be formed.

3.4. **Coating of polymer films in hollow spheres**

With the guidance of simulations and the above obtained results, it was possible to uniformly coat the inside of 2 mm diameter HDC shells with uniform dicyclopentadiene-based polymer gel films of different densities by using uniaxial rotation. These sol-gel systems differ from the viscosity standards discussed above in that their viscosity increases with time until the system transitions into the solid state at the sol-gel transition. To achieve spherical coatings for sol-gel systems, the film

needs to be in a uniform steady state before the transition from the liquid to the solid state is completed. Previous coating experiments with polymer aerogels described in chapter 2.3 revealed that the gelation time and viscosity at the gel point can be controlled by adjusting the amount of cross-linking through copolymerization with a monomer that only forms linear chains. For a 50 mg/cm^3 p-DCPD aerogel with a 5 wt.% (bis)iodo-norbornene, NB-I_2 co-polymer[14] and 0.2 wt.% Grubbs catalyst, the aerogel has a viscosity of 2350 cP at the gel point.[14] However, the viscosity around the sol-gel point increases rather rapidly[15] and the coating should already be uniform. Based on Figure 3-7, a rotational velocity of 1.95 rpm was chosen to generate 30 µm thick coatings inside a 2 mm spherical shell using the uniaxial coating process. The reason for adding (bis)iodo-norbornene instead of norbornene is described in great detail in chapter 6. For the experiments performed here, the (bis)iodo-norbornene was added to increase contrast in the radiographic images. The capsule was placed in a saturated toluene vapor environment to prevent densification of the gel around the capsule's fill hole and rotated for 23 h to ensure gelation was complete. The wet gel was subsequently supercritically dried by direct solvent exchange with carbon dioxide.[82] The resulting foam layer, characterized by phase contrast enhanced X-ray imaging,[195] is extremely uniform, as Figure 3-8 illustrates.

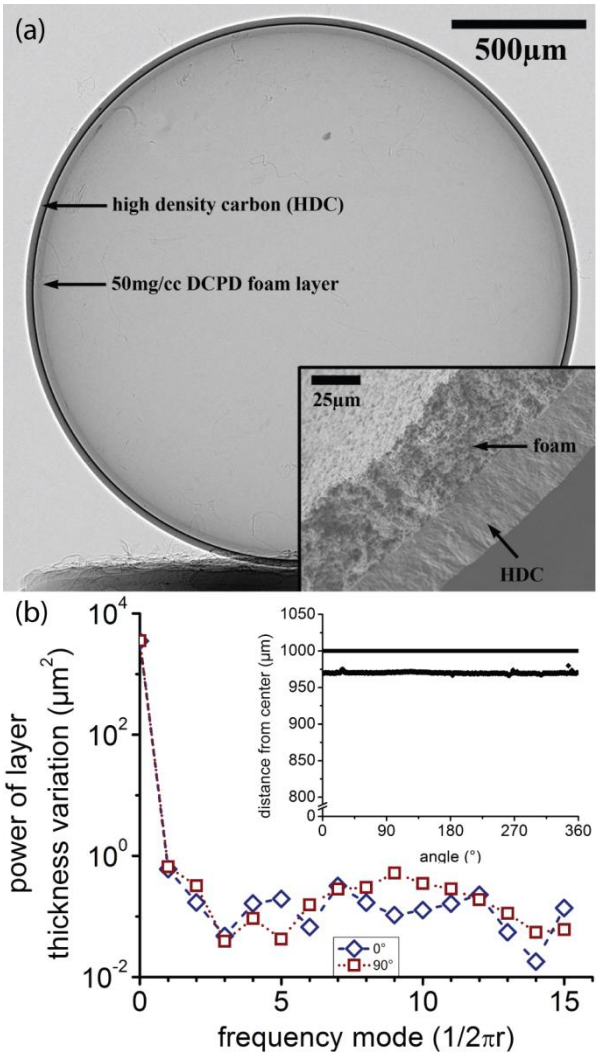

Figure 3-8: (a) Cross-sectional radiographic image of a 2 mm diamond sphere coated with a 30 µm thick (bis)iodo-doped p(DCPD-r-NB-I_2) foam layer (50 mg/cm³ DCPD, 5 wt.% NB-I_2, 0.2 wt.% catalyst, filled with ΔP = 104.5Torr, and uniaxially rotated at 1.95 rpm for 23 h). The polymer foam is distributed evenly in the hollow sphere and adheres well to the shell. The inlet shows an SEM image of the cross section of the foam-diamond-layers. (b) Two representative power spectra taken from orthogonal views of the inner foam surface summarizing the currently achieved foam shell uniformity.

The film is uniform around the shell and, as the analysis with scanning electron microscopy reveals, adheres well to the high density carbon shell. Concentricity, sphericity, and roughness of the foam layer were assessed by a Fourier analysis of the inner foam-air interface radius as a function of the angular position. To get a complete picture of the layer's distribution in the shell, it was imaged from an orthogonal view and analyzed (labeled as "90°" in Figure 3-8). The resulting power spectral density (PSD) plot shows that the foam layer's concentricity (expressed by mode 1 thickness uniformity) is well below 1 µm² and sphericity and roughness (higher modes) are below 0.6 µm². These results are very reproducible for different densities and layer

thicknesses if the rotational velocities are adjusted accordingly as illustrated in Figure 3-9. It was possible to achieve uniform coatings for different densities (25 mg/cm^3 to 250 mg/cm^3) and thicknesses (15 µm to 70 µm) and it was possible to get 150 µm thick coatings with an above 1 µm^2 non-uniformity.

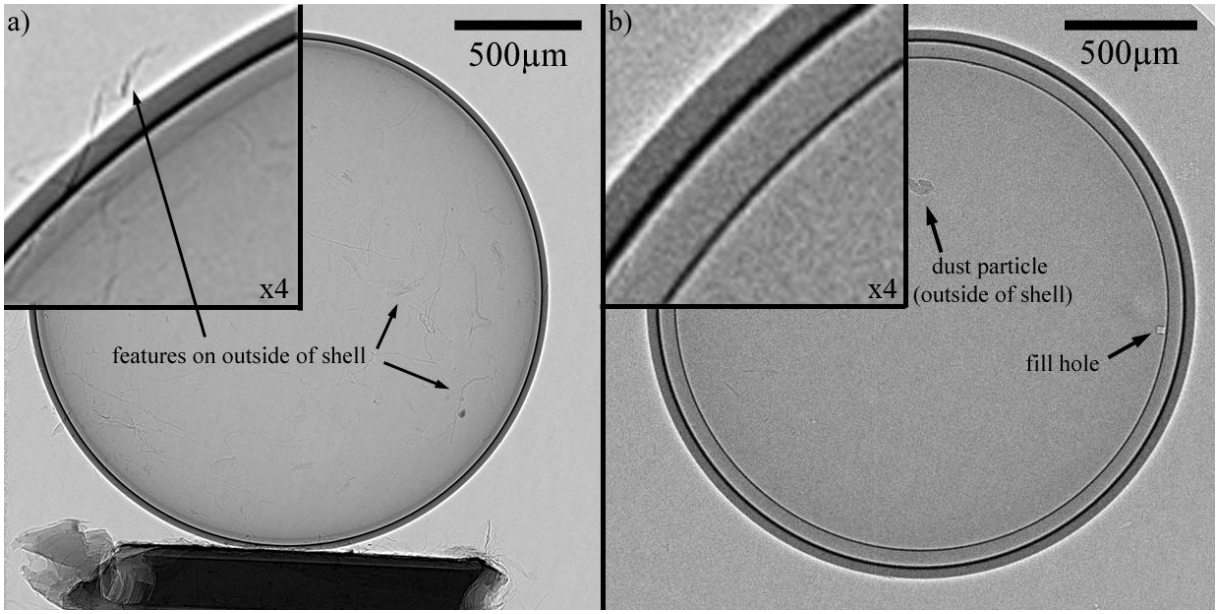

Figure 3-9: Cross-sectional radiographic images of 2 mm diamond spheres each coated with a uniform DCPD aerogel layer. a) 50 mg/cm^3 p(DCPD-r-NB-I_2), 5%NB-I_2, 0.2 wt.% catalyst, filled with Δp = 103.8 Torr, uniaxially rotated at 1.95 rpm for 22 h, and dried supercritically with CO_2 (see also chapter 6.1.2). b) 250 mg/cm^3 p(DCPD-r-NB) wet gel, 5%NB, 0.015 wt.% catalyst, filled with Δp = 148.7 Torr, and uniaxially rotated at 1.95 rpm for 20 h.

3.5. **Summary and Outlook**

In-situ real-time radiography was used to monitor the distribution of liquids in rotating hollow spherical shells. The experiments confirmed a surprising prediction made by computational fluid dynamics simulations, namely, that uniaxial rotation can result in the formation of extremely uniform thin film layers in hollow spherical shells if the right combination of the liquid's viscosity and rotational velocity are used. The universality of these model experiments was confirmed by fabricating uniform sol-gel chemistry derived porous polymer films inside 2 mm inner diameter high density carbon shells. The uniaxial coating process seems to be highly scalable and can easily be modified to generate porous coatings of different densities and thicknesses as well as using hollow spheres with different inner volumes. With a functional and reproducible process in place, work is currently in progress to expand the process to

different sphere diameters, foam compositions (see chapter 6), and geometries. As demonstrated above, the process requires precise control on various parameters and needs to be adjusted accordingly depending on a variety of parameters, including, but not limited to gel chemistry, density, layer thickness, and volume. Recent experiments with smaller (inner diameter) spherical shells and an optimized coating process, for example, yielded foam layers inside hollow spheres with all modes below 0.70 μm^2. The uniaxial rotation approach described here could potentially increase the use of coatings in a wide range of applications in the fields of material, industrial, and environmental science.

Chapter 4: Complete filling of shells

Some experiments at the National Ignition Facility can utilize shells that are completely filled with low density foams. For example, capsules filled with deuterated plastic foam and tritium gas could be imploded to measure the degree to which the foam and gas mixed,[196] which allows quantifying the effect of heterogeneous mix on fusion burn. In order to provide a complementary path for the fabrication of these targets, the existing filling setup was modified and proof of principle experiments were implemented to demonstrate its feasibility. The completely filled shells were then characterized using radiography.

4.1. Principle and modification to the filling procedure

One additional advantage of the filling procedure that is described above is that it can be modified to completely fill a capsule with low or high density foams. The flexibility of the sol-gel process, as described in the previous chapters, allows for generating complete porous fillings of different densities, porosities, or including dopants, as demonstrated in chapter 6. The setup additionally has the advantage that it is universal for hollow spheres with different inner volumes and wall thicknesses.

As previously discussed, the filling setup relies on a pressure differential to fill the capsule. Since the under-pressurized capsule is submerged in the precursor solution, and filled by re-pressurizing the chamber to atmospheric pressure,[12] a small air bubble remains in the capsule. (Figure 4-1 a) Its size depends on the vacuum that can be reached.

Increasing the pressure differential to $\Delta p = 700$ Torr and repeating the filling procedure multiple times did not remove the air bubble.

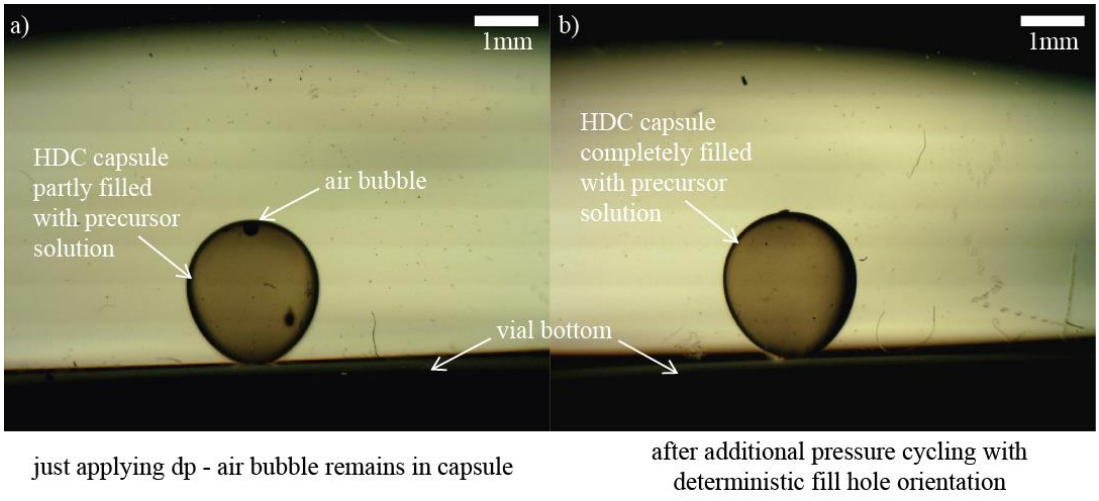

Figure 4-1: Picture of a 2 mm inner diameter hollow high density carbon shell (fill hole diameter 30 µm) submerged in a 50 mg/cm³ DCPD/toluene solution. (a) After submerging the capsule in the precursor solution and applying a pressure differential of ΔP=700 Torr multiple times, an air bubble remains in the shell. (b) With the fill hole orientation pointing up an additional pressure cycle removes the air bubble – leading to a completely filled shell.

The setup was therefore modified by adding a third step to the fill procedure. During this step, the capsule holder containing the capsule was removed from the linear feedthrough and placed in the precursor solution with the capsule's fill hole pointing upwards. The vial with the precursor solution remained in the vacuum chamber (Figure 4-2 c), which was then underpressurized again. Due to the orientation of the fill hole, part of the remaining air bubble expanded to the outside of the capsule during underpressurization. Lightly vibrating the entire setup released the air bubble from the capsule leaving a completely filled shell.

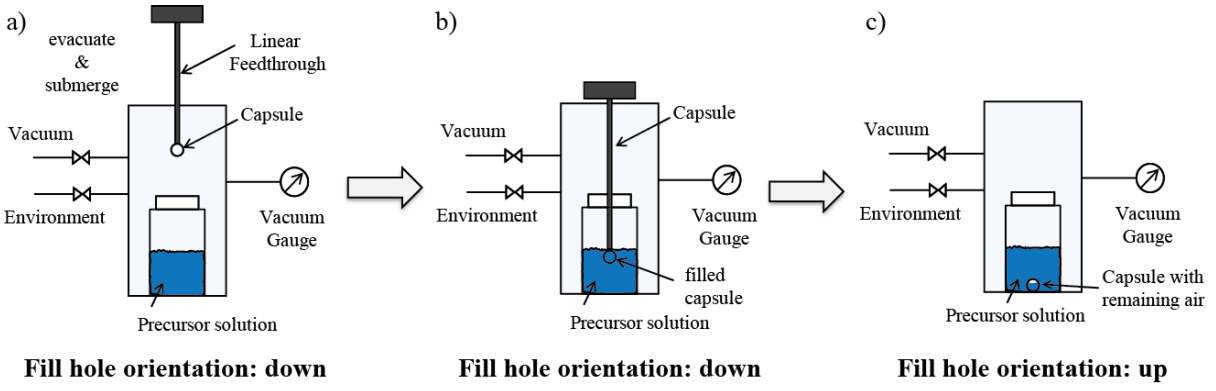

Figure 4-2: Schematic of the modified filling setup: (a) A vial with the precursor solution is placed in a vacuum chamber with a linear feedthrough to which the capsule is attached. The fill hole of the capsule is pointing down when the system is underpressurized (b) and the capsule is submerged. (c) After repressurization the capsule is removed from the linear feedthrough and placed in the same precursor solution with the fill hole orientation pointing up. The pressure differential is reapplied to force the remaining air out.

The last step of underpressurizing the system and vibrating the chamber was repeated until the air bubble had been removed. This led to reproducible results. Figure 4-1 b) shows an image of the completely filled shell after it has been removed from the capsule holder.

After completely filling the capsule with the precursor solution, it stayed submerged in the solution during gelation to prevent any air from entering the hollow sphere. The capsule sat in a PTFE capsule holder to ensure the fill hole position remained constant and for better visualization (Figure 4-3). No air bubble formed inside or on the outer surface of the capsule. Additionally, the gel inside the capsule seemed to behave as the gel surrounding the capsule (Figure 4-3 a - c), thus whatever is observed in the bulk gel was most likely the same for the gel inside the capsule.

Even though the gel point for a 50 mg/cm^3 DCPD/toluene aerogel is roughly reached after 550s and after 1000s for a 25 mg/cm^3 DCPD/toluene as described in (chapter 2.2), the capsule was left in the precursor solution for 24 hours to ensure gelation is complete.

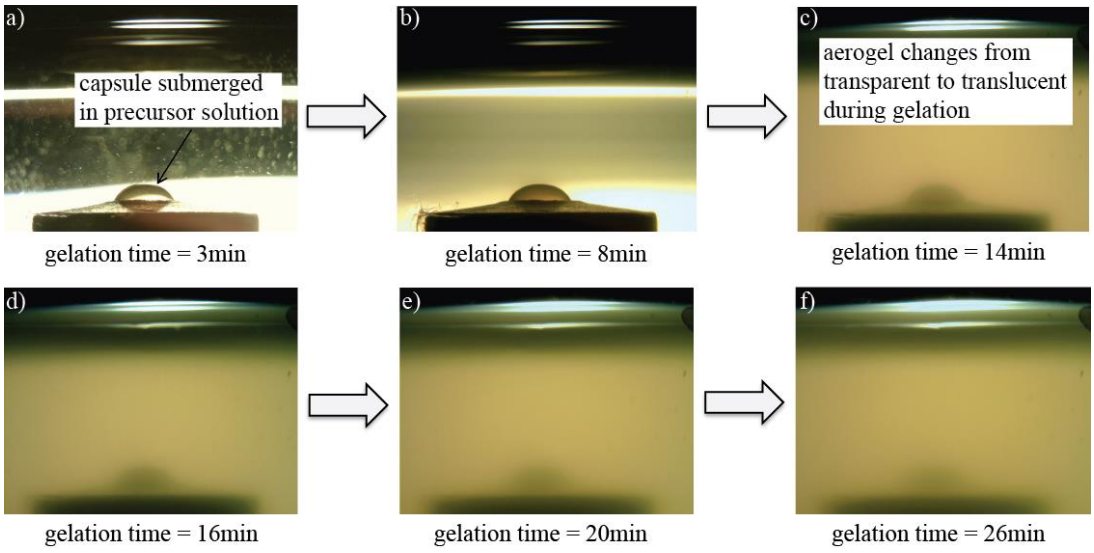

Figure 4-3: Picture of the completely filled capsule after the remaining air has been forced out. The capsule sits in a PTFE capsule holder with the fill hole direction still pointing upwards. Therefore, only the capsule's upper part is visible. The capsule is left in the precursor solution during gelation to ensure no additional air can get in.

After gelation, the bulk piece of aerogel with the capsule and its holder inside was supercritically dried by direct solvent exchange with carbon dioxide. The capsule was subsequently removed from the surrounding foam and capsule holder, leaving a

completely foam filled shell. The capsule then had to undergo additional cleaning steps to ensure the outside surface is free of any foam remains.

4.2. Radiographic analysis

Figure 4-4 shows the radiographic image of two different 2 mm inner diameter high density carbon shells that were completely filled with a 50 mg/cm^3 DCPD wet gel using the above mentioned method. The cross sectional radiographic image on the left (Figure 4-4 a) illustrates that foam densification or collapse are easily visible. The foam is clearly collapsed towards the fill hole as the solvent exchange from toluene to liquid carbon dioxide was not complete before reaching supercritical conditions. A detailed explanation of the failure's causes during supercritical drying can be found in chapter 5 of this thesis. The foam inside of the shell illustrated in Figure 4-4 b) does not show any signs of collapse or densification, which indicates that the shell is completely filled with intact foam. However, the cross sectional radiographic image does not give conclusive proof that the shell is indeed completely filled with foam as it is indistinguishable from a radiographic image of an empty shell.

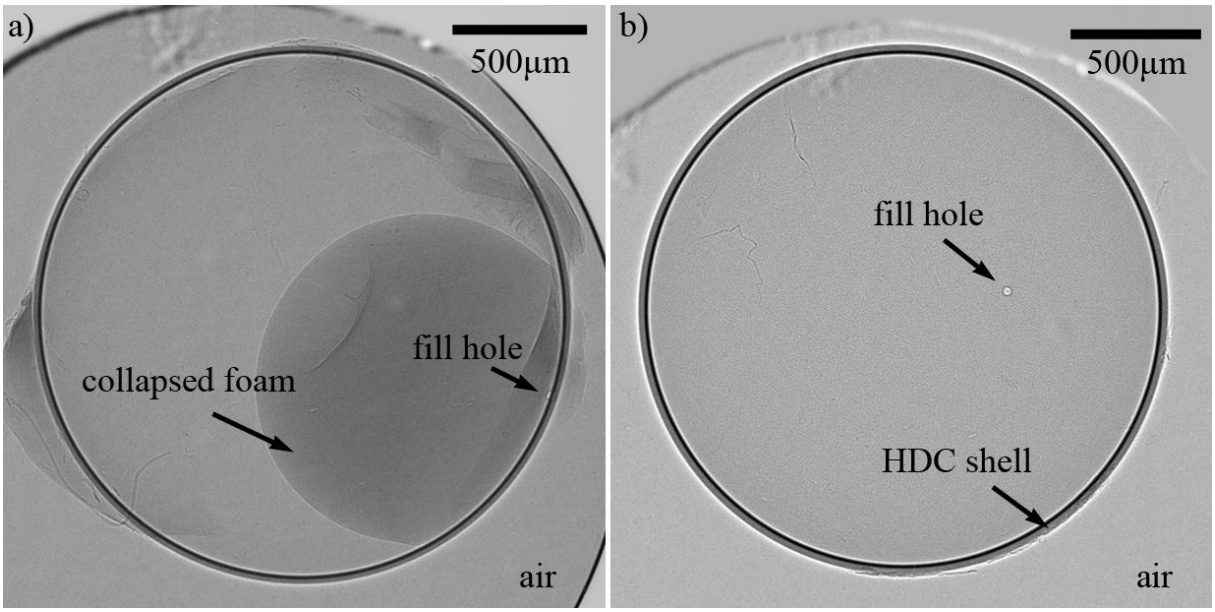

Figure 4-4: Cross-sectional radiographic image of two different 2 mm diamond spheres completely filled with p(DCPD) foam (50 mg/cm^3 DCPD, 0.2 wt.% catalyst, filled by using the method described above) after supercritical drying with liquid CO_2. a) The foam is clearly collapsed towards the fill hole as solvent exchange from toluene to liquid carbon dioxide was not complete before reaching supercritical conditions. (for a detailed explanation see chapter 5); b) The radiographic image indicates that the foam inside the shell is intact and shows no signs of collapse. Weight gain measurements confirm that the shell indeed contains foam.

Weight measurements of the empty shell and the filled shell using a XP56 microbalance (±0.001 mg, Mettler-Toledo, Switzerland) were therefore performed. These measurements indicated that the shell was completely filled with foam. Future experiments will include tomographic analysis of completely filled shells, doping of the foam after drying (see chapter 6 of this thesis) to increase the X-ray contrast, and, using destructive analysis, optical and scanning electron microscopy of the inside of the shells after breaking them open.

These proof of principle experiments show that the filling procedure can easily be modified to completely fill a hollow sphere with low- or high-density foams. The setup is universal for hollow spheres with different inner volumes and wall thicknesses and is advantageous for hollow spheres with small fill holes and fragile, ultra-low density foams. The foam can easily be modified to generate complete porous fillings of different densities, porosities, or include dopants, as demonstrated in chapter 6.

Chapter 5: Supercritical Drying

Part of this chapter was published and is reprinted (adapted for this thesis) here with permission from Braun, T.; Walton, Kim, S. H.; Biener M.M.; Hamza, A. V.; Biener, J., Supercritical Drying of Wet Gel Layers Generated Inside ICF Ablator Shells, Fusion Science and Technology 2018. This is an Accepted Manuscript of an article published by Taylor & Francis in Fusion Science and Technology on December 17th 2017, available online: http://www.tandfonline.com/10.1080/15361055.2017.1392203 on behalf of the American Nuclear Society, http://www.ans.org/.

In the previous chapters the successful synthesis and coating of the inner surface of hollow spheres with ultralow density p(DCPD-r-NB) wet gel layers was demonstrated. The pDCPD based wet gels were synthesized using a sol-gel process via ring opening metathesis polymerization (ROMP) with Grubbs' 1st generation catalyst and, as mentioned above, the transition from sol to gel occurs when the solid particles in the liquid join together to form a continuous solid phase. However, once this sol-gel process is completed, the wet gel still contains the organic solvent in its pores. In our case, toluene is used as the solvent, which needs to be removed to achieve ultra-low density materials.

Different techniques are commonly used to dry wet gels, resulting in different materials, such as *xerogels*, *cryogels*, and *aerogels*. (Figure 5-1)

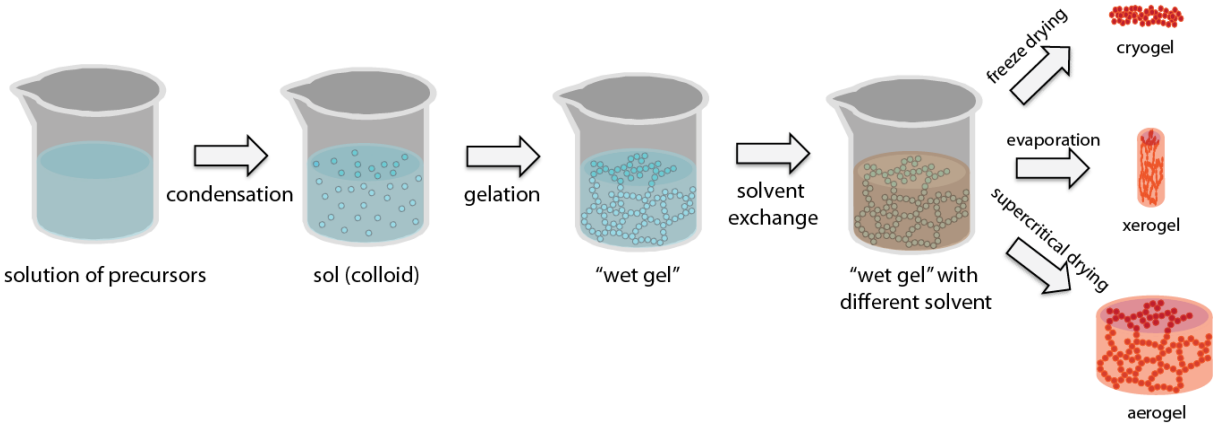

Figure 5-1: Different methods of preparing and drying wet gels, adapted from Garcia-Gonzalez (2012). Freeze drying techniques usually lead to cryogels, while ambient air drying is used to produce xerogels. Supercritical drying leaves the gel and pore structure mostly intact and is, therefore, the method of preference.

1. The evaporation of the liquid out of the gel matrix in ambient conditions or at elevated temperatures leads to *xerogels*,[197-198] a dense, solid material. Using this drying technique, it is usually not possible to conserve the gel structure as the capillary forces acting on the pore walls are high enough to collapse the nanoporous structure. This results in large shrinkage of the material and the destruction of the highly porous network. It should be noted that drying the gel under ambient conditions can lead to aerogels as well if certain steps are taken beforehand,[199-201] but were found not suitable for our purposes.

2. A different route to remove liquids from a gel structure is freeze drying. For this technique, the temperature of the liquid is lowered below its freezing point and the pressure is subsequently lowered to allow the now frozen solid in the gel to sublimate. The material obtained using this method is called *cryogel*.[202] During the crystallization of the liquid in the gel's pores, stress might be induced due to the volume change of the liquid, resulting in the potential destruction of the porous network. Because of this, cryogels are often obtained as powders.[117] Various attempts to produce aerogels from freeze drying have been reported in the literature.[203-206]

3. Supercritical drying on the other hand allows for the removal of liquid from the gel matrix without changing its open pore structure and large surface area, leading to a material called *aerogel*[97, 117, 207-208]. For this drying method, the liquid in the pore network is brought to supercritical conditions by taking it beyond its critical temperature (T_c) and pressure (P_c). Matson and Smith define a supercritical fluid as "a substance existing at temperatures and pressures above those at its critical point, or the precise conditions at which the liquid and gaseous phases of the substance are indistinguishable."[209] This indistinguishable phase has the advantage that it prevents any vapor-liquid interfaces and, therefore, capillary forces acting on the pore walls are avoided. Consequently, once supercritical conditions are reached in the system, the supercritical fluid can be removed from the porous material by depressurization under isothermal conditions, preventing a collapse of the fragile network structure. The process is illustrated schematically in Figure 5-2 using carbon dioxide as a supercritical fluid.

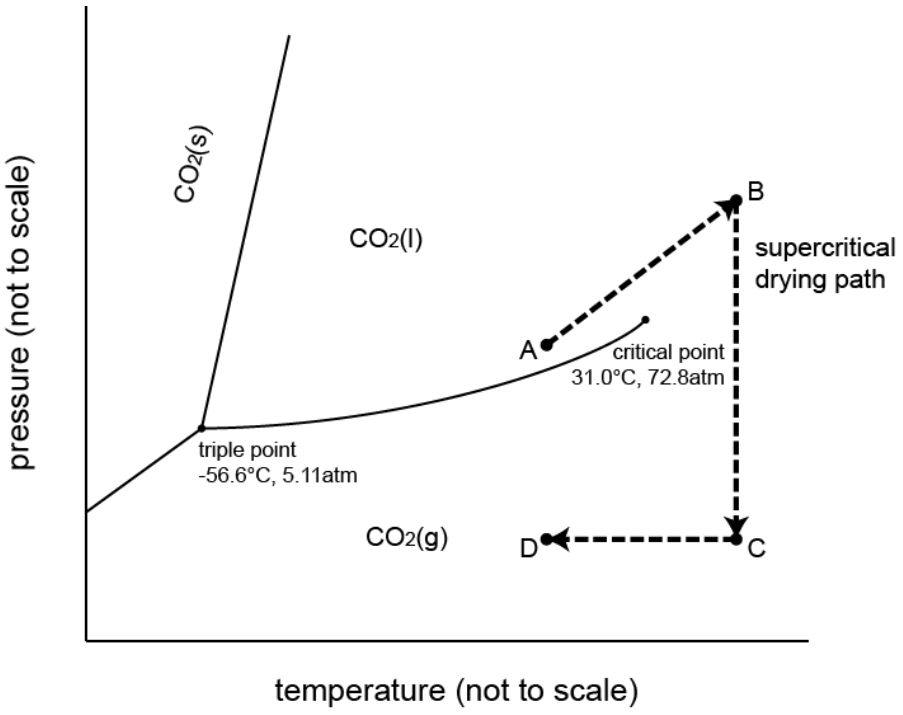

Figure 5-2: Principle of supercritical drying with carbon dioxide as the supercritical fluid. The sample is placed in a pressure chamber and exchanged with liquid CO_2. (Starting point A) The temperature and pressure in the chamber is then raised slightly above the critical point (A to B) bringing the fluid to supercritical conditions. The supercritical fluid is removed from the material by depressurization under isothermal conditions (B to C). After cooling the chamber (C to D) the sample is dried.

Depending on the critical temperature of the fluid, supercritical drying is often categorized into high[210] and low temperature[211] supercritical drying.

High temperature supercritical drying usually uses the organic solvents that were utilized during wet gel preparation as the supercritical fluid. However, these solvents often have very high critical temperatures as listed in Table 5-1, which could alter the internal structure of the aerogel. Wang et al. did small angle X-ray scattering experiments on samples that were dried with methanol as a supercritical fluid (T_c=239.4°C) and confirmed that the size distribution of the gel particles was narrowed during the process.[212] Additionally, it has been shown that certain functional organic groups incorporated in the network might be destroyed during high temperature supercritical drying.[213] It should also be mentioned that due to the high critical temperatures, high critical pressures, and flammability of most of the solvents used during high temperature supercritical drying additional safety precautions have to be taken into consideration. In 1984, a gasket in an autoclave used to produce large

aerogel samples in a facility in Sweden failed, which caused the release of over 1000 liters of methanol and ultimately considerable damage to the entire facility.[97]

Low temperature supercritical drying, as the name suggests, is done at much lower critical temperatures. Liquid carbon dioxide is one of the most commonly used supercritical fluids since it is non-flammable, inexpensive, chemically inert, and has the advantage of a very low critical temperature (T_c=31°C, see Table 5-1). Wang repeated his small angle X-ray scattering experiments on the aerogel samples, but used low temperature CO_2 supercritical drying. He found that it "can hardly affect the particle structure of the gel body."[212] However, using liquid CO_2 as a supercritical fluid requires exchanging the solvent in the gel matrix with liquid CO_2, which can be very time-consuming as the solvent exchange process in the network structure is done by diffusion. Additionally, not all solvents are miscible with CO_2, so sometimes an intermediate solvent exchange is necessary.[214] (Figure 5-1)

Table 5-1: Critical point parameters of common fluids[209]

Fluid	critical temperature T_c (°C)	critical pressure P_c (atm)
Water	374.1	217.6
Methanol	239.4	79.9
Ethanol	243.0	63.0
Toluene	**318.6**	**40.55**
Acetone	235.0	46.4
1-Propanol	263.5	51.0
2-Propanol	235.1	47.0
carbon dioxide	**31.0**	**72.8**

Other drying techniques have also been reported in the literature such as microwave drying[215-216] and vacuum drying[216]. Supercritical drying in a low temperature process using liquid CO_2 as the supercritical fluid, however, was found most suitable for our

purposes as it can lead to ultra-low density materials and doesn't change the intrinsic open pore structure and large surface area.

Although supercritical drying of wet gels with liquid CO_2 is commonly used and well described in the literature, no process has been developed for the specific conditions required for the synthesis of functional thin ultra-low density coatings inside hollow spheres. The commonly known processes require several adaptations as certain challenges arise since the aerogel is usually casted as a thin film on the *inside* of a hollow sphere and has an ultra-low density. In order to optimize the supercritical drying process for functional thin ultra-low density coatings inside hollow spheres, an in-depth knowledge of the different aspects of supercritical drying inside a hollow sphere is required.

As described above, the p(DCPD-r-NB), p(DCPD-r-NB-I_2), or p(DCPD-r-NB-r-NB-Sn) wet gel layers are prepared by using a ring opening metathesis polymerization (ROMP) of DCPD and norbornene in toluene (see chapter 2). To remove the toluene from inside of the porous polymer network via supercritical drying, it first needs to be exchanged with liquid CO_2, which can be quite challenging as this is a time-consuming, diffusion limited process. The wet gel layer is casted on the inside of a hollow sphere with a wall thickness of 50 µm or more[13] and a fill hole diameter of less than 30 µm. This means that the entire solvent exchange of toluene inside of the sphere and liquid CO_2 on the outside of the sphere takes place through the small fill hole of the shell.

On top of that, it needs to be taken into account that the wet gel layers that were cast into the shells usually have ultra-low densities. These ultra-low density materials need to withstand the solvent exchange without significant shrinkage or structural changes. Kim et al. showed how in some p(DCPD-r-NB) aerogel compositions a sudden decrease in BET surface area and deviation from the target density can be observed during solvent exchange from toluene to liquid CO_2.[82] Furthermore, some aerogels noticeably shrink during the drying process, which makes it difficult to obtain a layer of controlled, specific size and density. Most of the shrinkage in silica aerogels, for example, takes place during the decompression of CO_2 at the end of the drying process,[217] making it necessary to precisely control this step.

The combination of these challenges requires exact control of the drying parameters during this key aspect of the synthesis of functional thin ultra-low density coatings inside hollow spheres, which will be addressed in this chapter.

5.1. Solvent exchange time

One crucial stage in the drying process of p-DCPD aerogels is the solvent exchange from toluene to liquid CO_2. Since this process is mostly diffusion driven, understanding the diffusion kinetics of solvents in nano- and mesoporous materials is essential for designing a successful drying process. C.A. García-González reports that "as a rule-of-thumb, materials engineers overestimate the drying time to ensure that no remnant liquid is present in the dried gel, so that aerogels are formed."[218] This is certainly true for our aerogel system, as slight remaining amounts of the original solvent after supercritical drying would cause the aerogel to shrink or collapse. Figure 5-3 illustrates how an incomplete solvent exchange leads to collapsed foam in the shell. A 35 mg/cm^3 aerogel p(DCPD-r-NB) layer (5 wt.% NB, 0.2 wt.% catalyst, filled at $\Delta p = 105.4$ Torr, single axis rotation at 2 rpm for 24 hours) was casted in a shell by single axis rotation at 2 rpm for 24 hours. After exchanging the toluene for liquid CO_2, the capsule was placed in the critical point dryer and brought to supercritical conditions. The radiograph of the capsule shows that, after depressurization under isothermal conditions, the foam thickness was reduced from its original 50 µm to less than 10 µm (collapse, see Figure 5-3 a, inlet). The foam appears to still adhere to the wall, which is not always the case during collapsing. Figure 5-3 b) illustrates how the collapse of a foam layer can result in the foam almost completely detaching from the capsule wall. The cause of the incomplete solvent exchange seems to be a plugged fill hole (Figure 5-3 b, inlet), which reduced the amount of liquid that can get in and out of the capsule. The wet gel in the fill hole can, for example, partly collapse when exposed to air causing it to significantly densify and forming a plug. Figure 5-14 b) illustrates how severe the collapse of the aerogel can be, which causes an impenetrable barrier for any liquids. In the case of the two shells illustrated in Figure 5-3, remnant solvent was present in the shell and, when brought to supercritical conditions, caused the foam to collapse.

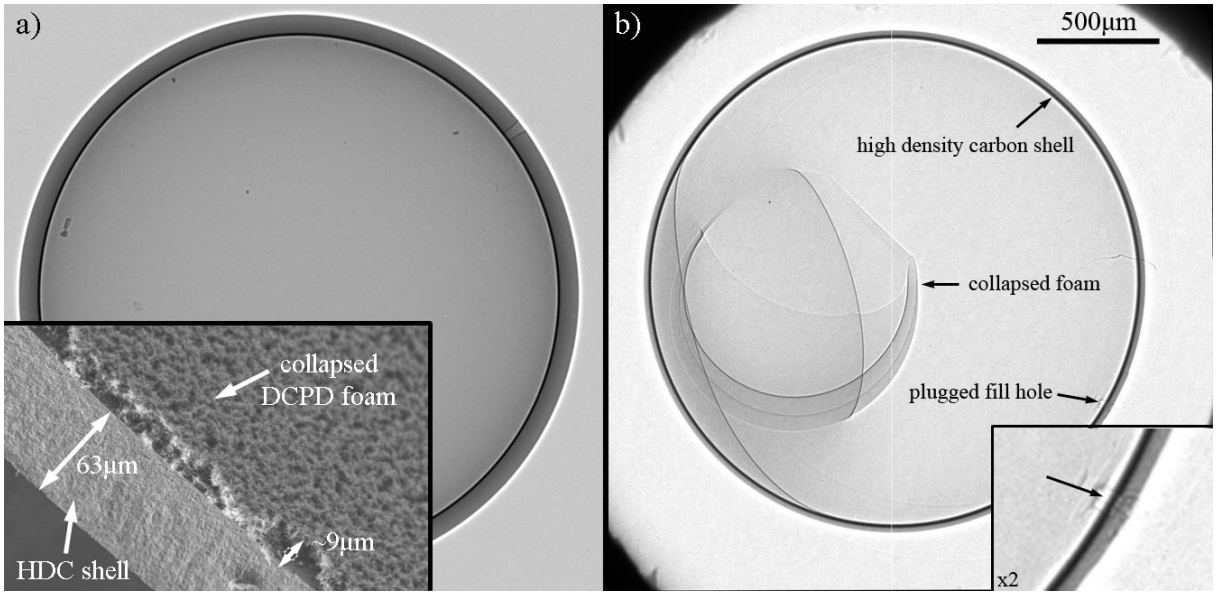

Figure 5-3: Cross-sectional radiographic image of HDC capsules after unsuccessful supercritical drying: a) Radiograph of a 1.688 mm HDC capsule (ID) with collapsed p(DCPD-r-NB) foam (35 mg/cm³ DCPD, 5 wt.% NB, 0.2 wt.% catalyst, filled at Δp= 105.4 Torr, single axis rotation at 2 rpm for 24 hours). The radiograph was taken after supercritical drying and the shell appears to be empty. After cracking open the shell and taking an SEM image (inlet), it is revealed that the foam in the shell is collapsed towards the wall. b) Radiograph of a 2 mm HDC capsule (ID) with collapsed p(DCPD-r-NB) foam (250 mg/cm³ DCPD, 5 wt.% NB, 0.02 wt.% catalyst, filled at Δp= 186.4 Torr, single axis rotation at 2 rpm for 18 hours). The radiograph was taken after supercritical drying and shows a complete collapse of the foam caused by a plugged fill hole.

It is, therefore, obvious that to achieve the anticipated density and thickness for the porous film layer in a hollow sphere, one must ensure that the solvent exchange is completed until there is only liquid CO_2 remaining in the pores. This solvent exchange step is the most time-consuming part of the entire synthesis process of forming thin ultra-low density coatings inside hollow spheres and, therefore, needs to be studied in great detail as a function of time. This allows for the optimization of the process, so that drying time does not need to be overestimated and can be controlled precisely.

5.1.1. Analytical approximation

The solvent exchange into and out of the capsule happens through the fill hole, which has a diameter of less than 30 µm and a length of up to 65 µm depending on the wall thickness of the capsule. However, after casting the aerogel film into the spherical shell the fill hole often contains some part of the wet gel material, which needs to be taken into account when calculating and optimizing the solvent exchange rate. This is illustrated in Figure 5-4, which shows the radiograph of a 2 mm HDC shell coated with a 50 mg/cm³ p(DCPD-NB) wet gel layer. The wet gel was doped with liquid

phase iodine (1.5 mg/cm^3 iodine/toluene, see chapter 6) for two days after rotation, which explains the excess solvent inside of the shell. The magnification of the fill hole shows a mostly intact wet gel inside of it, which means that the excess solvent in the capsule went through the material that plugs the fill hole.

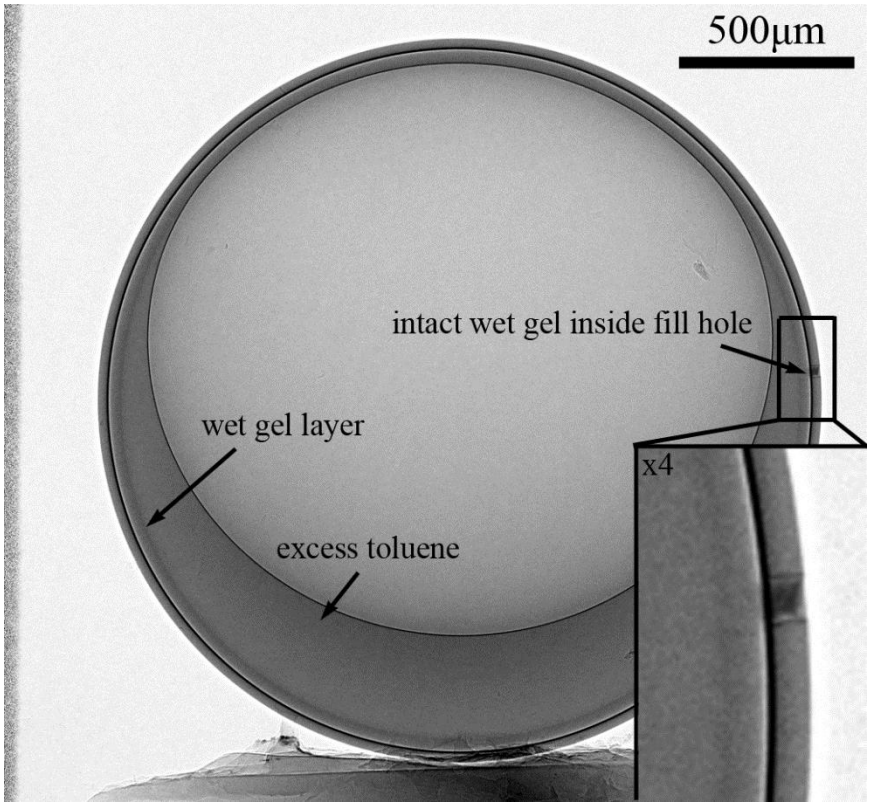

Figure 5-4: Radiograph of a 2 mm HDC capsule (ID) coated with a p(DCPD-r-NB) wet gel layer (50 mg/cm^3 DCPD, 10 wt.% NB, 0.1 wt.% catalyst, filled at Δp=102.1 Torr, rotated at 10/14.142 rpm for ~2.5 hours, doped with liquid phase iodine). The wet gel in the fill hole is still intact, but didn't prevent excess toluene from entering the shell.

Since intact aerogels can have a porosity up to 99.8%[219], a fairly free solvent exchange into and out of the capsule is imaginable. This is also true for p(DCPD-r-NB) aerogel films formed in hollow spheres under rotation as shown in Figure 5-5. To illustrate the pore structure of the 50 mg/cm^3 p(DCPD-r-NB) aerogel film in a hollow sphere, a capsule with said film was deliberately fractured and imaged with scanning electron microscopy. The image (Figure 5-5) shows the high porosity of the foam, which is exemplified in the magnified image (inlet). Therefore, relatively unrestricted solvent exchange through the porous network can be assumed if the wet gel remains undamaged.

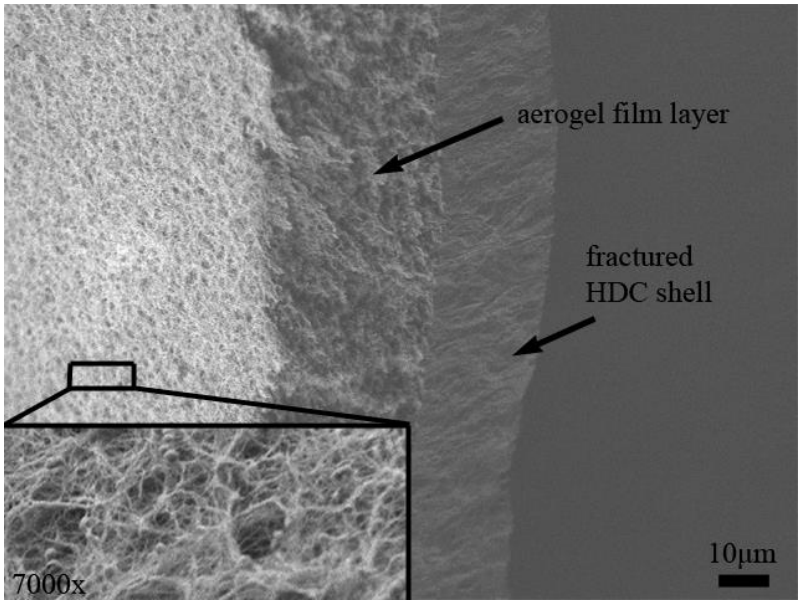

Figure 5-5: Scanning electron microscopy image of a p(DCPD-r-NB) foam layer (10 wt.% NB, 0.1 wt.% catalyst) casted in an HDC shell. The foam has a very high porosity, which is illustrated in the magnified image (inlet) and, therefore, relatively unrestricted solvent exchange through the porous network can be assumed.

As a first approximation, the plug of wet gel in the fill hole can be considered a cylinder with a diameter of 30 µm and a height of 50 µm. Using the early work of Fourier[220] and Fick[221] on liquid diffusion, the rate of transfer of diffusing substance through a unit area of a section can be expressed as

$$F = -D\,\partial C/\partial x,$$

"where F is the rate of transfer per unit area of section, C the concentration of diffusing substance, x the space coordinate measured normal to the section, and D is called the diffusion coefficient"[222] with its dimension of area per unit time. Using the cylindrical geometry of the fill hole and assuming one-dimensional diffusion with a constant diffusion coefficient, but changing concentration over the length of the fill hole (Figure 5-6), the rate of transfer of diffusing substance through two different unit areas F1 and F2, can be expressed as

$$F_1 = -D\{\partial C/\partial x\}_1$$

and

$$F_2 = -D\{\partial C/\partial x\}_2 \ .$$

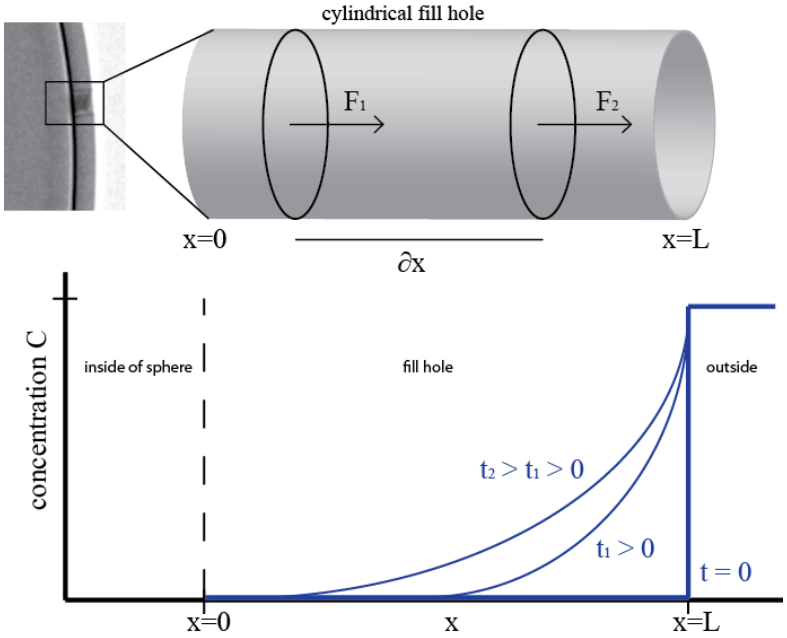

Figure 5-6: Schematic illustration of the cylindrical fill hole with two different unit areas F_1 and F_2, separated by a distance of ∂x. The rate of transfer of diffusing substance through the two different unit areas F_1 and F_2 is different depending on the gradient of concentration along the x-axis. As a Gedankenexperiment, where the solvent in the fill hole is completely exchanged, but the solvent inside of the sphere is not, the concentration change in the fill hole over time can be illustrated by the blue curves.

The rate of change in concentration in the volume element due to diffusion, can therefore be expressed by

$$\frac{\partial C}{\partial t} = \frac{(F_1 - F_2)}{\partial x},$$

which can be converted to

$$\frac{\partial C}{\partial t} = D\frac{\partial^2 C}{\partial x^2}$$

using the equation from above $F = -D\,\partial C/\partial x$ and assuming that the diffusion coefficient D is constant. One solution for this equation is

$$C = \frac{A}{\sqrt{t}}\exp(-x^2/4Dt)\,,$$

with A being a constant.[222] For diffusion through the fill hole, the equation for concentration at point x at time t, can be expressed by

$$C(x,t) = \frac{1}{2} C_0 \operatorname{erf} \frac{x}{2\sqrt{Dt}},$$

where C_0 is the initial concentration at the time $t = 0$ and $\operatorname{erf}(z) = \frac{2}{\pi} \int_0^z e^{-y^2} \mathrm{d}y$. The complete derivation of the solution for the diffusion problem was eloquently described by Crank (1975)[222] and is recommended for further studies.

5.1.2. Estimation of the diffusion time

The equation for the concentration at point x at time t depends on the initial concentration and diffusion coefficient and, therefore, allows to estimate the time needed for a complete exchange of the solvent inside of the fill tube and ultimately for the entire hollow shell with liquid carbon dioxide. Lai and Tan report a diffusion coefficient for toluene in supercritical carbon dioxide of $D = 2.81 \cdot 10^{-4}\,\mathrm{cm^2/s}$ at a temperature of 34.9°C and a pressure of 1089.2 psi.[223] However, the solvent in the capsule is exchanged with liquid carbon dioxide before reaching supercritical conditions, so the diffusion coefficient used in the calculation needs to be adjusted. Novak and Knez reported the diffusion coefficient of ethanol in liquid carbon dioxide inside a silica aerogel at 20°C to be $D = 3.18 \cdot 10^{-9}\,\mathrm{m^2/s}$.[224]

Using this value as an approximation and assuming an infinite supply of supercritical carbon dioxide on the outside of the sphere, it can be illustrated how the concentration distribution in a 60 µm fill hole filled with an aerogel changes over time.

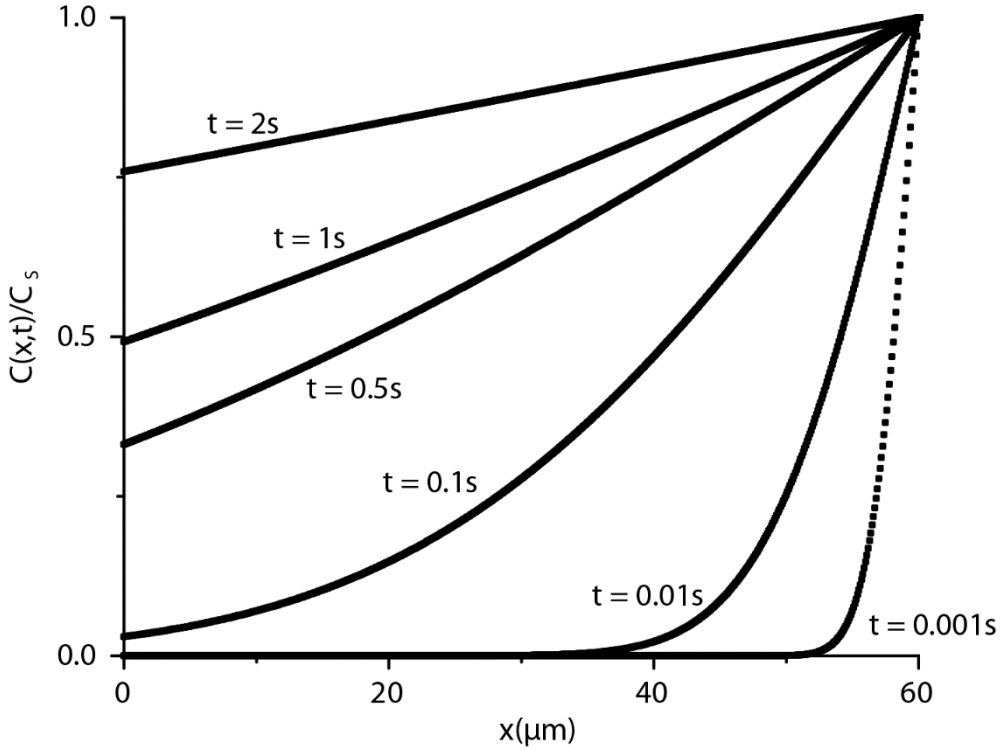

Figure 5-7: Concentration distribution at various times in the fill hole (length 60 µm) with initial concentration C_0=0 and surface concentration C_s. The supply of supercritical CO_2 on the outside of the fill tube is assumed infinite.

After $t = 10^{-3}$ s the edge of the concentration profile has advanced 5 µm into the fill tube and after $t = 0.1$ s the diffusion front has moved completely through the fill hole, suggesting a very quick solvent exchange. In order to estimate the amount of time needed to completely exchange the solvent in the entire sphere, the equations from above can be used by doing some approximations and using a 1 dimensional model. Assuming the wet gel layer has the same thickness as the fill hole diameter and that there is no excess solvent present in the hollow sphere, the diffusion front moves through the fill hole and continues to advance along a semicircle with a length of $^1/_2 \cdot 2\pi r = \pi r$.

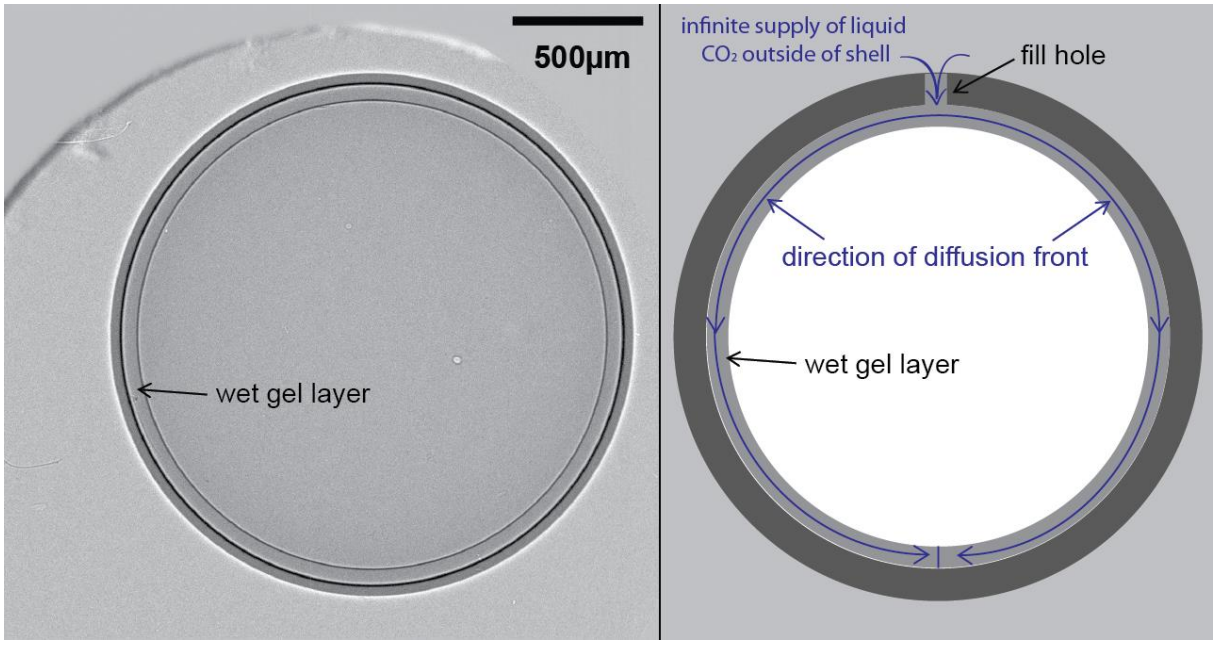

Figure 5-8: Converting the three dimensional problem of solvent exchange in thin aerogel film layers in hollow spheres into a one dimensional model to estimate diffusion time. Assuming an infinite supply of liquid CO_2 on the outside of the shell, the diffusion front in the wet gel moves through the fill hole and along the semicircles over the length of πr.

For a sphere with a radius of $r = 1$ mm and a fill hole length of 60 µm the diffusion front will move by $\pi \cdot 1000$ µm $+ 60$ µm ≈ 3200 µm. After $t = 1$ s the diffusion front has moved through the fill hole, which is consistent with the calculations above. The concentration distribution for the sphere (Figure 5-9) indicates that the edge of the concentration profile has advanced over 2000 µm into the semicircle after $t = 100$ s, but that it takes more than a day to completely exchange the solvent with liquid carbon dioxide. This is consistent with our observations (see below and chapter 5.2.2) and experiments done on similar aerogels. In these experiments, the solvent removal time for a free standing piece of aerogel with a length of 3 cm and a diameter of 1.2 cm has been reported to take up to $t = 20$ min[218] or even $t = 100$ min for a 1 cm diameter aerogel.[225]

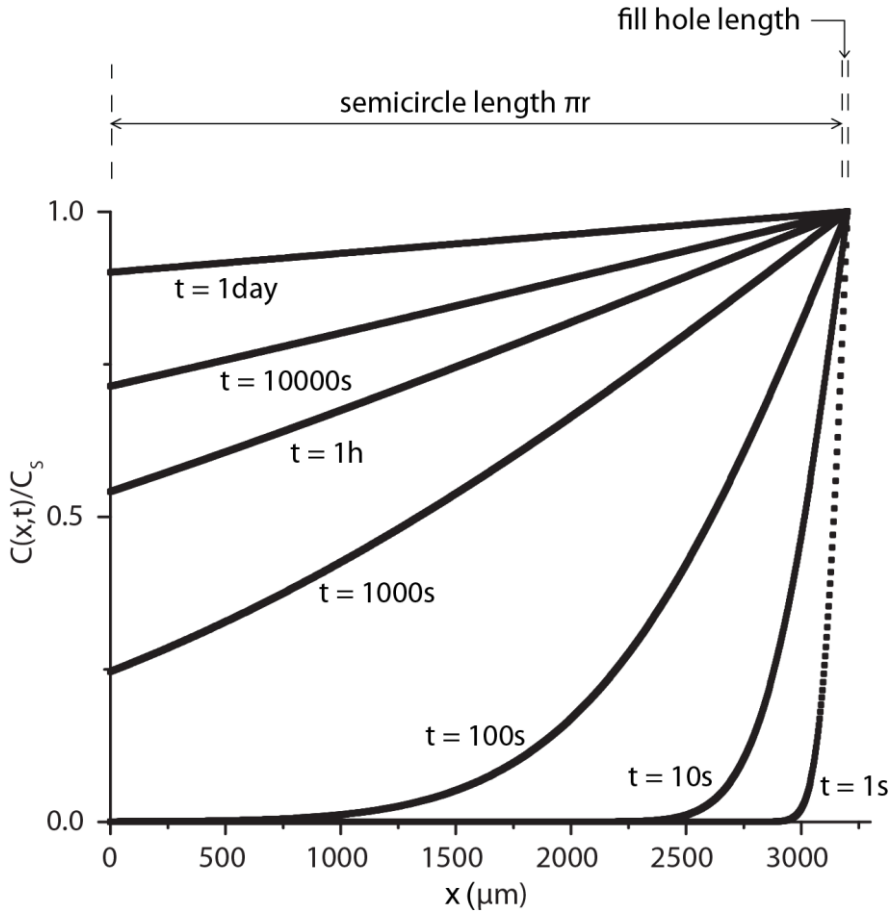

Figure 5-9: Concentration distribution for a 2 mm inner diameter sphere layered with a wet aerogel layer at different times *t* in the fill hole (length 60 μm) and semicircle (length πr = 3140 μm) with initial concentration C_0=0 and surface concentration Cs. The supply of liquid CO_2 on the outside of the sphere is assumed infinite.

The model used in this study to estimate the solvent exchange time in an aerogel layer inside of a hollow sphere does not take the following aspects not into consideration:

- The diffusion coefficient is a function of temperature[226] and concentration,[222, 227] but was assumed to be constant here. It increases with higher temperatures[226] and is reported to change by up to two orders of magnitude depending on the molar fraction of CO_2.[228] A method to measure the diffusion coefficient as a function of the CO_2 molar fraction inside an aerogel was recently proposed in the literature.[228]

- The porous network's structure has an influence on the diffusion coefficient in certain aerogels.[229] The pore size distribution, total pore volume, tortuosity, and connectivity of the pores affect the mass transport capabilities in the aerogels. Better connected pores lead to higher mass transport in the aerogel.[229]

- Perfect and instantaneous fluid mixing outside of the hollow sphere can be very difficult to achieve. Additionally, the concentration of liquid CO_2 directly on the outside of the shell might not be constant at all times as some solvent that diffuses out of the hollow sphere remains there before being transported away.
- Radial diffusion in the cylindrical fill hole and wet gel layer is not being considered in this model.
- The drying front velocity depends on the distance of the drying front from the outer surface. The drying front velocity initially depends on the flow rate of the CO_2, but equalizes once the drying front penetrates a certain distance into the aerogel.[217]

The simplified model does, however, give an estimation of the time required to completely replace the solvent in the aerogel with liquid carbon dioxide and was, therefore, used as a starting point for further experiments.

5.1.3. Diffusion through a p(DCPD) bulk piece

Due to the small size of the fill hole and the capsule itself, it was difficult to observe the solvent exchange process inside of the shell. Thus, different sets of diffusion experiments on bulk aerogels that were casted under stationary conditions, but were otherwise identical to the ones used inside of the hollow sphere were conducted. This allowed for the observation of the diffusion inside of the aerogels and a precise understanding and control over the solvent exchange process and its parameters. In order to estimate the time that is required for the solvent to diffuse through the pDCPD wet gel, 10 ml of 50 mg/cm^3 pDCPD gels were synthesized in a 20 ml glass vial. After gelation was complete, 1 ml of a 2 mg/cm^3 solvent blue 35/ toluene solution was added. Solvent Blue 35 or 1,4-bis[Butylamino]-9,10-anthraquinone (VWR) acts as a neutral dye and since the dyed toluene solution is blue in color it was possible to observe how the diffusion front moved through the white colored wet gel cylinder over time.

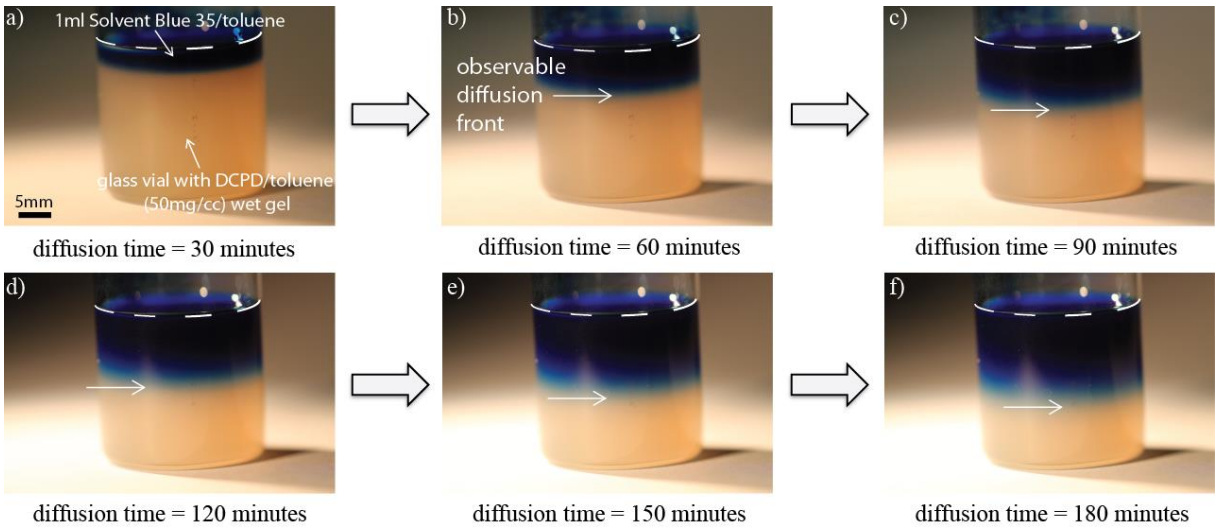

Figure 5-10: Photographs of a 20 ml glass vial filled with 10 ml of 50 mg/cm³ p(DCPD) wet gel (0.1 wt.% catalyst, gelled stationary for ~5 hours). 1 ml of a 2 mg/cm³ solvent blue 35/toluene solution was added after gelation was complete to observe the diffusion front moving through the wet gel. At t=0s the wet gel is translucent and white in color and the dyed toluene solution has not moved through the wet gel. (a) After t=30 minutes the diffusion front has moved by ~4 mm and has advanced an additional ~4 mm after t=60 minutes (b) and it can be seen to move further as time progresses (c) – (f), although at higher times the diffusion front seems to move slightly slower. f) After t=180 minutes the diffusion front has moved a bit further than halfway through the wet gel in the cylinder.

The initial pDCPD wet gel is translucent and white in color. After $t = 30$ minutes, the diffusion front had moved roughly 4 mm through the wet gel. It proceeded to advance to 12 mm after $t = 120$ minutes and to 14.5 mm after $t = 150$ minutes. Within 3 hours the diffusion front has moved almost 17 mm through the sample, which suggest a diffusion coefficient of $D \approx 1.1 \cdot 10^{-9}$ m^2/s.[222] This is consistent with the values that were used for the estimation of the diffusion time in the previous chapters and values reported in the literature.[224, 230-231]

With the understanding of how much time is required for the solvent to diffuse through the pDCPD wet gel, we have one milestone that is crucial to gain precise understanding and control over the solvent exchange process. It is, however, also essential to analyze how long it takes to completely remove the solvent out of the wet gel and replace it. As previously discussed, during supercritical drying with liquid carbon dioxide, no remnant liquid can be present in the gel as minor traces of solvent in the wet gel could cause shrinking or collapse. To analyze and optimize a complete solvent exchange, 1 ml of 50 mg/cm³ pDCPD/toluene wet gels were synthesized in a 1 cm³ glass cube with open ends on both sides and after completion of gelation the

wet gel was dyed with a 2 mg/cm³ solvent blue 35/ toluene solution. This causes the wet gel in the cube to turn dark blue as Figure 6-11 a) illustrates.

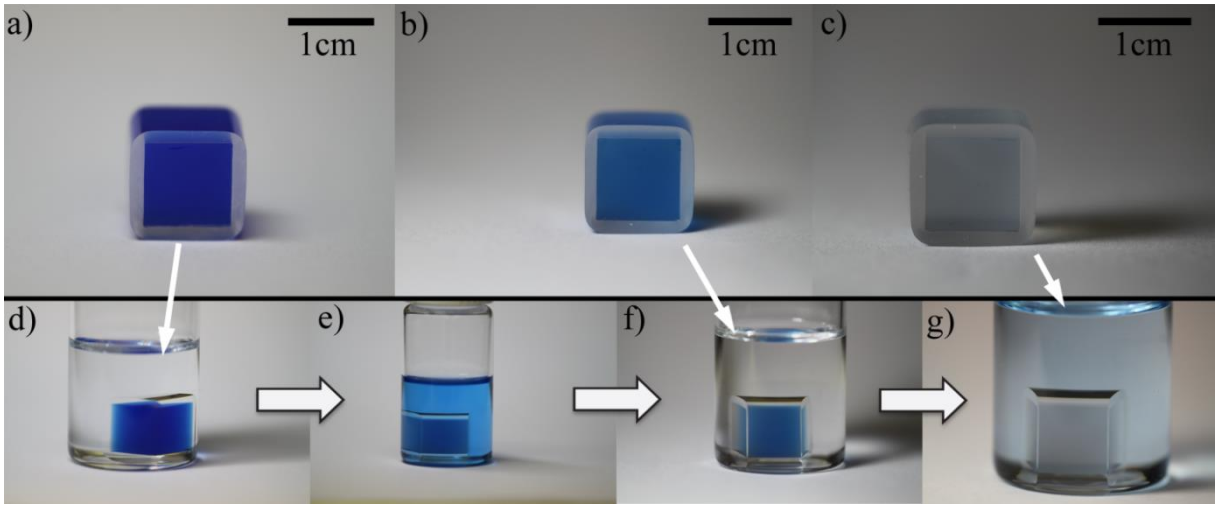

Figure 5-11: Photographs of 1 cm³ cubical glass cuvettes open on two parallel sides filled with 50 mg/cm³ p(DCPD) wet gel (0.1 wt.% catalyst, gelled stationary for ~5 hours, dyed with 2 mg/cm³ solvent blue 35/ toluene solution after gelation was complete) that were placed in a 20 ml vial filled with 10 ml pure toluene at room temperature. a) Initially, the wet gel is dark blue in color, but as the cube is placed in the toluene (d), the dyed toluene is being washed out of the gel (e). After exchanging the toluene in the vial for fresh toluene a few times (f-g), the dyed wet gel in the cube is removed (b), leaving a white and translucent wet gel (c).

The cube with blue dyed wet gel was then placed in a 20 ml vial filled with 10 ml of pure toluene, which caused the dyed toluene to be washed out of the gel (Figure 5-11 d-e). After 6.5 hours, the blue color of the wet gel inside of the cube is much lighter (Figure 5-11 b). The cube was placed in a vial with pure toluene once again (Figure 5-11 f) and left for an additional 16 hours. After this exchange, the wet gel looks white and translucent in color since almost all of the dyed toluene was washed out. An elongated exchange time with fresh toluene did not yield different results.

For the experimental setup, it was not possible to observe how the diffusion front moved through the wet gel; however, this experiment shows that the immersion fluid should be replaced regularly during the solvent exchange phase and should be much larger in volume compared to the volume of the fluid that is exchanged. The experiments were repeated with acetone as the immersion fluid and yielded similar results with the exception that the wet gel lost its translucency.

With the understanding of how the diffusion front moves inside of the wet gel and how to completely replace the solvent in pDCPD gels, we possess almost all key ingredients for understanding the solvent exchange step during the supercritical drying of p-DCPD wet gel liners inside of spherical capsules with their small fill holes. The question that remains: how can the solvent exchange in a pDCPD wet gel that is coated into a 2 mm spherical high density carbon shells be optimized so that the solvent exchange time is not underestimated and can be controlled precisely? As will be discussed in the next chapter, for wet gels that are coated inside of spherical shells, it is extremely challenging to tell if the solvent exchange from toluene to liquid carbon dioxide is complete.

To gain knowledge on the solvent exchange in spherical shells with small fill holes, a hollow 2 mm HDC capsule (ID) with a wall thickness of 30 μm was filled with a 1.5 mg/cm^3 iodine/toluene solution using a pressure differential of $\Delta P = 461.0$ Torr and submerged it into hexane. (Figure 5-12) The pressure differential was chosen so that the initial conditions of the shell are as close as possible to a gel layered shell before solvent exchange. (compare to Figure 5-4)

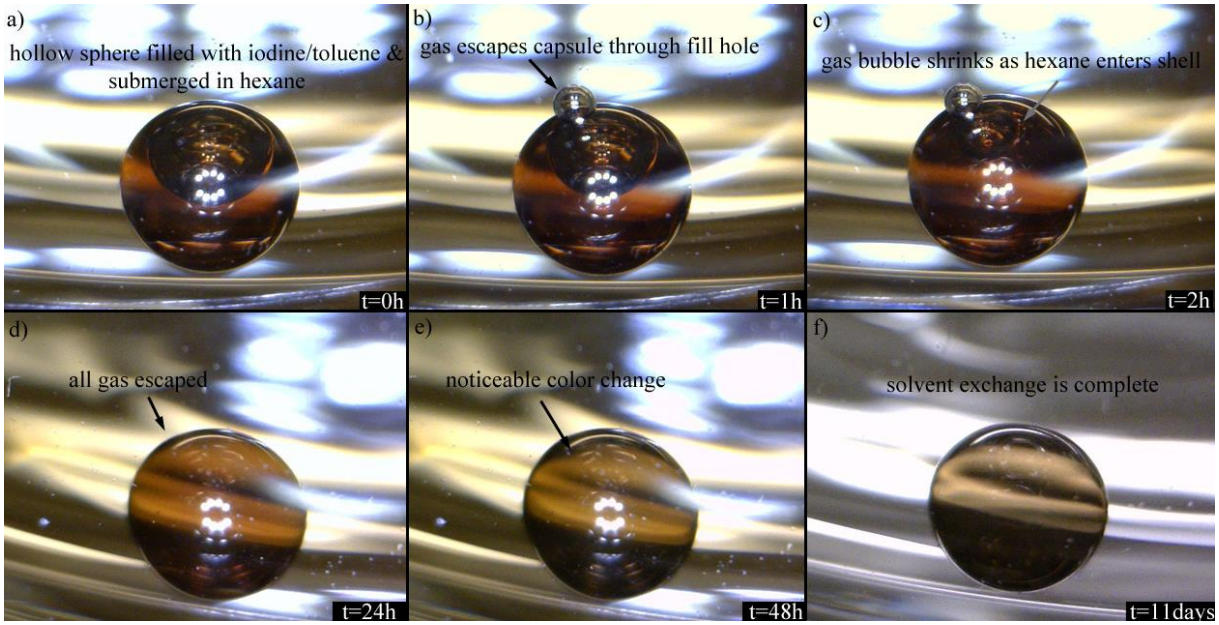

Figure 5-12: Solvent exchange in a hollow 2 mm HDC shell through a 30 μm fill hole. The capsule, partly filled with 1.5 mg/cm^3 iodine/toluene (red in color), is submerged in hexane (clear) and a picture is taken every 5 minutes for 11 days. a) At initial conditions (t=0 hours), the gas bubble in the shell is clearly visible and the liquid in the shell is dark red. b) As time progresses, the remaining gas escapes the shell through the fill hole, which causes the gas bubble inside of the shell to shrink. d-e) After all remaining gas has escaped the shell and the process becomes completely diffusion driven and as time progresses a noticeable color change is visible. f) After 11 days the color of the shell doesn't change and the solvent exchange is complete.

Since the iodine/toluene solution is red in color, the hexane is transparent, and the shell has a wall thickness of ~30 µm, it was possible to observe the diffusion in and out of the shell. As time progresses, the gas bubble escapes the shell through the fill hole, which causes the gas volume inside of the shell to decrease. (Figure 5-12 b) Once the escaping gas bubble on the outside of the shell gets big enough, it detaches from the shell and rises to the top of the hexane.

This process repeats multiple times until all remaining gas has escaped the shell and the solvent exchange process becomes completely diffusion driven. After 24 hours a significant amount of the iodine/toluene solution has diffused out of the shell and a noticeable color change is visible. This becomes even more apparent after 48 hours. Finally, after 11 days, no color change is observable as the solvent exchange is complete. (Figure 5-12 f) Using the correlation for diffusion through the fill hole from above, the described capsule dimensions, and assuming the capsule is completely filled the corresponding diffusion constant can easily be derived from this experiment to be $D_{\mathrm{exp}} \approx 0.5 \cdot 10^{-10}\,\mathrm{m^2/s}$. Compared to the literature values for the diffusion constant of toluene in hexane $D = 4.21 \cdot 10^{-9}\,\mathrm{m^2/s}$,[231] the experimental determined diffusion constant seems to differ by a factor of 80. However, as mentioned above the diffusion coefficient is a function of temperature and concentration. Also, [222, 227223, 228223, 228223, 228223, 228223, 228223, 228]perfect and instantaneous fluid mixing outside of the hollow sphere can be very difficult to achieve. The hexane in the vial was, for example, not stirred during the experiment, which could've facilitated the mixing. Therefore, the concentration of toluene directly on the outside of the shell might not have been constant at all times and some solvent that diffuses out of the hollow sphere remained there before being transported away.

With the information from this empirical study, each solvent exchange step was set to a minimum of 11 days to ensure all solvent has been fully exchanged. Depending on different factors, such as fill hole size, shell wall thickness, foam layer thickness, or foam layer density, the solvent exchange time needed to be adjusted.

5.2. **Supercritical drying of pDCPD aerogels**

With the knowledge of the required time for a complete solvent exchange, the remaining solvent can be removed out of the gel layer with supercritical drying. The

supercritical drying of the different aerogel samples and aerogel lined hollow spheres was performed in a commercially available critical point dryer E3100 (Quorum Technologies), which is comprised of a cylindrical, water-cooled pressure chamber (60 mm internal diameter x 78 mm long) with a wall thickness of 25 mm. (Figure 5-13)

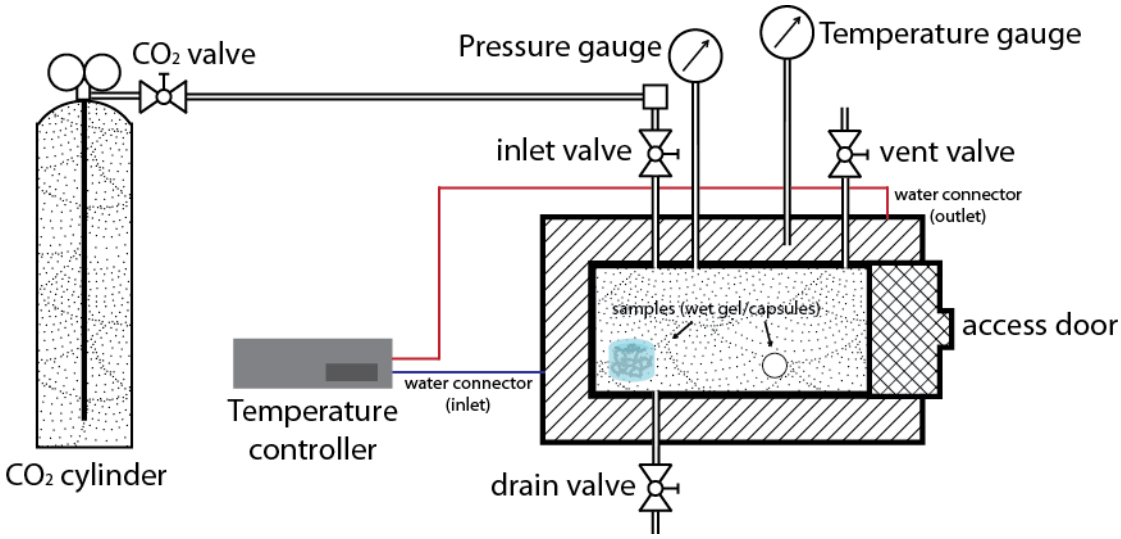

Figure 5-13: Critical Point Drying setup: The samples are placed in a 60 mm internal diameter x 78 mm long pressure chamber that is temperature controlled via a water chiller. The chamber is completely filled with the solvent that is present in the wet gel and cooled to 10°C. After the samples are placed into the chamber containing the solvent, the access is door is sealed and the CO_2 inlet valve is opened. Once the medium working pressure is reached, the drain valve is opened slightly until all the solvent is exchanged for liquid CO_2. The supercritical conditions are reached by closing all valves and increasing the temperature and controlling the pressure with the vent valve. After supercritical conditions are reached, the chamber is depressurized under isothermal conditions and subsequently cooled to extract the supercritically dried samples. Not shown is a safety valve, which is attached to the pressure chamber that bursts if the pressure in the chamber reaches critical levels.

The wall itself contains water pathways to precisely control the chamber's temperature when connected to a temperature controlled water supply. Pressure and temperature gauges allow for monitoring the conditions inside the chamber. The drying process is controlled with inlet and outlet valves, which are screwed directly into the chamber and sealed against a solvent resistant O-ring.

To dry the wet gel samples or the wet gel coated ablator shells, they are placed in the pressure chamber, which is cooled to 10°C and completely filled with the solvent that is present in the wet gel. After the samples are placed into the chamber containing the solvent, the access door is sealed and the CO_2 valve and the inlet valve are opened. The pressure in the chamber increases under isothermal conditions until the pressure

in the chamber is the same as in the CO_2 cylinder. Once the pressure has equalized, the drain valve is opened slightly to start the solvent exchange. The solvent drips out of the drain valve into a beaker and is properly disposed. This process can take up to a few days (see chapter 5.1.2) depending on the sample size. After all the solvent in the samples and the chamber is exchanged with liquid CO_2, all valves are closed and the temperature is increased to supercritical conditions. The pressure in the chamber can be controlled with the vent valve to avoid critical pressure levels. After supercritical conditions are reached, the chamber is depressurized under isothermal conditions and subsequently cooled to extract the supercritically dried samples. A detailed scheme of the drying process of a wet gel lined hollow sphere is shown in chapter 5.2.2.

5.2.1. Drying Bulk

Before drying a gel layer inside a hollow sphere, the influence of supercritical drying on the gel chemistry was analyzed in bulk pieces. For that, 5 ml to 10 ml of precursor solution was usually casted in different 20 ml glass vials (sometimes also 1 ml precursor solution in a 2 ml glass vial depending on the experiment) and then supercritically dried. Although not gelled under rotation, the bulk pieces served as a first indicator if the aerogel with its newly developed chemistry is capable of surviving the drying process.

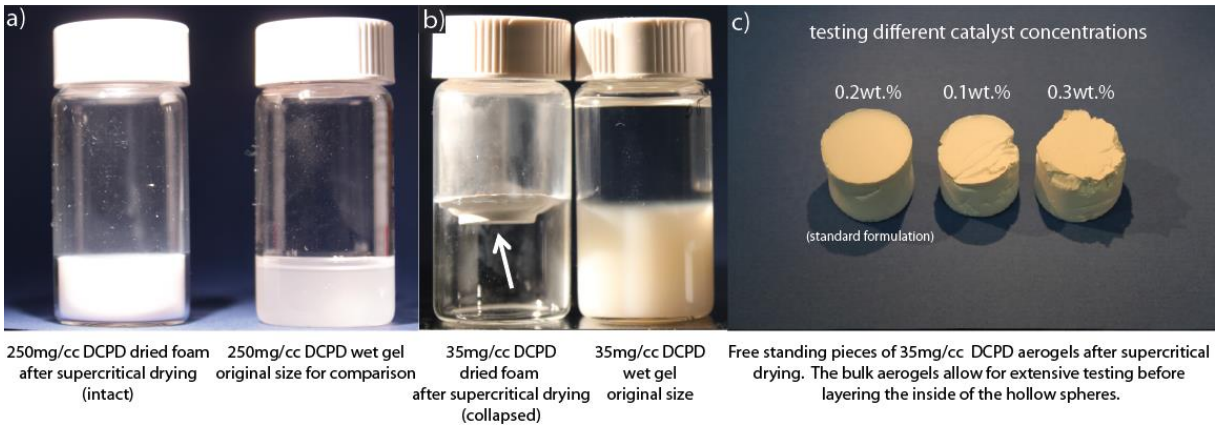

Figure 5-14: Comparing the wet gels and dried foams of different bulk pieces of DCPD allows for the exploration of the robustness of different precursor solution compositions, solvent exchange techniques, or drying procedures: a) p(DCPD-r-NB) wet gel and corresponding intact dried aerogel foam (250 mg/cm³ DCPD, 10 wt.% NB, 0.015 wt.% catalyst). The aerogel shows no signs of shrinkage after supercritical drying and keeps its shape during the process. b) Not allowing sufficient solvent exchange time caused the dried p(DCPD-r-NB) foam (35 mg/cm³ DCPD, 10 wt.% NB, 0.2 wt.% catalyst) to collapse to less than 5% of its original size, which when taking place in the fill hole, can hinder solvent into and out of the hollow sphere. c) Dried p(DCPD-r-NB) aerogel foams (35 mg/cm³ DCPD, 10 wt.%

NB) prepared with different catalyst concentrations show partial signs of collapse except for the developed standard formulation.

Additionally, many experiments on the influence of changing the gel chemistry or the incorporation of dopants into the gel network on the dried aerogel could be done with a bulk piece of aerogel. For these experiments, low-density (0.05 g/cm^3) p(DCPD-r-NB-R) gels were prepared by ring opening metathesis polymerization (ROMP) of DCPD and norbornene (NB-R) in toluene employing a first generation Grubbs' catalyst as the catalyst/initiator. Different p(DCPD-r-NB-R) (100/x) (wt./wt.) copolymer wet-gels were obtained by controlling the feed ratios of DCPD and NB-R by weight. For example, to fabricate 50 mg/cm^3 p(DCPD-r-NB-R) (100/20) (wt./wt.) aerogels, separate 50 mg/cm^3 solutions of DCPD and NB-R monomers in toluene were prepared and then mixed as needed (0.83 ml of the DCPD and 0.17 ml of the NB-R solution for a (100/20) (wt./wt.) aerogel). After adding an aliquot of the catalyst (0.1 mg) dissolved in toluene, the mixture was gelled in a sealed vial under ambient conditions. The wet gels were then placed in different solvents for 7 days each and afterwards supercritically dried. A picture was taken between each solvent exchange step. The drying setup remained the same as described in Figure 5-13. The vial containing the wet gel was placed in the supercritical dryer and underwent complete solvent exchange. The vial contained a custom-built lid that allowed free flow in and out of the vial while keeping the wet gel in place and underwent complete solvent exchange. Subsequently, the sample was brought to supercritical conditions and kept there for 2 to 4 hours. The chamber was then isothermally depressurized until reaching atmospheric conditions and the samples extracted and analyzed.

The addition of a linear cross linker such as norbornene into the polymer network significantly increases the uniformity of aerogel coatings as described in chapter 2.3 and by Braun[34] and Dawedeit[15]. Drying wet gels containing a high amount of norbornene, however, can affect the final density of the resulting aerogel as illustrated in Figure 5-15.

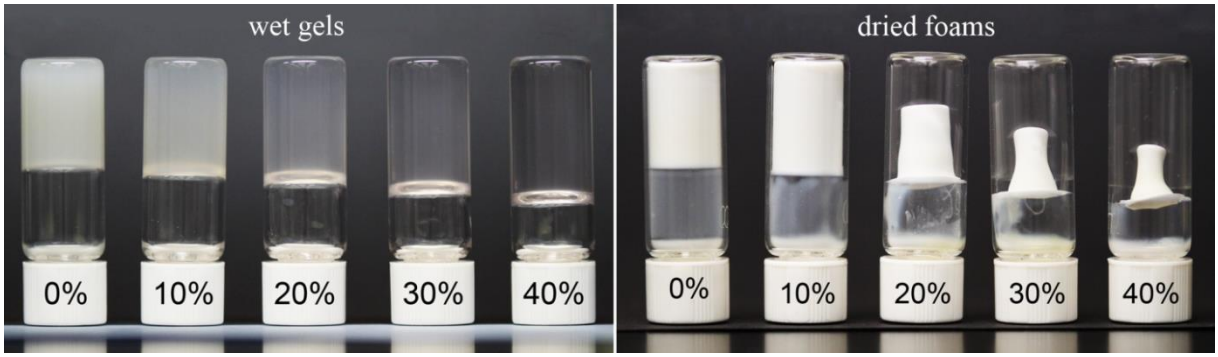

Figure 5-15: Effect of norbornene addition to 50 mg/cm³ p(DCPD-r-NB) precursor on the final density of the aerogel. Increasing the norbornene content leads to shrinkage for all foams with a >10 wt.% norbornene content after a 2-step solvent exchange drying process. (toluene to acetone to liquid CO_2). (image credit: C. Dawedeit, LLNL)

With increasing concentrations of norbornene the aerogel is more susceptible to shrinkage during supercritical drying. Pure pDCPD and p(DCPD-r-NB-R) (100/10) (wt./wt.) aerogels keep their shape during the solvent exchange phase (toluene to acetone to liquid CO_2) and drying process, but higher additions of norbornene lead to considerable shrinkage. The reason for the additional solvent exchange from toluene to acetone before exchanging with liquid CO_2 is that p(DCPD-NB) aerogels are fairly weak after gelation and are therefore aged in acetone to increase their strength.[101] As shown in Figure 5-15, the wet gel becomes increasingly transparent with increasing norbornene concentration, which indicates a decreasing feature size and, therefore, more difficult diffusion. In our case, it was found advantageous to first place the wet p(DCPD-NB) gels into an agitated acetone bath before transferring them into liquid CO_2.[82, 188] However, to minimize the shrinkage caused by the addition of >10 wt.% norbornene, a third solvent exchange step with hexane and ethyl ether was explored. For that, the toluene was exchanged with either hexane or ethyl ether for seven days before being replaced with acetone. Figure 5-16 and Figure 5-17 illustrate how the shrinkage can be completely avoided even for very high norbornene concentration using a three-step solvent exchange drying process.

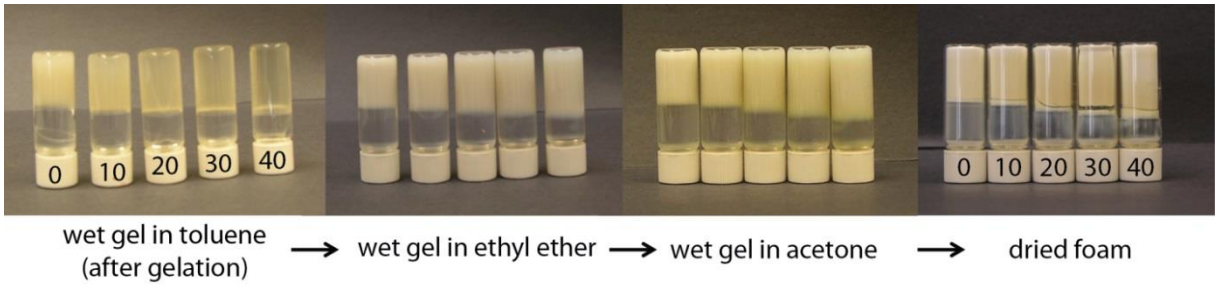

Figure 5-16: 50 mg/cm³ p(DCPD-NB) wet and aerogels with different concentrations of norbornene (percentage of norbornene relative to pDCPD is shown on vial caps) undergoing a three step solvent exchange. The toluene is exchanged for ethyl ether for seven days before acetone and liquid CO_2. The dried foam shows no sign of shrinkage. (image credit: S. H. Kim, LLNL)

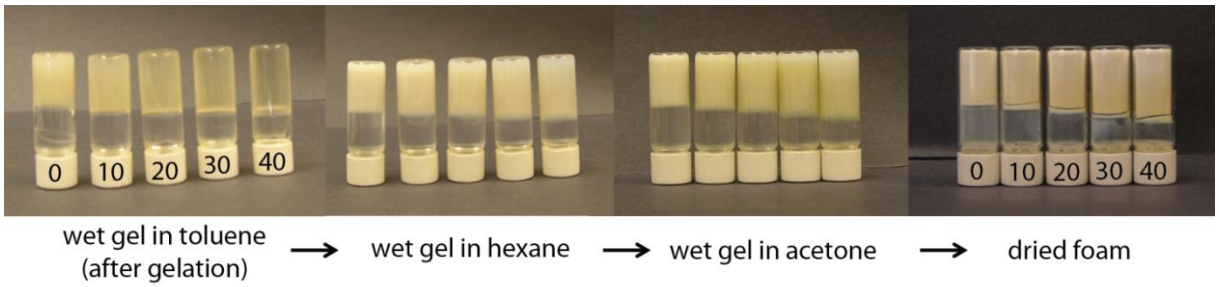

Figure 5-17: 50 mg/cm³ p(DCPD-NB) wet and aerogels with different concentrations of norbornene (percentage of norbornene relative to pDCPD is shown on vial caps) undergoing a three step solvent exchange. The toluene is exchanged for hexane before immersion into acetone and liquid CO_2. The dried foam shows no sign of shrinkage. (image credit: S. H. Kim, LLNL)

The solvent exchange step, however, is the most time consuming part of the drying process. Using the above developed model and a diffusion constant for toluene in hexane of $D = 4.21 \cdot 10^{-9}\,\mathrm{m^2/s}$,[231] the additional step of exchanging toluene to hexane in a wet gel layer inside a hollow sphere would add quite a significant amount of time in the order of days to the drying process. Therefore, for the application of coating uniform layers into hollow spheres, the addition of 10 wt.% norbornene "provides the best compromise as it is sufficient to allow for the formation of uniform thin gel films under rotation while it does not yet affect the robustness during supercritical drying."[15] This eliminates the need of an additional solvent exchange step with hexane or ethyl ether as the p(DCPD-r-NB-R) (100/10) (wt./wt.) aerogels keep their shape during the solvent exchange phase (toluene to acetone to liquid CO_2) and the drying process. (Figure 5-15)

In summary, drying experiments on bulk pieces provide a unique opportunity to quickly assess the strength of different aerogel compositions and their potential to

form uniform foam layers in hollow spheres. If the bulk piece shrinks during solvent exchange or supercritical drying, the precursor's components such as norbornene or catalyst concentration need to be modified or the solvents used for substituting the liquids need to be changed.

5.2.2. Drying of thin aerogel layers in hollow spheres

As mentioned above, the supercritical drying of thin ultra-low density p(DCPD-NB) aerogel layers in hollow spheres requires an in-depth understanding of the different aspects and steps involved in the process. The influence of different solvent exchange times, usage of different solvents, the order they are applied, and the precursor's composition on the aerogel's drying behavior have been discussed above and optimized to cast uniform foam layers in hollow spheres. However, if the procedure is not properly controlled, the fragile polymer network can be damaged and thus interfere with the drying process. This chapter will describe the process developed to successfully dry p(DCPD-r-NB) copolymer aerogel layers in hollow spheres.

The p(DCPD-r-NB) copolymer aerogel layers were prepared from ring opening metathesis polymerization (ROMP) in high-density carbon (HDC) shells using the above mentioned methods. Layer thicknesses ranged from 15 to 200 µm and fill hole sizes from 30 – 50 µm in diameter and coatings were performed using the uniaxial coating setup (chapter 3.1.3) at room temperature. The gel-coated ablator shells underwent solvent exchange in acetone at room temperature for 11 days as described above and then liquid CO_2 for 11 days at 10°C and 900 psi in a Polaron critical point dryer (Figure 5-13) to replace the toluene in the gel pores with liquid CO_2.

Every wet gel layer in a shell was accompanied by its own 10 ml witness piece in a 20 ml vial from which the precursor solution in the shell was drawn. These witness pieces allowed to extrapolate the state of the layer in the capsule to a certain degree without the need of X-ray imaging. For example, if the witness piece did not gel properly or shrank during supercritical drying, the aerogel layer inside the capsule also did not meet specifications.

Once only liquid CO_2 was assumed to be present in the pores of the gel network (see chapter 5.1.2), the temperature and pressure in the critical point dryer were increased

to reach the supercritical regime. Della Porter reported that an "[alginate] aerogel with a uniform internal nanostructure and the lowest shrinkage of 0.3% was obtained operating at 1450 psi and 38° C",[232] which is quite different from the parameters that were found optimal for the drying process (50° C and 1600 psi). The pressure was then allowed to slowly decrease to atmospheric pressure while keeping the temperature constant. A detailed step by step scheme of the drying procedure for wet gel layers in hollow spheres is illustrated on the following pages.

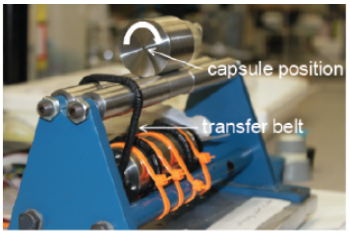

Take capsule off roller

Submerge capsule in agitated acetone bath for 11days

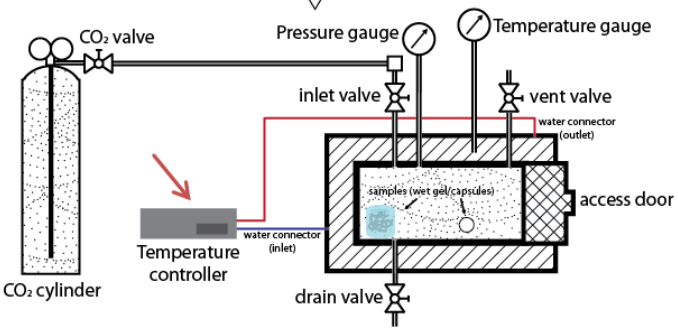

Bring critical point dryer's temperature to 10°C

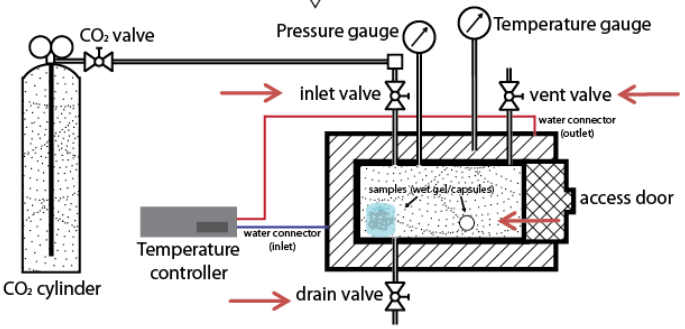

Close all valves on critical point dryer; Fill chamber with acetone and place samples into chamber; Close access door

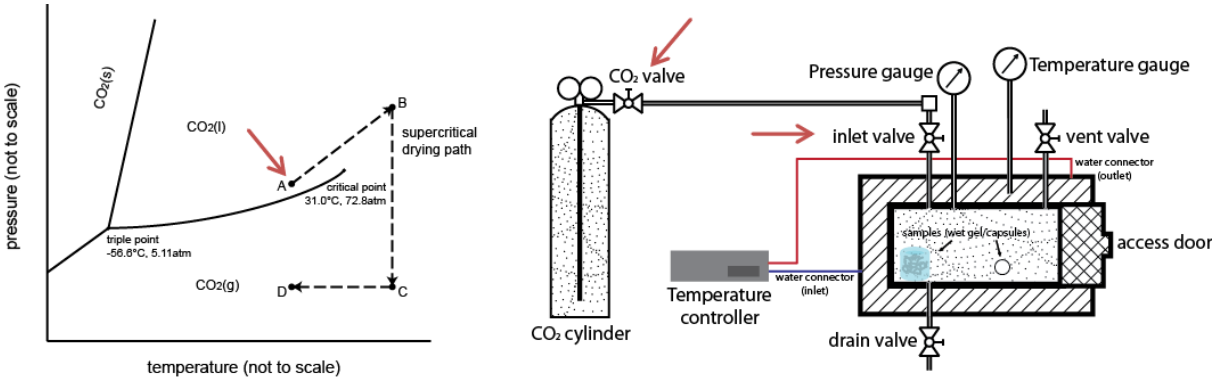

Open CO_2 and inlet valve

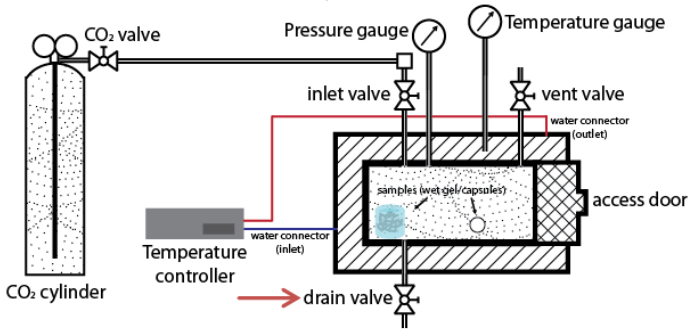

Once the pressure in the chamber is equal to the pressure in the CO_2 cylinder, open the drain valve, which starts the acetone exchange to liquid CO_2

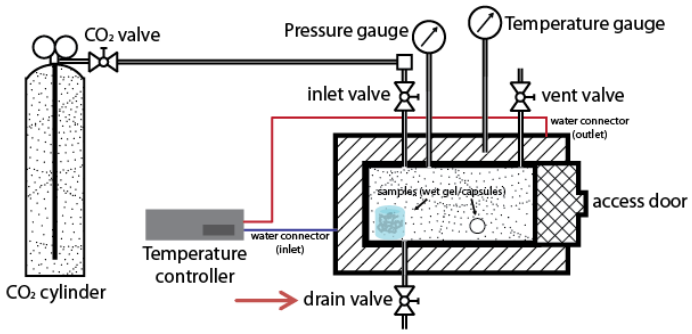

Once the chamber is filled only with liquid CO_2, close the drain valve and wait 24hours

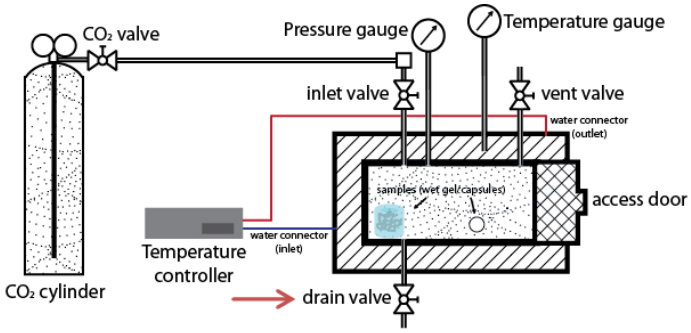

Every 12 hours, open drain valve slighly and flush chamber with fresh CO_2; Repeat for 10 days

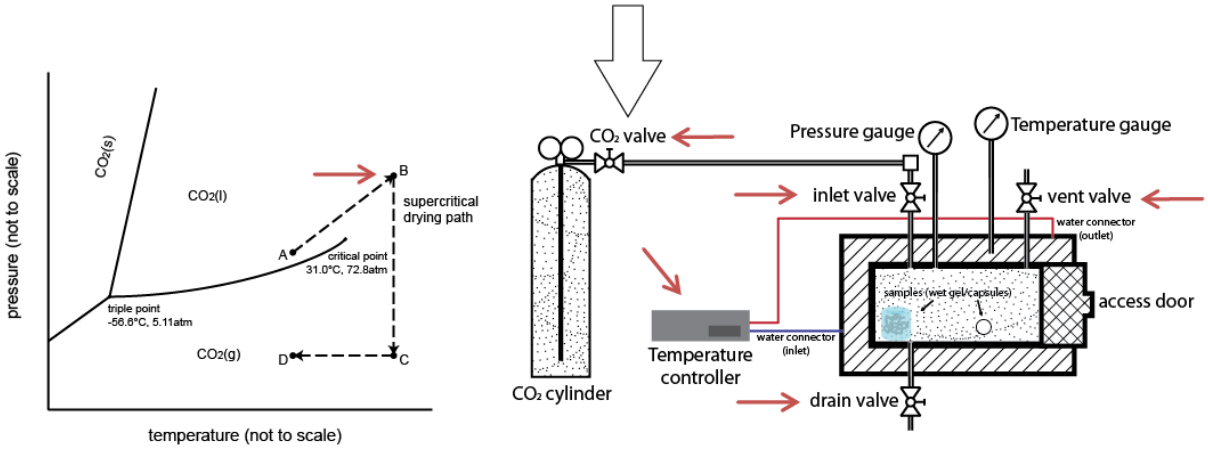

Close all valves and increase the temperature of the chamber to 55°C, which increases the pressure in the chamber (point A to B in left diagram); Once the pressure in the chamber reaches 1600psi, use the vent valve to hold that pressure until 55°C is reached. Close vent valve.

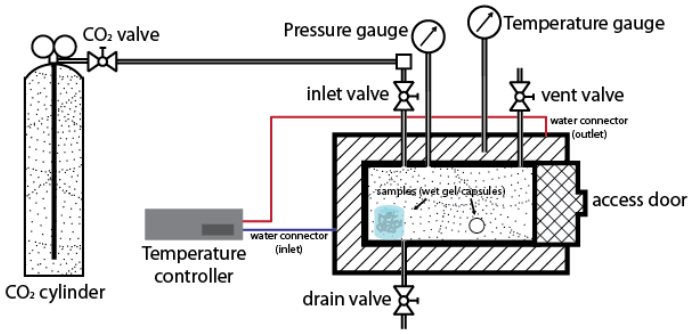

Keep the sample in supercritical conditions for 12 hours

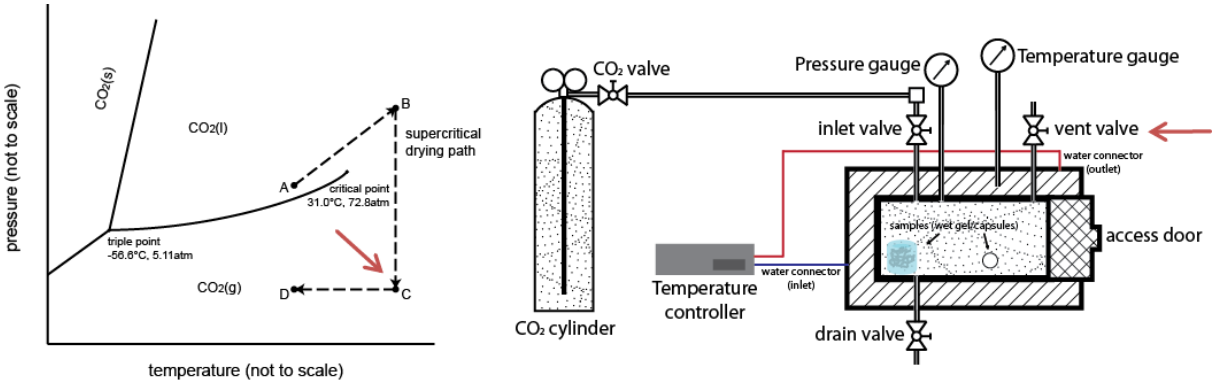

Slowly depressurize the chamber under isothermal conditions by opening the vent valve (point B to C in left diagram)

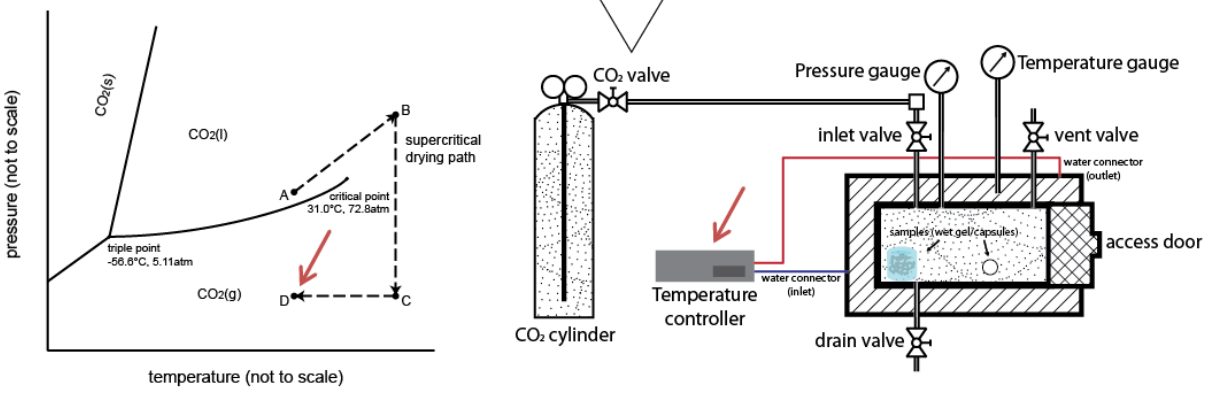

Bring critical point dryer's temperature to room temperature (point C to D in left diagram)

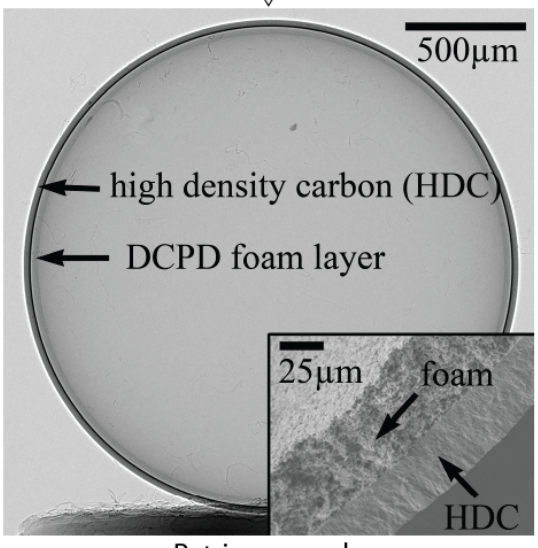

Retrieve sample

Slight deviations of the developed procedure often lead to collapsed or damaged foams inside the hollow sphere. For example, the magnitude of the flux of liquid carbon dioxide into the chamber during the first purge had an influence on the layer

quality. A high flux and therefore a fast increase in pressure inside of the chamber were found to be beneficial as it might have helped clear a potentially plugged fill hole. This prevented the obstruction of solvent diffusion in and out of the capsule and, therefore increased the chance of a successful drying without foam collapse, but it also increased the risk of pushing the wet gel plug into the sphere (Figure 5-18).

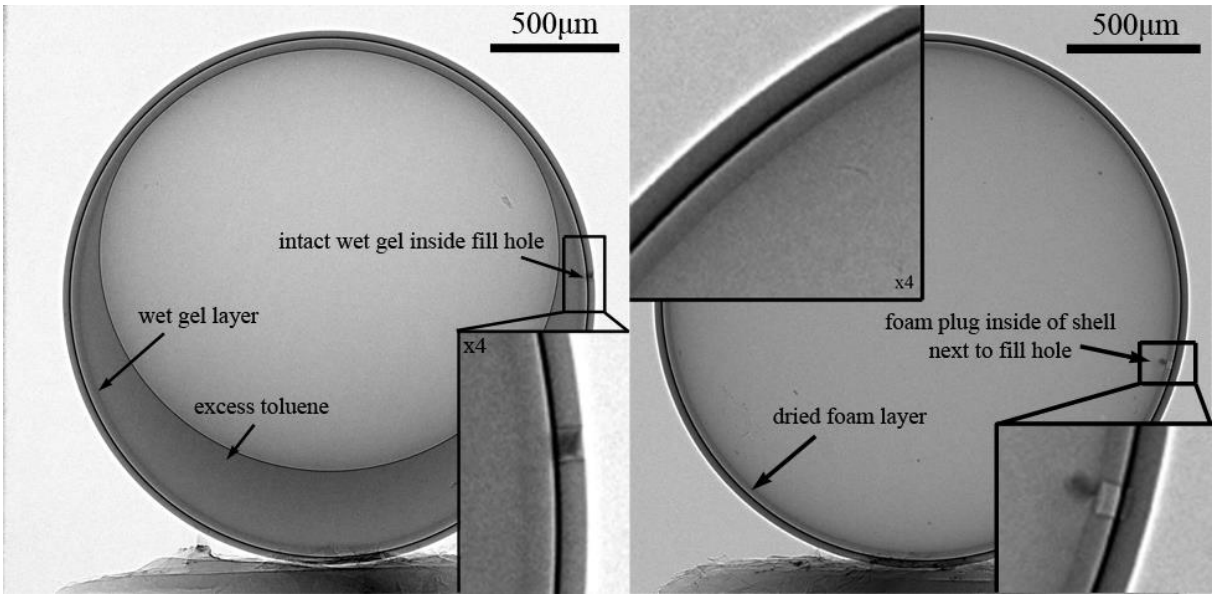

Figure 5-18: Radiograph of a 2 mm HDC capsule (ID) coated with a p(DCPD-r-NB) wet gel layer (50 mg/cm³ DCPD, 10 wt.% NB, 0.1 wt.% catalyst, filled at Δp=102.1 Torr, rotated at 10/14.142 rpm for ~2.5 hours, doped with 1 mg/cm³ iodine/toluene for 5 days [see chapter 6]) directly before and after supercritical drying. The wet gel in the fill hole is still intact and was pushed inside of the shell during the supercritical drying process.

Once the foam plug was inside the shell, it was impossible to remove it without damaging the shell. A process was therefore developed to prevent the plug from forming altogether (see chapter 5.3.1).

Additionally, a fast pressure increase in the drying chamber and, therefore, in the capsule itself could cause delamination of the foam around the fill hole as the influx of liquid CO_2 presses against the wet gel layer. (Figure 5-19)

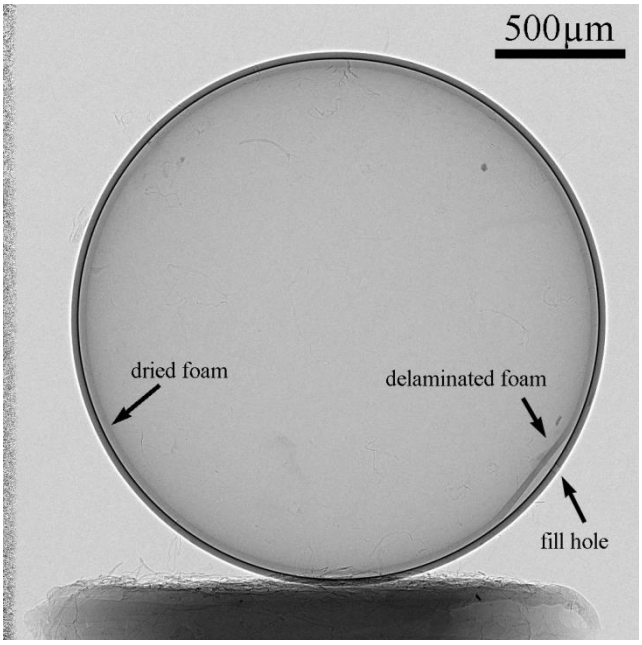

Figure 5-19: Radiograph of a 2 mm HDC capsule (ID) coated with a p(DCPD-r-NB-I_2) wet gel layer (50 mg/cm^3 DCPD, 5 wt.% NB-I_2, 0.2 wt.% catalyst, filled at Δp = 105.9 Torr, uniaxial rotation at 2 rpm for 24 hours). The foam layer delaminated around the fill hole during supercritical drying as a result of the CO_2 influx into the hollow shell.

The foam layer was detached from the high density carbon wall around the fill hole 150 µm in each direction. It seemed to be completely intact and the rest of the foam was well adhered to the shell wall. This still rendered the capsule unusable and, therefore, needed to be avoided. Although delamination of the foam layer during supercritical drying rarely occurred, it might be helpful for future experiments to develop a procedure to prevent it.

Following the above mentioned supercritical drying procedure for thin film layers in hollow spheres allowed reproducibly producing uniform polymer aerogel layers in hollow spheres and significantly increasing the yield.

5.3. **Optimization of the drying process**

Although the supercritical drying procedure was successfully optimized to our needs, there are several improvements to the process that can be considered and investigated to further improve the drying process. The main source of failure during supercritical drying of wet gel layers in hollow spheres is, as discussed above, partly or completely collapsed foam in the fill hole, which hinders or prevents solvent exchange entirely. Different techniques to either prevent any wet gel from forming in the fill hole

altogether, clearing the fill hole after a plug has been formed, and stimulate a faster solvent exchange rate in and out of the capsule were explored.

5.3.1. Preventing wet gel from forming inside the fill hole

One of the approaches that was developed to optimize the drying process is an artificial plug that can be inserted into the fill hole directly after filling the capsule with precursor solution. This prevents any wet gel formation in the fill hole during the coating process and would, after removal of the artificial plug, decrease the time required for complete solvent exchange.

Additionally, as outlined in chapter 5.1, any residual foam in the fill hole needs to be removed before the fill tube can be attached to the capsule. Figure 5-20 shows the cross sectional view of the fill hole of a 1.6 mm HDC capsule (ID) coated with a 35 mg/cm^3 p(DCPD-r-NB) aerogel layer that was successfully dried with foam residue in the fill hole.

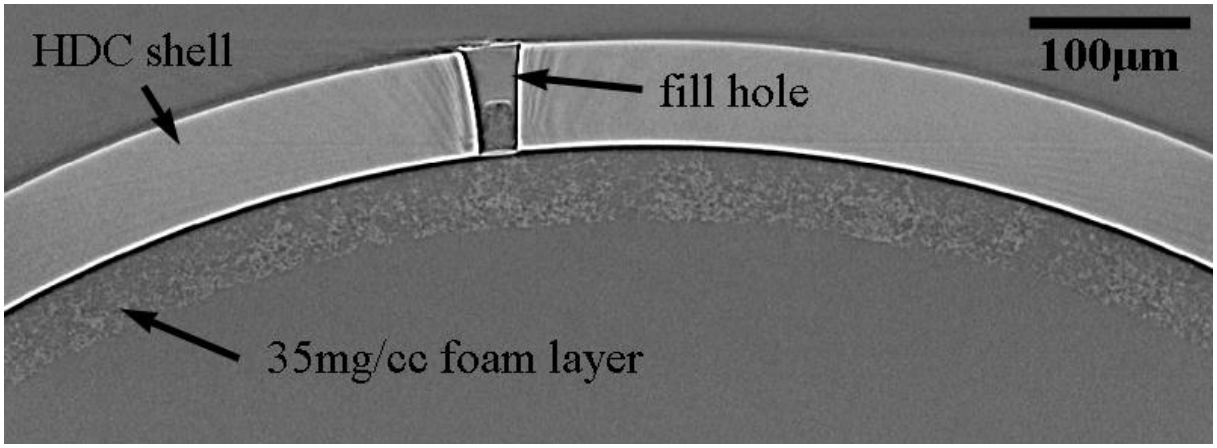

Figure 5-20: Cross sectional (tomographic) view of the fill hole of a 1.6 mm HDC capsule (ID) coated with a p(DCPD-r-NB) aerogel layer (35 mg/cm^3 DCPD, 5 wt.% NB, 0.2 wt.% catalyst, filled at Δp = 144.8 Torr, uniaxial rotation at 2 rpm for 24 hours). The 30 µm diameter fill hole contains residual foam, which needs to be removed before fill tube insertion. (tomography taken by Haibo Huang, General Atomics; analysis and picture extraction: Tom Braun)

In this case, the wet gel in the fill hole did not prevent complete solvent exchange and was supercritically dried as the rest of the foam layer inside of the capsule. Even though the upper part of the fill hole is empty, a fill tube cannot be attached to this capsule without removing the rest of the foam in the fill hole. An artificial plug that can be removed could consequently prevent the wet gel from forming inside of the fill

hole altogether with the additional advantage of decreasing solvent exchange time leading to a faster supercritical drying procedure.

Therefore, a structure that has a cone frustum with the inverse shape of the fill hole attached to a bigger base for handling purposes was built using additive manufacturing techniques. (Figure 5-21) The base would sit on the outside of the sphere while the cone frustum is inserted into the fill hole.

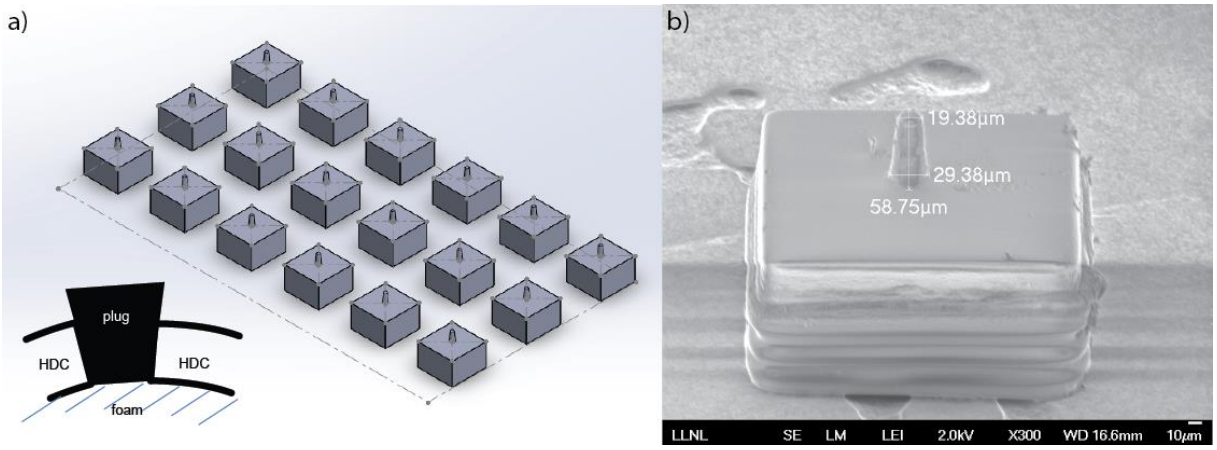

Figure 5-21: Artificially plugging the fill hole of the ablator shell - from design to completion. a) The plug consists of a cone frustum with the inverse shape of the fill hole attached to a bigger base for handling purposes. b) SEM image of the additively manufactured plug with the exact dimensions of the fill hole to fit precisely. (plugs designed by Tom Braun and printed by Julie Jackson, LLNL; SEM taken by Patrick Campbell, LLNL)

Due to the precise fit of the cone frustum in the fill hole, the plug is level with the inside wall of the hollow sphere, allowing for a uniform foam layer. The plug will be inserted into the fill hole after filling the precursor solution into the capsule and remain there for the entirety of the coating process. Once the wet gel layer inside of the hollow sphere is formed, the plug will be removed to allow solvent exchange in and out of the shell. Since the fill holes for the same batch of capsules are identical, the plug might be reusable.

For a proof of principle experiment, a plug was manufactured in cooperation with Julie Jackson, LLNL, using projection microstereolithography from a photosensitive polymer resin bath using 1,6-hexanediol diacrylate (HDDA).[233] As illustrated in Figure 5-21, the cone frustum has the exact dimensions of the fill hole and a stable base attached to it to support the insertion process into the fill hole. A test piece of the manufactured material with similar dimensions was submerged into toluene for

24 hours to test its ability to withstand exposure of the solvent. It did not show any sign of shrinkage or decomposition. The plug's cone frustum was then inserted into the fill hole of an empty 1.6 mm HDC capsule (ID) using a modified vacuum tool kit with a self-developed tip. (Figure 5-22) It seemed to form an exact fit and was held in place solely by friction without the use of any adhesive. It did not detach when rotating the shell in any direction or during a rocking motion. Using the modified vacuum tool kit, the plug was removable undamaged from the hollow sphere.

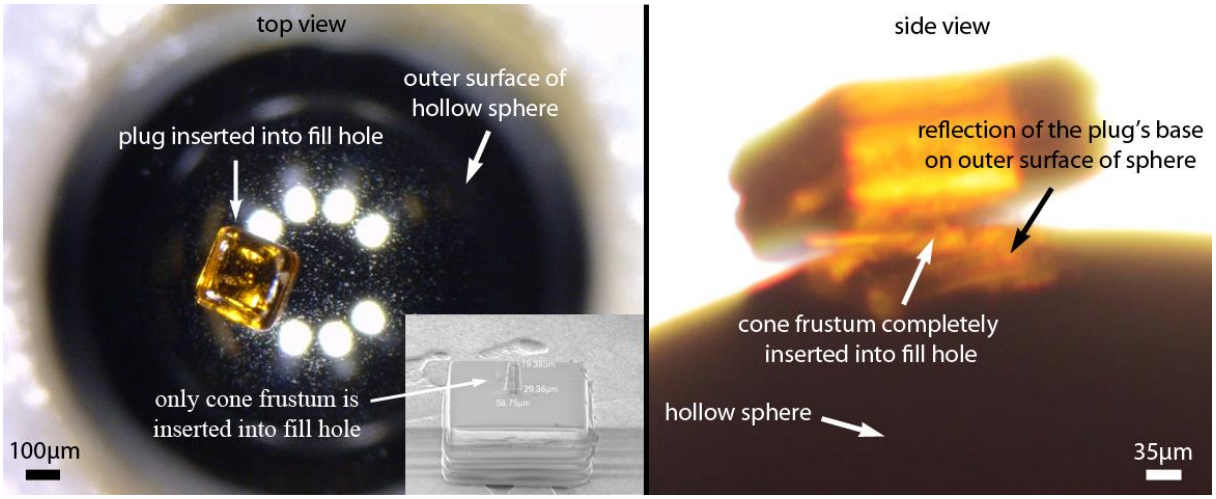

Figure 5-22: Photomicrograph of the plug inserted into the fill hole of a 1.6 mm HDC capsule (ID) with a fill hole length of 60 µm. The plug is held in place solely by friction without the use of any adhesive. It fits exactly into the fill hole and is easily removable.

These experiments have demonstrated that an additively manufactured plug can be inserted into the fill hole of a 1.6 mm HDC capsule (ID) and that it does not detach during rotation of the shell. The plug can be removed without any damage, which is a requirement for successfully implementing this approach.

Future experiments will include casting a foam layer inside the shell while the plug is in place and demonstrating that the removal of the manufactured plug does not damage the foam layer. Additionally, it needs to be tested that the foam surface directly next to the plug still allows for sufficient solvent exchanged after removal of the plug.

5.3.2. Clearing the fill hole

The second approach that was developed to optimize the drying process was the mechanical removal of the wet gel inside of the fill hole directly after the coating

process. Although the p(DCPD-r-NB) is very elastic in its wet gel stage, it might be possible to clear the fill hole mechanically by inserting a sharp needle-like object into it. This would clear the wet gel from the fill hole and accelerate the solvent exchange. The size of the fill hole (<30 µm) makes this a difficult task with the added complication that the capsule has to be submerged in the same solvent that is present in the wet gel to prevent collapse of the aerogel in the otherwise exposed fill hole. For the experiment, a hollow 2 mm HDC capsule (ID) was submerged into water with the fill hole pointed upwards. A sharp nano-tip that allowed control in spatial dimensions with sub-micron precision was then inserted into the fill hole. (Figure 5-23).

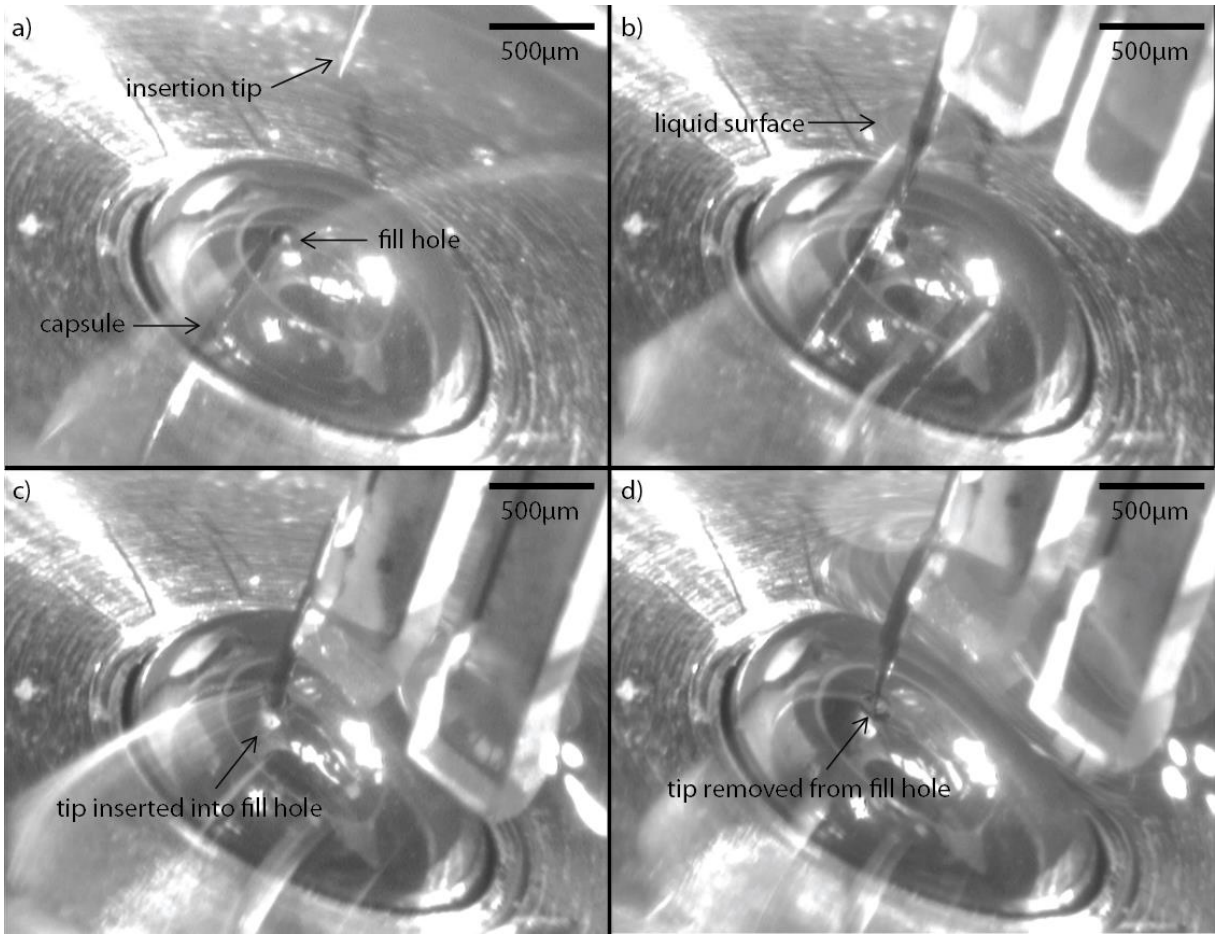

Figure 5-23: Photographs of the tip insertion process into the fill hole of a 2 mm HDC capsule (ID) submerged in water. a) The insertion tip was brought into the right position using two cameras mounted perpendicular to each other and then slowly lowered. The insertion tip was further lowered until it (b) penetrated the liquid's surface and then is (c) inserted into the fill hole. d) Once the tip is removed from the fill hole, no damage to the HDC capsule or fill hole was observed.

In order to observe the tip's position relative to the fill hole, two cameras were mounted perpendicular to each other pointing at the fill hole. The insertion tip was then slowly lowered into the liquid and carefully inserted into the fill hole. The

refraction indices of the respective liquids used have to be taken into consideration to avoid damage to the shell and the tip during the insertion process. Once the tip is successfully inserted into the fill hole, it can be removed to start the solvent exchange. Since the fill hole is cleared of any potentially collapsed or densified wet gel, the solvent exchange may be accelerated.

However, when performing this experiment with a layered capsule, an inherent risk of pushing the wet gel into the capsule and delaminating the layer around the fill hole exists. The experiment was repeated with a 2 mm HDC capsule (ID) coated with a p(DCPD-r-NB-I_2) aerogel layer (50 mg/cm^3 DCPD, 5 wt.% NB-I2, 0.2 wt.% catalyst, filled at $\Delta p = 100.9$ Torr, uniaxial rotation at 2 rpm for ~27 hours). (Figure 5-24). It needs to be noted that the insertion tip was slightly bent from a previous experiment.

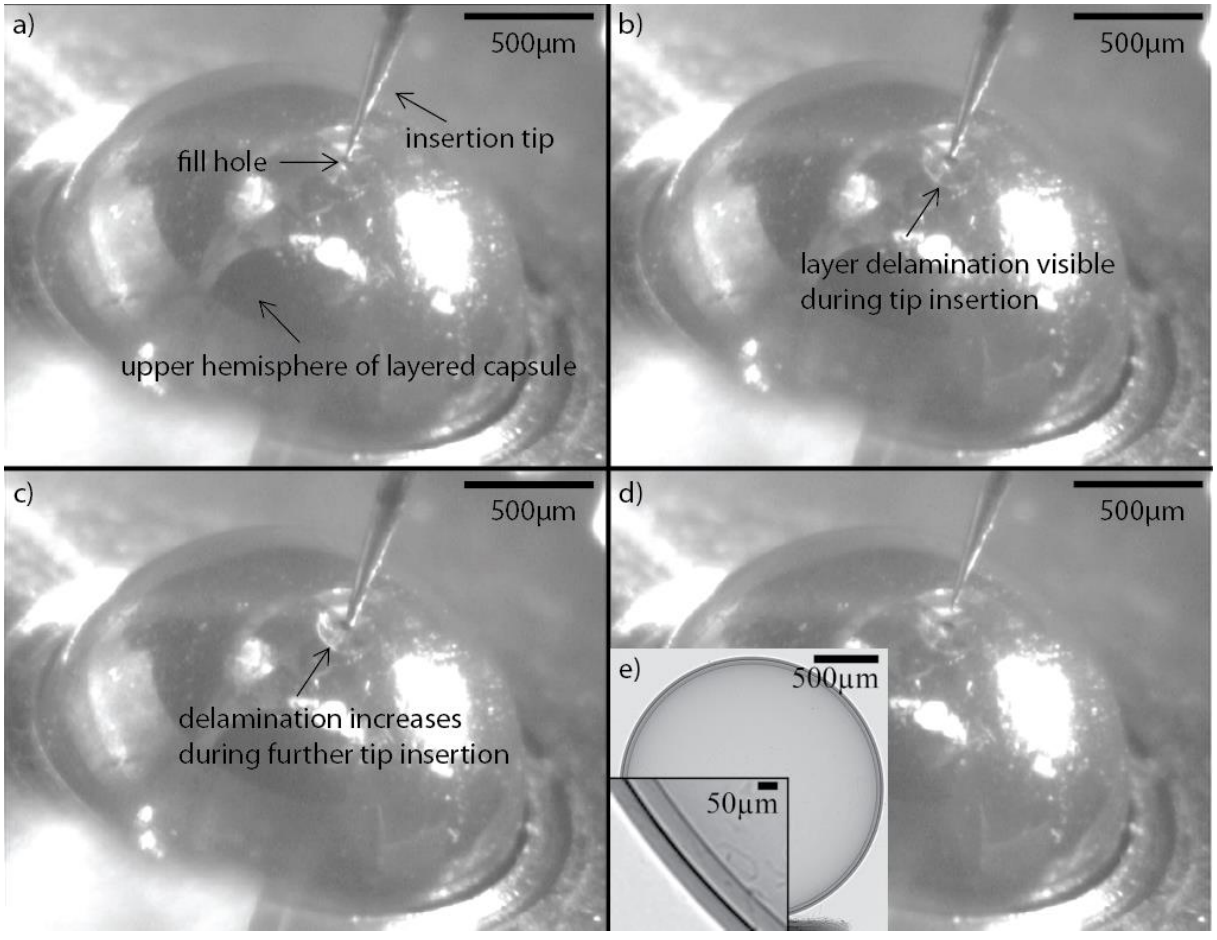

Figure 5-24: Photographs of the tip insertion process into the fill hole of a 2 mm HDC capsule (ID) coated with a p(DCPD-r-NB-I_2) aerogel layer (50 mg/cm^3 DCPD, 5 wt.% NB-I_2, 0.2 wt.% catalyst, filled at Δp=100.9 Torr, uniaxial rotation at 2 rpm for ~27 hours). a) The nano-tip was inserted into the shell which slightly delaminated the layer directly around the fill hole. b) and c) During further tip insertion the delamination of the aerogel layer around the fill increases. d) Once the insertion tip is removed from the shell, the layer does not go back into its original shape and stays delaminated. e) The inlet shows a radiograph of the original uniform aerogel layer inside of the shell.

The aerogel inside of the shell formed a uniform layer (Figure 5-24 - e) before the clearing attempt of the fill hole. A close radiograph of the fill hole was not obtained, so it was unclear before the experiment if the fill hole itself contained any wet gel. However, once the nano-tip was inserted into the fill hole, layer delamination around the fill hole could clearly be observed. The layer delaminated further the deeper the nano-tip was inserted into the layered capsule. The insertion tip went well beyond the fill hole length into the shell during the attempt of piercing the aerogel with the tip. After completely removing the nano-tip from the fill hole, the layer around the fill hole did not return into its original position and stayed delaminated.

A different approach that is starting to be explored is motivated by the particle extraction technique used to extract organics from aerogels captured from Comet 81P/Wild 2 by the Stardust Spacecraft, which was developed at the Space Sciences Laboratory, U.C. Berkeley.[234] Glass needles are pulled to fabricate microneedles which then are repetitively poked into the aerogel to cut it. To test this approach, prefabricated glass micropipette tips (Origio) with a diameter of 20 µm were used to successfully insert the micropipette tip into the sphere (Figure 5-25) and remove it undamaged. However, further studies are needed to determine if the wet gel inside of the fill hole was in fact pierced.

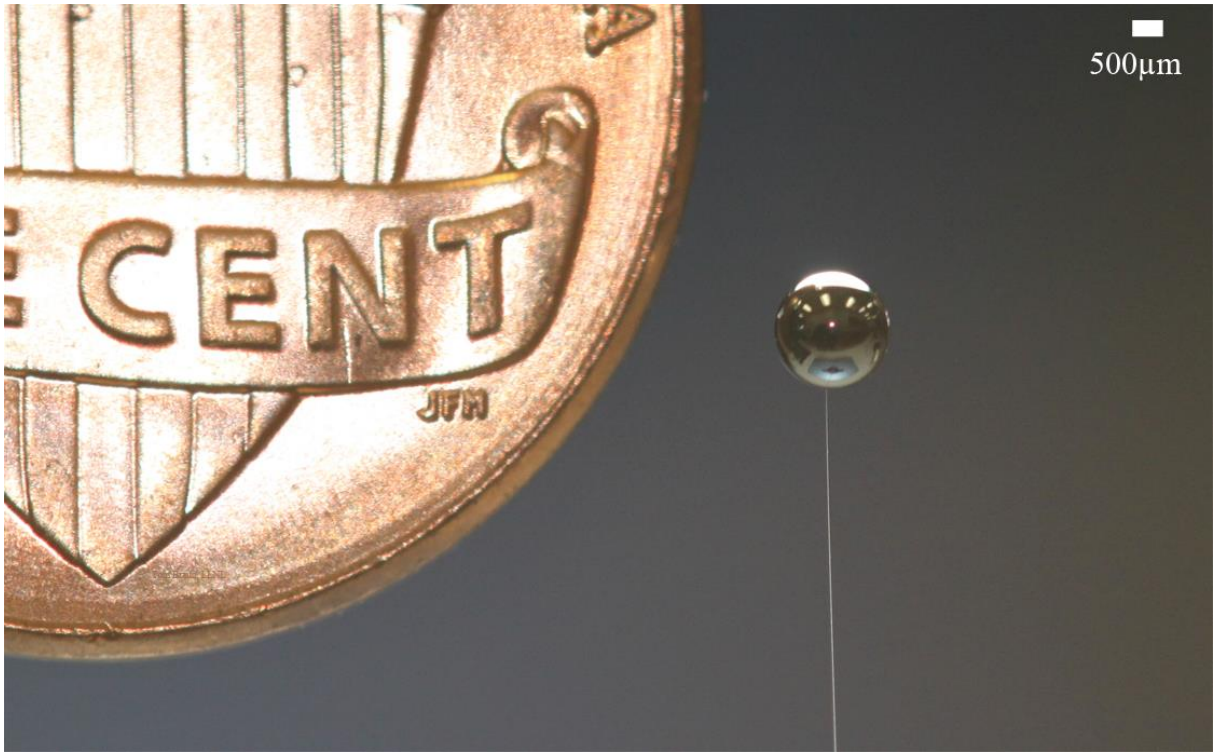

Figure 5-25: Glass micropipette tip inserted into the fill hole of a 1.6 mm (ID) high density carbon NIF ablator target. The fill hole size of this particular ablator shell is 30 µm, three times less than the average diameter of the human hair.

As demonstrated, it is feasible to clear the fill hole mechanically by inserting a sharp needle-like object into it in order to remove the wet gel inside of the fill hole directly after the coating process. Future experiments require a detailed study on how the piercing affects the aerogel in the fill hole and if this method is suitable to increase the solvent exchange rate. Given the wet gel's elasticity, the fill hole might close up after the sharp object is removed, rendering this approach ineffective. However, with the ability of inserting a micropipette into the sphere, it might be possible to facilitate the solvent exchange from toluene to acetone by piercing the micropipette tip through the wet gel and forcing acetone into the capsule through the pipette.

A laser drilling approach comparable to what is currently used to drill the micron-sized fill hole into the ablator shell[47, 235] might also be considered if accuracy permits. In cooperation with General Atomics, this approach is currently being used to remove dried foam residues from the fill hole.

5.3.3. Pressure gradient

A different method to increase the speed of the solvent exchange process that was developed is to not solely rely on diffusion, but rather force liquid in and out of the wet gel layered shell by submerging it in the second solvent and creating a pressure gradient. This process uses the same principle as the filling setup and has the potential to vastly decrease solvent exchange times. As shown in Figure 5-4 at the beginning of this chapter, the layered hollow spheres usually have solvent in the wet gel and some additional solvent, but also contain a gas bubble. This gas bubble can be compressed under pressure, which, when the hollow shell is submerged in a liquid, forces the liquid into the capsule. After depressurization, the gas bubble expands and liquid is pushed out of the shell.

To demonstrate this, a 2 mm HDC capsule (ID) was filled with 2 mg/cm^3 iodine/toluene using the standard filling setup and then submerged into a 20 ml vial filled with liquid hexane. The capsule sank to the bottom of the vial and due to the small wall thickness of the high density carbon shell the size of the gas bubble could clearly be distinguished. (Figure 5-26)

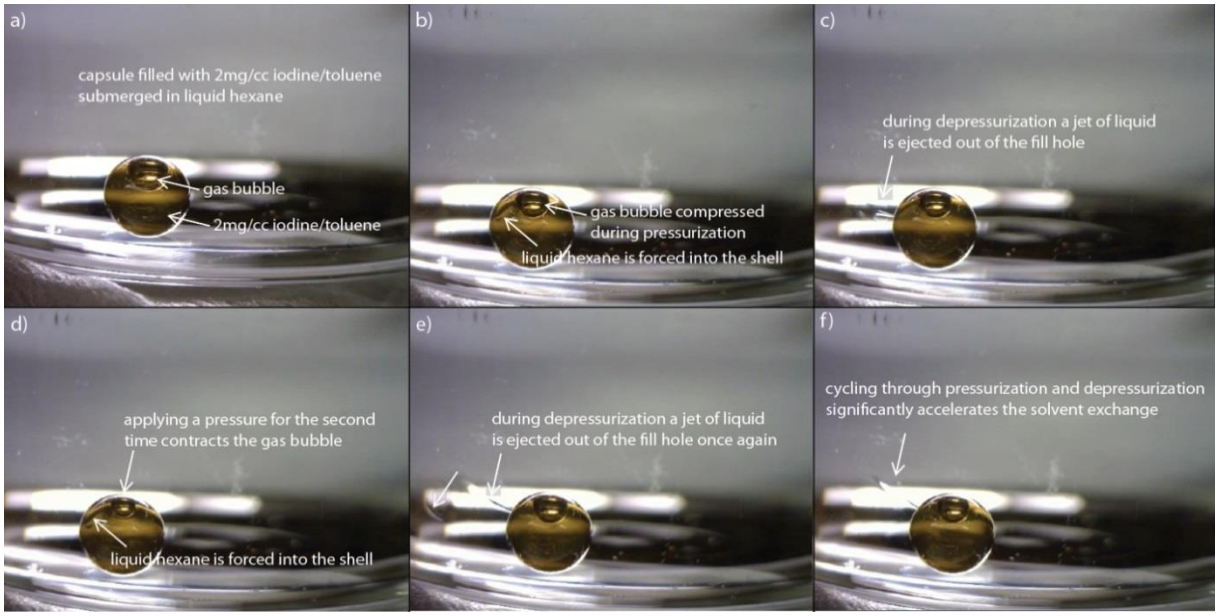

Figure 5-26: Photographs of a hollow 2 mm HDC capsule (ID) filled with 2 mg/cm^3 iodine/toluene submerged in liquid hexane undergoing cyclical pressurization and depressurization. a) The gas bubble in the submerged capsule under atmospheric conditions is well discernible due to the small wall thickness of the shell. b) Pressurizing the setup causes the gas bubble to compress and forces liquid hexane into the capsule. c) During depressurization, a jet of liquid is ejected out of the shell's fill hole as the gas bubble increases in size. d)-f) Cycling through pressurization and depressurization of the submerged capsule forces the solvents into and out of the capsule, which considerably decreases solvent exchange time.

A 100 ml syringe was then attached to the top of the vial and sealed, which allowed controlling the pressure inside the vial by changing the syringe's plunger position. Pressurizing the setup caused the gas bubble inside of the hollow sphere to compress and forced liquid hexane into the shell. Releasing the syringe's plunger to its original positions depressurized the setup, which prompted a jet of liquid from the inside of the shell out of the fill hole as the gas bubble increased in size. (Figure 5-26 – c) With the help of a syringe pump, it was possible to cycle through pressurization and depressurization of the submerged capsule, which significantly increased the solvent exchange rate.

The experiment was repeated with a layered sphere to test if the pressure cycling can be done successfully with a layered sphere. For that, a 2 mm HDC capsule (ID) was coated with a p(DCPD-r-NB) aerogel layer (25 mg/cm^3 DCPD, 15 wt.% NB, 0.2 wt.% catalyst, filled at Δp=250.1 Torr, uniaxial rotation at 10 rpm for ~23 hours) and submerged the shell in a 1.5 mg/cm^3 iodine/toluene solution. (Figure 5-27)

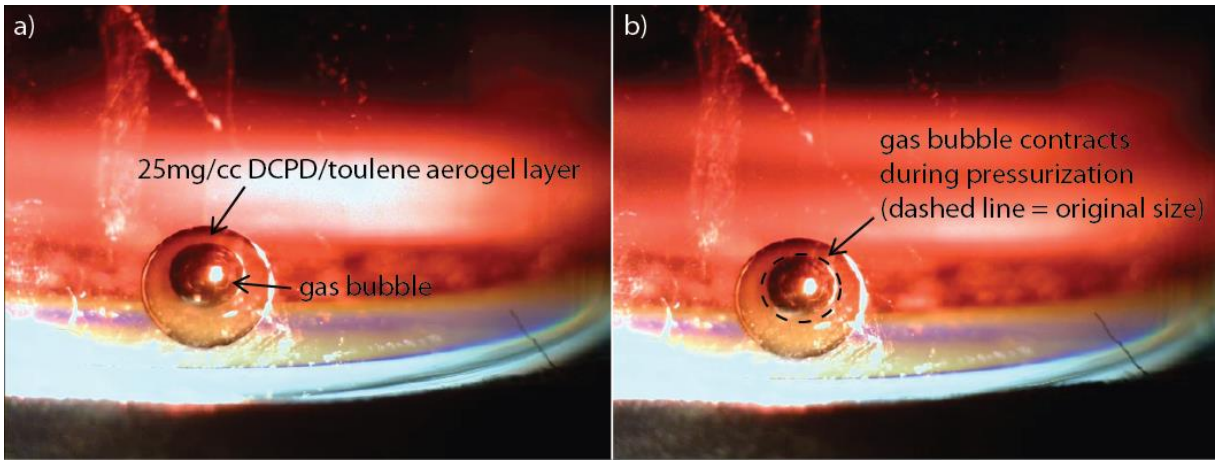

Figure 5-27: Photographs of the pressurization of a 2 mm HDC capsule (ID) coated with a p(DCPD-r-NB) aerogel layer (25 mg/cm^3 DCPD, 15 wt.% NB, 0.2 wt.% catalyst, filled at Δp=250.1 Torr, uniaxial rotation at 10 rpm for ~23 hours). a) The gas bubble in the hollow shell does not rise to the top edge of the shell (compare to Figure 5-26), but rather to the inner aerogel surface. b) Once the setup is pressurized, the gas bubble contracts even though an aerogel layer is present in the shell.

As in the previous experiment, the 100 ml syringe was attached to the top of the vial and sealed to control the pressure in the vial. Under atmospheric conditions, the gas bubble did not rise to the top of the shell as compared to the previous experiment (Figure 5-26 a), but rather to the inner surface of the aerogel layer. Pressurizing the setup caused the gas bubble inside of the hollow sphere to compress even though an

aerogel layer was present. During depressurization, the bubble expanded to its original size. A radiograph after pressure cycling confirmed that the aerogel layer did not delaminate during the process. (Figure 5-28)

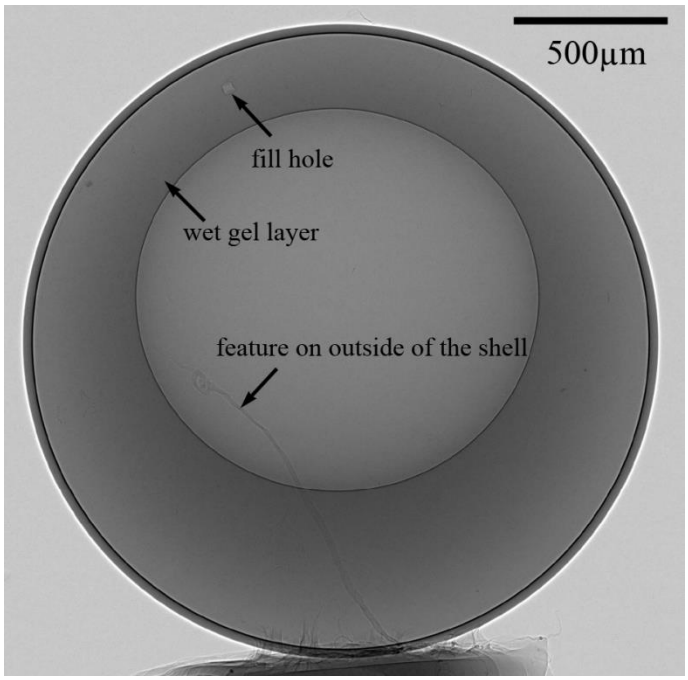

Figure 5-28: Radiograph of the 2 mm HDC capsule (ID coated with a p(DCPD-r-NB) aerogel layer (25 mg/cm^3 DCPD, 15 wt.% NB, 0.2 wt.% catalyst, filled at Δp=250.1 Torr, uniaxial rotation at 10 rpm for ~23 hours) after pressure cycling. The foam layer does not seem to have delaminated after pressure cycling the capsule.

As just demonstrated, the pressure cycling method is a viable tool to increase the solvent exchange rate in and out of the capsule. Future experiments will involve pressure cycling a capsule with a wet gel layer with liquid CO_2 inside of the critical point dryer, which if applicable, has the potential to vastly decrease solvent exchange times.

5.4. **Conclusions**

Supercritical drying of the wet gel layers inside of hollow spheres is currently the most successful approach to remove the solvent from the porous network. Liquid carbon dioxide is used as the supercritical fluid as it is a non-flammable liquid, chemically inert, inexpensive, and has a very low critical temperature of T_c=31°C. This, however, requires the solvent in the gel network to be exchanged for the supercritical fluid, which is a time-consuming process, especially for an aerogel in a hollow sphere. The

time required for solvent exchange in and out of the fill hole and the sphere was estimated to a first degree using a diffusion based model. Experiments on bulk pieces of p(DCPD-r-NB) aerogels allowed assessing the strength of different precursor compositions during the supercritical drying process and to identify different combinations of norbornene and catalyst concentration that do not shrink or collapse during solvent exchange and supercritical drying. Different solvents were tested and, in the case for producing foam layers in hollow spheres, solvent exchange from toluene to acetone to liquid carbon dioxide produced the most reproducible results. These extensive tests allowed developing and implementing a procedure to successfully dry p(DCPD-r-NB) copolymer aerogel layers in hollow spheres. Small changes in the procedure, however, can lead to collapsed foams, which is why different methods to optimize the process were developed and tested. The most promising methods were as follows:

1. Artificially plugging the fill hole after capsule filling. This procedure would prevent any wet gel formation in the fill hole during the coating process and would, after removal of the artificial plug, decrease the time required for complete solvent exchange.

2. Clearing the fill hole mechanically by inserting a sharp needle-like object into it. This has the potential to remove the wet gel from the fill hole and accelerate the solvent exchange.

3. Forcing liquid in and out of the wet gel layered shell by applying a pressure gradient.

All methods have the potential to further optimize the supercritical drying process of aerogel layers in hollow spheres. Further improvements that are currently under development are a stirring mechanism inside of the critical point dryer and immersion sonication during solvent exchange with liquid carbon dioxide.

Chapter 6: Doping of p-DCPD aerogel coatings with high-Z tracer elements

The intentional introduction of dopants into low-density polymer films is extensively discussed in the literature. The addition of such dopants into low-density polymer foams is utilized in a variety of different experiments such as long scale length plasma experiments,[236-237] extreme ultraviolet generation,[238] plasma radiation,[239] high energy density physics experiments,[240] laser plasma interaction experiments,[241] X-ray drive symmetry,[11] diagnostic analysis in laser interaction experiments,[242] and direct and indirect drive inertial confinement fusion experiments.[12, 243-248]

In the inertial confinement fusion community, doped low-density polymer films inside of spherical shells are being produced to bring dopants for diagnostics and nuclear physics experiments in direct or close contact with the deuterium-tritium fuel.[12, 14] To fabricate these doped foam lined shells two different options were explored:

1) Completely filling (see chapter 4) or casting an undoped pDCPD aerogel layer in a spherical target (see chapter 3) and doping the final aerogel structure by *halogenation of the unsaturated DCPD backbone* using iodine or bromine.[14, 249-251] The pDCPD polymer contains remaining C=C double bonds that can react with iodine or bromine.

2) *Copolymerizing the aerogel with functionalized monomers* while casting the foam in the shell. Functionalized monomers, such as NB-R, could be incorporated into the pDCPD polymeric structure using a ring opening metathesis polymerization (ROMP) reaction, which would yield p(DCPD-r-NB-R) aerogels. These aerogels can be casted in the hollow sphere during polymerization.

Both approaches allow the incorporation of high-Z tracer elements in to the polymer backbone and are discussed below. Doping of the foam liners in spherical shells allows for an increased use of polymeric aerogels and coatings in a wide range of applications and experiments. It has the additional advantage of increasing the foam's X-ray contrast, which significantly facilitates non-destructive characterization techniques of the aerogel layers in spherical hollow spheres.

6.1.1. Halogenation of the unsaturated pDCPD backbone

To achieve halogenation of the remaining C=C double bonds in the pDCPD polymer, two different approaches were explored: 1) immersion the polymerized wet gel into a solution of a halogen in toluene (*liquid phase doping*) or 2) exposing the dried aerogels to volatile reactants such as iodine.

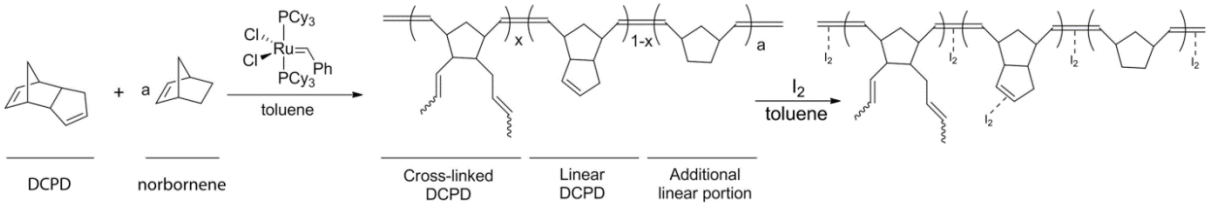

Figure 6-1: Ring opening metathesis polymerization (ROMP) of dicyclopentadiene (DCPD) and norbornene (NB) in toluene using Grubbs 1st generation catalyst followed by halogenation of the unsaturated DCPD backbone with iodine in toluene.

For the liquid phase doping, a pDCPD wet gel liner was usually casted in a hollow sphere and the entire sphere was then submerged into a solution of 1 mg/cm^3 iodine/toluene for seven days. In order to estimate the time that is required for the liquid phase doping of the DCPD wet gels with liquid iodine/toluene, 50 mg/cm^3 p(DCPD) wet gels were first synthesized in a 1 cm inner diameter glass cuvette with open ends on both sides. The cylinder was placed on top of the gap between two microscope slides that were 0.9 cm apart from each other to leave the bottom surface of the aerogel exposed. The microscope slides with the cylinder on top were then placed in a 1 mg/cm^3 iodine/toluene bath in a way that the bottom of the cylinder was exposed to the iodine/toluene bath, but left the rest of the glass cylinder exposed. (Figure 6-2) Since the iodine/toluene solution has a reddish color it was possible to observe the diffusion through the white colored aerogel cylinder over time. However, compared to chapter 5.1.3 in which a similar experiment was conducted the exact location of the diffusion front was not as clearly observable.

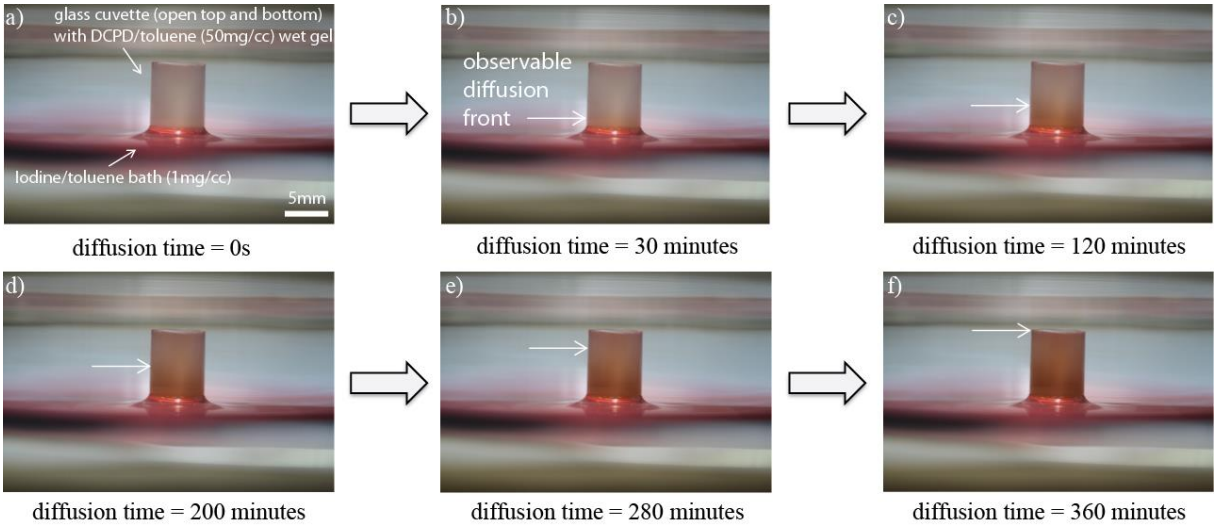

Figure 6-2: Photographs of a cylindrical glass cuvette open on both ends filled with 50 mg/cm³ p(DCPD) wet gel (0.1 wt.% catalyst, gelled stationary for ~5 hours). One end of the glass cuvette with the wet gel is placed in a 1 mg/cm³ iodine/toluene bath to observe diffusion in the wet gel. a) At t=0s the wet gel is translucent and white in color and the iodine solution has not moved through the wet gel. b) After t=30 minutes the diffusion front has moved by ~2 mm and can be seen to move further as time progresses (c) – (f). f) After t=360 minutes the diffusion front has moved completely through the wet gel in the cylinder.

After $t = 30$ minutes the diffusion front had moved roughly 2 mm through the wet gel. The front advanced to 4.5 mm after $t = 120$ minutes and to 5.5 mm after $t = 200$ minutes. Within 6 hours the diffusion front had moved completely through the sample. These results suggest a diffusion constant of $D_{\text{exp}} \approx 3 \cdot 10^{-10}\,\text{m}^2/\text{s}$, which is an order of magnitude slower than what was found in chapter 5.1.3. This result was therefore used as a lower limit to approximate diffusion times. With the analytical solvent exchange time approximations described in chapter 5.1.1, doping times between two and seven days were selected, depending on the fill hole size and wet gel layer parameters.

Figure 6-3 compares the pDCPD wet gel liner inside a hollow sphere before and after doping it with liquid phase iodine.

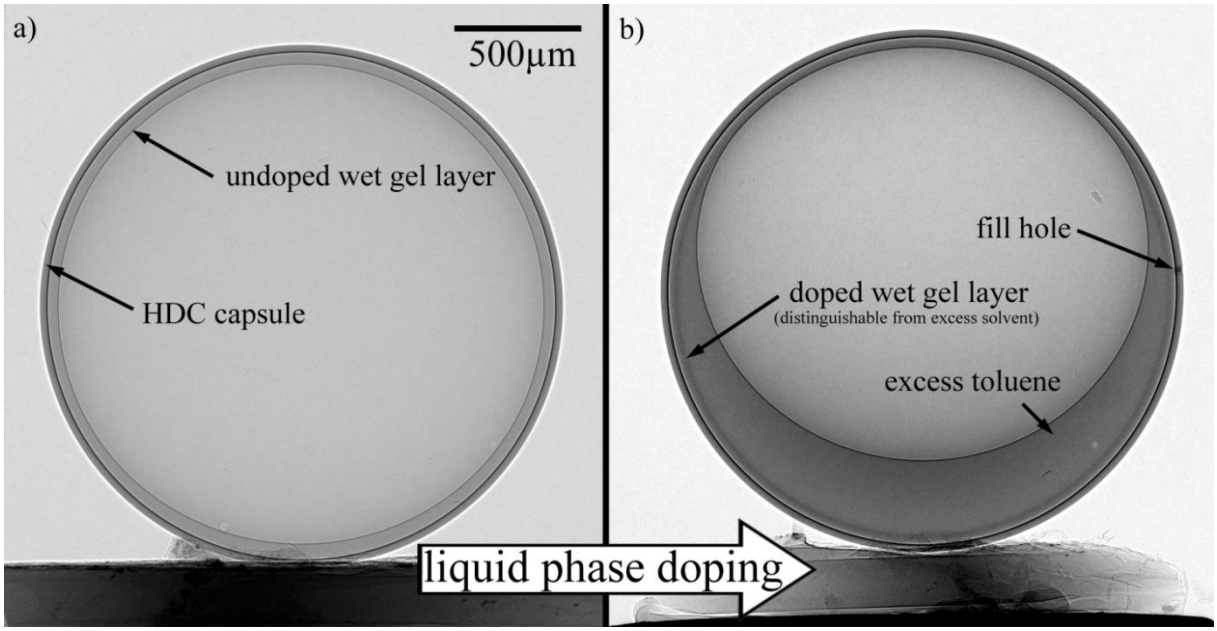

Figure 6-3: Cross-sectional radiographic image of a 2 mm diamond sphere coated with a 40 µm thick p(DCPD-NB) wet gel layer (50 mg/cm³ DCPD, 10 wt.% NB, 0.1 wt.% catalyst, filled with ΔP = 102.1 Torr, and rotated at 10/14.142 rpm for ~2.5 hours). a) The wet gel layer is distributed evenly in the hollow sphere and is adhering well to the shell. Some excess solvent can be seen at the bottom, but is undistinguishable from the actual wet gel layer. b) After liquid phase iodine doping, the doped wet gel layer is intact and distinguishable from the excess solvent. The additional solvent entered the hollow sphere while it was submerged in the solution of 1 mg/cm³ iodine/toluene.

The undoped wet gel layer inside of the hollow sphere was evenly distributed and adheres well to the wall. Although the layer appeared to be thicker in the bottom of the shell, it can be shown by rotation of the shell that it was, in fact, excess solvent. This is due to the fact that the spheres that contain wet gel layers were stored in toluene to prevent evaporation of solvent out of the shell, allowing excess solvent to enter the hollow sphere. Figure 6-3 b) illustrates this especially well. As mentioned above, the shell was submerged in a solution of 1 mg/cm³ iodine/toluene during liquid phase doping. After seven days of doping, the shell contained more excess liquid than before doping. Now, however, the wet gel layer was clearly distinguishable from the excess solvent as the iodine-doped p(DCPD-NB) wet gel provided a higher X-ray contrast than the undoped p(DCPD-NB) gel.

After removal of the solvent by supercritical drying (see chapter 5) the spherical shell contained an iodine doped aerogel layer. (Figure 6-4)

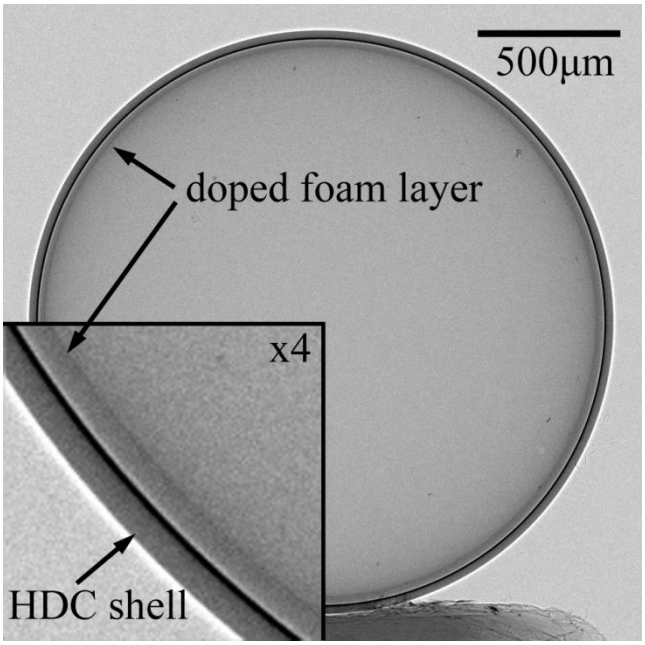

Figure 6-4: Cross-sectional radiographic image of a 2 mm diamond sphere coated with a 40 µm thick p(DCPD-NB) foam layer (50 mg/cm^3 DCPD, 10 wt.% NB, 0.1 wt.% catalyst, filled with ΔP = 102.1 Torr, rotated at 10/14.142 rpm for ~2.5 hours, and liquid phase iodine doped for 7 days) after supercritical drying.

After liquid phase doping the foam layer now showed a sufficient X-ray contrast due to the halogenation of the unsaturated pDCPD backbone. One major advantage of liquid phase doping is that it allows a quick and reliable assessment of the thickness profile and overall quality of the respective wet gel coating inside hollow spheres before removing the solvent. However, as outlined in chapter 5, the nondestructive removal of the solvent from the wet gel required a solvent exchange with acetone and liquid carbon dioxide. It can be observed that in the majority of the samples during this step and the supercritical drying, most of the iodine was washed out with the solvent. Rutherford backscattering spectrometry experiments on free standing pieces of liquid phase iodine doped foams done by S. H. Kim, LLNL, revealed a composition of $C_{10}H_{12}O_{1.5}I_{0.005}$, which indicates that only ~0.02 at.% of the iodine remained in the sample.[14] Repeating the experiment with a solution of bromine revealed a composition of $C_{10}H_{12}Br_{1.5}$, which attributes to ~7.6 at.% of bromine.[14]

Additionally, a second approach for halogenation was explored – *gas phase doping*. Here, the solvent was removed from the wet gel layer by supercritical drying, leaving an undoped foam layer in the shell. The foam filled shell was then exposed to volatile reactants such as iodine or bromine (iodine vapor pressure at 25°C was measured to be 0.305 Torr[252]) for two to three days. In the case of gas phase bromine doping, tests

on monolithic pieces of pDCPD aerogels showed signs of collapse during doping,[14] making this approach unusable. Using iodine vapor, on the other hand, showed promising results as the composition of the doped aerogel measured by Rutherford backscattering spectrometry (experiment done by S. H. Kim, LLNL) was $C_{10}H_{12}I_{0.43}$, which corresponds to ~1.9% at.% iodine and is an increase of a factor of 100 compared to the liquid phase doping. It is worth mentioning that the iodine detected after iodine vapor exposure doesn't necessarily need to be chemical bound (via I_2 addition to C=C double bonds), but can just be the result of I_2 condensation on the foam surface. Figure 6-5 shows a 2 mm inner diameter diamond hollow sphere that was completely filled with a 30 mg/cm^3 p(DCPD) foam and gelled stationary. The shell was then kept in a closed 20 ml vial containing iodine crystals for three days and subsequently analyzed.

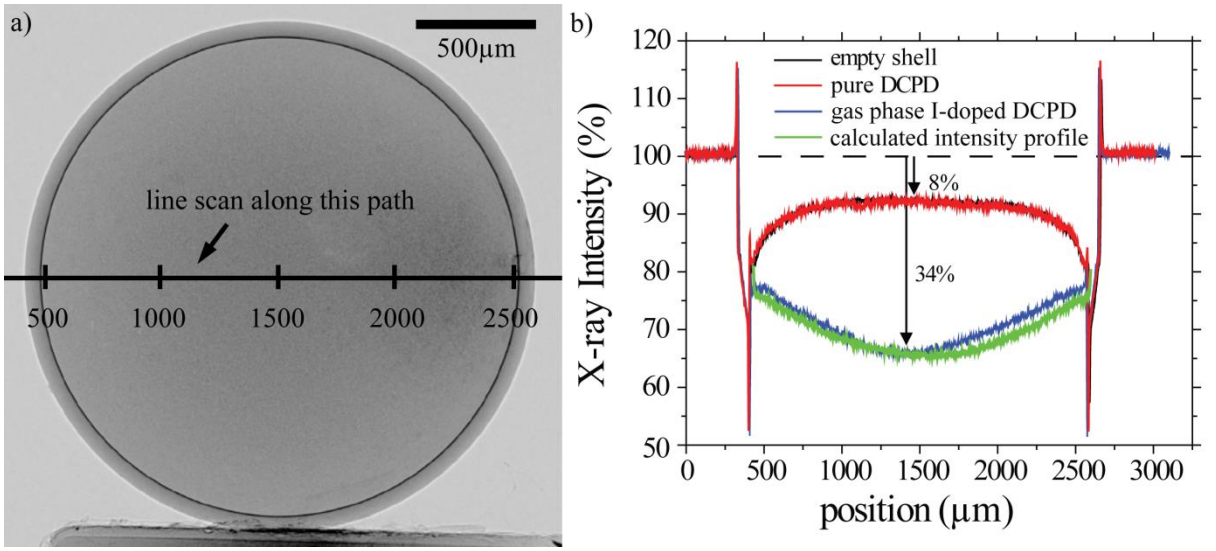

Figure 6-5: Gas phase doping of foam shells: a) Cross-sectional radiographic image of a 2 mm diamond sphere completely filled with a p(DCPD) foam (30 mg/cm^3, 0.1 wt.% catalyst, gelled stationary for ~7 hours, and gas phase iodine doped for three days) after supercritical drying. b) Line intensity profile of an empty shell (black curve), a shell completely filled with foam before (red) and after gas phase iodine doping (blue), as well as the predicted intensity profile. The intensity change from an undoped foam in a shell is indistinguishable from an empty shell, but changes significantly for a doped foam. (image credit: K. J. Wu, LLNL)

Nondestructive X-ray radiography characterization allowed to assess the quality of the doped foam in the shell using line intensity scans along the equator of the cross-sectional radiographic image. At first, an empty shell was imaged to measure the X-ray's intensity change during characterization (Figure 6-5 b), black curve). The intensity changes by roughly 8% for a 2 mm diamond sphere with a wall thickness of 30 µm. As previously discussed in chapter 4.2, filling the same shell with an undoped

30 mg/cm^3 p(DCPD) foam reveals no change in intensity during the line scan (red curve) as the undoped foam exhibits too little X-ray contrast to be detected. After three days of gas phase iodine doping, the line scan (blue curve) shows a significant change in intensity from 8% attenuation to 34%. The calculated intensity profile assumes uniform doping of the completely filled shell and is in good agreement with the experimentally observed intensity profile. This makes doping a viable asset for nondestructive characterizations of foam coatings in hollow spheres if an undoped foam layer does not provide enough attenuation.

However, the control over concentration and distribution of the dopant in the shell was very limited during halogenation of the unsaturated pDCPD backbone. After liquid phase iodine doping, for example, the solvent still needs to be removed and, as outlined above, in the majority of the samples most of the iodine is being washed out with the solvent, which changes the dopant's concentration in the foam. Additionally, the distribution of the dopant depends on diffusion kinetics in the porous polymer, which can lead to unevenly doped foam layers.
Therefore, a different, more deterministic approach was explored: copolymerizing the pDCPD with functionalized monomers.

6.1.2. Copolymerization with functionalized monomers

To deterministically incorporate high-Z elements into polydicyclopentadiene aerogels, different functionalized comonomers with the desired high-Z element have been developed by our group. Two of the monomers that were developed, bis-iodo-norbornene (NB-I_2) and tin-norbornene (NB-Sn), are shown in Figure 6-6. The synthesis is described in great detail by Kim et al.[14]

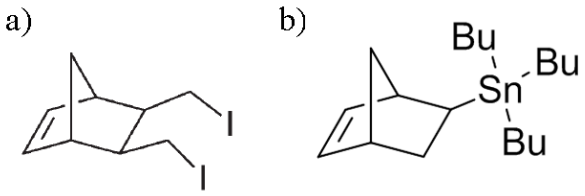

Figure 6-6: Functionalized comonomers that were synthesized by our group: a) bis-iodo-norbornene monomer (NB-I_2) and b) tin-norbornene (NB-Sn)

Similarly, a tin containing monomer (NB-Sn)[253-255] can be of interest as an aerogel layer containing tin in a hollow sphere could potentially help monitoring experimental conditions in nuclear fusion experiments.[14] These functionalized monomers (NB-I_2 and NB-Sn) can be incorporated into the pDCPD polymeric structure using a ring opening metathesis polymerization (ROMP) reaction, yielding p(DCPD-r-NB-I_2) and p(DCPD-NB-r-NB-Sn) aerogels as illustrated in Figure 6-7.

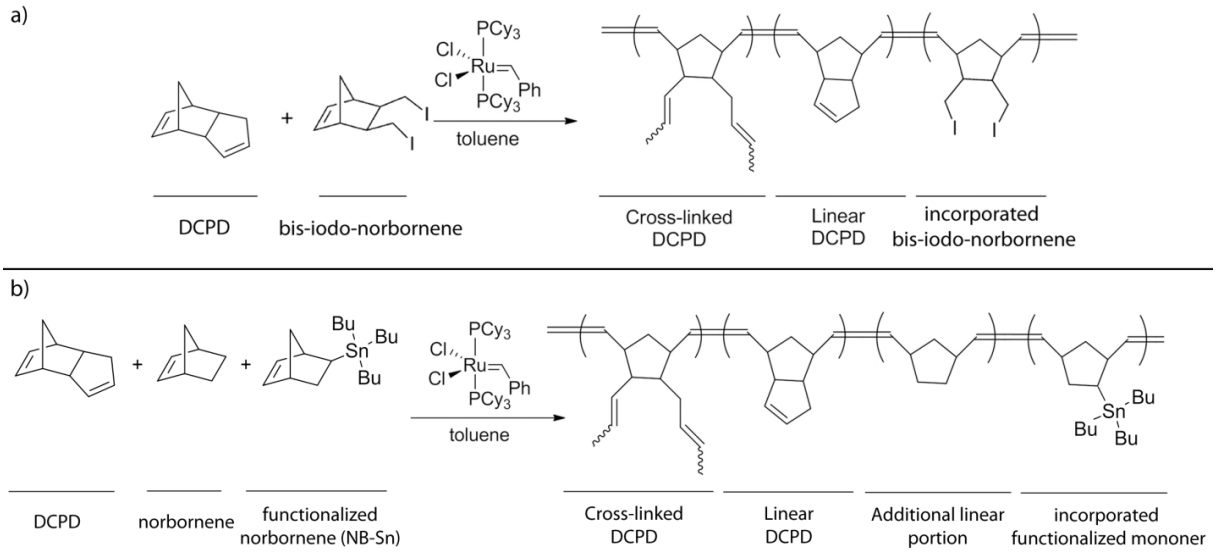

Figure 6-7: Copolymerization approach to iodine and tin doped pDCPD: a) Iodine doped aerogels can be prepared using a ring opening metathesis polymerization (ROMP) reaction of DCPD and bis-iodo-norbornene (NB-I_2) in toluene. b) Similarly, tin doped aerogels can be prepared using a ring opening metathesis polymerization (ROMP) reaction of DCPD, norbornene (NB), and tin-norbornene (NB-Sn) in toluene.

Scanning electron microscopy images of p(DCPD-r-NB-I_2) aerogels (Figure 6-8) show that they have the same structure of randomly oriented fibers as the pure pDCPD and the p(DCPD-r-NB) aerogels (compare to Figure 2-16 and Figure 2-17).

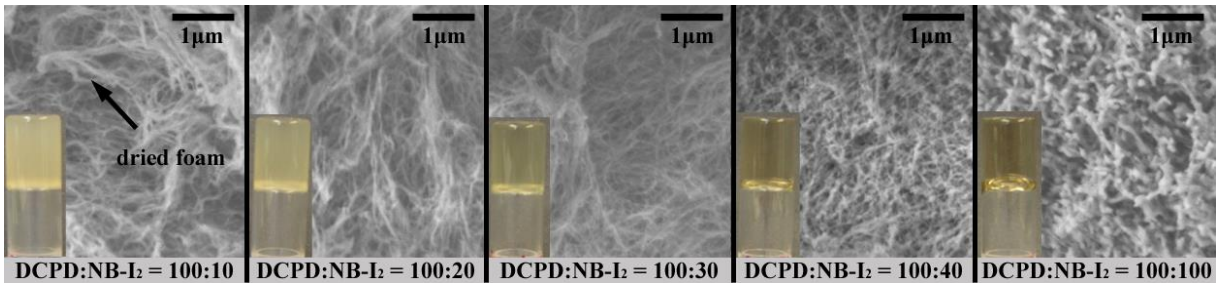

Figure 6-8: Scanning electron microscopy images of p(DCPD-r-NB-I_2) aerogels (50 mg/cm^3, 0.2 wt.% catalyst) with increasing bis-iodo-norbornene concentration. p(DCPD-r-NB-I_2) aerogels copolymerized with NB-I_2 have the same web-like morphology as p(DCPD-r-NB) aerogels. With higher bis-iodo-norbornene concentration, the length of the individual fibers decreases and the diameter of the individual fibers increases. The inlet in the picture for each bis-iodo-norbornene concentration shows a photograph of the respective p(DCPD-r-NB-I_2) wet gel in a 2 ml vial.

Similarly, to the p(DCPD-r-NB) aerogels, with a higher bis-iodo-norbornene concentration the length of the individual fibers decreases. However, with an increasing concentration of bis-iodo-norbornene the diameter of the individual fibers increases significantly. (Figure 6-8)

Rutherford backscattering spectrometry experiments on free standing pieces of 50 mg/cm^3 p(DCPD-r-NB-I_2) (DCPD : NB-I_2 = 100 : 5) foams copolymerized with bis-iodo-norbornene revealed a composition of $C_{10}H_{12}I_{0.15}$, which corresponds to an iodine concentration of ~0.81 at.% in the sample.[14] Further experiments showed that the measured iodine concentration in aerogels with different mixing ratios of DCPD and NB-I_2 is in excellent agreement with the predicted iodine concentration,[14] allowing a freely tunable, deterministic control of the incorporation of high-Z elements in polymers.

To test the X-ray absorption contrast in dependence of NB-I incorporation, 25 mg/cm^3 aerogel cubes copolymerized with different amounts of NB-I (25 mg/cm^3 DCPD-r-NB-r-NB-I with a ratio of (DCPD : NB : NB-I) = (100 : 15 : x), and x = percentage of NB-I, 0.2 wt.% catalyst) were prepared in a glass mold (1 cm x 1 cm x 1 cm) with two open sides. (Figure 6-9a)

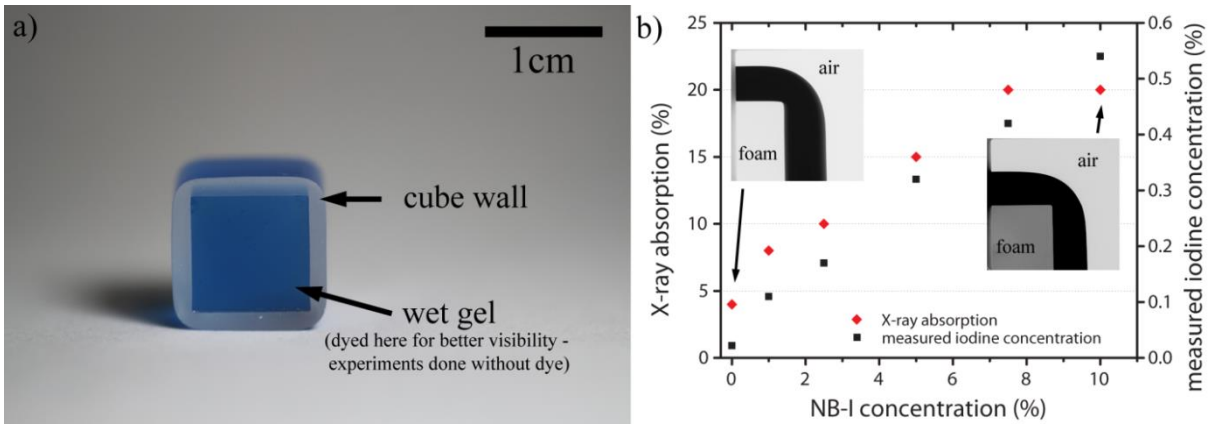

Figure 6-9: Aerogels copolymerized with different amounts of NB-I (25 mg/cm^3 DCPD-r-NB-r-NB-I with a ratio of (DCPD:NB:NB-I) = (100:15:x) and x = percentage of NB-I, 0.2 wt.% catalyst) show increasing X-ray attenuation depending on the doping level. a) Photograph of the wet gel in the glass mold with two open sides. The gel was dyed for the photograph to increase visibility; the X-ray attenuation experiments and RBS measurements were done without any dye. b) X-ray absorption and measured iodine concentration as a function of added NB-I copolymer. The measured iodine concentration scales almost linearly with the added copolymer, which influences the X-ray absorption.

The X-ray attenuation was measured for the different amounts of added copolymer after drying the aerogel in the cube with the imaging axis going through the two open sides of the cube. For the undoped 25 mg/cm^3 aerogel, the X-ray absorption contrast was 4%, while it increased to 10% for a NB-I copolymer concentration of 2.5%. For 5% NB-I, the X-ray absorption increased to 15% and, as Figure 6-9b illustrates, kept increasing almost linearly with increasing copolymer concentration. Rutherford backscattering spectrometry experiments confirmed the linear behavior of iodine concentration as a function of NB-I copolymer concentration, demonstrating that this approach provides precise control over the doping level in pDCPD aerogels even at very low dopant concentrations. The respective 50 mg/cm^3 p(DCPD-r-NB-r-NB-I_2) wet gels in which the norbornene was gradually substituted for bis-iodo-norbornene are shown in Figure 6-10.

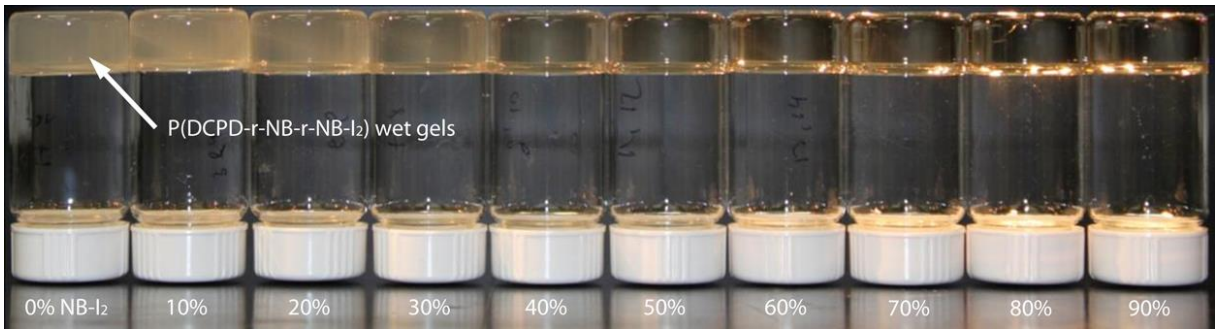

Figure 6-10: Photographs of 50 mg/cm^3 p(DCPD-r-NB-r-NB-I_2) wet gels in which the norbornene was gradually substituted for bis-iodo-norbornene: 50 mg/cm^3 p(DCPD-r-NB-r-NB-I_2) were prepared with 10wt. % NB (containing x% NB-I_2, y% NB), and 0.1wt. % catalyst in which the norbornene was gradually substituted for bis-iodo-norbornene. The wet gels become more transparent as the bis-iodo-norbornene concentration increases.

Extensive tests in 2 mm inner diameter hollow spheres revealed that for 50 mg/cm^3 p(DCPD-r-NB-I_2) wet gels, uniform coatings could be obtained with minimal ratios of DCPD to NB-I_2 = 100:5. (Figure 6-11)

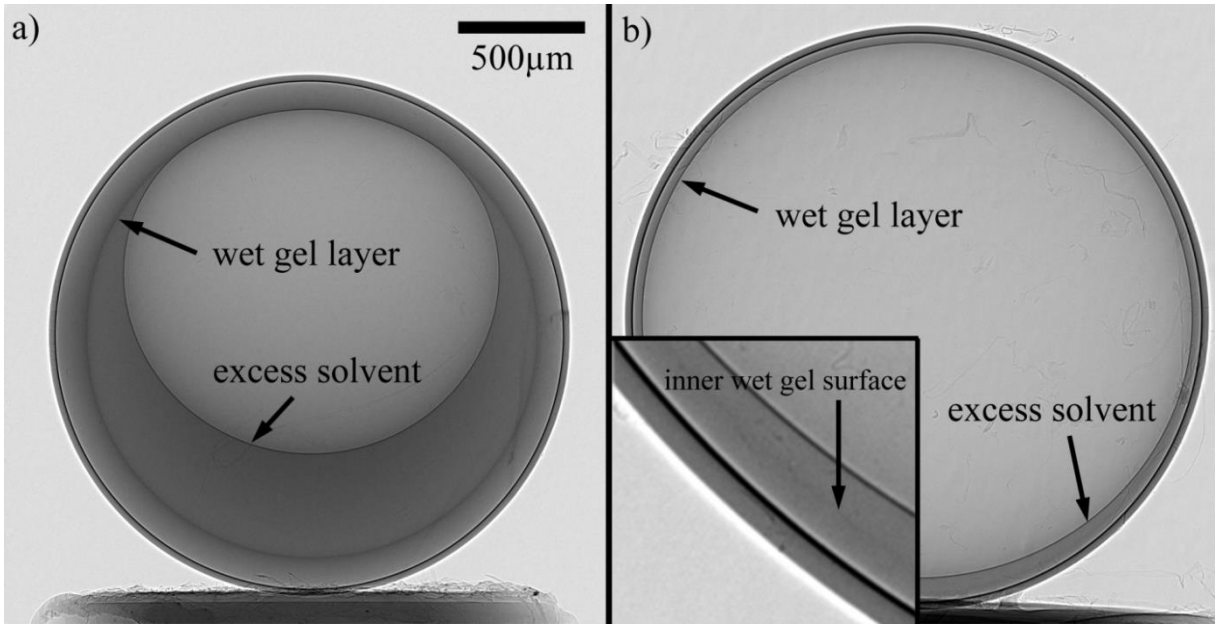

Figure 6-11: Cross-sectional radiographic image of 2 mm diamond spheres coated with p(DCPD-r-NB-I_2) wet gel layers: a) 50 mg/cm^3 p(DCPD-r-NB-I_2), 5%NB-I_2, 0.2 wt.% catalyst, filled with Δp = 374.3 Torr, and uniaxially rotated at 1.95 rpm for 24 h. The coating appears to be homogeneous and smooth, albeit there is some excess solvent present at the bottom of the shell. b) 50 mg/cm^3 p(DCPD-r-NB-I_2), 5%NB-I_2, 0.2 wt.% catalyst, filled with Δp = 103.8 Torr, and uniaxially rotated at 1.95 rpm for 22 h. The coating of the inner surface of the hollow sphere appears to be very homogeneous.

The doped wet gel layer is clearly distinguishable from the excess solvent in the capsule and appears to be homogeneous, smooth, and uniform in thickness for different layer thicknesses. In both wet gel lined capsules, hair-like features can be seen on the shell, which were deposited during capsule handling and are on the outside of the shell.

Removing the solvent out of the hollow sphere by supercritical drying with carbon dioxide (see chapter 5) leaves a uniform p(DCPD-r-NB-I_2) doped foam layer. For example, the wet gel layer shown in Figure 6-11b) remains intact after supercritical drying yielding a uniform doped foam layer in a hollow sphere as illustrated in Figure 6-12.

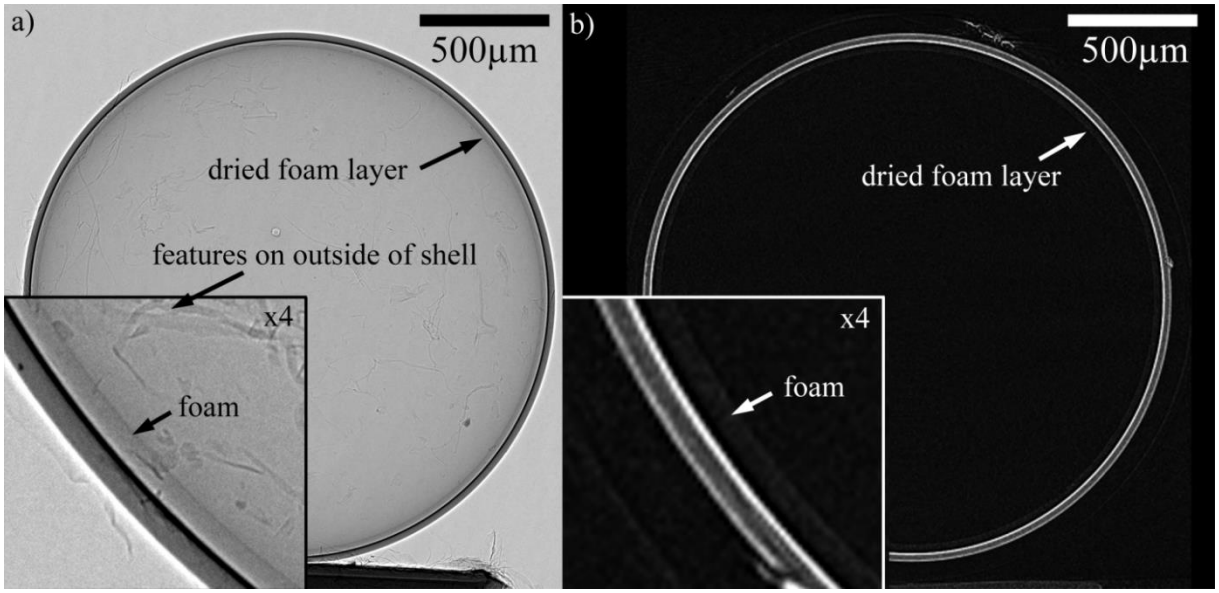

Figure 6-12: Cross-sectional radiographic image of 2 mm diamond sphere coated with a p(DCPD-r-NB-I_2) foam layer: a) 50 mg/cm³ p(DCPD-r-NB-I_2), 5%NB-I_2, 0.2 wt.% catalyst, filled with Δp = 103.8 Torr, and uniaxially rotated at 1.95 rpm for 22h. The coating of the inner surface of the hollow sphere appears to be very homogeneous. b) Three dimensional computerized tomography (CT) scan of the same p(DCPD-r-NB-I_2) foam coating inside of the 2 mm diamond sphere. The homogeneity of and within the foam layer is evident in the CT scan.

Since the comprehensive three dimensional foam structure is not known from the radiographs alone, a computerized tomography (CT) scan of the foam only was done to help characterize the doped foam layer. The foam appears to be uniform in the shell and shows no signs of heterogeneity, demonstrating that a uniformly doped, dried foam shell can be produced using a copolymerization approach with functional monomers. Different combinations of bis-iodo-norbornene concentrations, layer thickness, and densities were successfully tested yielding uniform layers.

As mentioned above, aerogel layers containing tin in hollow spheres could potentially help monitoring experimental conditions in nuclear fusion experiments.[14] Therefore, a tin norbornene monomer (NB-Sn) was synthesized[14] and then mixed with DCPD and norbornene in toluene to prepare tin containing aerogel coatings. The tin doped aerogels were prepared using a ring opening metathesis polymerization (ROMP) reaction of DCPD, norbornene (NB), and tin-norbornene (NB-Sn) in toluene. (Figure 6-7 b)

Scanning electron microscopy images of the p(DCPD-r-NB-r-NB-Sn) aerogels (Figure 6-13) show that they have the same structure of randomly oriented fibers as the pure pDCPD and the p(DCPD-r-NB) aerogels (compare to Figure 2-6 and Figure 2-16).

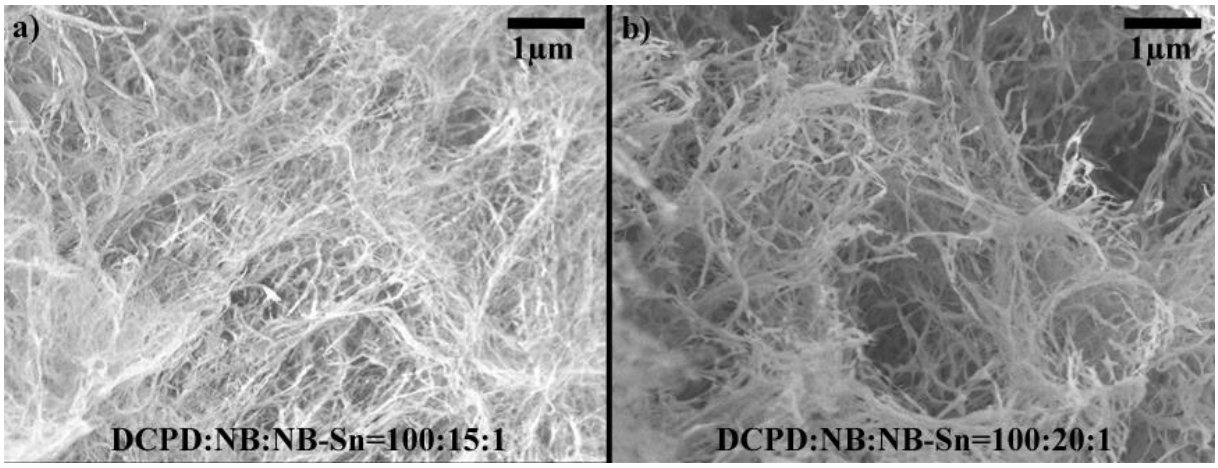

Figure 6-13: Scanning electron microscopy image of p(DCPD-r-NB-r-NB-Sn) aerogels (35 mg/cm^3, 0.2 wt.% catalyst) with different norbornene concentration. p(DCPD-r-NB-r-NB-Sn) aerogels copolymerized with NB-Sn have the same web-like morphology as p(DCPD-r-NB) aerogels. As seen above, with higher norbornene concentration the length of the individual fibers decreases and the diameter of the individual fibers increases. (SEM taken by: Sung Ho Kim, LLNL)

As expected, with an increasing norbornene concentration the length of the individual fibers decreases and the diameter of the individual fibers slightly increases. Pure norbornene was added in all copolymerization experiments with tin doped aerogels as the gel point did not increase with the sole addition of NB-Sn. Adding the norbornene ensured a high gel point viscosity, which increased the gel's robustness during coating experiments. For a 50 mg/cm^3 tin doped p(DCPD-r-NB-r-NB-Sn) aerogel with a ratio of DCPD : NB : NB-Sn = 100 : 10 : 1, the final composition measured by Rutherford backscattering spectrometry is $C_{10}H_{12}Sn_{0.015}$, which corresponds to ~0.068 at.% of Sn in the polymer backbone.[14]

Extensive testing showed that a successful ratio for uniform tin doped 50 mg/cm^3 p(DCPD-r-NB-r-NB-Sn) aerogel coating is DCPD:NB:NB-Sn=100:5:0.7 and DCPD : NB : NB-Sn = 100 : 5 : 0.8. Both ratios lead to uniform and homogeneous coating layers in hollow spheres.

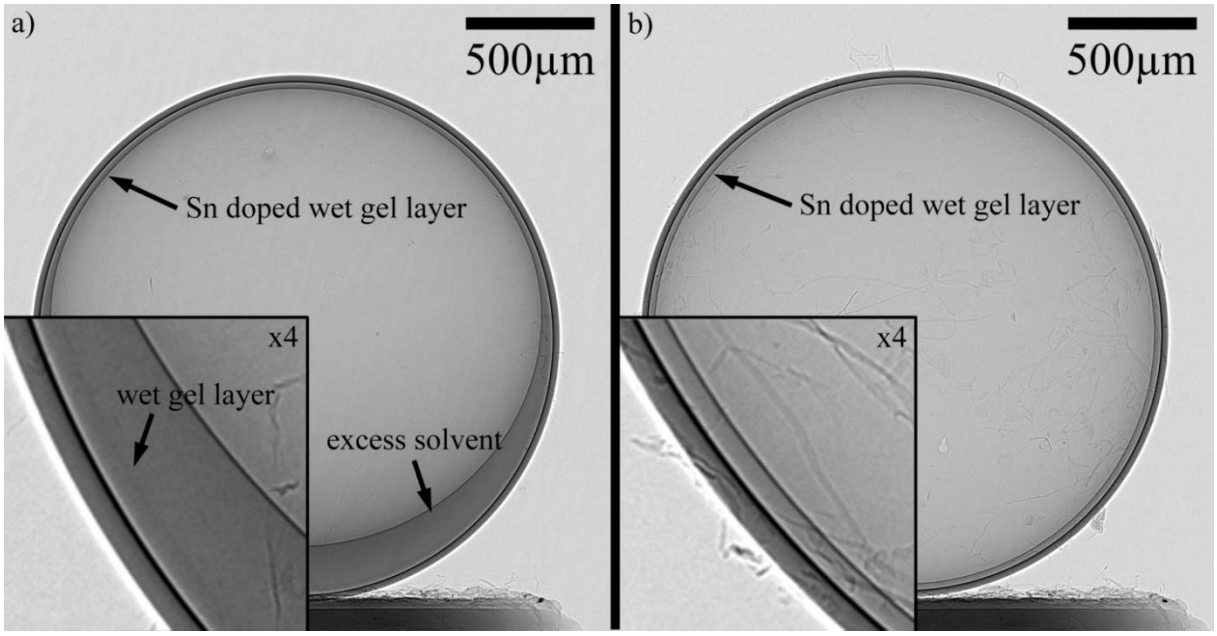

Figure 6-14: Cross-sectional radiographic image of 2 mm diamond spheres coated with p(DCPD-r-NB-r-NB-Sn) wet gel layers: a) 50 mg/cm^3 p(DCPD-r-NB-r-NB-Sn), 5% NB, 0.7% NB-Sn, 0.2 wt.% catalyst, filled with Δp = 106.1 Torr, and uniaxially rotated at 1.95 rpm for 23 h. The coating appears to be homogeneous and smooth, albeit some excess solvent present at the bottom of the shell. b) 50 mg/cm^3 p(DCPD-r-NB-r-NB-Sn), 5% NB, 0.8% NB-Sn, 0.2 wt.% catalyst, filled with Δp = 100.0 Torr, and uniaxially rotated at 1.95 rpm for 23 h. The coating of the inner surface of the hollow sphere appears to be homogeneous and uniform.

In summary, copolymerizing the aerogel with functionalized monomers offers several advantages as it provides precise and deterministic control of the dopant level in the pDCPD polymers and their coatings. This method is especially suited for low doping levels of the polymer and has the benefit of yielding very uniform layers in spherical shells.

Chapter 7: Conclusions and Outlook

In conclusion, ultra-low density coatings were fabricated inside hollow spheres that meet the required specifications to be used in indirect drive ICF experiments based on spin-coating the inside of prefabricated ablator shells with a polymer precursor solution and subsequent removal of the solvent. The main results of this work can be summarized as follows:

Synthesizing polymer foams on spherical surfaces requires detailed understanding of the fundamental chemical polymerization process. By characterizing the rheological properties and the evolution of the storage shear modulus G' and loss shear modulus G" during polymerization, it was possible to understand how the polymer is formed and how the density of the aerogel influences the gel point. Coating a rotating object with a uniform layer of the liquid precursor solution results in shear forces due to the velocity gradient within the liquid that is caused by friction and gravity. The shear forces can lead to non-uniform coatings, but by adapting a copolymerization approach using a linear crosslinker and characterizing the rheological properties of the resulting polymer it was possible to control and manipulate the rheological properties and the strength at the sol-gel transition and, therefore, drastically increase the uniformity of the coatings in hollow spheres. The resulting aerogels formed with this copolymerization approach have similar mechanical properties to many other low-density materials.

Injecting precursor solution reproducibly into a hollow sphere with 0.01 µl precision can be accomplished by using a pressure gradient method that is almost independent of the fill hole diameter. By doing *in situ* real-time radiography on rotating shells filled with the precursor solution, the distribution of liquids in rotating hollow spherical shells was monitored. The experiments confirm a surprising prediction made by computational fluid dynamics simulations, namely, that uniaxial rotation can result in the formation of extremely uniform thin film layers in hollow spherical shells if the right combination of the precursor's viscosity and rotational velocity is used. With this knowledge highly uniform porous polymer films were fabricated inside 2 mm inner diameter high density carbon shells. The uniaxial coating process seems to be highly

scalable and can easily be modified to generate porous coatings of different densities and thicknesses as well as using hollow spheres with different inner volumes.

Once the uniform wet gel layer inside of the hollow sphere is formed, the solvent needs to be removed from the pores of the polymer. A solvent exchange and a drying method for the aerogel was further developed using acetone and supercritical carbon dioxide which was then implemented and optimized to produce foam-lined ICF targets. Several improvements to the process were considered and investigated to further optimize the drying process. Different techniques to either prevent wet gel from forming in the fill hole altogether, clearing the fill hole after a plug has been formed, and stimulate a faster solvent exchange rate in and out of the capsule were explored.

Two different approaches to introduce dopants into low-density polymer films in hollow spheres were discussed. Halogenation of the unsaturated DCPD backbone using iodine did not yield the required control over concentration and distribution of the dopant in the shell. However, copolymerizing the aerogel with functionalized monomers while casting the foam in the shell provides precise and deterministic control of the dopant level in the pDCPD polymers and their coatings. This method is especially suited for low doping levels of the polymer and yielded very uniform doped layers in hollow spherical shells.

The experiments in particular that lead to these conclusions were:

- Initial rheology measurements during the polymerization of DCPD/toluene wet gels with different densities (25, 30, 50, 80, 100, 250mg/cc) allowed to find the optimal combination of catalyst concentration, gel time, and gel point viscosity to achieve thin film coatings.
- A theoretical and experimental analysis of the precursor solution's shear forces under rotation showed that an elevated viscosity at the gel point can reduce the shear that the pDCPD gel experiences during polymerization. Using this knowledge, a copolymerization approach with norbornene was used, which resulted in more homogeneous wet gel films in hollow spheres.
- Subsequent rheology measurements during the polymerization of the copolymerized wet gels with different densities (35, 80, 100 mg/cc) and

different norbornene concentrations (0, 2.5, 5, 10%) allowed to compare the viscosity at the gel point for each composition and to find optimal concentrations of norbornene for different densities.

- SEM imaging of aerogels with different densities and concentrations of norbornene enabled the study of morphology and microscopic structure.
- The elastic and inelastic behavior of the aerogels was characterized with spherical nanoindentation and showed how the elastic modulus increases as a function of density. It was shown that the scaling is comparable to various other man-made ultra-low density materials.
- Once the optimal composition for the precursor solution was found, it was shown that a pressure differential filling setup has the required accuracy to precisely control the layer thickness in a hollow spherical shell and has the advantage that is can easily be modified for different shell sizes and volumes.
- A slight modification of the pressure filling setup was developed to completely fill hollow shell with precursor solution and foams.
- *In-situ* real-time radiography was then used to monitor the distribution of liquids in rotating hollow spherical shells. The experiments confirmed a surprising prediction made by computational fluid dynamics simulations, namely, that uniaxial rotation can result in the formation of extremely uniform thin film layers in hollow spherical shells if the right combination of the liquid's viscosity and rotational velocity are used.
- To remove the solvent from the wet gel and achieve ultra-low density aerogels, the time for complete solvent exchange of uniform wet gels in hollow spheres was approximated analytically and the diffusion constant of solvents diffusing through wet gels was determined. This allowed to establish a lower time limit for the diffusion driven process.
- A supercritical drying process with liquid carbon dioxide was further developed to successfully remove the solvent from the porous network.
- Drying experiments on bulk pieces of p(DCPD-r-NB) aerogels allowed assessing the strength of different precursor compositions during the supercritical drying process. Different combinations of norbornene and catalyst concentration were

identified that do not shrink or collapse during solvent exchange and supercritical drying.

- Different solvents were tested and, in the case for producing foam layers in hollow spheres, solvent exchange from toluene to acetone to liquid carbon dioxide produced the most reproducible results.
- To further improve the drying process, an additively manufactured plug was developed that would prevent wet gel formation in the fill hole during the coating process. Subsequently, a process was developed to clear the fill hole mechanically by inserting a sharp needle-like object into it, which has the potential to remove the wet gel from the fill hole and accelerate the solvent exchange.
- An accelerated solvent exchange technique was developed that forces liquid in and out of wet gel layered shells by applying a pressure gradient. This has the potential to vastly decrease solvent exchange time.
- Lastly, two different methods of doping foam lined shells were explored: halogenation of the unsaturated DCPD backbone using iodine or bromine and copolymerizing the aerogel with functionalized monomers. Uniform doped foam liners were casted in hollow spheres using both methods; however, the copolymerization approach yielded the most reproducible results.

The combination of these experiments and the successful development of this wetted foam target design have a broad impact for the inertial confinement fusion community and beyond. The target design, for example, was recently used to study new ignition regimes with the first ever liquid deuterium-tritium (DT) fuel layer implosion at the National Ignition Facility, Lawrence Livermore National Laboratory.[244, 256] Beyond that the foam layer in hollow spherical shells enables the study of hot spot formation and evolution of plasma conditions in nuclear physics experiments. Functional, uniform thin film coatings on spherical surfaces are also increasingly being used for spherical reflectors[1], integrating spheres[2-3], and site[4-5] or time specific[6] drug delivery. More uniform coatings in all applications have the potential to increase performance and decrease error and performance deterioration.

References

1. L. TINGYE, "A study of spherical reflectors as wide-angle scanning antennas," *Antennas and Propagation, IRE Transactions on*, **7**, *3*, 223-226 (1959).
2. J. A. JACQUEZ; H. F. KUPPENHEIM, "Theory of the Integrating Sphere," *J. Opt. Soc. Am.*, **45**, *6*, 460-466 (1955).
3. D. G. GOEBEL, "Generalized Integrating-Sphere Theory," *Appl. Optics*, **6**, *1*, 125-128 (1967).
4. D. FITZPATRICK et al., "Rapid profiling of enteric coated drug delivery spheres via Broadband Acoustic Resonance Dissolution Spectroscopy (BARDS)," *Analyst*, **139**, *5*, 1000-1006 (2014).
5. N. KÁLLAI et al., "Evaluation of Drug Release From Coated Pellets Based on Isomalt, Sugar, and Microcrystalline Cellulose Inert Cores," *AAPS PharmSciTech*, **11**, *1*, 383-391 (2010).
6. P. ROY; A. SHAHIWALA, "Multiparticulate formulation approach to pulsatile drug delivery: Current perspectives," *Journal of Controlled Release*, **134**, *2*, 74-80 (2009).
7. H. GOEHLER et al., "Functionalized Metallic Hollow Sphere Structures," *Advanced Engineering Materials*, **16**, *3*, 335-339 (2014).
8. R. A. SACKS; D. H. DARLING, "DIRECT DRIVE CRYOGENIC ICF CAPSULES EMPLOYING D-T WETTED FOAM," *Nucl. Fusion*, **27**, *3*, 447-452 (1987).
9. M. TAKAGI et al., "DEVELOPMENT OF FOAM SHELL WITH PLASTIC ABLATOR FOR CRYOGENIC LASER FUSION TARGET," *Journal of Vacuum Science & Technology a-Vacuum Surfaces and Films*, **11**, *5*, 2837-2845 (1993).
10. A. NIKROO et al., "Fabrication and properties of overcoated resorcinol-formaldehyde shells for omega experiments," *Fusion Sci. Technol.*, **45**, *2*, 84-89 (2004).
11. R. R. PAGUIO et al. "Fabrication Capabilities for Spherical Foam Targets Used in ICF Experiments", *Fusion Engineering 2005, Twenty-First IEEE/NPS Symposium on*, Sept. 2005; (2005).
12. J. BIENER et al., "A new approach to foam-lined indirect-drive NIF ignition targets," *Nucl. Fusion*, **52**, *6*, (2012).

13. R. E. OLSON; R. J. LEEPER, "Alternative hot spot formation techniques using liquid deuterium-tritium layer inertial confinement fusion capsules," *Phys. Plasmas*, **20**, *9*, 092705 (2013).
14. S. H. KIM et al., "Deterministic Control over High-Z Doping of Polydicyclopentadiene-Based Aerogel Coatings," *ACS Applied Materials & Interfaces*, **5**, *16*, 8111-8119 (2013).
15. C. DAWEDEIT et al., "Tuning the rheological properties of sols for low-density aerogel coating applications," *Soft Matter*, **8**, *13*, 3518-3521 (2012).
16. C. LUSTIG-GUSTAFSSON et al., "The influence of water content and drug solubility on the formulation of pellets by extrusion and spheronisation," *European Journal of Pharmaceutical Sciences*, **8**, *2*, 147-152 (1999).
17. J. BIENER et al., "Diamond spheres for inertial confinement fusion," *Nucl. Fusion*, **49**, *11*, (2009).
18. P. C. KNEE, "Investigation of the uniformity and ageing of integrating spheres," *Analytica Chimica Acta*, **380**, *2–3*, 391-399 (1999).
19. L. FELTON, "Characterization of coating systems," *AAPS PharmSciTech*, **8**, *4*, 258-266 (2007).
20. L. HELLÉN; J. YLIRUUSI, "Process variables of instant granulator and spheroniser: III. Shape and shape distributions of pellets," *International Journal of Pharmaceutics*, **96**, *1–3*, 217-223 (1993).
21. T. WATARI et al., "Rayleigh-Taylor instability growth on low-density foam targets," *Phys. Plasmas*, **15**, *9*, (2008).
22. S. ENSSLIN et al., "Modulating pH-independent release from coated pellets: Effect of coating composition on solubilization processes and drug release," *European Journal of Pharmaceutics and Biopharmaceutics*, **72**, *1*, 111-118 (2009).
23. M. J. EDWARDS et al., "Progress towards ignition on the National Ignition Facility," *Phys. Plasmas*, **20**, *7*, 10 (2013).
24. B. A. REMINGTON et al., "From microjoules to megajoules and kilobars to gigabars: Probing matter at extreme states of deformation," *Phys. Plasmas*, **22**, *9*, 090501 (2015).

25. R. F. SMITH et al., "Ramp compression of diamond to five terapascals," *Nature*, **511**, *7509*, 330-333 (2014).
26. J. D. LAWSON, "Some criteria for a power producing thermonuclear reactor," *Proc. Phys. Soc. B*, **70**, 2-1010 (1957).
27. J. D. LAWSON, "Power from Nuclear Fusion," *Nature*, **180**, *4590*, 780-782 (1957).
28. M. A. ABDOU et al., "Conceptual design of a Tokamak reactor," *Texas Symposium on the Technology of Controlled Thermonuclear Fusion Experiments and the Engineering Aspects of Fusion Reactors. (Abstracts only received)*, 45-4545 (1972).
29. L. SPITZER, "THE STELLARATOR CONCEPT," *Phys. Fluids*, **1**, *4*, 253-264 (1958).
30. C. OLSON, "Development path for Z-pinch IFE," *Fusion Sci. Technol.*, **47**, *3*, 633-640 (2005).
31. M. E. CUNEO et al., "Progress in symmetric ICF capsule implosions and wire-array z -pinch source physics for double-pinch-driven hohlraums," *Plasma Physics and Controlled Fusion*, **48**, *2*, R1 (2006).
32. J. NUCKOLLS et al., "Laser Compression of Matter to super-high densities - thermonuclear (CTR) applications," *Nature*, **239**, *5368*, 139-& (1972).
33. J. NUCKOLLS et al., "LASER IMPLOSION OF DT TO DENSITIES GREATER-THAN 1000 G/CM3 - OPTIMUM PULSE SHAPE - FUSION YIELD VS LASER ENERGY," *Bulletin of the American Physical Society*, **17**, *11*, 1034-1035 (1972).
34. T. BRAUN. Development of aerogel-lined targets for inertial confinement fusion experiments. 2013.
35. S. HAAN et al., "Update on NIF indirect drive ignition target fabrication specifications," *Fusion Sci. Technol.*, **45**, *2*, 69-73 (2004).
36. J. MILOVICH et al. "Hohlraum design for doped-HDC ablator ignition capsule", *APS Meeting Abstracts*, (2013).
37. O. JONES et al. "Hohlraum fill gas density scaling of x-ray drive, symmetry, and laser coupling backscatter in 6.72-mm NIF hohlraums", *APS Meeting Abstracts*, (2014).

38. D. CALLAHAN et al. "Hohlraum Design for a High Foot, High Adiabat Implosion on NIF", *APS Meeting Abstracts*, (2013).
39. Y. V. AFANASEV et al., "THERMONUCLEAR LASER TARGETS WITH LARGE ENERGY GAIN COEFFICIENTS," *Nucl. Fusion*, 119-121 (1975).
40. R. J. MASON; R. L. MORSE, "TAMPED THERMONUCLEAR BURN OF DT-MICROSPHERES," *Nucl. Fusion*, **15**, *5*, 935-938 (1975).
41. R. J. MASON; R. L. MORSE, "HYDRODYNAMICS AND BURN OF OPTIMALLY IMPLODED DEUTERIUM-TRITIUM SPHERES," *Phys. Fluids*, **18**, *7*, 814-828 (1975).
42. B. J. KOZIOZIEMSKI et al., "DEUTERIUM-TRITIUM FUEL LAYER FORMATION FOR THE NATIONAL IGNITION FACILITY," *Fusion Sci. Technol.*, **59**, *1*, 14-25 (2011).
43. S. W. HAAN et al., "Design and simulations of indirect drive ignition targets for NIF," *Nucl. Fusion*, **44**, *12*, S171 (2004).
44. D. S. CLARK et al., "Plastic ablator ignition capsule design for the National Ignition Facility," *Physics of Plasmas (1994-present)*, **17**, *5*, 052703 (2010).
45. R. MCEACHERN et al., "Sputter-deposited Be ablators for NIF target capsules," *Fusion Sci. Technol.*, **31**, *4*, 435-441 (1997).
46. D. C. WILSON et al., "The development and advantages of beryllium capsules for the National Ignition Facility," *Physics of Plasmas (1994-present)*, **5**, *5*, 1953-1959 (1998).
47. J. BIENER et al., "Diamond ablators for inertial confinement fusion," *Fusion Sci. Technol.*, **49**, *4*, 737-742 (2006).
48. A. MACKINNON et al., "High-density carbon ablator experiments on the National Ignition Facilitya)," *Physics of Plasmas (1994-present)*, **21**, *5*, 056318 (2014).
49. J. ROSS et al., "High-density carbon capsule experiments on the national ignition facility," *Physical Review E*, **91**, *2*, 021101 (2015).
50. T. R. DITTRICH et al., "Capsule design for the National Ignition Facility," *Laser and Particle Beams*, **17**, *2*, 217-224 (1999).
51. S. HAAN et al., "Design and simulations of indirect drive ignition targets for NIF," *Nucl. Fusion*, **44**, *12*, S171 (2004).

52. S. HAAN et al., "Update on specifications for NIF ignition targets," *Fusion Sci. Technol.*, **51**, *4*, 509-513 (2007).
53. J. LINDL, "Development of the indirect-drive approach to inertial confinement fusion and the target physics basis for ignition and gain," *Phys. Plasmas*, **2**, *11*, 3933-4024 (1995).
54. J. D. LINDL et al., "The physics basis for ignition using indirect-drive targets on the National Ignition Facility," *Phys. Plasmas*, **11**, *2*, 339-491 (2004).
55. A. CHERNOV et al., "Single crystal growth and formation of defects in deuterium-tritium layers for inertial confinement nuclear fusion," *Applied Physics Letters*, **94**, *6*, 064105 (2009).
56. B. KOZIOZIEMSKI et al., "Plastic deformation of solid hydrogen in fusion targets," *J. Appl. Phys.*, **105**, *9*, 093512 (2009).
57. J. MOODY et al. "Status of cryogenic layering for NIF ignition targets", *Journal de Physique IV (Proceedings)*, EDP sciences (2006).
58. T. J. B. COLLINS et al., "One-megajoule, wetted-foam target-design performance for the National Ignition Facilitya)," *Phys. Plasmas*, **14**, *5*, 056308 (2007).
59. R. COOK et al., "LOW-DENSITY–FOAM SHELLS," *INERTIAL CONFINEMENT*, (1996).
60. M. TAKAGI et al., "Development of deuterated polystyrene shells for laser fusion by means of a density-matched emulsion method," *Journal of Vacuum Science & Technology A: Vacuum, Surfaces, and Films*, **9**, *4*, 2145-2148 (1991).
61. M. TAKAGI et al., "Development of foam shell with plastic ablator for cryogenic laser fusion target," *Journal of Vacuum Science & Technology A: Vacuum, Surfaces, and Films*, **11**, *5*, 2837-2845 (1993).
62. D. SCHROEN-CAREY et al., "Hollow foam microshells for liquid-layered cryogenic inertial confinement fusion targets," *Journal of Vacuum Science & Technology A: Vacuum, Surfaces, and Films*, **13**, *5*, 2564-2568 (1995).
63. N. K. KIM et al., "Fabrication of hollow silica aerogel spheres by a droplet generation method and sol--gel processing," *Journal of Vacuum Science & Technology A: Vacuum, Surfaces, and Films*, **7**, *3*, 1181-1184 (1989).

64. L. M. HAIR et al., "Low-density resorcinol–formaldehyde aerogels for direct-drive laser inertial confinement fusion targets," *Journal of Vacuum Science & Technology A*, **6**, *4*, 2559-2563 (1988).

65. F. ITO et al., "Optimization of gelation to prepare hollow foam shell of resorcinol-formalin using a phase-transfer catalyst," *Fusion Sci. Technol.*, **49**, *4*, 663-668 (2006).

66. K. NAGAI et al., "Fabrication of aerogel capsule, bromine-doped capsule, and modified gold cone in modified target for the Fast Ignition Realization Experiment (FIREX) Project," *Nucl. Fusion*, **49**, *9*, 095028 (2009).

67. C. CHEN et al. *Low-density hydrocarbon foams for laser fusion targets: Progress report, 1986*; Lawrence Livermore National Lab., CA (USA): 1987.

68. J. STREIT; D. SCHROEN, "Development of divinylbenzene foam shells for use as inertial fusion energy reactor targets," *Fusion Sci. Technol.*, **43**, *3*, 321-326 (2003).

69. B. HAENDLER et al., "Low-density hydrocarbon foams for laser fusion targets," *Lawrence Livermore National Laboratory Report, UCID-21080-87 (June 1987)*, (1988).

70. S. M. LAMBERT et al., "Fabrication of low-density foam shells from resorcinol-formaldehyde aerogel," *J. Appl. Polym. Sci.*, **65**, *11*, 2111-2122 (1997).

71. T. NORIMATSU et al., "Cryogenic targets and related technologies at ILE Osaka University," *Journal of Vacuum Science & Technology A*, **12**, *4*, 1293-1301 (1994).

72. R. PAGUIO et al., "Development and fabrication of NIF-scale resorcinol formaldehyde foam shells for ICF experiments," *Fusion Sci. Technol.*, **59**, *1*, 199-204 (2011).

73. C. CHEN et al., "Development of foam shells for cryogenic laser fusion target," *Journal of Vacuum Science & Technology A*, **9**, *2*, 340-344 (1991).

74. R. COLLIER et al., "Target developments program to prepare LMJ campaigns," *J. Phys., Conf. Ser.*, **244**, *3*, 032037 (2010).

75. C. LATTAUD et al., "Influence of a density mismatch on TMPTMA shells nonconcentricity," *J. Appl. Polym. Sci.*, **124**, *6*, 4882-4888 (2012).

76. T. SAKAIYA et al., "Ablative Rayleigh-Taylor instability at short wavelengths observed with moire interferometry," *Phys. Rev. Lett.*, **88**, *14*, (2002).
77. H. AZECHI et al., "Comprehensive diagnosis of growth rates of the ablative Rayleigh-Taylor instability," *Phys. Rev. Lett.*, **98**, *4*, (2007).
78. J. P. KNAUER et al., "Single-mode, Rayleigh-Taylor growth-rate measurements on the OMEGA laser system," *Phys. Plasmas*, **7**, *1*, 338-345 (2000).
79. C. J. PAWLEY et al., "Observation of Rayleigh-Taylor growth to short wavelengths on Nike," *Phys. Plasmas*, **6**, *2*, 565-570 (1999).
80. S. POLLAINE et al., "Spectral Analysis of ICF Capsule Surfaces," *1994 ICF Annual Report, Lawrence Livemore National Laboratory Report No. UCRL-LR-105820-94 (June, 1995)*,
81. J. M. ELSON; J. M. BENNETT, "CALCULATION OF THE POWER SPECTRAL DENSITY FROM SURFACE PROFILE DATA," *Appl. Optics*, **34**, *1*, 201-208 (1995).
82. S. H. KIM et al., "Exploration of the versatility of ring opening metathesis polymerization: an approach for gaining access to low density polymeric aerogels," *Rsc Advances*, **2**, *23*, 8672-8680 (2012).
83. J. KILKENNY et al., "From one-of-a-kind to 500,000 high quality ignition targets per day," (2004).
84. D. T. GOODIN et al., "A cost-effective target supply for inertial fusion energy," *Nucl. Fusion*, **44**, *12*, S254 (2004).
85. R. SALIGER et al., "High surface area carbon aerogels for supercapacitors," *Journal of Non-Crystalline Solids*, **225**, *1*, 81-85 (1998).
86. D. KALPANA et al., "A new class of alkaline polymer gel electrolyte for carbon aerogel supercapacitors," *Journal of Power Sources*, **157**, *1*, 621-623 (2006).
87. T. Y. WEI et al., "A cost-effective supercapacitor material of ultrahigh specific capacitances: spinel nickel cobaltite aerogels from an epoxide-driven sol–gel process," *Advanced materials*, **22**, *3*, 347-351 (2010).
88. J. MILLER et al., "Deposition of ruthenium nanoparticles on carbon aerogels for high energy density supercapacitor electrodes," *Journal of the Electrochemical Society*, **144**, *12*, L309-L311 (1997).

89. H. PRÖBSTLE et al., "Button cell supercapacitors with monolithic carbon aerogels," *Journal of Power Sources*, **105**, *2*, 189-194 (2002).
90. M. A. WORSLEY et al., "Synthesis of Graphene Aerogel with High Electrical Conductivity," *J. Am. Chem. Soc.*, **132**, *40*, 14067-14069 (2010).
91. J. BIENER et al., "Advanced carbon aerogels for energy applications," *Energy & Environmental Science*, **4**, *3*, 656-667 (2011).
92. M. MIRZAEIAN; P. J. HALL, "Preparation of controlled porosity carbon aerogels for energy storage in rechargeable lithium oxygen batteries," *Electrochimica Acta*, **54**, *28*, 7444-7451 (2009).
93. G. X. WANG et al., "Nanostructured Si–C composite anodes for lithium-ion batteries," *Electrochemistry Communications*, **6**, *7*, 689-692 (2004).
94. F. COUSTIER et al., "A 400 mAh/g Aerogel-like V 2 O 5 Cathode for Rechargeable Lithium Batteries," *Journal of The Electrochemical Society*, **145**, *5*, L73-L74 (1998).
95. H. LI et al., "High-surface vanadium oxides with large capacities for lithium-ion batteries: from hydrated aerogel to nanocrystalline VO 2 (B), V 6 O 13 and V 2 O 5," *Journal of Materials Chemistry*, **21**, *29*, 10999-11009 (2011).
96. H. GESSER; P. GOSWAMI, "Aerogels and related porous materials," *Chemical Reviews*, **89**, *4*, 765-788 (1989).
97. J. FRICKE; A. EMMERLING, "Aerogels," *J. Am. Ceram. Soc.*, **75**, *8*, 2027-2035 (1992).
98. J. M. SCHULTZ et al., "Super insulating aerogel glazing," *Solar energy materials and solar cells*, **89**, *2*, 275-285 (2005).
99. K. I. JENSEN et al., "Development of windows based on highly insulating aerogel glazings," *Journal of Non-Crystalline Solids*, **350**, 351-357 (2004).
100. H. YOKOGAWA, "„Hydrophobic Silica Aerogel," *Handbook of sol-gel science and technology*, **3**, 73-84 (2005).
101. J. K. LEE; G. L. GOULD, "Polydicyclopentadiene based aerogel: a new insulation material," *J. Sol-Gel Sci. Technol.*, **44**, *1*, 29-40 (2007).
102. R. FU et al., "Formation of graphitic structures in cobalt-and nickel-doped carbon aerogels," *Langmuir*, **21**, *7*, 2647-2651 (2005).
103. G. PAJONK, "Aerogel catalysts," *Applied Catalysis*, **72**, *2*, 217-266 (1991).

104. C. MORENO-CASTILLA; F. MALDONADO-HÓDAR, "Carbon aerogels for catalysis applications: An overview," *Carbon*, **43**, *3*, 455-465 (2005).
105. M. SCHNEIDER; A. BAIKER, "Aerogels in catalysis," *Catalysis Reviews*, **37**, *4*, 515-556 (1995).
106. J. S. KING et al., "Ultralow loading Pt nanocatalysts prepared by atomic layer deposition on carbon aerogels," *Nano letters*, **8**, *8*, 2405-2409 (2008).
107. P. TSOU, "Silica aerogel captures cosmic dust intact," *Journal of Non-Crystalline Solids*, **186**, 415-427 (1995).
108. M. J. BURCHELL et al., "Cosmic dust collection in aerogel," *Annu. Rev. Earth Planet. Sci.*, **34**, 385-418 (2006).
109. F. HÖRZ et al., "Impact features and projectile residues in aerogel exposed on Mir," *Icarus*, **147**, *2*, 559-579 (2000).
110. F. SABRI et al., "Investigation of Polyurea-Crosslinked Silica Aerogels as a Neuronal Scaffold: A Pilot Study," *PLoS ONE*, **7**, *3*, e33242 (2012).
111. J. CAI et al., "Cellulose–silica nanocomposite aerogels by in situ formation of silica in cellulose gel," *Angewandte Chemie*, **124**, *9*, 2118-2121 (2012).
112. F. LIEBNER et al., "Aerogels from Unaltered Bacterial Cellulose: Application of scCO2 Drying for the Preparation of Shaped, Ultra-Lightweight Cellulosic Aerogels," *Macromolecular bioscience*, **10**, *4*, 349-352 (2010).
113. M. BETZ et al., "Preparation of novel whey protein-based aerogels as drug carriers for life science applications," *The Journal of Supercritical Fluids*, **72**, 111-119 (2012).
114. F. LIEBNER et al., "Cellulose aerogels: highly porous, ultra-lightweight materials," *Holzforschung*, **62**, *2*, 129-135 (2008).
115. L. W. HRUBESH, "Aerogel applications," *Journal of Non-Crystalline Solids*, **225**, 335-342 (1998).
116. A. C. PIERRE; G. M. PAJONK, "Chemistry of aerogels and their applications," *Chemical Reviews*, **102**, *11*, 4243-4266 (2002).
117. N. HÜSING; U. SCHUBERT, "Aerogels—Airy Materials: Chemistry, Structure, and Properties," *Angewandte Chemie International Edition*, **37**, *1-2*, 22-45 (1998).

118. C. J. BRINKER; G. W. SCHERER, *Sol-gel science: the physics and chemistry of sol-gel processing*. Academic press: 2013.
119. M. DOMÍNGUEZ et al., "Co–SiO 2 aerogel-coated catalytic walls for the generation of hydrogen," *Catalysis Today*, **138**, *3*, 193-197 (2008).
120. P. A. LEVKIN et al., "Porous polymer coatings: a versatile approach to superhydrophobic surfaces," *Advanced functional materials*, **19**, *12*, 1993-1998 (2009).
121. J. A. HILLER et al., "Reversibly erasable nanoporous anti-reflection coatings from polyelectrolyte multilayers," *Nat Mater*, **1**, *1*, 59-63 (2002).
122. S. KIIL, "Quantitative analysis of silica aerogel-based thermal insulation coatings," *Progress in Organic Coatings*, **89**, 26-34 (2015).
123. P. SCHWAB et al., "Synthesis and applications of RuCl2(=CHR')(PR(3))(2): The influence of the alkylidene moiety on metathesis activity," *J. Am. Chem. Soc.*, **118**, *1*, 100-110 (1996).
124. N. LEVENTIS et al., "Polyimide Aerogels by Ring-Opening Metathesis Polymerization (ROMP)," *Chemistry of Materials*, **23**, *8*, 2250-2261 (2011).
125. A. G. BORST; J. W. A. VAN LOON, "Technology and Developments for the Random Positioning Machine, RPM," *Microgravity Sci. Technol.*, **21**, *4*, 287-292 (2009).
126. D. ROBIN et al., "Superbend upgrade on the Advanced Light Source," *Nucl. Instrum. Methods Phys. Res. Sect. A-Accel. Spectrom. Dect. Assoc. Equip.*, **538**, *1-3*, 65-92 (2005).
127. T. A. DAVIDSON; K. B. WAGENER, "The polymerization of dicyclopentadiene: an investigation of mechanism," *Journal of Molecular Catalysis A: Chemical*, **133**, *1–2*, 67-74 (1998).
128. M. R. KESSLER; S. R. WHITE, "Cure kinetics of the ring-opening metathesis polymerization of dicyclopentadiene," *J. Polym. Sci. Pol. Chem.*, **40**, *14*, 2373-2383 (2002).
129. G. YANG; J. K. LEE, "Curing Kinetics and Mechanical Properties of endo-Dicyclopentadiene Synthesized Using Different Grubbs' Catalysts," *Industrial & Engineering Chemistry Research*, **53**, *8*, 3001-3011 (2014).

130. G. O. WILSON et al., "Evaluation of ruthenium catalysts for ring-opening metathesis polymerization-based self-healing applications," *Chemistry of Materials*, **20**, *10*, 3288-3297 (2008).
131. G. YANG; J. K. LEE, "Effect of Grubbs' catalysts on cure kinetics of endo-dicyclopentadiene," *Thermochimica Acta*, **566**, 105-111 (2013).
132. A. BANG et al., "Polydicyclopentadiene aerogels from first- versus second-generation Grubbs' catalysts: a molecular versus a nanoscopic perspective," *J. Sol-Gel Sci. Technol.*, **75**, *2*, 460-474 (2015).
133. J. D. RULE; J. S. MOORE, "ROMP Reactivity of endo- and exo-Dicyclopentadiene," *Macromolecules*, **35**, *21*, 7878-7882 (2002).
134. R. H. GRUBBS, "Olefin-metathesis catalysts for the preparation of molecules and materials (Nobel lecture)," *Angew. Chem.-Int. Edit.*, **45**, *23*, 3760-3765 (2006).
135. X. SHENG et al., "Influence of cross-link density on the properties of ROMP thermosets," *Polymer*, **50**, *5*, 1264-1269 (2009).
136. H. H. WINTER, "Can the gel point of a cross-linking polymer be detected by the G′ – G″ crossover?," *Polymer Engineering & Science*, **27**, *22*, 1698-1702 (1987).
137. P. J. HALLEY; M. E. MACKAY, "Chemorheology of thermosets—an overview," *Polymer Engineering & Science*, **36**, *5*, 593-609 (1996).
138. F. J. V. SANTOS et al., "Standard Reference Data for the Viscosity of Toluene," *J. Phys. Chem. Ref. Data*, **35**, *1*, 1-8 (2006).
139. H. K. MOFFATT, "BEHAVIOR OF A VISCOUS FILM ON OUTER SURFACE OF A ROTATING CYLINDER," *Journal De Mecanique*, **16**, *5*, 651-673 (1977).
140. F. MELO, "Localized states in a film-dragging experiment," *Physical Review E*, **48**, *4*, 2704-2712 (1993).
141. D. TAKAGI; H. E. HUPPERT, "Flow and instability of thin films on a cylinder and sphere," *J. Fluid Mech.*, **647**, 221-238 (2010).
142. D. KANG et al., "Dynamics and equilibria of thin viscous coating films on a rotating sphere," *J. Fluid Mech.*, **791**, 495-518 (2016).
143. A. LEE et al., "Fabrication of slender elastic shells by the coating of curved surfaces," *Nat Commun*, **7**, (2016).

144. A. J. ROBERTS; Z. Q. LI, "An accurate and comprehensive model of thin fluid flows with inertia on curved substrates," *J. Fluid Mech.*, **553**, 33-73 (2006).
145. A. ORON et al., "Long-scale evolution of thin liquid films," *Rev. Mod. Phys.*, **69**, *3*, 931-980 (1997).
146. P. F. CHEN et al., "Inversion of Band Patterns in Spherical Tumblers," *Phys. Rev. Lett.*, **102**, *14*, (2009).
147. J. F. GILCHRIST; J. M. OTTINO, "Competition between chaos and order: Mixing and segregation in a spherical tumbler," *Physical Review E*, **68**, *6*, (2003).
148. S. W. MEIER et al., "A dynamical systems approach to mixing and segregation of granular materials in tumblers," *Adv. Phys.*, **56**, *5*, 757-827 (2007).
149. L. NAJI; R. STANNARIUS, "Axial and radial segregation of granular mixtures in a rotating spherical container," *Physical Review E*, **79**, *3*, (2009).
150. S. KIDA; K. NAKAYAMA, "Helical Flow Structure in a Precessing Sphere," *Journal of the Physical Society of Japan*, **77**, *5*, 054401 (2008).
151. F. AUTERI; L. QUARTAPELLE, "Navier–Stokes spectral solver in a sphere," *Journal of Computational Physics*, **228**, *19*, 7197-7214 (2009).
152. G. SEIDEN; P. J. THOMAS, "Complexity, segregation, and pattern formation in rotating-drum flows," *Rev. Mod. Phys.*, **83**, *4*, 1323-1365 (2011).
153. P. J. FLORY, *Principles of polymer chemistry*. Cornell University Press: 1953.
154. S. KOVACIC et al., "On the mechanical properties of HIPE templated macroporous poly(dicyclopentadiene) prepared with low surfactant amounts," *J. Mater. Chem. A*, **1**, *3*, 487-490 (2013).
155. N. R. CAMERON et al., Colloidal Templating. In *Porous Polymers*, John Wiley & Sons, Inc.: 2011; pp 119-172.
156. S. O. KUCHEYEV et al., "Depth-sensing indentation of low-density brittle nanoporous solids," *Acta Materialia*, **57**, *12*, 3472-3480 (2009).
157. L. J. GIBSON; M. F. ASHBY, *Cellular Solids: Structure and Properties*. 2 ed.; Cambridge University Press: Cambridge, 1997.
158. R. W. PEKALA et al., "Organic aerogels: microstructural dependence of mechanical properties in compression," *Journal of Non-Crystalline Solids*, **125**, *1*, 67-75 (1990).

159. T. PHAM et al., "Nanoscale structure and superhydrophobicity of sp 2-bonded boron nitride aerogels," *Nanoscale*, **7**, *23*, 10449-10458 (2015).
160. M. A. WORSLEY et al., "Toward Macroscale, Isotropic Carbons with Graphene-Sheet-Like Electrical and Mechanical Properties," *Advanced Functional Materials*, **24**, *27*, 4259-4264 (2014).
161. N. LEVENTIS et al., "Nanoengineering strong silica aerogels," *Nano letters*, **2**, *9*, 957-960 (2002).
162. A. C. FISCHER-CRIPPS, Contact mechanics. In *Nanoindentation*, Springer: 2011; pp 1-19.
163. W. C. OLIVER; G. M. PHARR, "An improved technique for determining hardness and elastic modulus using load and displacement sensing indentation experiments," *Journal of Materials Research*, **7**, *6*, 1564-1583 (1992).
164. J. S. FIELD; M. V. SWAIN, "A simple predictive model for spherical indentation," *Journal of Materials Research*, **8**, *2*, 297-306 (1992).
165. I. N. SNEDDON, "The relation between load and penetration in the axisymmetric boussinesq problem for a punch of arbitrary profile," *International Journal of Engineering Science*, **3**, *1*, 47-57 (1965).
166. H. HERTZ, *Miscellaneous papers*. Macmillan: 1896.
167. B. R. LAWN, "Indentation of ceramics with spheres: a century after Hertz," *J. Am. Ceram. Soc.*, **81**, *8*, 1977-1994 (1998).
168. S. BASU et al., "On the determination of spherical nanoindentation stress–strain curves," *Journal of Materials Research*, **21**, *10*, 2628-2637 (2011).
169. S. R. KALIDINDI; S. PATHAK, "Determination of the effective zero-point and the extraction of spherical nanoindentation stress–strain curves," *Acta Materialia*, **56**, *14*, 3523-3532 (2008).
170. M. SWAIN, "Mechanical property characterisation of small volumes of brittle materials with spherical tipped indenters," *Materials Science and Engineering: A*, **253**, *1*, 160-166 (1998).
171. AUTHOR, Oxford: 1951.
172. L. H. HE et al., "Elastic modulus and stress–strain response of human enamel by nano-indentation," *Biomaterials*, **27**, *24*, 4388-4398 (2006).

173. M. A. WORSLEY et al., "Mechanically robust and electrically conductive carbon nanotube foams," *Applied Physics Letters*, **94**, *7*, 073115 (2009).
174. J. GROSS et al., "Mechanical properties of SiO 2 aerogels," *Journal of Physics D: Applied Physics*, **21**, *9*, 1447 (1988).
175. A. BANG et al., "Polydicyclopentadiene aerogels from first- versus second-generation Grubbs' catalysts: a molecular versus a nanoscopic perspective," *J. Sol-Gel Sci. Technol.*, **75**, *2*, 460-474 (2015).
176. J. GROB; J. FRICKE, "Scaling of elastic properties in highly porous nanostructured aerogels," *Nanostructured Materials*, **6**, *5*, 905-908 (1995).
177. A. H. ALAOUI et al., "Comparison between flexural and uniaxial compression tests to measure the elastic modulus of silica aerogel," *Journal of Non-Crystalline Solids*, **354**, *40*, 4556-4561 (2008).
178. L. J. GIBSON; M. F. ASHBY "The mechanics of three-dimensional cellular materials", *Proceedings of the Royal Society of London A: Mathematical, Physical and Engineering Sciences*, The Royal Society (1982).
179. L. J. GIBSON, "The mechanical behaviour of cancellous bone," *Journal of Biomechanics*, **18**, *5*, 317-328 (1985).
180. H. FAN et al., "Modulus–density scaling behaviour and framework architecture of nanoporous self-assembled silicas," *Nat. Mater.*, **6**, *6*, 418-423 (2007).
181. A. BARTY et al., "Three-dimensional coherent x-ray diffraction imaging of a ceramic nanofoam: determination of structural deformation mechanisms," *Phys. Rev. Lett.*, **101**, *5*, 055501 (2008).
182. P. MEAKIN, "Formation of Fractal Clusters and Networks by Irreversible Diffusion-Limited Aggregation," *Phys. Rev. Lett.*, **51**, *13*, 1119-1122 (1983).
183. T. WOIGNIER et al., "Different kinds of structure in aerogels: relationships with the mechanical properties1," *Journal of Non-Crystalline Solids*, **241**, *1*, 45-52 (1998).
184. T. BRAUN et al., "In Situ Real-Time Radiographic Study of Thin Film Formation Inside Rotating Hollow Spheres," *ACS Applied Materials & Interfaces*, **8**, *4*, 2600-2606 (2016).
185. B. A. HAMMEL et al., "High-mode Rayleigh-Taylor growth in NIF ignition capsules," *High Energy Density Physics*, **6**, *2*, 171-178 (2010).

186. R. H. H. SCOTT et al., "Numerical Modeling of the Sensitivity of X-Ray Driven Implosions to Low-Mode Flux Asymmetries," *Phys. Rev. Lett.*, **110**, *7*, 075001 (2013).
187. C. DAWEDEIT Functional foam coatings inside tubing and custom developed diamond ignition targets.
188. C. DAWEDEIT et al., "Coating functional sol–gel films inside horizontally-rotating cylinders by rimming flow/state," *J. Sol-Gel Sci. Technol.*, 1-8 (2012).
189. P.-J. CHEN et al., "Low volume fraction rimming flow in a rotating horizontal cylinder," *Phys. Fluids*, **19**, *12*, 128107 (2007).
190. S. T. THORODDSEN; L. MAHADEVAN, "Experimental study of coating flows in a partially-filled horizontally rotating cylinder," *Exp. Fluids*, **23**, *1*, 1-13 (1997).
191. A. E. HOSOI; L. MAHADEVAN, "Axial instability of a free-surface front in a partially filled horizontal rotating cylinder," *Phys. Fluids*, **11**, *1*, 97-106 (1999).
192. R. E. JOHNSON, "STEADY-STATE COATING FLOWS INSIDE A ROTATING HORIZONTAL CYLINDER," *J. Fluid Mech.*, **190**, 321-342 (1988).
193. J. ASHMORE et al., "The effect of surface tension on rimming flows in a partially filled rotating cylinder," *J. Fluid Mech.*, **479**, 65-98 (2003).
194. D. R. LIDE, *CRC handbook of chemistry and physics*. CRC press: 2004.
195. B. J. KOZIOZIEMSKI et al., "Quantitative characterization of inertial confinement fusion capsules using phase contrast enhanced x-ray imaging," *J. Appl. Phys.*, **97**, *6*, (2005).
196. T. J. MURPHY et al., "Progress in the development of the MARBLE platform for studying thermonuclear burn in the presence of heterogeneous mix on OMEGA and the National Ignition Facility," *J. Phys., Conf. Ser.*, **717**, *1*, 012072 (2016).
197. A. KUHN, "On synaresis," *Kolloid-Z*, **46**, *4*, 299-314 (1928).
198. S. S. KISTLER et al., "Sorption and surface area in silica aerogel," *J. Am. Chem. Soc.*, **65**, 1909-1919 (1943).
199. S. S. PRAKASH et al., "Silica aerogel films prepared at ambient pressure by using surface derivatization to induce reversible drying shrinkage," *Nature*, **374**, *6521*, 439-443 (1995).
200. J. H. HARRELD et al., "Ambient pressure synthesis of aerogel-like vanadium oxide and molybdenum oxide," *Mater. Res. Bull.*, **33**, *4*, 561-567 (1998).

201. M. SCHWAN; L. RATKE, "Flexibilisation of resorcinol-formaldehyde aerogels," *J. Mater. Chem. A*, **1**, *43*, 13462-13468 (2013).
202. V. I. LOZINSKY et al., "Polymeric cryogels as promising materials of biotechnological interest," *Trends in Biotechnology*, **21**, *10*, 445-451 (2003).
203. Y. SI et al., "Ultralight nanofibre-assembled cellular aerogels with superelasticity and multifunctionality," *Nat Commun*, **5**, (2014).
204. H. JIN et al., "Nanofibrillar cellulose aerogels," *Colloids and Surfaces A: Physicochemical and Engineering Aspects*, **240**, *1–3*, 63-67 (2004).
205. E. DEGN EGEBERG; J. ENGELL, "FREEZE DRYING OF SILICA GELS PREPARED FROM SILICIUMETHOXID," *Journal de Physique Colloques*, **50**, *C4*, C4-23-C24-28 (1989).
206. D. KLVANA et al., "A NEW METHOD OF PREPARATION OF AEROGEL-LIKE MATERIALS USING A FREEZE-DRYING PROCESS," *Journal de Physique Colloques*, **50**, *C4*, C4-29-C24-32 (1989).
207. S. S. KISTLER, "Coherent expanded aerogels and jellies," *Nature*, **127**, 741-741 (1931).
208. D. W. SCHAEFER; K. D. KEEFER, "STRUCTURE OF RANDOM POROUS MATERIALS - SILICA AEROGEL," *Phys. Rev. Lett.*, **56**, *20*, 2199-2202 (1986).
209. D. W. MATSON; R. D. SMITH, "SUPERCRITICAL FLUID TECHNOLOGIES FOR CERAMIC-PROCESSING APPLICATIONS," *J. Am. Ceram. Soc.*, **72**, *6*, 871-881 (1989).
210. S. HENNING; L. SVENSSON, "Production of Silica Aerogel," *Physica Scripta*, **23**, *4B*, 697 (1981).
211. P. H. TEWARI et al., "Ambient-temperature supercritical drying of transparent silica aerogels," *Materials Letters*, **3**, *9*, 363-367 (1985).
212. P. WANG et al., "HIGH-TEMPERATURE AND LOW-TEMPERATURE SUPERCRITICAL DRYING OF AEROGELS - STRUCTURAL INVESTIGATIONS WITH SAXS," *J. Appl. Crystallogr.*, **24**, 777-780 (1991).
213. N. HÜSING et al., "Influence of supercritical drying fluid on structure and properties of organically modified silica aerogels," *Journal of Non-Crystalline Solids*, **186**, 37-43 (1995).

214. R. W. PEKALA, "ORGANIC AEROGELS FROM THE POLYCONDENSATION OF RESORCINOL WITH FORMALDEHYDE," *J. Mater. Sci.*, **24**, *9*, 3221-3227 (1989).

215. N. TONANON et al., "Preparation of resorcinol formaldehyde (RF) carbon gels: Use of ultrasonic irradiation followed by microwave drying," *Journal of Non-Crystalline Solids*, **352**, *52–54*, 5683-5686 (2006).

216. L. ZUO et al., "Polymer/Carbon-Based Hybrid Aerogels: Preparation, Properties and Applications," *Materials*, **8**, *10*, 5343 (2015).

217. L. M. SANZ-MORAL et al., "View cell investigation of silica aerogels during supercritical drying: Analysis of size variation and mass transfer mechanisms," *The Journal of Supercritical Fluids*, **92**, 24-30 (2014).

218. C. A. GARCIA-GONZALEZ et al., "Supercritical drying of aerogels using CO2: Effect of extraction time on the end material textural properties," *J. Supercrit. Fluids*, **66**, 297-306 (2012).

219. R. MUKHOPADHYAY, *Solid State Physics: Proceedings of the D. A. E. Solid State Physics Symposium*. University Press: 1999.

220. J. FOURIER, *Theorie analytique de la chaleur*. Chez Firmin Didot, père et fils: 1822.

221. A. FICK, "V. On liquid diffusion," *The London, Edinburgh, and Dublin Philosophical Magazine and Journal of Science*, **10**, *63*, 30-39 (1855).

222. J. CRANK, *The mathematics of diffusion / by J. Crank*. Clarendon Press: Oxford [England], 1975.

223. C.-C. LAI; C.-S. TAN, "Measurement of Molecular Diffusion Coefficients in Supercritical Carbon Dioxide Using a Coated Capillary Column," *Industrial & Engineering Chemistry Research*, **34**, *2*, 674-680 (1995).

224. Z. NOVAK; Ž. KNEZ, "Diffusion of methanol–liquid CO2 and methanol–supercritical CO2 in silica aerogels," *Journal of Non-Crystalline Solids*, **221**, *2–3*, 163-169 (1997).

225. P. WAWRZYNIAK et al., "Effective diffusion coefficient in the low temperature process of silica aerogel production," *Journal of Non-Crystalline Solids*, **285**, *1–3*, 50-56 (2001).

226. P. WAWRZYNIAK et al., "Diffusion of ethanol–carbon dioxide in silica gel," *Journal of Non-Crystalline Solids*, **225**, 86-90 (1998).
227. C. C. HAN; A. ZIYA AKCASU, "Concentration dependence of diffusion coefficient at various molecular weights and temperatures," *Polymer*, **22**, *9*, 1165-1168 (1981).
228. J. QUIÑO et al., "Supercritical drying of aerogel: In situ analysis of concentration profiles inside the gel and derivation of the effective binary diffusion coefficient using Raman spectroscopy," *The Journal of Supercritical Fluids*, **108**, 1-12 (2016).
229. A. B. JARZBSKI; J. LORENC, "Pore network connectivity and effective diffusivity of silica aerogels," *Chemical Engineering Science*, **50**, *2*, 357-360 (1995).
230. D. E. REILLY; E. M. PETERSON, "Self-Diffusion Coefficients and Rotational Correlation Times in Polar Liquids. III. Toluene," *The Journal of Chemical Physics*, **56**, *5*, 2262-2266 (1972).
231. C. R. WILKE; P. CHANG, "Correlation of diffusion coefficients in dilute solutions," *AIChE Journal*, **1**, *2*, 264-270 (1955).
232. G. DELLA PORTA et al., "Supercritical Drying of Alginate Beads for the Development of Aerogel Biomaterials: Optimization of Process Parameters and Exchange Solvents," *Industrial & Engineering Chemistry Research*, **52**, *34*, 12003-12009 (2013).
233. X. ZHENG et al., "Ultralight, ultrastiff mechanical metamaterials," *Science*, **344**, *6190*, 1373-1377 (2014).
234. S. A. SANDFORD et al., "Organics Captured from Comet 81P/Wild 2 by the Stardust Spacecraft," *Science*, **314**, *5806*, 1720-1724 (2006).
235. J. P. ARMSTRONG et al., "Micron-scale deep hole drilling for beryllium capsule fill applications," *Fusion Sci. Technol.*, **49**, *4*, 822-831 (2006).
236. P. GOBBY et al. "Low density gas and foam targets for ICF long scale length plasma experiments: Fabrication and characterization", *CONFERENCE SERIES-INSTITUTE OF PHYSICS*, IOP PUBLISHING LTD (1995).
237. M. A. MITCHELL et al., "Low density doped foams for ICF long scale length plasma experiments," *Fusion Sci. Technol.*, **28**, *5*, 1844-1848 (1995).

238. F. ITO et al., "Tin-Doped Resorcinol-Formaldehyde Aerogel with Decanano-Cell Structure," *Plasma and Fusion Research*, **4**, S1011-S1011 (2009).
239. K. B. FOURNIER et al., "Efficient multi-keV x-ray sources from Ti-doped aerogel targets," *Phys. Rev. Lett.*, **92**, *16*, 4 (2004).
240. C. E. HAMILTON et al., "Incorporation of Tracer Elements Within Aerogels and CH Foams," *Fusion Sci. Technol.*, **59**, *1*, 194-198 (2011).
241. J. HUND et al., "Silica, metal oxide, and doped aerogel development for target applications," *Fusion Sci. Technol.*, **49**, *4*, 669-675 (2006).
242. I. G. SCHNEIR; B. MCQUILLAN, "Preparation of a low density polymer foam with dopants," *Fusion Sci. Technol.*, **28**, *5*, 1849-1853 (1995).
243. W. P. STECKLE; A. NOBILE, "Low-density materials for use in inertial fusion targets," *Fusion Sci. Technol.*, **43**, *3*, 301-306 (2003).
244. R. E. OLSON et al., "Wetted foam liquid fuel ICF target experiments," *J. Phys., Conf. Ser.*, **717**, *1*, 012042 (2016).
245. C. CROIX et al., "New Gold-Doped Foams by Copolymerization of Organogold(I) Monomers for Inertial Confinement Fusion (ICF) Targets," *Journal of Inorganic and Organometallic Polymers and Materials*, **18**, *3*, 334-343 (2008).
246. L. MOREAU et al., "Recent advances in development of materials for laser target," *Laser and Particle Beams*, **27**, *04*, 537-544 (2009).
247. N. KEIJI et al., "Foam materials for cryogenic targets of fast ignition realization experiment (FIREX)," *Nucl. Fusion*, **45**, *11*, 1277 (2005).
248. N. KEIJI et al., "Fabrication of aerogel capsule, bromine-doped capsule, and modified gold cone in modified target for the Fast Ignition Realization Experiment (FIREX) Project," *Nucl. Fusion*, **49**, *9*, 095028 (2009).
249. C. M. DETTMER et al., "Synthesis and Functionalization of ROMP-Based Gradient Copolymers of 5-Substituted Norbornenes," *Macromolecules*, **37**, *15*, 5504-5512 (2004).
250. O. VOGL et al., "Head to head polymers," *Progress in Polymer Science*, **24**, *10*, 1481-1525 (1999).

251. P. P. M. A. DOLS et al., "Halogen addition to endo- and exo-tricyclo[5.2.1.02,6]deca-4,8-dien-3-ones," *Tetrahedron*, **49**, *48*, 11373-11382 (1993).

252. G. P. BAXTER et al., "THE VAPOR PRESSURE OF IODINE," *J. Am. Chem. Soc.*, **29**, *2*, 127-136 (1907).

253. H. J. KUIVILA et al., "ADDITION OF TRIMETHYLTIN HYDRIDE AND METHYLHALOTIN HYDRIDES TO NORBORNADIENE," *J. Org. Chem.*, **36**, *15*, 2083-& (1971).

254. J. D. KENNEDY et al., "PREPARATION AND PROPERTIES OF SOME TRIMETHYLTIN SUBSTITUTED BICYCLO 2.2.1 CARBOCYCLES, 3-NORTRICYCLYLTRIMETHYLTIN AND NORBORN-2-EN-7-YLTRIMETHYLSILANES," *J. Organomet. Chem.*, **61**, *1*, 167-177 (1973).

255. M. ZYDER; T. SZYMANSKA-BUZAR, "Hydrostannation of norbornadiene by (Bu3SnH)-Bu-n and Ph3SnH with molybdenum catalysts," *J. Organomet. Chem.*, **695**, *12-13*, 1734-1737 (2010).

256. J. L. KLINE et al., "Developing one-dimensional implosions for inertial confinement fusion science," *High Power Laser Science and Engineering*, **4**, (2016).

Auspices and Disclaimer

This work was performed under the auspices of the U.S. Department of Energy (DOE) by Lawrence Livermore National Laboratory under Contract DE-AC52-07NA27344. [LLNL-TH-712699] Part of the research in this thesis also used resources of the Advanced Photon Source, a U.S. Department of Energy Office of Science User Facility operated for the DOE Office of Science by Argonne National Laboratory under Contract No. DE-AC02-06CH11357 and the Advanced Light Source, which is a DOE Office of Science User Facility under contract no. DE-AC02-05CH11231.

List of Figures

EDUCATION

2018	**Technical University Darmstadt, Germany** PhD in Materials Science Thesis: “Synthesis and Characterization of Thin, Ultra-Low Density Functional Coatings in Hollow Spheres”, advisor: Prof. Dr.-Ing. Horst Hahn
2013	**Technical University Munich, Germany** MS in Physics Thesis: “Development of Aerogel-Lined Targets for Inertial Confinement Fusion Experiments”, advisor: Prof. Dr. Sibylle Günter, Scientific Director Max-Planck-Institute for Plasma Physics (IPP)
Fall 2012	**Argonne National Laboratory and Oak Ridge National Laboratory** 14th National School on Neutron and X-Ray Scattering
Fall 2010	**Max-Planck-Institute for Plasma Physics (IPP), Germany** IPP Summer University on Plasma Physics and Fusion Research
2010	**University of Granada, Spain** ERASMUS Student Exchange Program with Specialization in Theory of Fusion Physics and Data Transmission

ACADEMIC AWARDS

2016	Director's Science and Technology (S&T) Award, Lawrence Livermore National Laboratory
2016	Directorate Award, National Ignition Facility and Photon Science, Lawrence Livermore National Laboratory
2014	Director's Science and Technology (S&T) Award, Lawrence Livermore National Laboratory
2014	Excellence in Publication - Directorate Award, Physical and Life Sciences, Lawrence Livermore National Laboratory
2013	Scholarship, Sociedad Mexicana de Materiales and Materials Research Society
2013	Director's Science and Technology (S&T) Award, Lawrence Livermore National Laboratory
2012	Best Presentation Award, Argonne National Laboratory
2010	Scholarship, Advanced Technology Higher Education Network/Socrates
2010	Scholarship, ERASMUS Student Exchange Program
2009	Scholarship, MAN Foundation
2009	Award, German Energy Agency GmbH (DENA)
2008	Scholarship, Robert Bosch Foundation
2008	Scholarship, German Academic Exchange Service (DAAD)
2007	Scholarship, Robert Bosch Foundation
2007	Scholarship, Manage&More, UnternehmerTUM GmbH
2007	Scholarship, German Academic Exchange Service (DAAD)
2005	Scholarship, German National Academic Foundation (Studienstiftung)
2005	Award, German Physical Society (DPG)
2004	Award, Berlin Physical Society (PGzB)

PUBLICATIONS

1. **Confining cryogenic hydrogen in low-density nanoporous foams**

   T. Braun, T. M. Willey, K. J. Wu, B. Kozioziemski, J. Sater, J. Ilavsky, A. W. van Buuren, A.V. Hamza, and J. Biener

   In preparation

2. **Variable convergence liquid layer implosions on the National Ignition Facility**

   Zylstra, A. B., S. A. Yi, B. M. Haines, R. E. Olson, R. J. Leeper, T. Braun, J. Biener, J. L. Kline, S. H. Batha, L. B. Hopkins, S. Bhandarkar, P. A. Bradley, J. Crippen, M. Farrell, D. Fittinghoff, H. W. Herrmann, H. Huang, S. Khan, C. Kong, B. J. Kozioziemski, G. A. Kyrala, T. Ma, N. B. Meezan, F. Merrill, A. Nikroo, R. R. Peterson, N. Rice, J. D. Sater, R. C. Shah, M. Stadermann, P. Volegov, C. Walters, and D. C. Wilson

   Physics of Plasmas, **2018**, 25(5): 056304

3. **D2 and D-T Liquid-Layer Target Shots at the National Ignition Facility**

   C. Walters, E. Alger, S. Bhandarkar, K. Boehm, T. Braun, F. Espinosaloza, B. Haid, R. Heredia, J. Kline, B. Kozioziemski, J. Kroll, D. Malone, A. Nikroo, P. Opsahl, J. Sater, and A. Zylstra

   Fusion Science and Technology, **2018**, 73(3): 305-314

4. **Supercritical Drying of Wet Gel Layers Generated Inside ICF Ablator Shells**

   T. Braun, S. H. Kim, D. R. Malone, C. Walters, C. Dawedeit, M. M. Biener, A. V. Hamza, and J. Biener

   Fusion Science and Technology, **2018**, 73(2): 229-236

5. **Hugoniot and release measurements in diamond shocked up to 262 Mbar**

   M. C. Gregor, D. E. Fratanduono, C. A. McCoy, D. N. Polsin, J. R. Rygg, G. W. Collins, T. Braun, P. M.Celliers, J. H. Eggert, T. R. Boehly, and D. D. Meyerhofer

   Physical Review. B, **2017**, 95 (14), 144114

6. **Developing one-dimensional implosions for inertial confinement fusion science**

   J. L. Kline, S. A. Yi, A. N. Simakov, R. E. Olson, D. C. Wilson, G. A. Kyrala, T. S. Perry, S. H. Batha, E. L. Dewald, J. E. Ralph, D. J. Strozzi, A. G. MacPhee, D. A. Callahan, D. Hinkel, O. A. Hurricane, R. J. Leeper, A. B. Zylstra, R. R. Peterson, B. M. Haines, L. Yin, P. A. Bradely, R. C. Shah, T. Braun, J. Biener, B. J. Kozioziemski, J. D. Sater, M. M. Biener, A. V. Hamza, A. Nikroo, L. F. Berzak Hopkins, D. Ho, S. LePape, N. B. Meezan, D. S. Montgomery, W. S. Daughton, E. C. Merritt, T. Cardenas, and E. S. Dodd

   High Power Laser Science and Engineering, **2016**, 4 *(featured in themed section of High Energy Density Physics and High Power Laser 2016)*

7. **First Liquid Layer Inertial Confinement Fusion Implosions at the National Ignition Facility**

   R. E. Olson, R. J. Leeper, J. L. Kline, A. B. Zylstra, S. A. Yi, J. Biener, T. Braun, B. J. Kozioziemski, J. D. Sater, P. A. Bradley, R. R. Peterson, B. M. Haines, L. Yin, L. F. Berzak Hopkins, N. B. Meezan, C. Walters, M. M. Biener, C. Kong, J. W. Crippen, G. A. Kyrala, R. C. Shah, H. W. Herrmann, D. C. Wilson, A. V. Hamza, A. Nikroo, and S. H. Batha

   Physical Review Letters, **2016**, 245001 *(highlighted as Editor's Suggestion)*

8. **Wetted foam liquid fuel ICF target experiments**

   R.E. Olson, R.J. Leeper, S.A. Yi, J. L. Kline, A. B. Zylstra, R. R. Peterson, R. Shah, T. Braun, J. Biener, and B. J. Kozioziemski

   Journal of Physics: Conference Series, **2016**, 717 012042

PUBLICATIONS – continued

9. ***In situ* real-time radiographic study of thin film formation inside rotating hollow spheres**
   T. Braun, C. C. Walton, C. Dawedeit, M. M. Biener, S. H. Kim, T. M. Willey, X. Xiao, A. W. van Buuren, A. V. Hamza, and J. Biener
   ACS Applied Materials & Interfaces, **2016**, 8 (4)

10. **Ramp compression of diamond to five terapascals**
    R. F. Smith, J. H. Eggert, R. Jeanloz, T. S. Duffy, D. G. Braun, J. R. Patterson, R. E. Rudd, J. Biener, A. E. Lazicki, A. V. Hamza, J. Wang, T. Braun, L. X. Benedict, P. M. Celliers, and G. W. Collins
    Nature, **2014**, 511(7509) *(featured on cover)*

11. **Grain size dependent physical and chemical properties of thick CVD diamond films for high energy density physics experiments**
    C. Dawedeit, S. O. Kucheyev, S. J. Shin, T. M. Willey, M. Bagge-Hansen, T. Braun, Y. M. Wang, B. S. El-Dasher, N. E. Teslich, M. M. Biener, J. Ye, L. Kirste, C.-C. Roehlig, M. Wolfer, E. Woerner, A. W. van Buuren, A. V. Hamza, C. Wild, and J. Biener
    Diamond and Related Materials, **2013**, 40(0)

12. **Deterministic Control over High-Z Doping of Polydicyclopentadiene-based Aerogel Coatings**
    S. H. Kim, S. J. Shin, J. M. Lenhardt, T. Braun, J. D. Sain, C. A. Valdez, R. N. Leif, S. O. Kucheyev, K. J. J. Wu, J. Biener, J. H. Satcher, and A. V. Hamza
    ACS Applied Materials & Interfaces, **2013**, 5(16)

13. **Coating functional sol–gel films inside horizontally-rotating cylinders by rimming flow/state**
    C. Dawedeit, C. C. Walton, A. A. Chernov, S. H. Kim, M. A. Worsley, T. Braun, S. A. Gammon, J. H. Satcher, K. J. Wu, A. V. Hamza, and J. Biener
    Journal of Sol-Gel Science and Technology, **2013**, 65(2)

14. **A new approach to foam-lined indirect-drive NIF ignition targets**
    J. Biener, C. Dawedeit, S. H. Kim, T. Braun, M. A. Worsley, A. A. Chernov, C. C. Walton, T. M. Willey, S. O. Kucheyev, S. J. Shin, Y. M. Wang, M. M. Biener, J. R. I. Lee, B. J. Kozioziemski, T. van Buuren, K. J. J. Wu, J. H. Satcher, and A. V. Hamza
    Nuclear Fusion, **2012**, 52(6)

15. **Exploration of the versatility of ring opening metathesis polymerization: an approach for gaining access to low density polymeric aerogels**
    S. H. Kim, M. A. Worsley, C. A. Valdez, S. J. Shin, C. Dawedeit, T. Braun, T. F. Baumann, S. A. Letts, S. O. Kucheyev, K. J. J. Wu, J. Biener, J. H. Satcher, and A. V. Hamza
    RSC Advances, **2012**, 2(23)

16. **Tuning the rheological properties of sols for low-density aerogel coating application**
    C. Dawedeit, S. H. Kim, T. Braun, M. A. Worsley, S. A. Letts, K. J. Wu, C. C. Walton, A. A. Chernov, J. H. Satcher, A. V. Hamza, and J. Biener
    Soft Matter, **2012**, 8(13)

SELECTED CONFERENCE PRESENTATIONS

- **Forming ultra-low density aerogel layers inside of HDC capsules – talk**
  T. Braun, C. C. Walton, S. H. Kim, T. van Buuren, B. Kozioziemski, D. R. Malone, J. D. Sater, C. Walters, M. M. Biener, A. V. Hamza, M. Stadermann, A. Nikroo, and J. Biener
  MRS Spring Meeting & Exhibit, Phoenix, AZ, April 17 – 21, 2017

SELECTED CONFERENCE PRESENTATIONS – continued

- **Fabrication and Characterization of Wetted Foam Targets – talk**
  T. Braun, S. H. Kim, C. C. Walton, T. van Buuren, B. Kozioziemski, J. D. Sater, D. R. Malone, C. Walters, M. M. Biener, A. V. Hamza, M. Stadermann, A. Nikroo, and J. Biener
  22nd Target Fabrication Meeting, Las Vegas, NV, March 12-16, 2017

- **Wetted Foam Liquid Fuel ICF Target Experiments – talk**
  R.E. Olson, S.A. Yi, T. Braun, J. Biener, J.L. Kline, D.T. Casey, S. Le Pape, L. Berzak Hopkins, D. Ho, J.D. Sater, B.J. Kozioziemski, A.V. Hamza, R.R. Peterson, B.M. Haines, B. Hammel, R.C. Shah, D. Turnbull, L. Divol, S. Ross, N.B. Meezan, B.K. Spears, A.J. MacKinnon, S.H. Batha, R.J. Leeper
  9th International Conference on Inertial Fusion Sciences and Applications (IFSA 2015), Seattle, WA, September 20 – 25, 2015

- **Advances in Fabrication of ICF Targets – talk**
  M. Stadermann, C. Aracne - Ruddle, T. F. Baumann, S. H. Baxamusa, S. Bhandarkar, J. Biener, T. Braun, T. Bunn, P. Ehrmann, F. Espinosa - Loza, M. Farrell, S. A. Gammon, M. Havre, J. Hayes, B. Kozioziemski, T. Laurence, A. Nikroo, J. Sater, Y. M. Wang
  9th International Conference on Inertial Fusion Sciences and Applications (IFSA 2015), Seattle, WA, September 20 – 25, 2015

- **Mechanically robust graphene macro assemblies with hierarchical porosity: morphology control, functionalization, and energy storage applications – invited talk**
  P. G. Campbell, M. A. Worsley, T. Braun, B. C. Wood, T. F. Baumann, J. Biener
  XXIV International Materials Research Congress, Cancun, Mexico, August 16 – 20, 2015

- **Foam lined ignition targets – Integration of ultra-low density CH foam films into HDC capsules – talk**
  T. Braun, S. H. Kim, C. Dawedeit, C. C. Walton, T. M. Willey, T. van Buuren, M. A. Worsley, A. A. Chernov, M. M. Biener, K. J. Wu, J. H. Satcher, Jr., A. V. Hamza, and J. Biener
  21st Target Fabrication Meeting, Las Vegas, NV, June 21 – 25, 2015

- **Reduced convergence implosions using liquid layer wetted foam capsules on the National Ignition Facility – talk**
  S. A. Yi, R. E. Olson, R. J. Leeper, J. L. Kline, R. R. Peterson, B. M. Haines, R. C. Shah, S. H. Batha, T. Braun, J. Biener, M. M. Biener, A. V. Hamza, D. T. Casey, S. Le Pape, L. F. Berzak Hopkins, D. D. Ho, J. D. Sater, B. J. Kozioziemski, B. A. Hammel, D. P. Turnbull, L. Divol, J. S. Ross, N. B. Meezan, B. K. Spears, and A. J. MacKinnon
  45th Annual Anomalous Absorption Conference, Ventura Beach, CA, June 14 – 19, 2015

- **Forming ultra-low density foam layers inside of diamond capsules – talk**
  T. Braun, C. C. Walton, S. H. Kim, C. Dawedeit, T. M. Willey, T. van Buuren, M. M. Biener, A. V. Hamza, and J. Biener
  Postgraduate Seminar Series, Darmstadt, Germany, May 2015

- **Functionalized Graphene Macro Assemblies – talk**
  P. G. Campbell, T. Braun, M. A. Worsley, T. F. Baumann, and J. Biener
  MRS Spring Meeting & Exhibit, San Francisco, CA, April 6 – 10, 2015

- **In-situ Real-Time Radiographic Study of Thin Film Formation Inside Rotating Hollow Spheres – talk**
  T. Braun, C. C. Walton, S. H. Kim, T. M. Willey, T. van Buuren, C. Dawedeit, M. A. Worsley, A. A. Chernov, K. J. Wu, J. H. Satcher, Jr., A. V. Hamza, and J. Biener
  MRS Spring Meeting & Exhibit, San Francisco, CA, April 21 – 25, 2014

SELECTED CONFERENCE PRESENTATIONS – continued

- **Ring Opening Metathesis Polymerization Approach to Low Density Polymeric Aerogel Coatings on Non-planar Substrates and Its Doping with High-Z Atoms – talk**
  S. H. Kim, C. Dawedeit, T. Braun, J. M. Lenhardt , C. A. Valdez, S. J. Shin, M. A. Worsley, S. O. Kucheyev, K. J. J. Wu, J. Biener, J. H. Satcher and A. V. Hamza
  MRS Spring Meeting & Exhibit, San Francisco, CA, April 1 – 5, 2013

PROFESSIONAL MEMBERSHIPS

Member, German Physical Society (DPG)

Member, Materials Research Society (MRS)

Member, Model United Nations TU München MUNTUM e.V.

ACTIVITIES

2013 – present	Member in the Lawrence Livermore Postdoc Association
	• Developed career and social networking opportunities for students and postdocs and acted as a conduit between the students, postdocs, and Lab management
2009 – 2011	Deputy Chairman of Model United Nations TU Munich Society
	(Model United Nations TU München MUNTUM e.V.)
Spring 2007	Harvard University World Model United Nations
	Head Delegate for Technical University Munich
2005 – 2010	Student President, Department of Physics

LANGUAGES

German	mother tongue
English	business fluent
Spanish	fluent